



Metallography

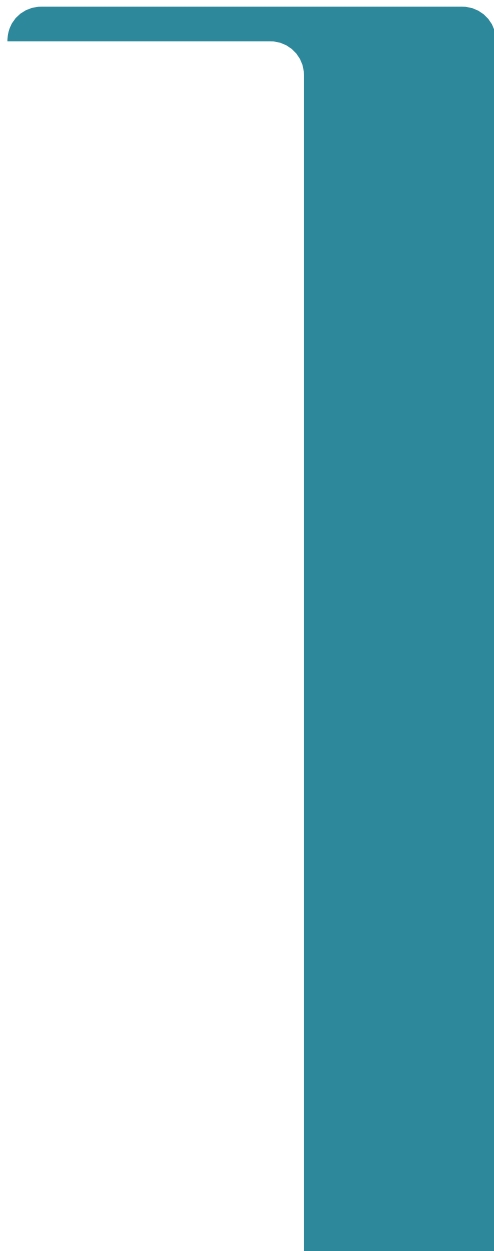
Höganäs Handbook for Sintered Components

6

Metallography

Handbook for Sintered Components

© Copyright Höganäs AB (publ.), 2015 / 0886HOG. All rights reserved.
Höganäs Handbook Metallography is intended for customer use.
The data presented in the handbook has been obtained
from test specimens, sintered under well-controlled conditions,
in the Höganäs laboratory. Note that data established
for any particular production equipment or conditions
may differ from those presented in this handbook.
All trademarks mentioned in this handbook are owned by Höganäs AB,
Sweden and are registered in all major industrial countries.



Metallography

Theory 7

1.1 Nomenclature	8
1.2 Equilibrium Phase Diagrams and Microstructures . . .	17
1.3 Phase Transformations and Microstructures	35
1.4 Diffusion of alloying Elements and Microstructure . . .	61
1.5 Mechanical Properties and Microstructures	86

Metallographic Atlas 99

2.1 Sponge Iron Powder	101
2.2 Atomised Iron Powder	125
2.3 Diffusion Alloyed Grades	143
2.4 Pre-alloyed Powder	159
2.5 Stainless Steel Powder	173
2.6 Continuous Cooling Transformation (CCT).	179
2.7 Heat Treatment	247
2.8 Index	264

Metallographic Sample Preparation 273

3.1 General Considerations	274
3.2 Cutting	276

3.3 Mounting	277
3.4 Mechanical Preparation	278
3.5 Etching	280
Defective Microstructures	285
4.1 Defects in Pressing	286
4.2 Defects in Mixing and Powder Feeding	289
4.3 Defects in Sintering	291
4.4 Defects after Secondary Operation	298
4.5 Defects after Sample Preparation	299
4.6 Defects in Heat Treatment	300

Foreword

The main purpose of this handbook is to guide the reader when interpreting microstructures of manufactured ferrous powder materials common in iron powder metallurgy (PM). The handbook focuses on microstructures obtained after sintering. Some attention is also given to microstructures obtained with sintering followed by heat treatment.

This Metallographic Handbook will be of particular help in creating metallographic competence among producers of PM parts. It will help build appreciation of what a powerful tool metallography can be (e.g. in solving various types of quality problems and as a most effective mean for quality control). The reader will appreciate the importance of knowing how such processing can change microstructures in a desired direction.

The handbook contains a theoretical foundation, a metallographic atlas, a guide for metallographic work and a chapter showing common defects in sintered components. The theoretical discussion covers common nomenclature used for visualised phases and structures of metallographic specimens. Binary phase diagrams are used to explain the relative quantity of different phases and structures present in materials studied with a metallic microscope. The influence of cooling rates on the microstructures of defined materials is explained with phase transformation diagrams (TTT/CCT). Microstructural changes obtained with variations in sintering temperature and/or time are explained in terms of diffusion phenomena. Strength levels of phases and structures present in defined materials are also discussed, in relation to the overall performance of each material.

The metallographic atlas in this handbook includes a collection of images of metallographic structures. The atlas will serve as a reference guide for microstructures of ferrous materials common in iron powder metallurgy. The handbook will also guide the reader in metallographic preparation, and help when selecting appropriate metallographic equipment.

The final chapter of the handbook presents images showing various common microstructural defects in sintered and/or heat treated components. This will be useful when analysing defects to determine their probable causes.

Acknowledgments

Special thanks is due to Monica Carlsson who prepared the high quality micrographs. Images of this standard are necessary for accurate analysis of the structures and phases presented in this volume.

Theory

1.1	Nomenclature	8
1.2	Equilibrium Phase Diagrams and Microstructures	17
1.3	Phase Transformations and Microstructures . .	35
1.4	Diffusion of alloying Elements and Microstructure	61
1.5	Mechanical Properties and Microstructures . .	86

1.1 Nomenclature

In metallographic literature many designations are used to describe metallic phases and structures. In this metallographic handbook only the most common designations of phases and structures are used.

A range of basic and important PM material structures are defined in this chapter according to standard micrographic terminology.

1.1.1 Ferrite

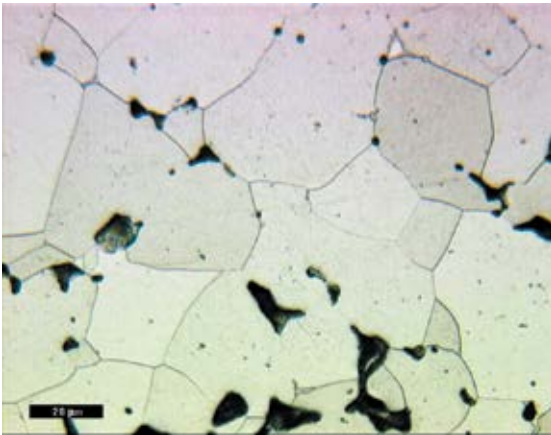


Figure 1.1 Example of ferritic microstructure.

The material in *figure 1.1* is ASC100.29 (atomised iron powder grade) which has been etched with 1% Nital. This etchant attacks the grain boundaries and reveals the grain structure of the ferrite material.

1.1.2 Pearlite

In *figure 1.2* pearlite is illustrated. The material is ASC100.29 + 0.75% C etched with 1% Nital.

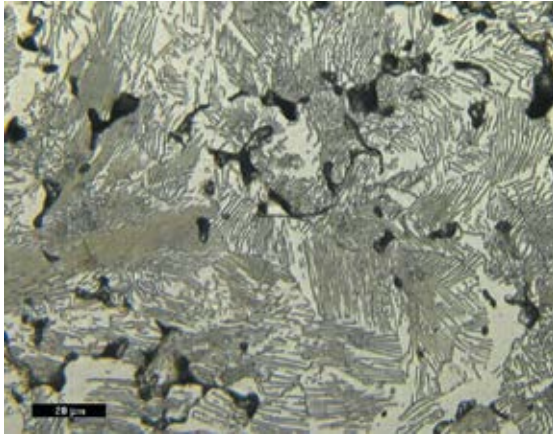


Figure 1.2 Example of pearlitic microstructure

Pearlite is a lamellar aggregate of ferrite and cementite (Fe_3C), formed when austenite is cooled at a slow rate. Pearlite starts to form just below the eutectoid temperature (see section 1.2.2.4 on page 25) according to the reaction below:



During pearlite formation, austenite transforms to ferrite, having low carbon concentration (α -phase), and to cementite (Fe_3C) which has high carbon concentration. For carbon atoms to segregate to the cementite phase, diffusion is necessary. Carbon atoms diffuse away from the ferrite region to the cementite layers, giving a concentration of 6.7 wt.-% C. The layered pearlite forms because the carbon atoms need to diffuse only minimal distances within this structure*.

Nucleation of pearlite usually occurs at the austenite grain boundaries. The pearlite assumes a nodular form and the nodules grow in all directions. Usually the nucleation of new pearlite nodules continues during slow cooling, until all the available austenite grain boundary area is occupied. The growth of each nodule proceeds until impingement with other nodules occurs**.

* "Material Science and Engineering-An introduction" William D. Callister, John Wiley & Sons, Inc. 1985.

** "Die Ferri Metallographia II", Verlag Stahleisen M. B. H., 1966.

During etching ferrite is attacked and the typical lamella structure can be observed. The pearlite structure has an average carbon content of 0.8%.

In metallurgy literature very fine pearlite is sometimes called troostite or sorbite. Here only the designations pearlite or *fine pearlite* are used. The term fine pearlite is used when the pearlite lamellas cannot be resolved by means of a metallic microscope.

1.1.3 Cementite

When carbon content exceeds 0.8%, cementite appears with a characteristic network pattern at the grain boundaries. This is called grain boundary cementite (*see figure 1.3*).

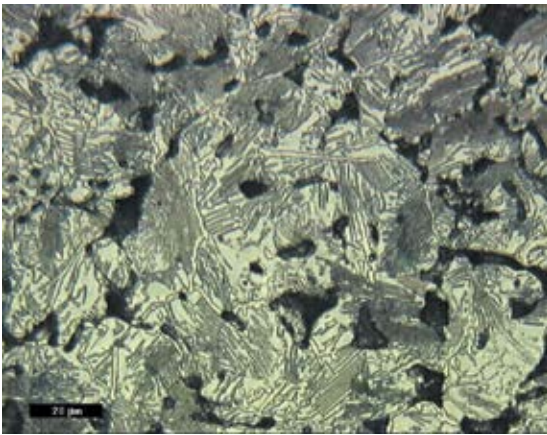


Figure 1.3 Example of cementite network in the grain boundaries.

The material is NC100.24 + 1% C etched with 1% Nital. Cementite is very hard and brittle and should be avoided in grain boundaries for performance reasons.

1.1.4 Bainite

Bainite consists of a non-lamellar aggregate of ferrite and carbides. The principal variants of bainite in steels are called upper bainite and lower bainite. See *figures 1.4* and *1.5* respectively.

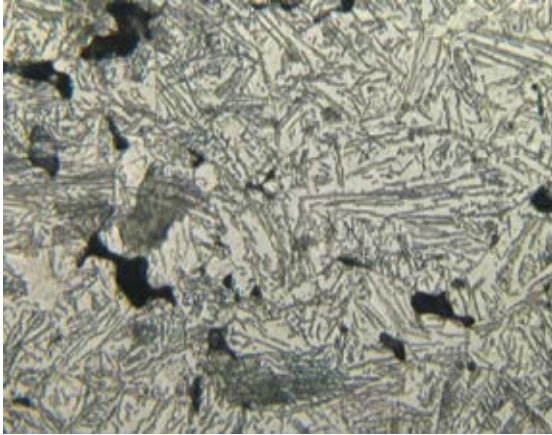


Figure 1.4 Example of upper bainite structure.

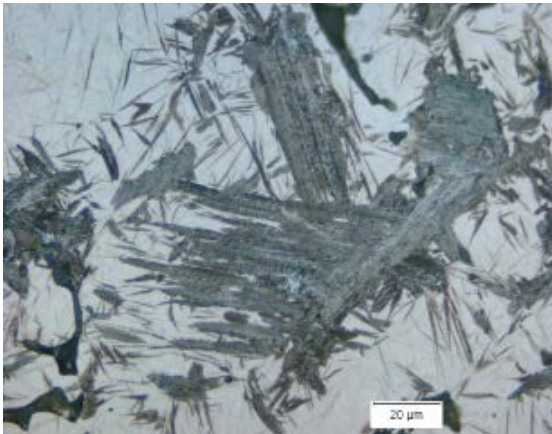


Figure 1.5 Example of lower bainite structure.

The distinction between upper and lower bainite is based on whether the carbides are distributed between the individual ferrite regions (upper bainite) or within them (lower bainite). The diffusion rate of carbon during formation of lower bainite is so slow that the carbon atoms cannot move fast enough to avoid getting trapped inside the fast growing ferrite platelets. The formation of upper bainite or lower bainite is also determined by whether the transformation temperature is above or below approximately 350°C. The transition temperature varies depending on the content of alloying elements in the material*.

1.1.5 Martensite

Martensite is formed by rapidly cooling austenite to temperatures below approximately 200°C. In contrast to ferrite and cementite, martensite is a phase resulting from a diffusionless transformation of austenite. The martensitic transformation occurs almost instantaneously when the cooling rate is rapid enough to prevent diffusion.

With increased carbon content, martensite needles appear coarser and darker after etching.

*"Material Science and Engineering-An introduction" William D. Callister, John Wiley & Sons, Inc. 1985.

Examples of martensite with different carbon content are shown in *figures 1.6* and *1.7* respectively.

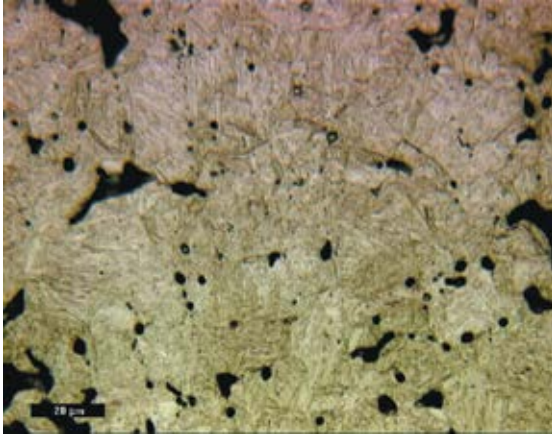


Figure 1.6 Example of martensite having low carbon content.

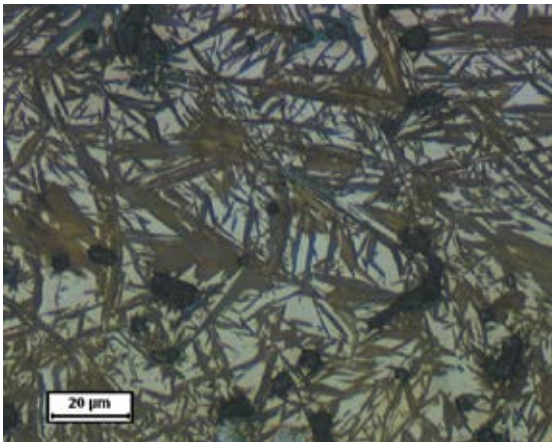


Figure 1.7 Example of martensite having high carbon content.

1.1.6 Austenite

Austenite is often found in sintered steel products made from partially pre-alloyed powders (the so called diffusion alloyed grades). Austenite areas are white with a diffuse border to the martensite (*figure 1.8*).

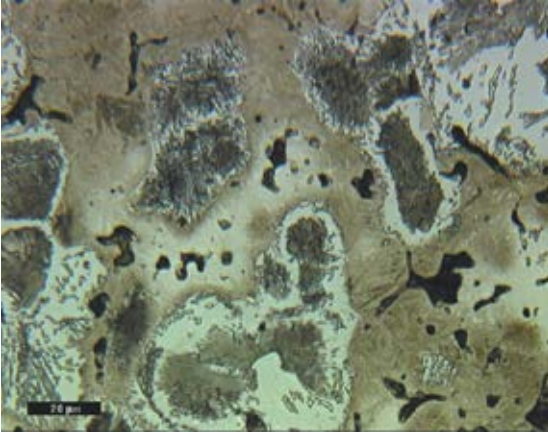


Figure 1.8 Example of austenite present in heterogeneous structure.

Austenite is sometimes found at the surface of heat-treated steels (e.g. carburised or carbonitrided) when the carbon content is high. Its appearance is due to the carbon stabilising the austenite, *see figure 1.9*.

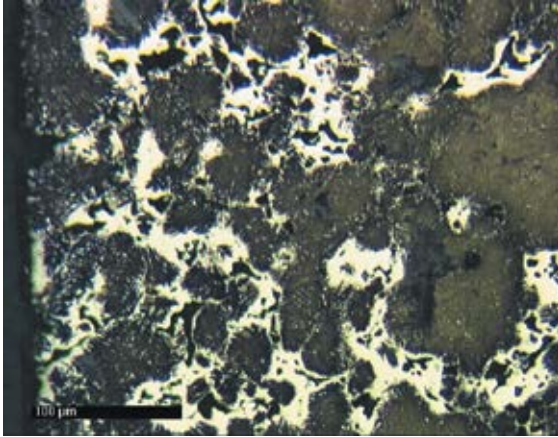


Figure 1.9 Example of austenite present at the surface of carburised material.

In austenitic stainless steels twins are often found which makes it possible to distinguish this phase from the ferritic phase (*figure 1.10*).

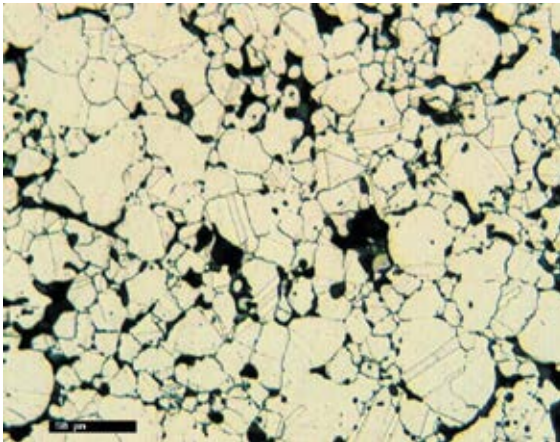


Figure 1.10 Example of austenitic microstructure.

1.1.7 Multiphase structure

Materials based on Distaloy® contain all the phases and structures described above and are therefore very illustrative (*figure 1.11*).

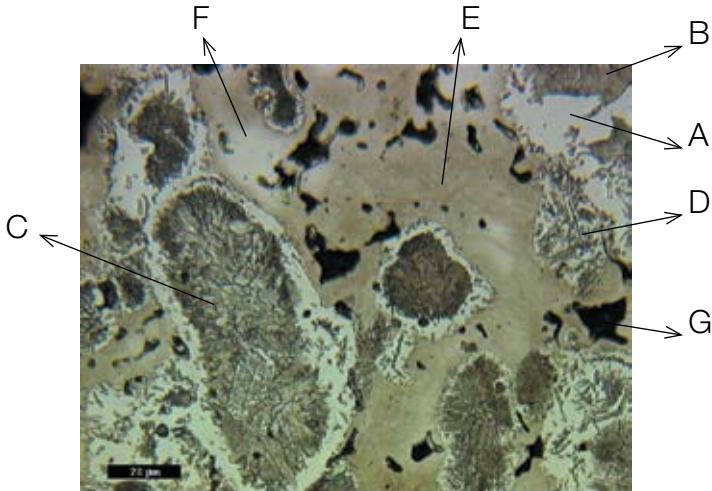


Figure 1.11 Example of multi phase structure present in heterogeneous materials.

The letters in *figure 1.11* refer to the following phases:

- | | |
|-------------------|----------------|
| A = Ferrite | E = Martensite |
| B = Pearlite | F = Austenite |
| C = Fine Pearlite | G = Pores |
| D = Upper Bainite | |

1.2 Equilibrium Phase Diagrams and Microstructures

This section deals with the principal construction of different types of binary phase diagrams. The most important phase diagrams used in iron powder metallurgy are discussed, along with an outline of how/when these can explain what is observed in material microstructures.

The main limitation when using phase diagrams to describe visualised phases and structures is that actual structures seldom show conditions at equilibrium. On the other hand, an understanding of phase diagrams will help the reader to realise what is happening in the material during formation of the phases and structures.

Of all binary alloy systems, the most important is that of iron and carbon. However, in practice the metastable Fe-C system is used rather than the stable Fe-C system. The metastable system is the more significant when explaining the actual structures found in components. Metastability means that most of the phases and structures seen are not thermodynamically stable.

In this section metallographic structures are explained by looking mainly at binary phase diagrams (i.e. two-element systems). When there are more than two elements present in the material, which is most often the case in practice, ternary or quaternary systems, or even more complex element systems, should be used to explain the metallographic structures.

However, the interpretation of ternary and more complex phase systems is difficult. Although most PM steels contain more than two elements, the microstructure can be explained, with good approximation, by using the respective binary systems. But it should be remembered that ternary (etc.) base systems are important to fully explain the microstructures of many high-alloyed steels.

More detailed information on phase diagrams is found elsewhere in the Höganäs Handbook for Sintered Components (see Handbook 1, Chapters 1.4 and 1.5).

1.2.1 Introduction

Some clarification of terminology is required to ensure understanding of further discussion related to phase diagrams. Several key terms are defined below.

Much of the information about the control of the microstructure of a particular alloy system is displayed in what is known as a *phase diagram* (also often termed an equilibrium diagram). Many microstructures develop from phase transformations, the changes that occur between phases when the temperature is altered. This may involve a transformation from one phase to another, or the appearance or disappearance of a phase.

Equilibrium phase diagrams represent the relationship between temperature and the compositions and the quantities of phases at equilibrium. External pressure is also a parameter that influences phase structure. However, in most practical processing of PM steels, pressure remains constant at approximately one atmosphere, and thus the phase diagrams presented here are for constant pressure in one atmosphere.

Not all types of microstructures can be explained by using equilibrium diagrams. For example, these diagrams are not helpful for through-hardened and case-hardened materials.

1.2.2 Equilibrium phase diagrams

1.2.2.1 Binary isomorphous system

Binary diagrams (two-element systems) can be established by means of thermal analysis. The most elementary binary system is when both elements are completely soluble in both the liquid and in the solid state. An important example of this is the system Cu-Ni. In *figure 1.12* a schematic representation of the cooling behaviour of various compositions in such a system is illustrated in conjunction with the phase diagram.

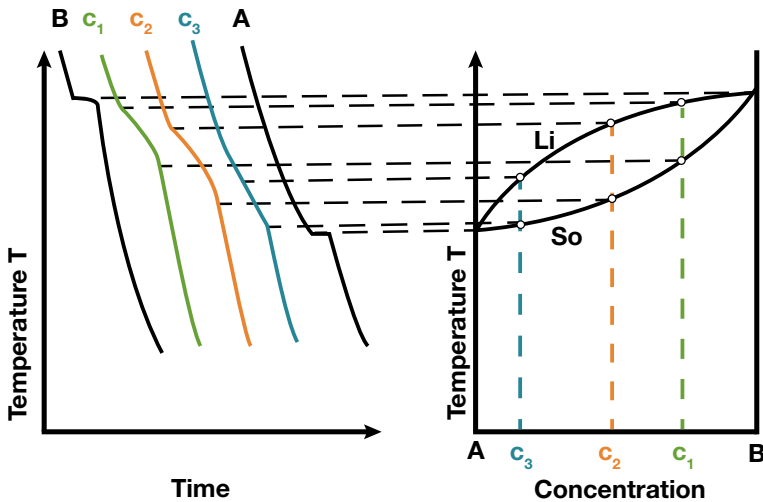


Figure 1.12 Experimental derivation of a phase diagram by means of thermal analysis. Left: cooling curves for two pure metals (A and B) and for three of their alloys (c_1 , c_2 and c_3). Right: phase diagram derived from cooling curves.

When the pure element (A or B) is transformed from liquid phase to solid phase during cooling, heat is generated which results in temperature plateaux. However, when a liquid alloy containing both A and B (c_1 , c_2 or c_3) is cooled, there is a temperature interval during solidification when both liquid and solid exist. A reduced cooling rate occurs during this temperature interval because heat is continuously generated when solid crystals are precipitated from the liquid. The formed crystals continue to grow until the melt is consumed and a single solid phase is formed. At any particular temperature, a maximum of two phases (liquid and solid) can exist in this system.

The above phase diagram shows the relative content of the solid and liquid phases, at any temperature, for any average composition of the material. The phase diagram for such a complete solid soluble system shows a liquidus line (Li) and a solidus line (So). The Lever Rule of Phases defines the relative content of solid and liquid phases present at any given temperature. In *figure 1.13* the Lever Rule of Phases is presented in schematic form. This diagram shows how the rule can be used for calculations, as explained below.

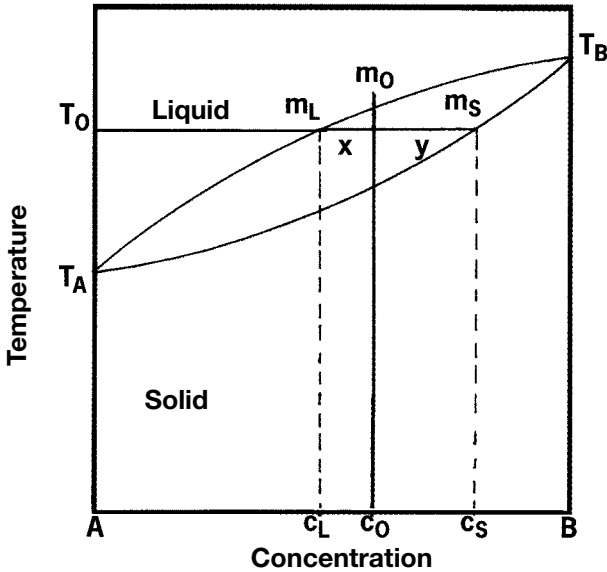


Figure 1.13 The Lever Rule of Phases: m_0 = initial amount of molten alloy with concentration c_0 ; m_L and m_S are the respective amounts of liquid and solid phases present at temperature T_0 ; c_L and c_S are the corresponding concentrations in the liquid and solid phases.

According to the diagram, when the temperature at T_0 is reached for a melt with an average composition c_0 , the residual melt has the mass m_L (with the composition c_L) and the formed solid has the mass m_S (with the composition c_S). The Lever Rule of Phases states that the distance x times m_L equals the distance y times m_S .

By studying this melt which is cooled to room temperature, we see that the solidified structure will reach a composition which follows the solidus line, and the remaining liquid will reach a composition which follows the liquidus line. When the average composition of the material passes the solidus line the entire melt has solidified. As the solidified material will have compositions deviating from the average composition, solid state diffusion occurs and concentration differences gradually disappear with time, under ideal conditions.

Frequently, during solidification of molten alloys, a characteristic phenomenon called *crystal segregation* occurs (i.e. a concentration gradient inside individual crystal grains of the solidified alloy). For more details see Handbook 1, Chapter 1.4.4, of the Höganäs Handbook for Sintered Components.

Metallographic study of materials in the binary isomorphous system will reveal homogeneous structures. By making grain boundary etchings, the grain size of the material can be evaluated. In *figure 1.14*, grain boundary etching has been performed on a completely ferritic unalloyed powder steel.

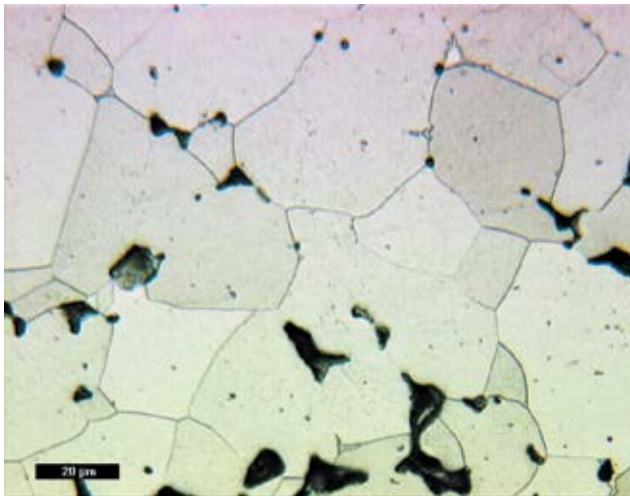


Figure 1.14 Example of microstructure in a one phase system (ferrite).

1.2.2.2 Binary eutectic system

Another type of common and relatively simple phase diagram is found for alloy materials in the binary eutectic system. See *figure 1.15* (an important example is the system Al-Si).

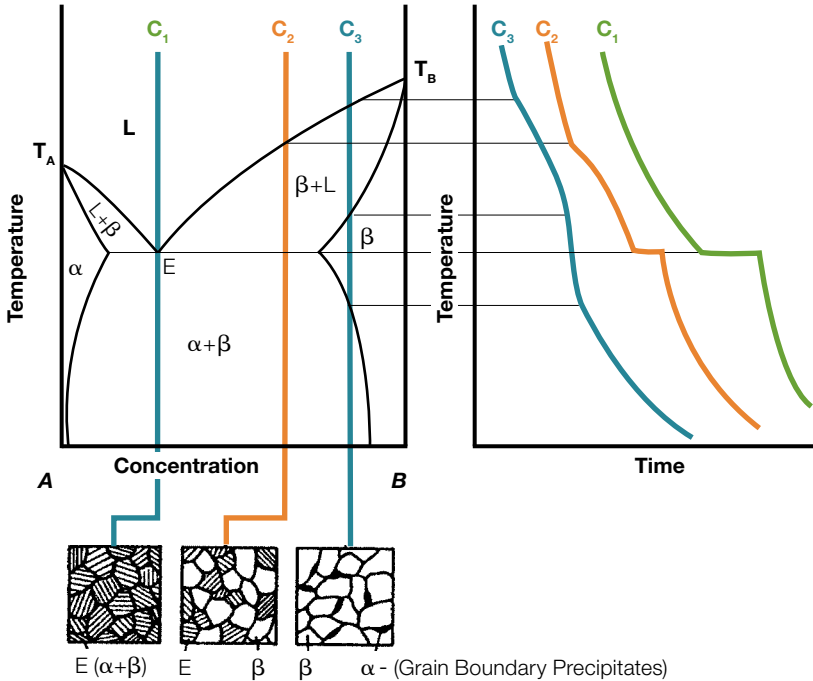


Figure 1.15 Experimental derivation of the phase diagram for a eutectic system of two components A and B.

This is known as binary eutectic phase diagram. In the eutectic system the liquid is miscible in all proportions, as in isomorphous systems, but miscibility in the solid state is limited.

The distinctive feature of eutectic system is that three phases (viz. a solid A-rich α -phase, a solid B-rich β -phase, and a liquid phase L) can exist in equilibrium at the temperature called the eutectic temperature. The equilibrium relation between the three phases is represented in *figure 1.15*, by the eutectic line.

Alloys with three different chemical compositions (c_1 , c_2 , c_3) are to be studied. The composition c_1 is often called eutectic composition.

In the solid state, a metallographic study reveals a structure with two phases each of the compositions c_2 and c_3 respectively, and a eutectic structure with the composition c_1 .

Composition c_2 shows a pro-eutectic beta phase and a eutectic structure consisting of alpha and beta phases. The average composition of the material at the eutectic temperature shows the relative content of the pro-eutectic phase and a eutectic structure (alpha phase + beta phase), as per the Lever Rule of Phases. The two phases generally co-precipitate when the eutectic point is reached, resulting in a regular appearance of the structure when examined microscopically. Normally the eutectic structure appears striped due to a cut-effect (as can be seen in white cast iron, for example). There is a change in the solid solubility of the respective elements in each other, when the temperature is lowered. Thus the relation pro-eutectic phase/eutectic structure in the solidified material at the eutectic temperature differs somewhat from that predicted by the Lever Rule of Phases.

Composition c_1 shows an entire eutectic structure consisting of alpha phase + beta phase. The material solidifies at one and the same temperature (i.e. the eutectic temperature) according to the reaction:

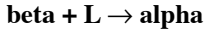


The formation speed of the structure is governed by the diffusion rate of A and B atoms to the respective alpha phase and beta phase, plus the effect of heat transfer.

Composition c_3 results primarily in a one-phase structure. This cannot be separated in a metallographic section unless grain boundary etching is performed and the different grains are visualised. The alpha phase starts to precipitate preferentially at the grain boundaries, when the material is cooled below the border line alpha+beta and beta.

1.2.2.3 Binary Peritectic Systems:

The distinctive feature of binary peritectic systems is that a formed solid phase reacts with the liquid phase in the system. Thus a new solid phase is formed according to the reaction:



Due to the consumption of the solid phase this reaction is slow compared to eutectic reactions where the structure is formed entirely from a liquid phase. A typical peritectic system is Cu-Sn (bronze). In this case we will study four different compositions in a schematic peritectic system (*figure 1.16*).

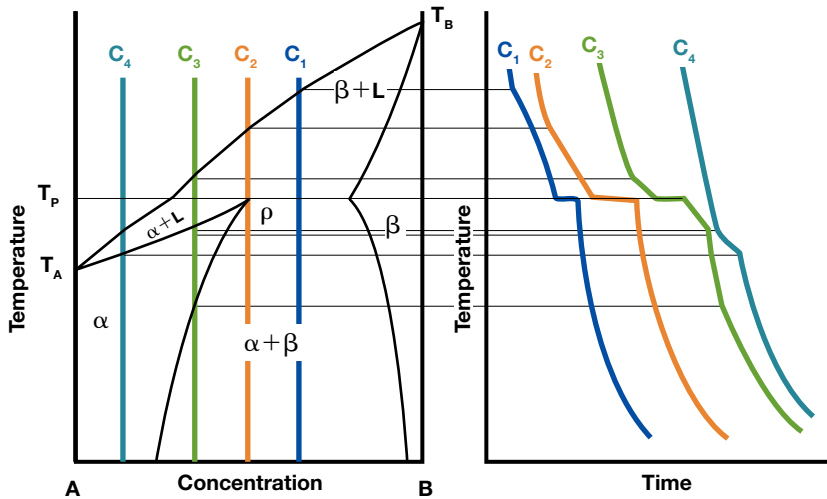


Figure 1.16 Experimental derivation of the phase diagram of a peritectic system of two components A and B.

Composition c_1 shows a precipitated solid beta phase reacting at the peritectic temperature with the remaining liquid phase, so that an alpha phase is formed. For melts with composition c_2 , the liquid phase and the solid beta phase are consumed, and an alpha phase is formed.

In composition c_3 all of the beta phase is consumed together with the liquid phase. From the remaining liquid an alpha phase is formed. Composition c_4 will only produce an alpha phase after solidification.

1.2.2.4 The Binary System Fe-C:

The Fe-C system is of major importance to understanding of formed structures in iron powder metallurgy. In *figure 1.17* the entire Fe-C binary phase diagram is described.

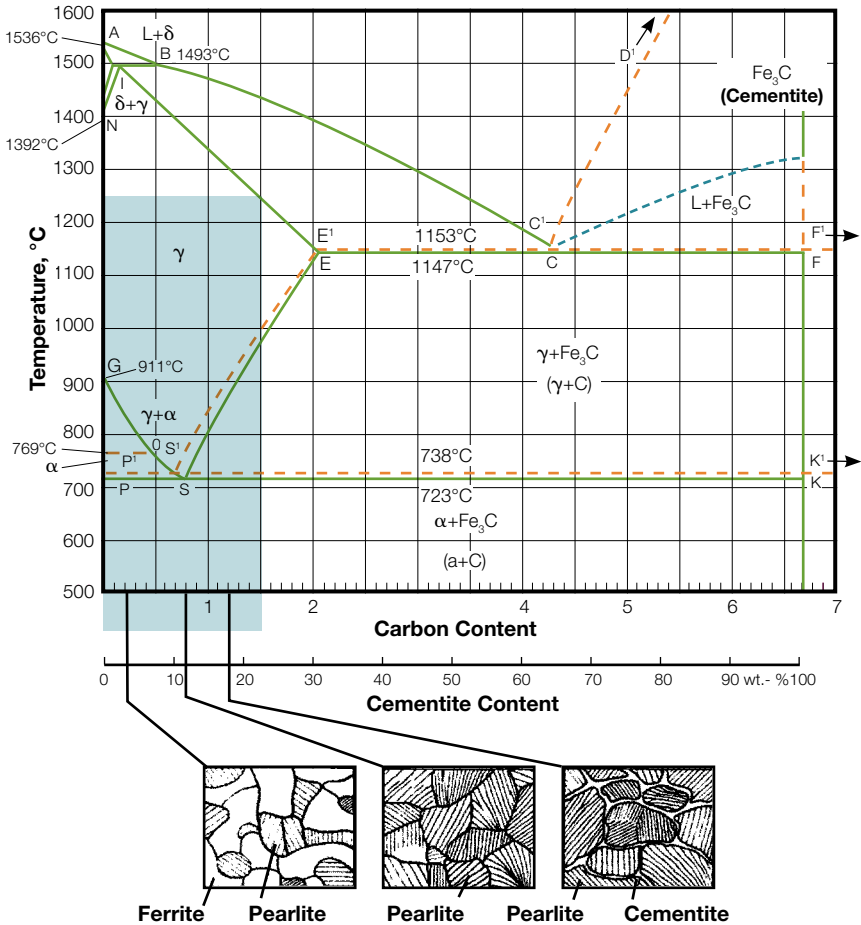


Figure 1.17 Equilibrium phase diagram of the system Fe-C (fully drawn lines = metastable system; dotted lines = stable system).

Three sub-diagrams can be distinguished in *figure 1.17*:

- a) one peritectic, situated at low carbon and high temperatures
- b) one eutectic which is the basis for the formation of all types of cast irons
- c) one eutectoid diagram being the most important one in the case of sintered steel, marked with a square in *figure 1.17*.

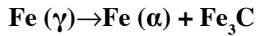
The eutectoid reaction is analogous to the eutectic one, but it involves one solid phase which is transferred to two other solid phases.

Pure Fe appears in different modifications during cooling down from the liquid state. Fe solidifies to δ -Fe (or ferrite with BCC-structure) at 1536°C. BCC is short for body centered cubic. During further cooling the δ -Fe transforms into γ -Fe (or austenite with FCC-structure) at 1392°C. FCC is short for face centered cubic. The austenite modification is kept until 911°C where it transforms again to α -Fe (or ferrite with BCC-structure). α -Fe is ferro-magnetic below 769°C. Fe alloyed with C up to approximately 2% is referred to as steel and Fe with higher C-content is referred to as cast iron. Steel structures are governed by the binary eutectoid part of the phase diagram Fe-C and cast irons are governed by the binary eutectic part of the phase diagram Fe-C. As soon as there is liquid which has undergone eutectic solidification the material is a cast iron. Fe together with C forms the phase Fe_3C (cementite). Cementite is a meta-stable phase because when annealed for long times at high temperatures it decomposes to iron and graphite.

Depending on whether carbon occurs as bonded in cementite or as free graphite, the corresponding phase diagram Fe-C is referred to as meta-stable (presence of cementite) or stable (presence of graphite). Transformations in steel and in white cast irons proceed according to the meta-stable system (fully drawn lines), while transformations in graphite-containing grey cast irons proceed according to the stable system (dotted lines). For practical purposes, steel components are formed according to what is found in the meta-stable phase diagram Fe-C.

During cooling of Fe-C alloys (with less than approximately 2% C) the transformation from austenite to ferrite and cementite occurs in the solid state. If the carbon content is below 0.8% (hypoeutectoid steels) pro-eutectoid ferrite first appears in the old austenite grain boundaries, down to the eutectoid temperature.

At the eutectoid temperature the remaining austenite starts to transform into pearlite according to the following reaction (eutectoid reaction):



Pearlite is a lamellar structure formed by ferrite and cementite. The relative content of cementite and ferrite in pearlite is determined according to the Lever Rule of Phases. The average C-content in pearlite is approximately 0.8% i.e. equal to the eutectoid composition.

If the carbon content is exceeding 0.8% (hypereutectoid steels) pro eutectoid cementite will first appear in the old austenite grain boundaries down to the eutectoid temperature. At the eutectoid temperature the remaining austenite starts to transform into pearlite.

The carbon content of a sintered material can be estimated on a metallographic section from the area fraction of pearlite where 100% pearlite is equivalent to approximately 0.8% carbon. Carbon dissolves rapidly in iron at temperatures normally used during sintering of carbon steels and it is unusual to see uncombined carbon in sintered steels.

1.2.2.5 The Binary System Fe-Cu

Copper is a very common alloying element in iron powder metallurgy and is one of the first alloying elements used to improve the performance of PM parts. Copper cannot be used in wrought steels due to severe hot working problems. The Fe-Cu phase diagram is reported in *figure 1.18*.

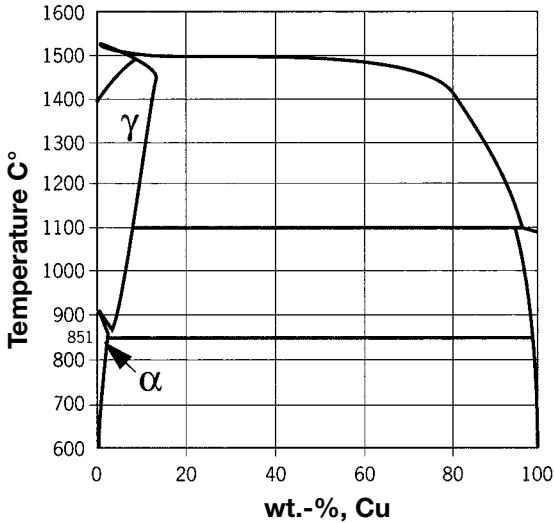


Figure 1.18 A schematic representation of the phase diagram Fe-Cu.

This diagram can, however, seldom be used when explaining the microstructure in Cu-alloyed steels. The reason is that Cu additions to PM steels can be made with a variety of copper grades or copper “carriers” such as

- elemental additions with different particle sizes (e.g. Cu-100, Cu-200)
- partially prealloyed alloys or master alloys (e.g. Distaloy[®] AE, Distaloy[®] Cu)
- fully prealloyed master alloys (e.g. Astaloy[™] 20 Cu)

This means that in practice Cu is seldom fully homogenised on a micro-structural level after sintering. Consequently, the phase diagram has limited use because the Cu concentration in the visualised structure is uneven.

During sintering Cu melts which gives a fast distribution of copper over the matrix followed by diffusion into the iron particles (and Fe diffuses into the Cu-melt). The diffusion rate is low for Cu in Fe but there is sufficient diffusion to enable effective strengthening of the material.

According to the phase diagram, at very long times an iron rich phase and a Cu-rich phase will occur in the system Fe-Cu. This will however never appear in practice and due to the relative slow diffusion rate of Cu in Fe at sintering temperatures normally used (approximately 1120°C), no homogeneous distribution of Cu will occur on a micro scale (where the observation is done). On a macro scale the material behaves like it was fully homogeneous. A typical microstructure of sintered Fe-Cu material is showed in the following *figure 1.19*.

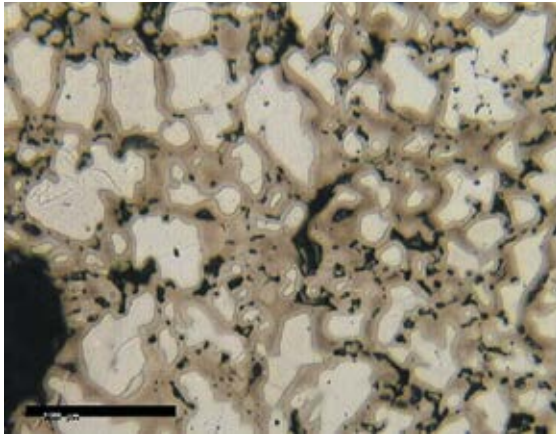


Figure 1.19 Microstructure of sintered Fe-Cu material.

When Fe-Cu material is etched, Cu-rich areas appear as a brown-yellow network. It is easy to see in this material that the Cu phase is close to the large pores. This is logical, since the Cu was initially concentrated in between the original iron particles where the pores remain after sintering.

1.2.2.6 The Binary System Fe-P

Phosphorous is a common element in powder metallurgy and similar to Cu it can be used to improve performance in PM but cannot be used in ingot metallurgy due to heavy segregation during solidification, which leads to the formation of a brittle P-rich phase. Unlike Cu, P is ferrite stabilising which can be seen in the phase diagram where the austenite area shrinks when increasing the P-content in Fe (*figure 1.20*).

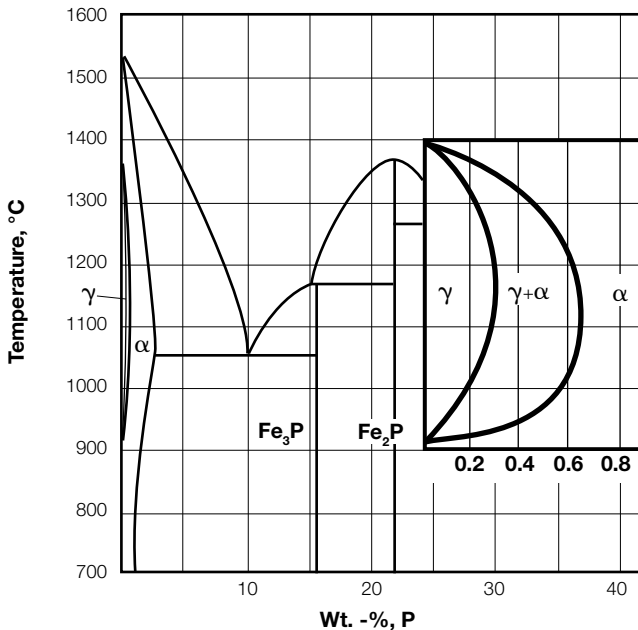


Figure 1.20 Binary phase diagram Fe-Fe₃P with eutectic at 1050°C.

Normally, P is added to a powder mix as Fe₃P. During heating to the sintering temperature, the Fe₃P melts. Via capillary forces the melt penetrates the area between the original iron particles. Contrary to what happens in the Fe-Cu system, sintering occurs in the ferrite phase (where the local P-content is high), which means the sintering process is enhanced. This is evident in the microstructure (*see figure 1.21*) where the pores are much more rounded than in other common PM systems which stabilise austenite, such as Fe-Cu and Fe-Ni.

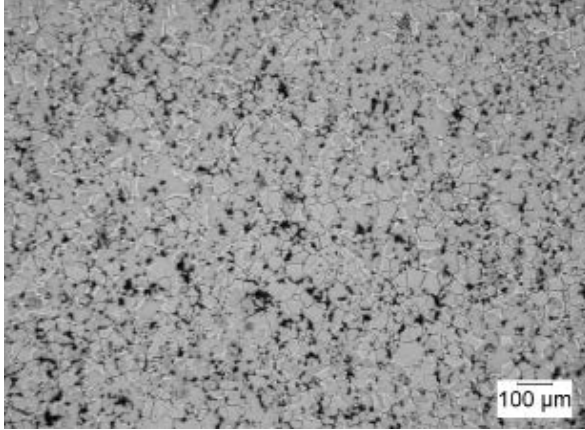


Figure 1.21 Microstructure of sintered Fe-P material.

1.2.2.7 The Binary Systems Fe-Ni and Fe-Mo

Nickel and Molybdenum are both common elements in iron powder metallurgy. Ni is an austenite stabilising element and Mo is a ferrite stabilising element. This is clearly seen in the respective phase diagrams: (*figures 1.22 and 1.23*).

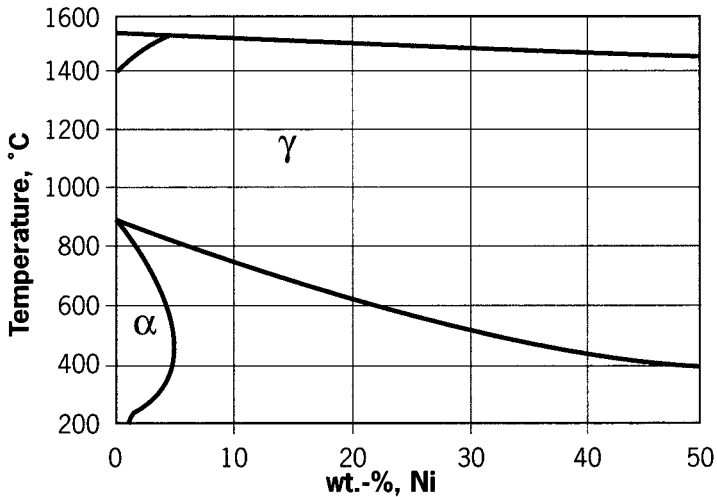


Figure 1.22 A schematic representation of the phase diagram Fe-Ni.

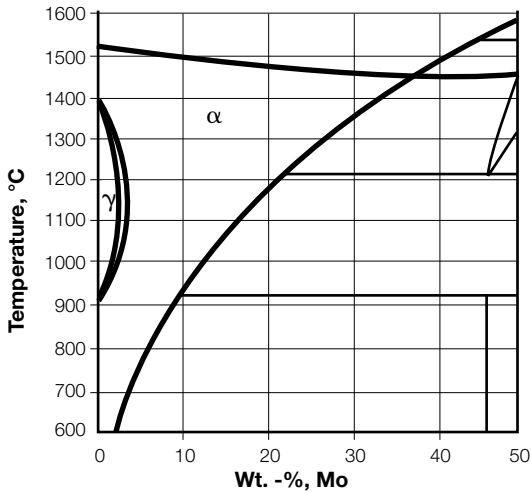


Figure 1.23 A schematic representation of the phase diagram Fe-Mo.

In the Fe-Ni system, the austenite area swells when the Ni content is increased, while in the Fe-Mo system, the austenite area shrinks when the Mo content is increased. In the pure Fe-Ni and Fe-Mo systems, the respective microstructures do not reveal any specific features because only a single phase appears in these systems.

In commercial PM alloys the Ni-content seldom exceeds approximately 5%. However, in heterogeneous PM steels, such as diffusion alloyed grades, the Ni content locally exceed approximately 8%. In this case, austenite phase is present in the material.

1.2.2.8 Diffusion alloyed materials

Diffusion alloyed materials are based either on pure iron powder (SC100.26 or ASC100.29) or fully prealloyed powder (Astaloy™ Mo*). The characteristic of diffusion alloyed materials is that the alloying elements (Ni, Cu, Mo) are bonded by diffusion to the base powder. The material is diffusion bonded or partially prealloyed.

The microstructure below (*figure 1.24*) shows a typical sintered structure of Distaloy® AE + 0.5% C processed at 1120°C for 30 minutes. Distaloy AE is partially prealloyed with 1.5% Cu, 4% Ni and 0.5% Mo. After sintering, carbon (fast diffusion rate) is homogeneously distributed through the material but Cu, Ni and Mo (slow diffusion rate) are heterogeneously distributed.

When etched microstructures of diffusion alloyed materials are observed, the binary system Fe-C can be distinguished. However, a number of ternary systems (i.e. 3-element systems) are also distinguished. These are based upon Fe-C but with either Cu, Ni or Mo as the third element.

The areas shown in *figure 1.24* are structures which are revealed from phase diagrams of different alloying systems. Each area is described below the figure.

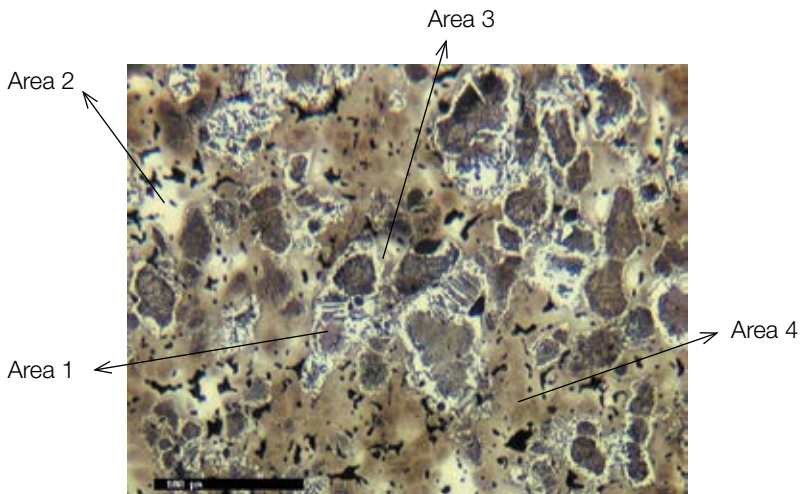


Figure 1.24 Microstructure of sintered Distaloy AE + 0.5% C.

* Astaloy Mo is a water atomised steel powder prealloyed with 1.5% Mo.

Area 1 is an example of Fe-C system where pearlite is distinguished but to some extent disturbed (deformed pearlite pattern) during the formation. The disturbances are coming from the other alloying elements and mainly Mo which stabilises the α -phase and therefore diffuses more rapidly than Cu and Ni do. The diffusion rate in α -phase is approximately 100 times higher than in γ -phase.

Area 2 is an example of Fe-Ni-C system where the elements Ni and C stabilise the austenite phase.

Area 3 is an example of Fe-Mo-C where the relatively good diffusion rate of Mo into the original iron particles forms bainite together with C. This is due to the fact that Mo improves hardenability which means that the formation of pearlite and ferrite is suppressed by Mo (see Section 1.3.4).

Area 4 is an example of Fe-Cu-C system where Cu (which diffuses somewhat slower than Mo) and C forms martensite due to the increased hardenability of Cu and C which suppress the formation of ferrite, pearlite and bainite. Therefore martensite is formed during cooling. Due to the slow diffusion rate of Cu, no martensite is found in the center of the original iron powder particles. Ni diffuses even slower than Cu which is the reason that austenite areas (containing more than approximately 8% Ni) is found in the structure.

1.3 Phase Transformations and Microstructures

In this chapter the influence of the cooling rate on the microstructure of commonly used PM steels is examined. This is preceded by a short discussion regarding the kinetics of phase transformations in iron-carbon alloys. Time-Temperature-Transformation (or TTT) diagrams and Continuous-Cooling-Transformation (or CCT) diagrams are also taken into account.

1.3.1 Introduction

There are several types of phase transformations in the solid state phase and they can be classified as follows:

- a) Allotropic transformations in which there is a change in the crystal structure, but not in the number and composition of the phases present, as is for example the case for iron. During cooling the iron lattice transforms from BCC* to FCC** at 1392°C and then transforms again from FCC to BCC at 911°C.
- b) Transformations in which changes in phase compositions and often in the number of phases present take place (e.g. precipitation, eutectoid reactions etc.). These transformations imply the movement of atoms through the lattice of distances that are at least as great as the interatomic distance. The movement of atoms through the crystal lattice is called diffusion.
- c) Order-disorder transformations in which an ordered structure is formed. Normally in substitutional solid solutions the solute atoms are distributed at random in the lattice structure of the solvent. Some of these solid solutions, when cooled down slowly, undergo a rearrangement of atoms where the solute atoms move into well defined positions in the crystal lattice.
- d) Martensitic or diffusionless transformations in which a new phase is formed by co-operative movement of atoms from a position in the crystal lattice to a neighbouring one. During a martensitic transformation the atoms move through a distance which is a fraction of the interatomic distance.

* BCC: Body centered cubic. See Handbook 1. Chapter 1 for further information

** FCC: Face centered cubic. See Handbook 1. Chapter 1 for further information

In this Metallographic Handbook the attention will be posed on the transformations described in points b) and d).

In Section 1.2 phase diagrams (or equilibrium diagrams) were examined. These diagrams summarise the phase changes that occur in metals and alloys. The state of a system which is in equilibrium depends on the variables of temperature, pressure and chemical composition. However, for most phase transformations in the solid state, pressure can be assumed as constant at the atmospheric value. Thus the equilibrium structure is a function only of temperature and chemical composition.

Phase diagrams show the phase or phases that exist at equilibrium when changes are made to the temperature and composition of a given alloy.

One limitation of phase diagrams is that they do not give any information regarding the rate, i.e. the kinetics of a phase transformation. Information regarding the time required for a transformation to start and to finish, at a given temperature, can be found in the isothermal transformation diagrams, also called *time-temperature-transformation* (or TTT) diagram. Information regarding the transformations occurring during continuous cooling can be found in CCT-diagrams.

Equilibrium structures are achieved only if an alloy is heated or cooled at extremely slow rates. In practice, phase transformations tend to occur at slightly higher or lower temperatures than indicated in the equilibrium phase diagram, depending upon the rate at which the alloy is heated or cooled. The higher the cooling or heating rate, the greater the shift towards lower or higher transformation temperatures.

Figure 1.25 shows the displacement of austenite-to-ferrite and austenite-to-pearlite transformations when the cooling rate is increased for a steel containing 0.45% carbon. As can be observed, the austenite-to-ferrite transformation moves more quickly to lower temperatures than the austenite-to-pearlite transformation. As a consequence, when the cooling rate is increased, the formation of proeutectoid ferrite is reduced more and more, and eventually suppressed. At higher cooling rates, new phases are formed, such as bainite and martensite.

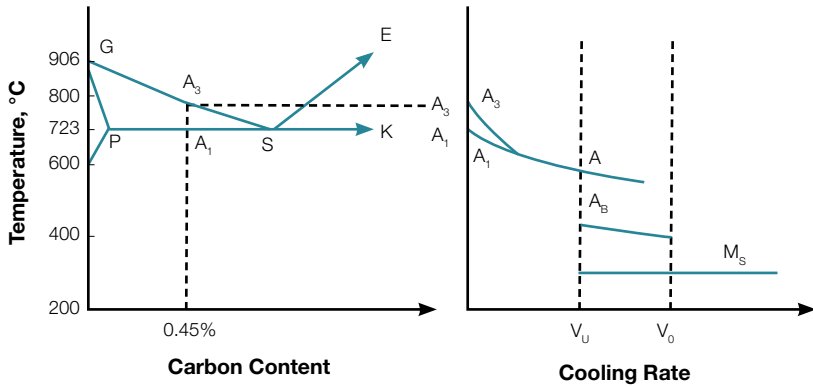


Figure 1.25 Influence of the cooling rate on the temperature of austenite-to-ferrite and austenite-to-pearlite transformations for an iron-carbon alloy with 0.45% C*.

1.3.2 The kinetics of solid state transformations

During a phase transformation in the solid state, two stages can be distinguished: nucleation and growth. During the first stage very small particles, or nuclei, of the new phase precipitate from the “mother” phase. The nuclei of the new phase precipitate preferentially at imperfections sites such as grain boundaries. During the second stage the nuclei, which incidentally exceed a critical minimum size, is growing. The transformation reaches completion, if growth of the new phase particles is allowed to proceed until the equilibrium is achieved.

The growth rate of the new phase is proportional to the residue of untransformed mother-phase, i.e. at the beginning, the new phase grows fast, but as the amount of mother phase decreases the growth rate of the new phase decreases. *Figure 1.26* shows the typical kinetic behaviour of many isothermal solid state transformations. In this diagram the fraction of material that has transformed at a given temperature is reported as a function of the time.

* W. Schatt, Einführung in die Werkstoffkunde, VEB Deutscher Verlag für Grundstoffindustrie, Leipzig 1981.

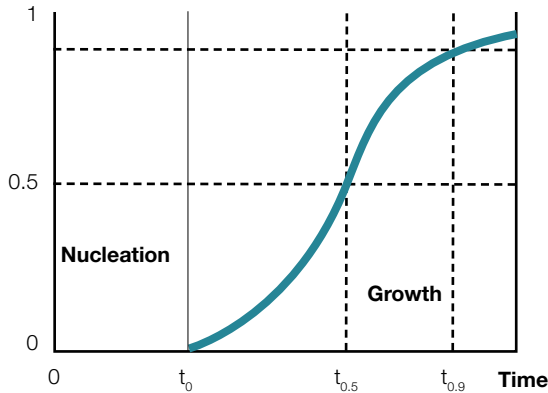


Figure 1.26 S-shaped curve typical for most solid state transformations. Nucleation and growth stage can be observed.

1.3.3 Phase transformations in Fe-C alloys: TTT and CCT-diagrams

1.3.3.1 Austenite-to-pearlite transformation

The austenite-to-pearlite transformation is diffusion-dependent. As all diffusion-dependent transformations its rate is a function of the temperature. Information regarding the time required for austenite to begin to transform, to proceed half-way and to be completely transformed, at a given temperature, is reported in TTT-diagrams. Information about the construction of TTT-diagrams can be found in Handbook 1. Chapter 1.6.1.

The TTT-diagram for an Fe-C alloy of eutectoid composition is reported in figure 1.27. This diagram shows the time required, at a given temperature, for austenite to transform. The two solid curves in the diagram represents the time required at each temperature for the austenite to start and finish to transform. The dashed curve corresponds instead to 50% of transformation completion. To the left of the transformation start curve, only austenite (unstable) will be present. To the right of the finish curve mixes of ferrite and carbides will be present while in the areas between the two solid lines, austenite will coexist with pearlite. The eutectoid reaction (727°C) is represented in the diagram by a horizontal line.

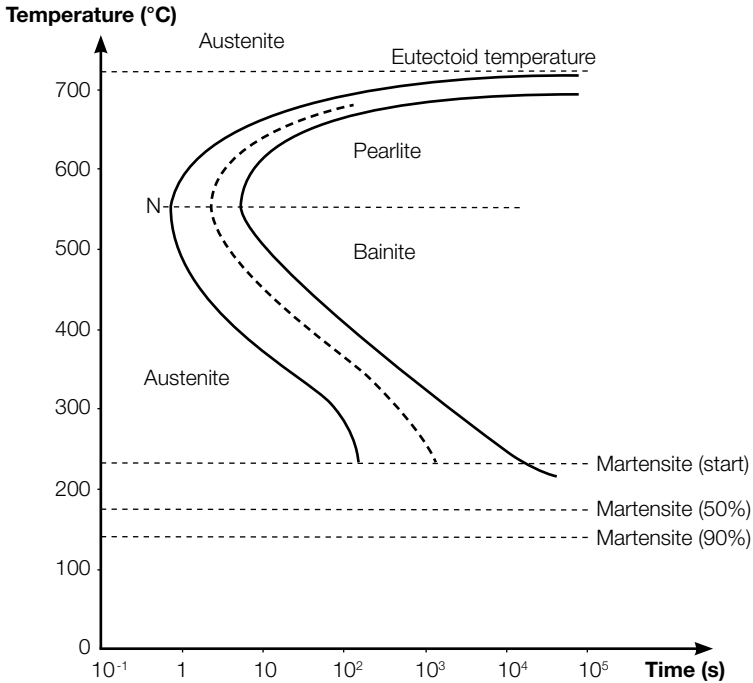


Figure 1.27 TTT-diagram for a Fe-C alloy of eutectoid composition.

At low degrees of under-cooling (i.e. at temperatures just below the eutectoid one), very long times are required for austenite to transform into pearlite. The start and finish curves for the transformation of austenite to pearlite are nearly parallel and approach the eutectoid line asymptotically.

The transformation rate increases with decreasing temperature, until it reaches a maximum at approximately 550°C . The transformation rate decreases again at temperatures lower than 550°C . As a result the TTT-plots have a typical S-shaped form and show a nose (indicated by point N in figure 1.27), where the transformation rate is maximal. The explanation for this nose is that at temperatures close to the eutectoid one (i.e. at low degrees of undercooling) the diffusion rate of carbon is high, whereas the nucleation rate of pearlite is low. When increasing the degree of undercooling, the pearlite nucleation rate increases, whereas the diffusion rate of carbon decreases. As a result of these two

processes, transformation time has a minimum between low and high degrees of undercooling.

The thickness of ferrite and cementite lamellae in pearlite is a function of temperature. The higher the transformation temperature, the thicker the ferrite and cementite lamellae. Pearlite formed at temperatures just below the eutectoid is sometimes called *coarse pearlite*. At temperatures closer to the eutectoid, carbon atoms diffuse relatively long distances, which results in the formation of thick lamellae. With decreasing temperature, the carbon diffusion rate decreases and consequently the pearlite lamellas become progressively thinner. When the structure of the lamellas cannot be resolved in a light optical microscope, the expression *fine pearlite* is used.

1.3.3.2 Austenite-to-bainite transformation

At temperatures below approximately 550°C, the bainite transformation replaces the pearlitic one.

The time required for austenite to transform into bainite, as a function of the temperature, is also reported in the TTT-diagrams. The bainitic and pearlitic transformations are competitive with each other. At higher temperatures the bainite reaction is slower than the pearlitic one as it depends upon the frequent nucleation of ferrite and carbides and the nucleation rate increases when decreasing the temperature. The bainite reaction becomes dominant when decreasing the temperature because it requires less diffusion of carbon*.

In the case of a eutectoid steel, pearlite forms in the temperature range 727-550°C and bainite in the range 550-215°C. In *figure 1.27* it can be observed that the bainite transformation rate decreases when temperature is decreasing. This is because the transformation is controlled by the diffusion of carbon towards carbides nuclei and the diffusion rate of carbon decreases with temperature.

1.3.3.3 Austenite-to-martensite transformation

The term martensite is used for microstructures formed by diffusionless phase transformations. In the case of steels or iron-carbon alloys, martensite is formed

* "Höganäs Handbook for Sintered Components", No 1-3. Höganäs 2013.

by rapidly cooling austenite to temperatures lower than 200°C . At high cooling rates, diffusion processes which lead to the formation of products such as ferrite or pearlite become impossible. The martensitic transformation occurs almost instantaneously, or in other words, its rate is not dependent on time.

Martensite forms by a shear mechanism. During this transformation a large number of atoms experience cooperative movements. Each atom is displaced relative to its neighbours through a distance which is a fraction of the interatomic distance.

Martensite might be regarded as ferrite supersaturated with carbon. At high cooling rates, carbon atoms cannot move fast enough to avoid getting trapped inside the spontaneously forming ferrite. Carbon atoms in the interstitial solution of ferrite cause a distortion of the ferrite BCC lattice which becomes tetragonal. An example of martensite cell is shown in *figure 1.28*. As the carbon atoms occupy positions such as C, the distance between the host atoms increases in the y-direction while decreasing in the x-direction.

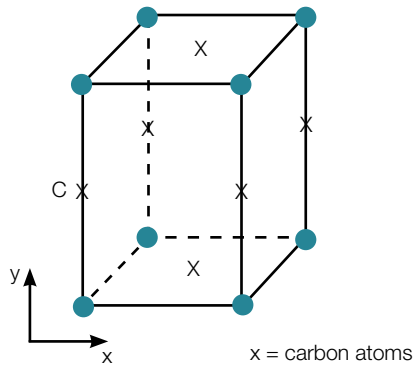


Figure 1.28 The body-centered tetragonal unit cell for martensite showing the position of iron and carbon atoms.

The austenite to martensite transformation can be explained with a TTT-diagram. The temperature at which martensite begins to form is called M_s . As the rate austenite-to-martensite transformation is instantaneous, the amount of martensite can be increased only by decreasing the temperature. At the point M_f , 90% of the austenite has transformed into martensite. The temperatures at which

the martensite transformation starts and finishes depend upon the chemical composition of the alloy quenched. Carbon and most alloying elements decrease both the M_s and M_f temperatures, so that in certain steels the martensite transformation starts below room temperature.

1.3.3.4 CCT-diagrams

As stated above, TTT-diagrams provide information on the times required for a transformation to begin, proceed halfway and finish, at any selected temperature. However, in practice, phase transformations take place during continuous cooling and not at a constant temperature. To account for continuous cooling, transformation diagrams also called CCT-diagrams must be used.

As a first approximation, the CCT-diagram is the TTT-diagram shifted to lower temperatures and longer times. TTT and CCT-plots are, in a sense, phase diagrams in which the parameter time is introduced*. These diagrams are experimentally determined for an alloy of specified composition.

1.3.3.5 Influence of alloying element on TTT and CCT-diagrams

The primary objective of adding alloying element to steels, is to increase hardenability, i.e. to delay the time required for austenite to transform into pearlite and ferrite. This allows slower cooling rates to produce fully bainitic or martensitic structures. Hardenability factors arising from various alloying element are shown in *figure 1.29*. It can be observed that Mo, Cr and Mn are among the most powerful elements with respect to hardenability.

* "Atlas of Isothermal Transformation and Cooling Transformation diagrams", American Society for Metals, 1977.

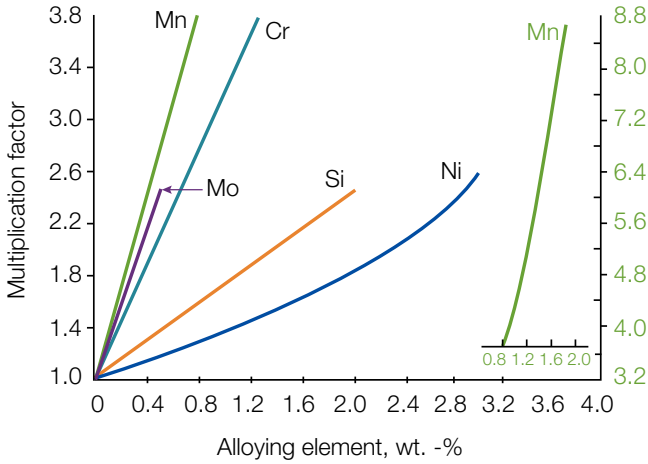


Figure 1.29 Influence of alloying element on hardenability.

The shape and position of the curves constituting TTT and CCT-diagrams, are dependent, with respect to the time axis, on the amount of alloying elements and on the grain size of austenite. However, with few exceptions, an increase in the content of alloying elements or in grain size of the austenite, decreases the rate of austenite-to-pearlite and austenite-to-ferrite transformations.

Basically there are two ways by which alloying elements can reduce the rate of austenite transformation: they can reduce either the nucleation or the growth rate of ferrite, pearlite or bainite. The austenite transformation delay is probably due to the fact that it is necessary to wait for the alloying elements to diffuse before the nuclei of the new phases may form and grow*.

* "Höganäs Handbook for Sintered Components", No 1-3. Höganäs 2013.

1.3.4 Influence of cooling rate on the microstructure of PM steels

The mechanical properties of a steel depend on its microstructure, which in turn depends on the chemical composition of the steel and on the rate at which it was cooled. This section focuses on the influence of alloying elements and cooling rates on the microstructure of materials commonly used in powder metallurgy.

1.3.4.1 Fe-C

ASC100.29 + 0.5% C was cooled at different rates in the range 0.1-100°C/second. The microstructural products and the amount of phases obtained at the cooling rates examined, are reported in *figures 1.30, 1.31 and 1.32*, respectively.

It can be observed that by increasing the cooling rate, the ferrite and pearlite grains become finer. The amount of ferrite is decreased whilst the proportion of pearlite increases. Thus the carbon content of the pearlite must decrease accordingly, as the carbon content in the cementite is fixed. The cementite lamellae in the pearlite become thinner and shorter. The interlamellar spacing decreases. Eventually, the pearlite becomes so fine that individual lamellae cannot be resolved by means of a light optical microscope.

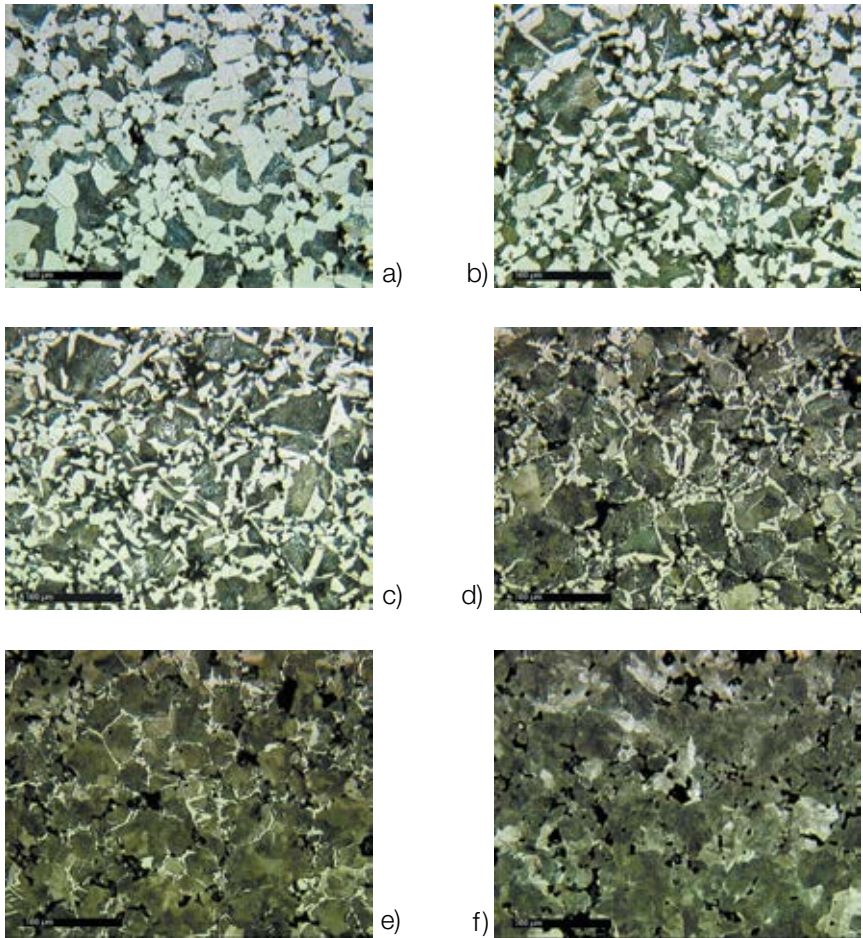


Figure 1.30 Microstructures of ASC100.29 + 0.5% C, sintered at 1120°C for 30 minutes, cooled from 1120°C at (a) 0.1°C/s, (b) 0.5°C/s, (c) 1°C/s, (d) 5°C/s, (e) 20°C/s, (f) 100°C/s.

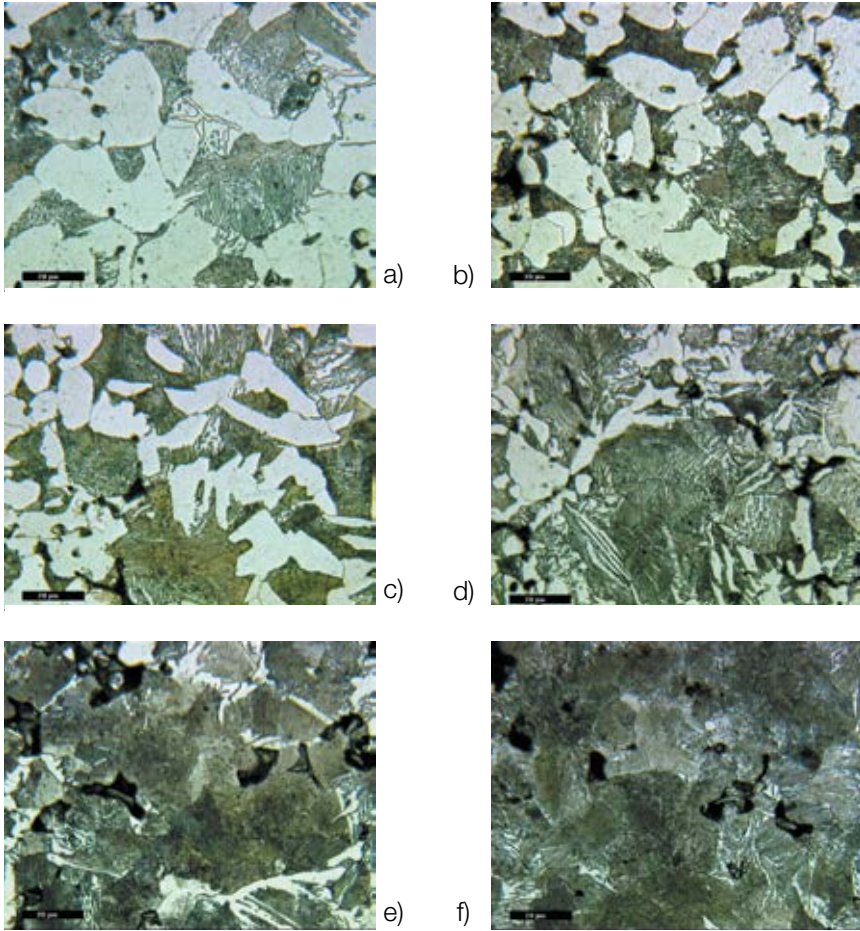


Figure 1.31. As per *figure 1.30* but with higher magnification.

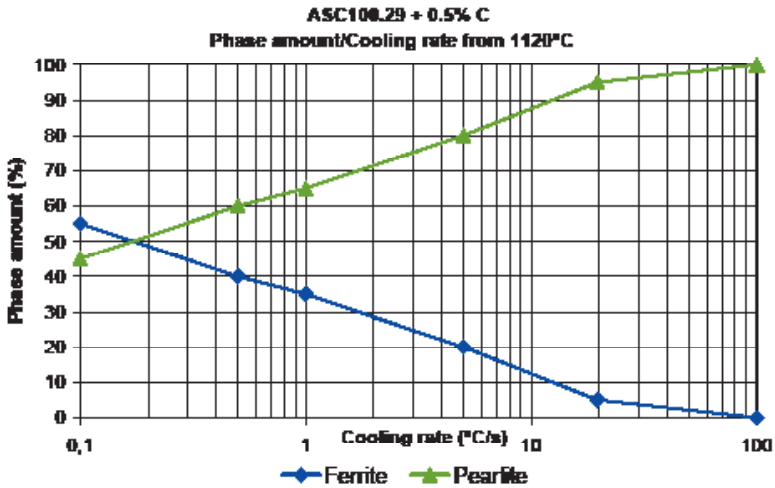


Figure 1.32 Amount of phases for ASC100.29 + 0.5% C, sintered at 1120°C for 30 minutes, as a function of the cooling rate (cooled from 1120°C).

To start with, consider the behaviour of ferrite when cooling rates are increased. When a hypoeutectoid steel, such as ASC100.29 + 0.5% C, is cooled below Ar_3^* , ferrite nucleates predominantly at the austenite grain boundaries. Ferrite may also precipitate within the austenite grains. Possible nucleation sites are, in this case, inclusions. However the nucleation rate within grains is normally lower than in the grain boundaries.

At low cooling rates, ferrite nuclei have time to form and to grow. Carbon rejected from the ferrite into the austenite grains has sufficient time to diffuse over large distances. Thus the austenite grains should maintain a uniform composition, close to the equilibrium phase diagram. Finally the austenite reaches the eutectoid composition and transforms to pearlite. It can be observed that the quantity of ferrite (approximately 55% at 0.1°C/second) is higher than that described in the Fe-C phase diagram. However in *figure 1.31* it can be seen that a thick film of cementite is present in the ferrite grain boundaries.

* Ar_3 = The temperature at which ferrite begins to separate from austenite, when cooled from a temperature in the austenite region. (See Handbook 1. Ch. 1.5.2, for more details.)

At this low rate of cooling, the carbon diffusion rate is sufficiently high to allow the cementite to become somewhat coarse. If the sample was kept at temperatures slightly below A1 (i.e. approximately 700°C) for a sufficiently long time (i.e. several hours) a new phase called spheroidite would appear. In spheroidite Fe₃C appears as spheres in a ferritic matrix. The driving force for Fe₃C spheroidisation is a decrease in the ferrite-Fe₃C grain boundary areas.

Ferrite nucleation rate increases markedly with increasing cooling rates. Large areas of the grain boundary region are covered by ferrite nuclei. On the other hand, carbon diffusion rate which controls ferrite grain growth decreases when increasing the cooling rate. This results in finer ferrite grains. It can also be observed that the morphology of ferrite changes when the cooling rate is increased (*figure 1.31*). For cooling rates in the range 0.1-1°C/second ferrite grows in a rounded or blocky manner. For larger cooling rates of 5-100°C/second ferrite shows an increased tendency to grow from the austenite grain boundaries in the form of plates known as Widmanstätten side-plates. These plates become finer with increased cooling rates. Widmanstätten ferrite forms along a well defined crystallographic plane, the plane {111} in the austenite lattice. The reason for the transition from “blocky” ferrite to Widmanstätten ferrite with increased undercooling is not completely understood*.

The behaviour of pearlite when cooling rates are increased is now examined. The rate of nucleation increases while the carbon diffusion rate decreases, when higher cooling rates are used. At a low cooling rate (e.g. 0.1°C/s) carbon atoms can diffuse rather long distances, which results in the formation of thick ferrite and cementite lamellae. When the cooling rate is raised, the pearlite lamellas thickness decreases in as much as the carbon diffusion rates decreases. For cooling rates between 20-100°C/second the lamellas can no longer be resolved by means of a light optical microscope. It can be observed that when the cooling rate is raised, the quantity of pearlite increases and that for a cooling rate of 100°C/second almost only pearlite is formed. This occurs when austenite is simultaneously supersaturated with respect to both cementite and ferrite. Pearlite formed in this case has more ferrite and less cementite than the eutectoid pearlite, and it is softer.

Normally bainite does not form when an alloy of eutectoid composition, or any other plain carbon steel, is continuously cooled to room temperature. As the bainite nose is well hidden below the pearlite nose, a totally pearlitic or totally martensitic material, or a mix of pearlite and martensite, will form. To produce bainite, an isothermal heat treatment (i.e. austempering) is necessary.

* “Phase transformation in Metals and Alloys”, D.A Porter, K.E. Easterling, 1981.

1.3.4.2 Fe-Cu-C

Figure 1.33 shows the microstructure of ASC100.29 + 2% Cu + 0.5% C when cooled at rates in the range 0.1-100°C/second. Copper and carbon were admixed to the iron powder. This results in heterogeneous Cu distribution and homogeneous C distribution after sintering at 1120°C for 30 minutes. (See Section 1.4 for further information.)

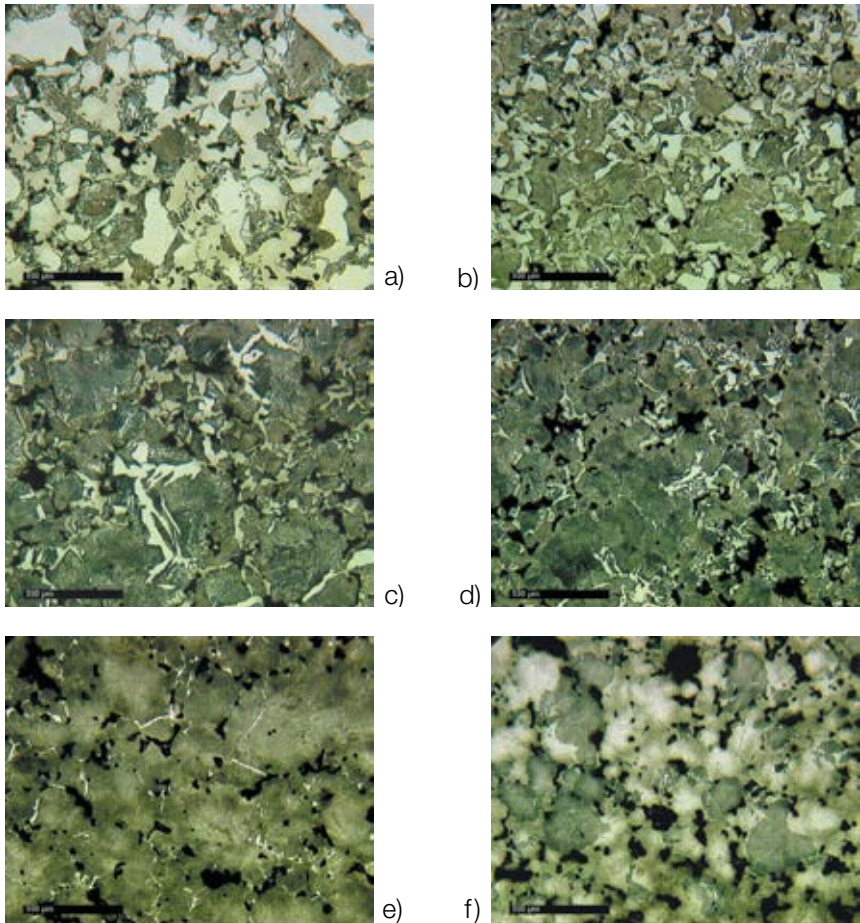


Figure 1.33 Microstructure of ASC100.29 + 2% Cu + 0.5% C sintered at 1120°C for 30 minutes and cooled from 1120°C at (a) 0.1°C/s, (b) 0.5°C/s, (c) 1°C/s, (d) 5°C/s, (e) 20°C/s, (f) 100°C/second.

The amount of phases obtained as a function of the cooling rate is reported in *figure 1.34*. It can be observed that the quantity of ferrite decreases whilst the quantity of pearlite increases, when the cooling rate is raised. At the same time, the thickness of pearlite lamellas decreases. Martensite can be observed when cooling at a rate of 100°C/second.

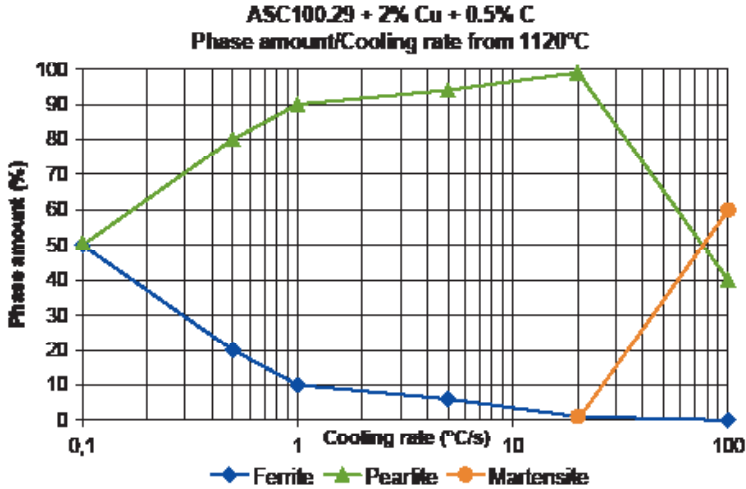


Figure 1.34 Amount of phases as function of the cooling rate for ASC100.29 + 2% Cu + 0.5% C sintered at 1120°C for 30 minutes and cooled from 1120°C.

Let us compare the microstructures of two alloys made with ASC100.29 + 0.5% C and ASC100.29 + 2% Cu + 0.5% C respectively, when cooled at the same rate. The quantity of ferrite is decreased while the quantity of pearlite is increased when Cu is present in the material. Further martensite formation is observed with a cooling rate of 100°C/second. Martensite forms in the regions with higher Cu content. In these areas the transformation rate of austenite is reduced to such an extent that neither pearlite nor bainite can form. In the regions with lower Cu content, fine pearlite is formed.

1.3.4.3 Fe-Mo-C

The influence of cooling rates on the microstructure of Astaloy™ Mo + 0.4% C is examined in this section. Astaloy Mo is an iron powder grade prealloyed

with 1.5% molybdenum. The distribution of molybdenum in the material is homogeneous as the molybdenum is prealloyed to the iron. The microstructures obtained when Astaloy™ Mo + 0.4% C is cooled at rates in the range 0.25-56°C/second is reported in *figure 1.35*. The amount of the phases obtained as a function of the cooling rate is reported in *figure 1.36*.

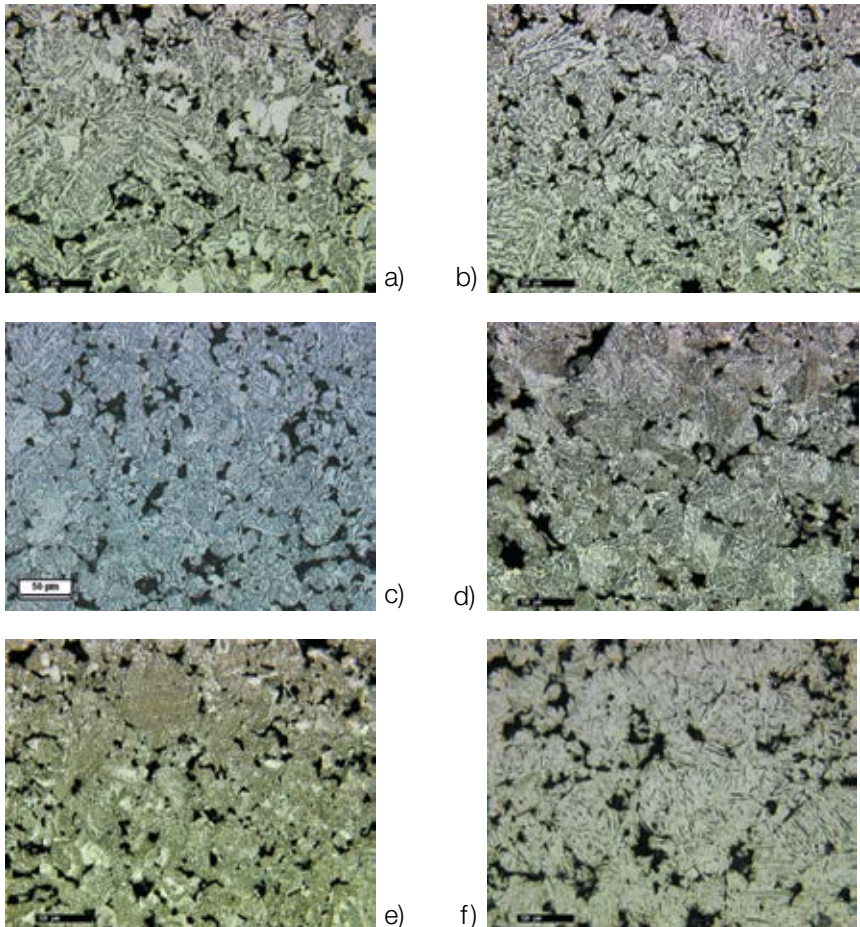


Figure 1.35 Microstructure of Astaloy Mo + 0.4% C sintered at 1120°C for 30 minutes; cooled from 1120°C at (a) 0.25°C/s, (b) 0.5°C/s, (c) 0.85°C/s, (d) 2.5°C/s, (e) 8°C/s, (f) 56°C/s.

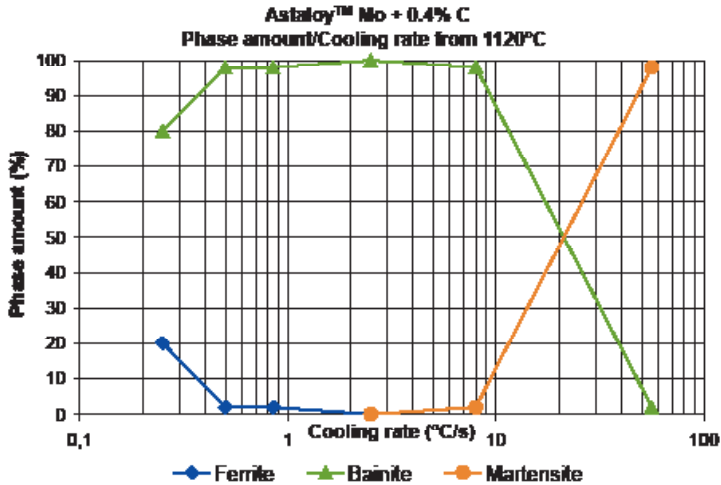


Figure 1.36 Phase amount as a function of the cooling rate for Astaloy Mo + 0.4% C cooled from 1120°C.

The presence of Mo in the iron lattice retards the formation of pearlite with respect to bainite. Formation of pearlite is not possible at rather low cooling rates, such as 0.25°C/second. At this rate a mixture of bainite and ferrite forms. When the cooling rate is increased, the quantity of ferrite decreases. This is due to the fact that with faster cooling rates, the carbon diffusion rate, which controls ferrite growth, is decreased. For cooling rates of 0.5 and 0.85°C/second, only small amounts of ferrite can be found.

Upper bainite forms with cooling rates in the range 0.25-2.5°C/second. The higher the cooling rate, the finer the bainite becomes. Lowering the transformation temperature results in the formation of finer bainite. This is due to precipitation of ferrite laths in intimate contact with carbides, and more generally to an increased precipitation of carbides. At a cooling rate of 8°C/second, a mixture of upper and lower bainite can be observed. Very small quantities of martensite are observed when this material is cooled at 8°C/second. At a cooling rate of 56°C/second, almost only martensite is formed. At this cooling rate neither molybdenum, nor iron, nor carbon atoms, have sufficient time to diffuse.

The hardenability of Astaloy™ Mo + 0.4% C can be significantly increased by increasing the carbon content from 0.4% to 0.6%. If Astaloy Mo + 0.6% C is cooled at a rate of 8°C/second, an almost entirely martensitic structure with small amounts of low bainite is obtained.

1.3.4.4 Fe-Cr-Mo-C

Astaloy CrM® is an iron powder grade prealloyed with 3% chromium and 0.5% molybdenum. As in the case of Astaloy Mo, the alloying elements Cr and Mo are distributed homogeneously in the material. The influence of cooling rates on the microstructure of Astaloy CrM® + 0.3% C, and the amount of different phases obtained as a function of the cooling rate, are shown in *figure 1.37* and *figure 1.38*, respectively.

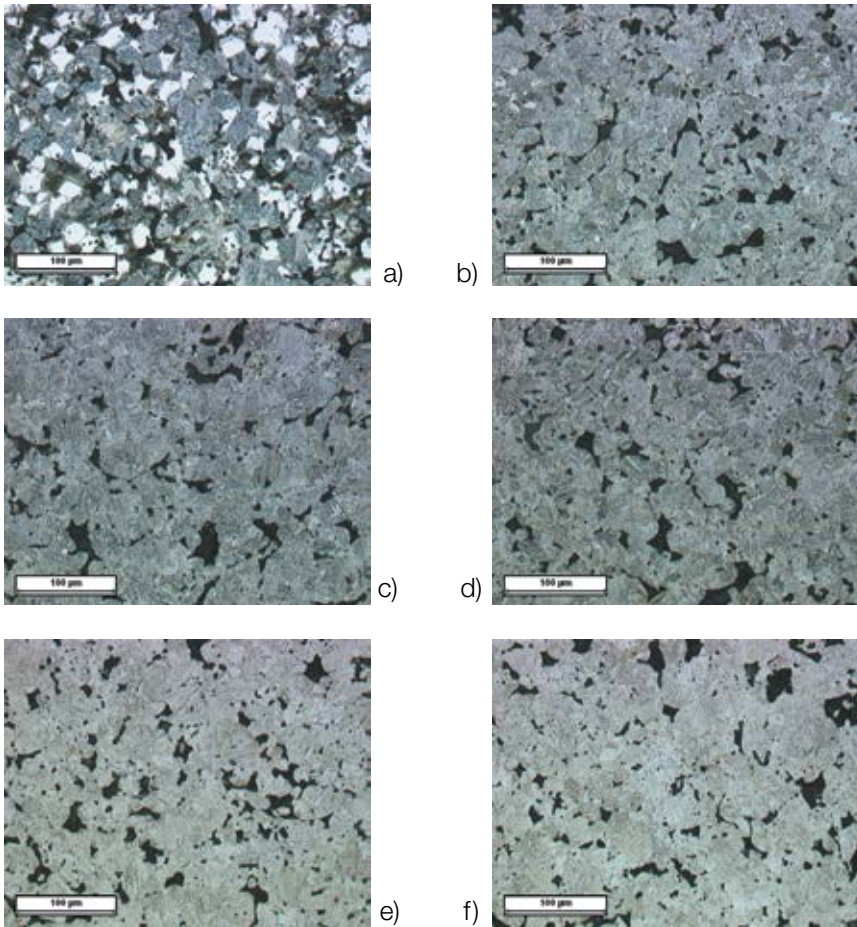


Figure 1.37. Microstructure of Astaloy CrM[®] + 0.3% C sintered at 1120°C for 30 minutes; cooled from 1120°C at (a) 0.1°C/s, (b) 0.5°C/s, (c) 1°C/s, (d) 2°C/s, (e) 12°C/s, (f) 25°C/s.

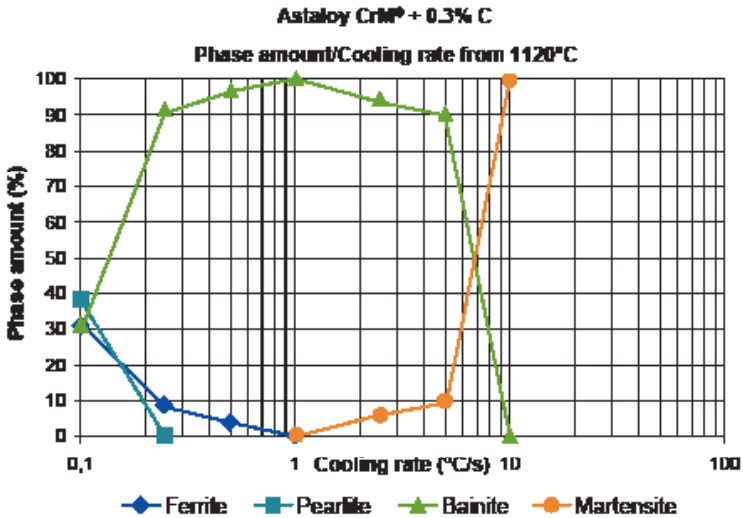


Figure 1.38 Amount of phases as a function of the cooling rate for Astaloy CrM + 0.3% C sintered at 1120°C for 30 minutes; cooled from 1120°C.

The presence of Cr and Mo retards the pearlite reaction. Fine pearlite, admixed with upper bainite, and some ferrite can be observed at a cooling rate of 0.1°C/second. When increasing the cooling rate the quantity of ferrite decreases whilst the amount of bainite increases. An entirely bainitic structure (upper bainite) is observed at a cooling rate of 0.5°C/second. At cooling rates faster than 2°C/second, some martensite is formed. However the material does not become fully martensitic until the cooling rate reaches 8°C/second. As observed in the case of Astaloy™ Mo + 0.4% C, the higher the cooling rate, the finer the bainite.

Due to the larger quantity of alloying elements, the hardenability of Astaloy CrM® + 0.3% C is higher compared with Astaloy™ Mo + 0.4% C. When Astaloy CrM + 0.3% C is cooled at a rate of 8°C/second, an entirely martensitic structure is obtained, while in the case of Astaloy Mo + 0.4% C, a totally bainitic structure is obtained.

1.3.4.5 Fe-Ni-Cu-Mo-C

The behaviour of Distaloy[®] AE + 0.5% C when cooled at different rates is examined in this section. Distaloy AE is partially prealloyed with Cu, Ni and Mo. A heterogeneous distribution of these elements is obtained after sintering, due to their low diffusion rate at the sintering temperatures normally used. This chemical heterogeneity appears in the microstructure as a mixture of different phases. The relative amount of these phases is a function of the cooling rate.

Figure 1.39 shows the microstructural products obtained when Distaloy[®] AE + 0.5% C is cooled at different rates. The amount of phases obtained as a function of the cooling rate is reported in *figure 1.40*. It can be observed that the quantity of ferrite decreases, while the amount of martensite increases, as the cooling rate is raised. The amount of pearlite/bainite remains almost constant when the cooling rate is raised from 0.1 to 1°C/second, and then decreases at cooling rates higher than 1°C/second. It is very difficult to quantify the amount of bainite and pearlite in diffusion alloyed grades as these two phases are intimately mixed with each other. Therefore, only the total amount of bainite/pearlite is reported. The amount of austenite present after sintering does not depend on the cooling rate, and is stable at round 3-5%.

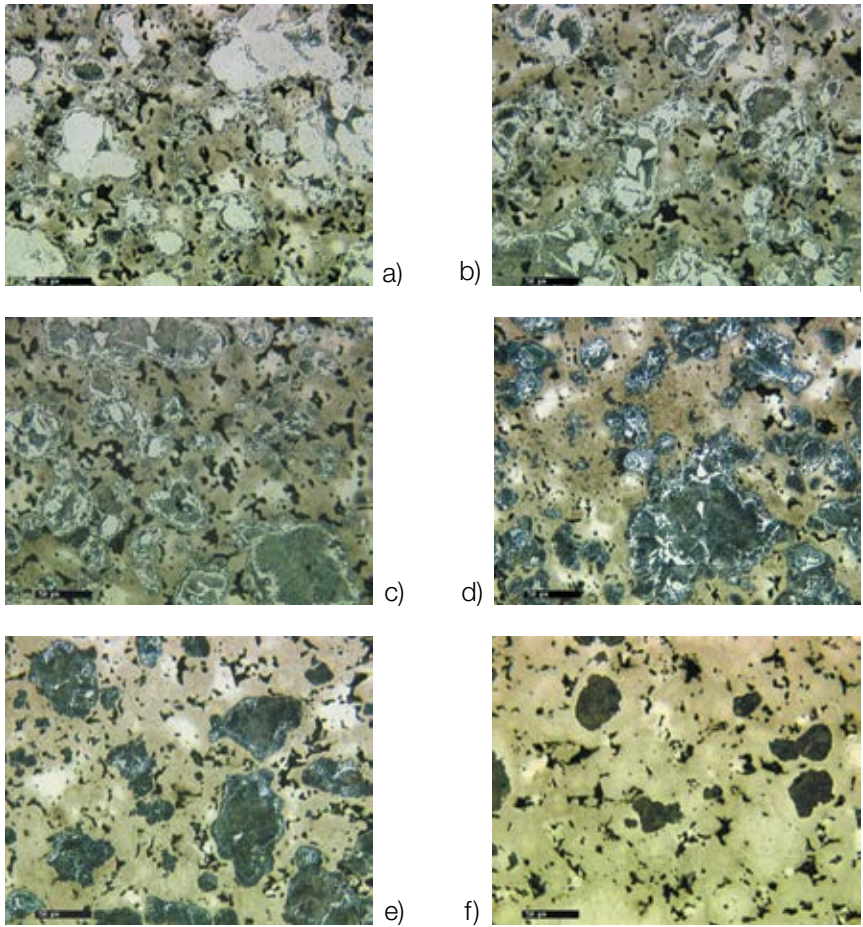


Figure 1.39 Microstructure for Distaloy AE + 0.5% C sintered at 1120°C for 30 minutes; cooled from 850°C at (a) 0.1°C/s, (b) 0.5°C/s, (c) 1°C/s, (d) 5°C/s, (e) 10°C/s, (f) 100°C/s.

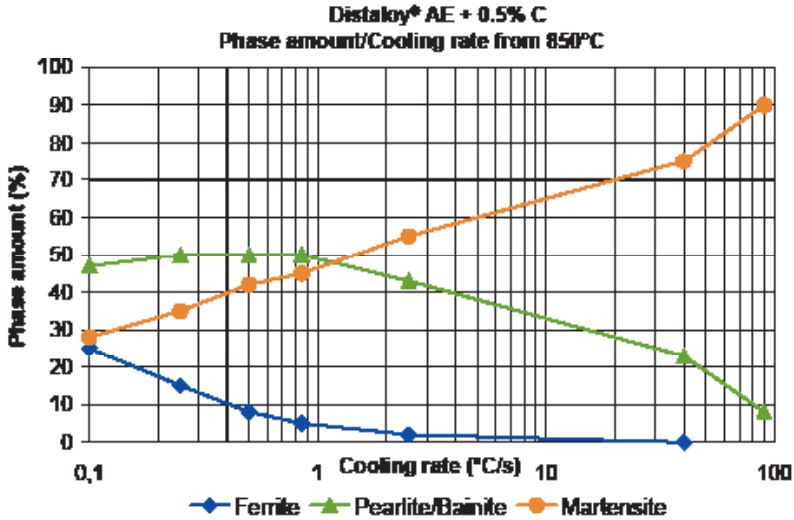


Figure 1.40 Amount of phases as a function of cooling rate for Distaloy AE + 0.5% C sintered at 1120°C for 30 minutes; cooled from 850°C.

During sintering, Ni, Cu and Mo diffuse from the surface of iron powder particles towards their centre, as described in Section 1.4. The diffusion time for Ni, Cu, and Mo is very long at 1120°C. Therefore a concentration gradient in Ni, Cu and Mo occurs from the surface to the centre of the original iron powder particles.

At low cooling rates, ferrite and pearlite form mainly in the areas with the least concentration of the alloying elements (Ni, Cu, Mo), i.e. in the middle of the original Fe powder particles. Austenite forms in the areas with highest Ni and Cu content. Martensite is observed in the areas rich in Cu and Ni. The Ni content in the martensitic areas is high, but not as high as in the austenitic areas. Bainite forms in the areas where the alloying content is lower than in martensite but higher than in the ferrite+pearlite areas.

1.3.4.6 Fe-Mo-Cu-C

An alloy made with Distaloy[®] DH + 0.4% C is now examined. Distaloy DH is manufactured by diffusion annealing Astaloy[™] Mo with 2% Cu. The microstructures and amount of phases obtained when Distaloy DH + 0.4% C is cooled at different rates are reported in *figures 1.41 and 1.42*, respectively.

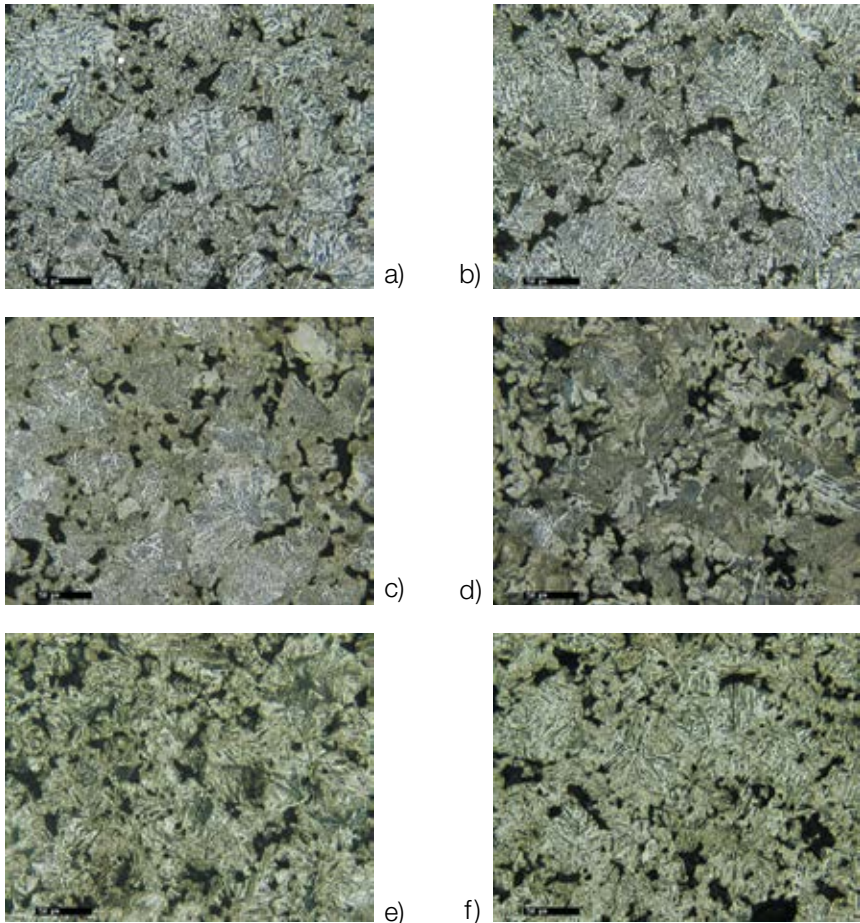


Figure 1.41 Microstructure of Distaloy DH + 0.4% C sintered at 1120°C for 30 minutes; cooled from 1120°C at (a) 0.25°C/s, (b) 0.5°C/s, (c) 0.85°C/s, (d) 2.5°C/s, (e) 8°C/s, (f) 56°C/s.

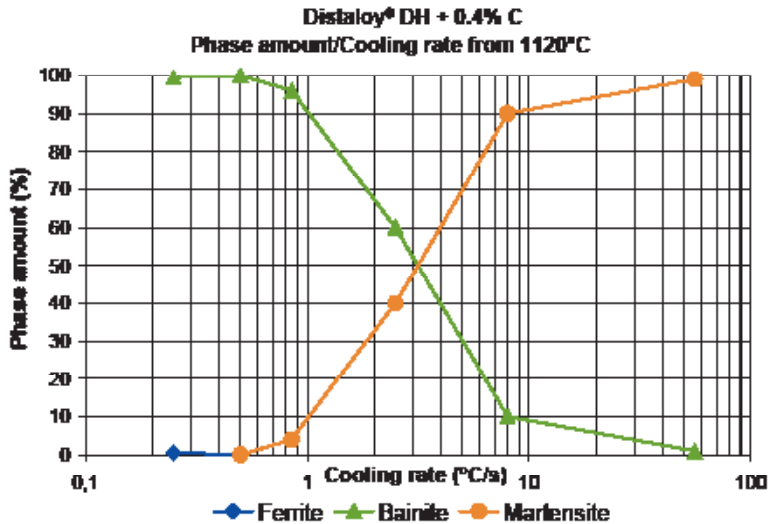


Figure 1.42 Amount of phases as a function of the cooling rate for Distaloy DH + 0.4% C sintered at 1120°C for 30 minutes, cooled from 1120°C.

The formation of ferrite is suppressed in the case of Distaloy® DH + 0.4% C at a cooling rate as low as 0.25°C/second. A totally bainitic structure is obtained at cooling rates in the range 0.25-0.85°C/second. A mixture of martensite (approximately 40%) and bainite (60%) is formed at a cooling rate of 2.50°C/second. Martensite forms in the areas with higher Cu content. When further increasing the cooling rate, the amount of martensite increases whilst the amount of bainite decreases.

Let us compare the microstructure of Astaloy™ Mo + 0.4% C with that of Distaloy DH + 0.4% C, when the materials are cooled at the same rate. The addition of Cu to Astaloy Mo suppresses the formation of ferrite. At a given cooling rate, finer bainite is observed for Distaloy DH + 0.4% C. Lower cooling rates are needed to produce martensite in the case of Distaloy DH + 0.4% C.

Astaloy Mo + 0.4% C has an entirely bainitic structure when cooled at a rate of 2.5°C/second, while approximately 40% martensite and 60% bainite is found in the case of Distaloy DH + 0.4% C.

1.4 Diffusion of alloying Elements and Microstructure

In this section attention is focused on diffusion of alloying elements in solid metals. More precisely, the section deals with (1) the mechanisms of diffusion, (2) the laws that govern diffusion, (3) the influence of temperature, diffusing species and diffusion mechanisms on the diffusion rate, and (4) the relationship between alloying element diffusion and microstructure in PM steels.

1.4.1 Introduction

Many reactions that are important in metallurgy imply the transfer of atoms either within a solid, or from a gas, liquid or solid phase to another solid. The migration of atoms through the crystal lattice is called **diffusion**.

When the temperature of a solid metal is raised above absolute zero atoms move in two different ways:

- a) they vibrate around their main position in the crystal lattice
- b) they wander from one lattice site to another

The fact that atoms migrate through the crystal lattice seems strange at first, because this is not part of our daily experience. Take an example: a steel teaspoon is sometimes plated with silver and the silver layer remains stable, apparently forever. At room temperature the mixing of atoms between the silver layer and the base material is very slow. Therefore no changes are observed. However, if the teaspoon is heated to high temperatures, the atoms will migrate faster so that the silver layer rapidly disappears.

A diffusion couple can be used for studying diffusion in solids (*see figure 1.43*). Two specimens (of the substances A and B) are put in contact with each other and heated for an extended period of time, at an elevated temperature (but below their melting points). A-atoms migrate or diffuse into the B bar, while B-atoms diffuse into the A bar. This results in a net transfer of A-atoms from high to low concentration areas. The same is true for the B-atoms (*see figure 1.44*). Migration or diffusion of one metal into another is often called **interdiffusion**. If A and B are miscible in all proportions, equilibrium conditions are achieved

when the chemical composition is homogeneous through the couple. The longer the heating time at elevated temperatures, the more homogeneous will be the distribution of A and B through the couple.

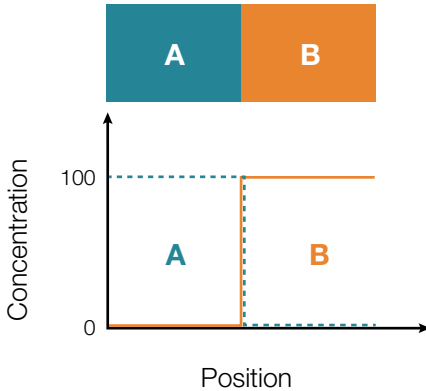


Figure 1.43 Concentration profile for A and B as a function of the position across the couple before heating.

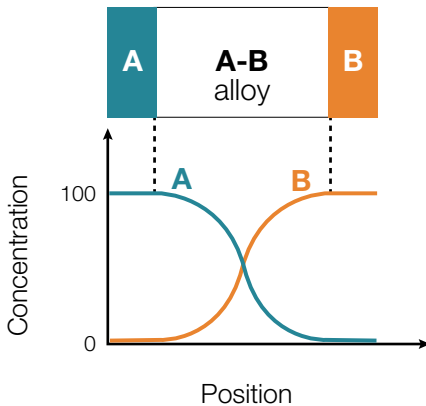


Figure 1.44 Concentration profiles for substances A and B as a function of their position after heating at elevated temperatures for a given time. A and B are miscible in all proportions.

In the absence of a concentration gradient, the net flow of atoms ceases. However, the atoms of an alloy continuously move from one site to the other in the lattice. This occurs also in pure metals where atoms of the same type exchange position with each other. Diffusion in pure metals is called self-diffusion and can be studied by using radioactive tracers.

Diffusion almost certainly takes place in single steps. Each atom in a crystal lattice vibrates continuously about its site. Occasionally the vibration of it and its neighbours becomes strong enough to allow it to make a jump to a neighbouring site. This can happen only if the atom in question has sufficiently high vibrational energy and if there is an empty site to which it can jump. As the vibrational energy increases with higher temperatures, the diffusion rate also increases.

1.4.2 Fick's laws of diffusion

It was pointed out above that differences in concentrations through a material tend to level out through the movement of atoms. If the diffusion flux is constant during the whole diffusion process, steady state conditions exist and diffusion can be described by Fick's first law of diffusion (Equation 4.1):

$$J = -D \frac{dC}{dx} \quad (4.1)$$

Where J is the flux of atoms that crosses a plane perpendicular to the direction of diffusion at any instant (its unit is $\text{kg/m}^2 \text{-s}$ or $\text{atoms/m}^2 \text{-s}$); dC/dx is the concentration gradient that exists at the plane in question; and D is a constant called diffusion coefficient and is expressed in square meters per second. The minus sign in Equation 4.1 indicates that atoms of a given species migrate from the regions where their concentration is high towards regions where their concentration is low.

Steady-state diffusion conditions exist for example through the thin steel wall of a furnace muffle which is exposed to a carburising atmosphere on one side and a decarburising atmosphere at the other side. The concentration of the diffusing species is held constant on both surfaces of the muffle (*see figure 1.45*).

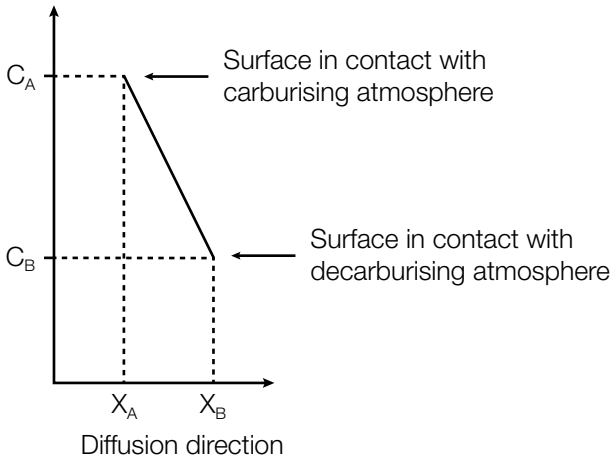


Figure 1.45 Example of concentration profile for steady-state diffusion.

In most practical situations the concentration of the diffusing species changes everywhere in the material (non-steady state diffusion conditions). In this case Fick's second law of diffusion is used (Equation 4.2)

$$\frac{\partial c}{\partial t} = \frac{\partial}{\partial x} \left(D \frac{\partial c}{\partial x} \right) \quad (4.2)$$

If the diffusion coefficient can be considered independent of the concentration (C), Equation 4.2 simplifies to:

$$\frac{\partial c}{\partial t} = D \frac{\partial^2 C}{\partial x^2} \quad (4.3)$$

A solution to this expression (concentration in terms of both position and time) is only possible if physically meaningful boundary conditions are specified.

Carburising of steel is an example of a process where non-steady state diffusion conditions exist. Carburising is achieved by placing a steel with an initial carbon content of C_0 in a carburising atmosphere at a temperature around 900°C . The atmosphere maintains the carbon concentration at the sample surface at the composition $C_s > C_0$. Carbon concentration in the steel varies with distance and time, as represented in *figure 1.46*.

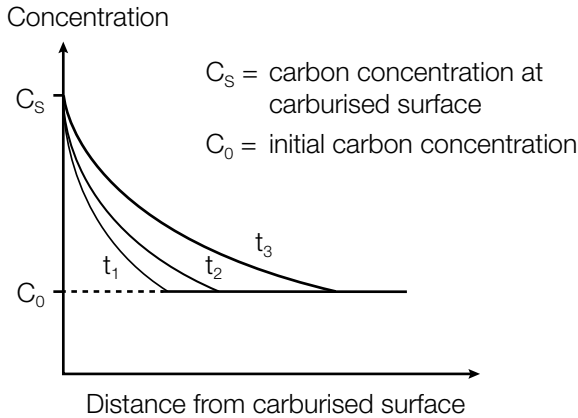


Figure 1.46 Profile for carbon concentration at three different set-times, $t_1 < t_2 < t_3$.

We can assume that the steel piece is semi-infinite* and that the following boundary conditions are valid:

1. Carbon concentration is constant through the part and equal to C_0 , before carburising starts.
2. During carburising the carbon concentration is equal to C_s at $x=0$ for all values of time.
3. Carbon concentration is equal to C_0 at $x = \infty$

Application of the boundary conditions above, to Equation 4.3, yields to the following solution:

$$\frac{C_x - C_0}{C_s - C_0} = 1 - \operatorname{erf}\left(\frac{x}{2\sqrt{Dt}}\right) \tag{4.4}$$

Where C_x represents the concentration at depth x after time t . The expression $\operatorname{erf}(x/2\sqrt{Dt})$ is called the Gaussian error function of $x/2\sqrt{Dt}$ and is listed in special tables.

* A bar of solid material is considered to be semi-infinite if none of the diffusing atoms reaches the bar end during the time in which diffusion takes place.

From Equation 4.4 it can be deduced that for a particular value of C_x

$$\frac{x}{2\sqrt{Dt}} = \text{constant} \quad (4.5)$$

Or in other words:

$$x \propto \sqrt{Dt} \quad (4.6)$$

The “time law” (4.6) is significant not only for carburising of steel but for most diffusion processes. It is important because it allows us to simplify a number of diffusion calculations.

1.4.3 Diffusion mechanisms

In the case of metals the most important diffusion mechanisms are vacancy diffusion and interstitial diffusion.

Vacancy diffusion, or substitutional diffusion, occurs when an atom from a normal lattice position jumps into an adjacent vacant site. *Figure 1.47a* shows how a vacancy moves through the lattice. Since diffusing atoms and vacancies exchange positions, the vacancy path is in the direction opposite to the atomic flux. Self-diffusion and interdiffusion occur by this mechanism.

Interstitial diffusion involves the jumping of an atom from an interstitial position to an adjacent position which is empty (*figure 1.47b*). This diffusion mechanism is typical for atoms of small dimensions (compared with the host atoms), such as hydrogen, carbon and nitrogen. Host or substitutional atoms do not diffuse via this mechanism.

In most metal alloys, interstitial diffusion is more rapid than vacancy diffusion. The reasons for this are (a) the interstitial atoms are smaller and thus more mobile, (b) the probability of an atom jumping from one interstice to another is greater than for vacancy diffusion, as the number of interstitial sites is larger than that of vacant sites*.

*"Material Science and Engineering - An introduction", William D. Callister, John Wiley & Sons, Inc. 1985

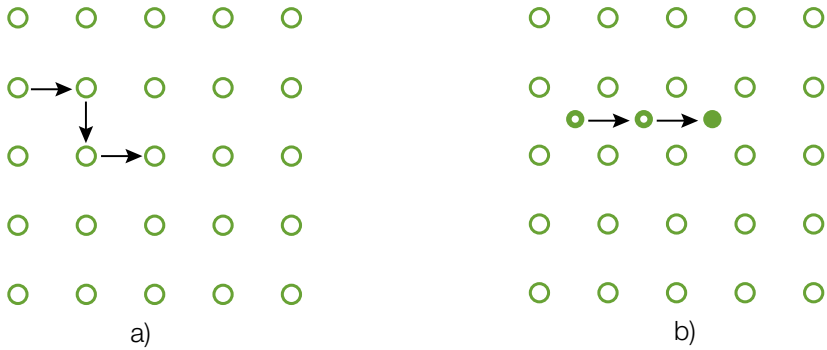


Figure 1.47 Vacancy diffusion (a) and interstitial diffusion (b).

1.4.4 Influence of the temperature on diffusion rate

The diffusion coefficient (D) is a measure of the diffusion rate. D depends on the mechanism of atom movement inside the metal, and most particularly on temperature. The diffusion coefficient varies with temperature according to Equation 4.7:

$$D = D_0 \exp\left(-\frac{Q}{RT}\right) \quad (4.7)$$

where D_0 is a constant, Q is the activation energy for diffusion, R is the gas constant, and T is the absolute temperature (K). The activation energy is the energy that an atom must have to be capable of jumping from one position to another in the lattice.

According to Equation 4.7, when plotting the logarithm of D as a function of $1/T$, a straight line is obtained if a single diffusion mechanism is involved. This has been confirmed in many experimental investigations. The values of Q and D_0 are obtained from the slope and intercept of the straight line.

The diffusion coefficients D and D_0 , and the activation energy Q , for some important diffusion systems are presented in Table 1.2 of Vol. 1 of The Höganäs Handbook for Sintered Components.

1.4.5 Diffusing species and diffusion rate

Figure 1.48 shows the diffusion rate expressed as $\log D$ versus $1/T$ for carbon, copper, nickel and molybdenum in the iron lattice. As shown in the figure, the difference in diffusion rates for carbon and the other elements is very large due to the different diffusion mechanisms at work. Note that there is a large difference in the diffusion rate for interstitial solute carbon compared with the substitutional solutes: nickel, molybdenum and copper. However there are also differences among the diffusion rates for the substitutional solutes (copper, nickel and molybdenum). There are various reasons for these differences.

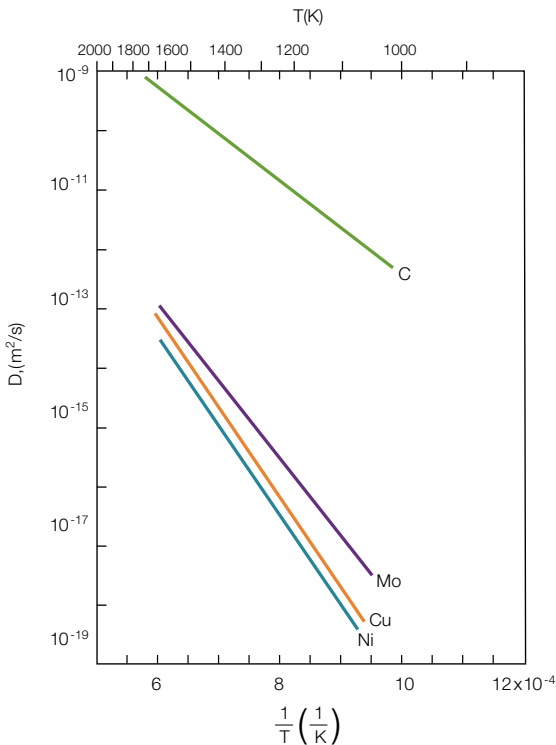


Figure 1.48 Diffusion rates for various elements in Fe expressed as $\log D$ versus $1/T$.

The size of copper and nickel atoms is comparable to that of iron atoms. However copper diffuses in the iron lattice faster than nickel. The melting point of copper is lower than that of nickel and as a consequence, at the same sintering temperature, the mobility of copper atoms is much higher than that of the nickel atoms. Copper atoms have a larger probability of penetrating the iron lattice compared with nickel atoms. This results in a faster diffusion rate for copper atoms in the iron lattice.

Molybdenum has the largest diffusion rate in the iron lattice, compared with copper and nickel, despite it having the largest atomic radius and the highest melting point. The crystal structure of iron, at the sintering temperature, is face-centered cubic (FCC) but as soon as a relatively small amount of molybdenum has penetrated the FCC iron lattice, this will transform into body-centered cubic (BCC) lattice. The diffusion rate in the BCC lattice is approximately 100 times larger than in the FCC lattice, at a given temperature. Therefore the diffusion rate of molybdenum in iron is larger than that of copper and nickel, which are in contrast FCC stabilisers. Moreover, the high molybdenum diffusion rate results in a large molybdenum concentration gradient at the BCC/FCC interface, which further increases the diffusion rate.

1.4.6 "Short-circuit" diffusion paths

Atoms can migrate not only through the crystal lattice but also along dislocations, grain boundaries, and external surfaces. These diffusion mechanisms are sometimes called "*short-circuit*" *diffusion paths* as they are much faster than volume diffusion. *Figure 1.49* shows that diffusion along external surfaces is faster than grain boundary diffusion, which is in its turn faster than volume diffusion. However, in most cases the contribution of the "*short-circuit*" *diffusion paths* to the total diffusion process is very small.

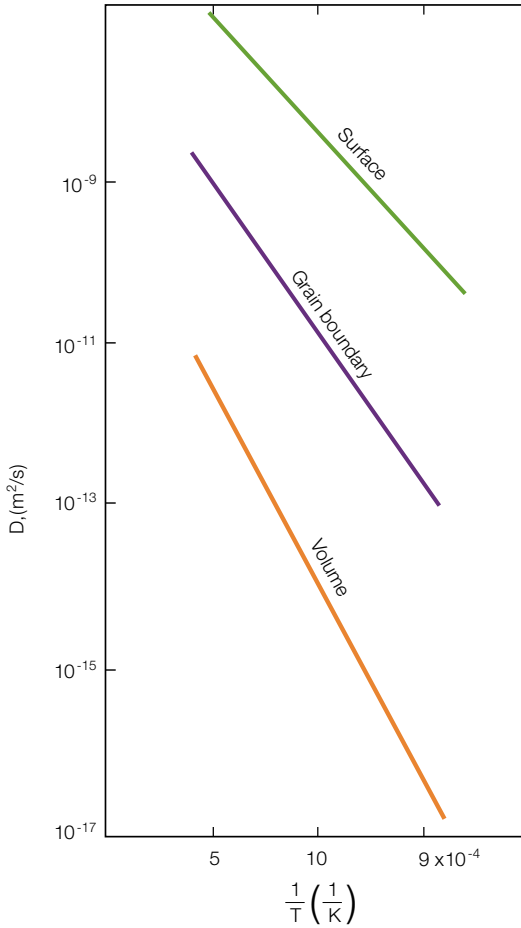


Figure 1.49 Relative diffusion rates for surface diffusion, grain boundary diffusion, and volume diffusion, respectively.

1.4.7 Diffusion and microstructure of PM steels

In powder metallurgy, alloying elements such as nickel, copper, molybdenum and Carbon are normally admixed to iron powder. During practical sintering, interstitial solutes such as carbon can homogeneously be distributed over the material due to their relatively fast diffusion rate. Substitutional solutes such as copper and nickel need much longer times for homogenisation, and consequently they are heterogeneously distributed in the material after sintering. This chemical heterogeneity appears as a mixture of different phases in the material. Sintered materials based on fully prealloyed powders will, however, achieve more homogeneous structure after sintering, due to the homogeneous distribution of alloying elements in the original based powder.

1.4.7.1 Fe-C

A very efficient way of improving the strength and hardness of sintered iron is to alloy it with carbon. The homogenisation of carbon, as well as that of other alloying elements, is a function of sintering time and temperature. *Figures 1.50 and 1.51* show the influence of sintering temperature on the diffusion rate of carbon. A material based on MH80.23 + 1% C was sintered at 1050°C for 30 minutes, while a material based on MH80.23 + 0.8% C was sintered at 1120°C for 30 minutes.

According to the Fe-C phase diagram (*figure 1.17*) pearlite and cementite is to be expected in the case of MH80.23 + 1% C while an entirely pearlite structure is to be expected in the case of MH80.23 + 0.8% C. However, ferrite, pearlite and some free graphite are found when sintering at 1050°C for 30 minutes. The reason for this is that the diffusion time is too short for graphite to completely dissolve and diffuse into the Fe lattice. This results in the presence of free graphite in the material. As less than 0.8% graphite is dissolved into the iron lattice, pearlite and ferrite can be observed after sintering. Larger quantities of graphite can be dissolved in the iron lattice at 1050°C by increasing the sintering time.

At 1120°C graphite dissolves and diffuses more rapidly in iron than at 1050°C. Therefore no free graphite is found in the pores and a totally pearlitic structure is obtained.

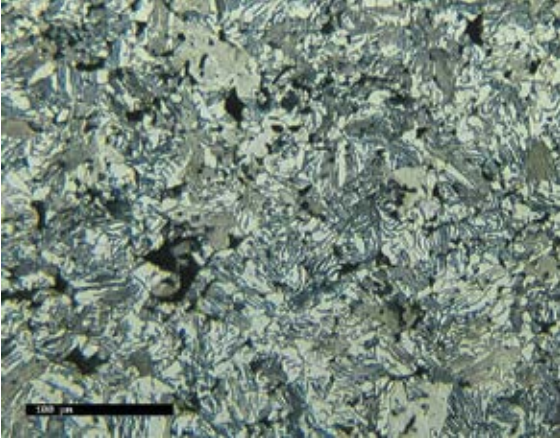


Figure 1.50 MH80.23 + 1% C, sintered at 1050°C for 30 minutes.

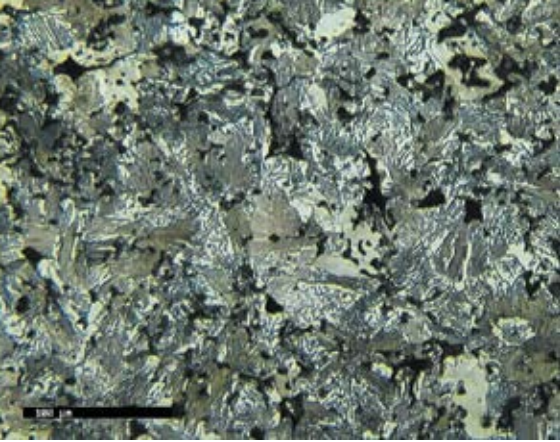


Figure 1.51 MH80.23 + 0.8% C, sintered at 1120°C for 30 minutes.

1.4.7.2 Fe-Cu and Fe-Cu-C

The iron-copper-carbon system is one of the most common alloying systems used in iron powder metallurgy. Copper is usually added to the basic iron powder in the range 1.5-4% wt. *Figures 1.52 and 1.53* show typical microstructures of iron-copper and iron-copper-carbon alloys, respectively, after sintering at 1120°C for 30 minutes.

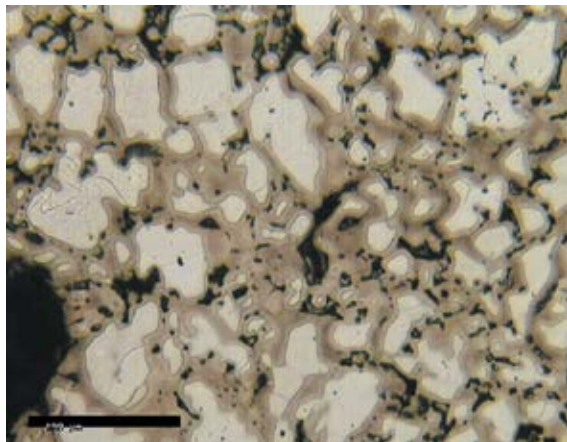


Figure 1.52 ASC100.29 + 2% Cu-100, sintered at 1120°C for 30 minutes.

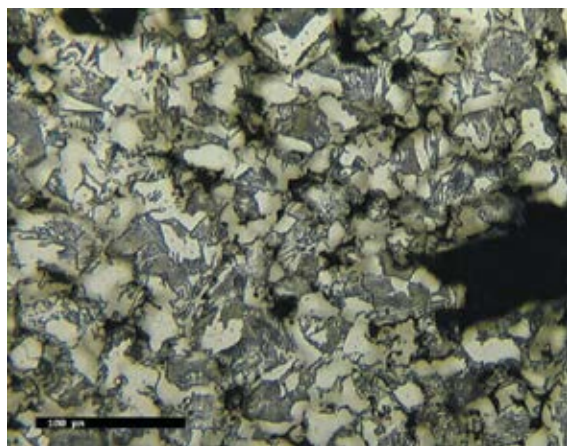
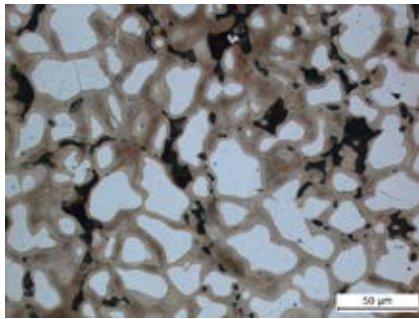


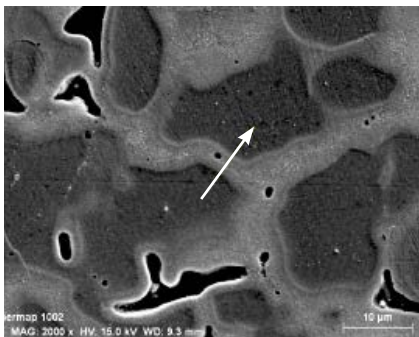
Figure 1.53 ASC100.29 + 2% Cu-100 + 0.5% C, sintered at 1120°C for 30 minutes.

The above microstructures consist of ferrite in the case of the iron-copper system, and ferrite and pearlite in the case of the iron-copper-carbon system. It can clearly be seen that copper is not homogeneously distributed in the iron matrix. Regions with higher copper concentration appear in the micrographs as brownish.

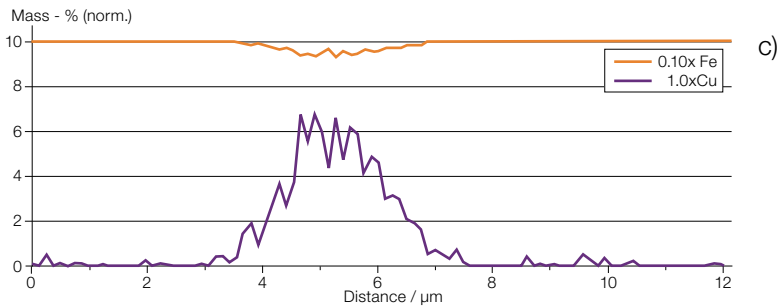
At the sintering temperature normally used (1120°C) copper melts ($T_f=1083^\circ\text{C}$). Liquid copper penetrates the gaps between the powder particles and the grain boundaries within single powder particles. From here copper atoms diffuse into the iron lattice and vice versa: Fe atoms diffuse into liquid copper. As copper is a substitutional element its diffusion rate into the iron lattice is slow. After 30 minutes sintering at 1120°C, a higher Cu concentration is found in the proximity of the pores left by the melted Cu particles, at the iron particle surface, and at the grain boundaries (*see figure 1.54*). Several hours are needed to achieve homogeneous Cu distribution at 1120°C. Homogenisation rates can be improved by increasing the sintering temperature. *Figure 1.55* shows the microstructure of ASC100.29 + 2% Cu -100 sintered at 1250°C for 30 minutes. A more homogeneous Cu distribution can be observed in the ferritic matrix.



a)



b)



c)

Figure 1.54 ASC100.29 + 2% Cu sintered at 1120° C for 30 minutes.

(a) As seen in a light optical microscope LOM.

(b) As seen in a scanning electron microscope SEM.

(c) Cu distribution along the line reported in (b) measured by energy dispersion spectrometry (EDS). Note that (a) and (b) do not have the same magnification.

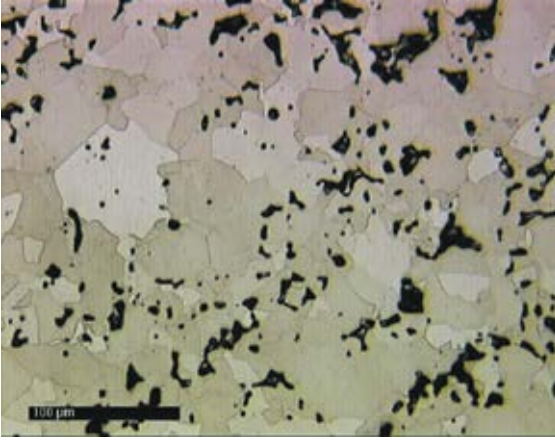


Figure 1.55 ASC100.29 + 2% Cu-100, sintered at 1250°C for 30 minutes.

If sintering is carried out at temperatures lower than the Cu melting point, free copper particles can be found after sintering and copper diffusion is limited only to the regions around the copper particles. *Figure 1.56* shows the microstructure of MH80.23 + 2% Cu-100 + 0.5% C, sintered at 1050°C for 30 minutes. Ferrite and pearlite can be observed together with free Cu particles.

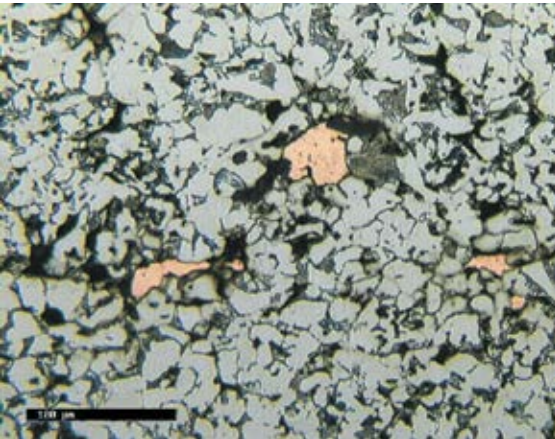


Figure 1.56 MH80.23 + 2% Cu-100 + 0.5% C, sintered at 1050°C for 30 minutes.

1.4.7.3 Fe-Ni-C

Nickel is used in powder metallurgy for improving strength and ductility. *Figure 1.57* shows the microstructure of a mix comprising ASC100.29 + 3% Ni + 0.5% C, sintered at 1120°C, for 30 minutes. Pearlite, ferrite, martensite and austenite can be observed.

Nickel is a substitutional element, and as is the case with copper, its diffusion rate is very slow. However, differently from copper, it does not melt at the temperatures normally used for sintering ($T_f=1455^\circ\text{C}$). Nickel remains concentrated around the areas where the original nickel particles were located.

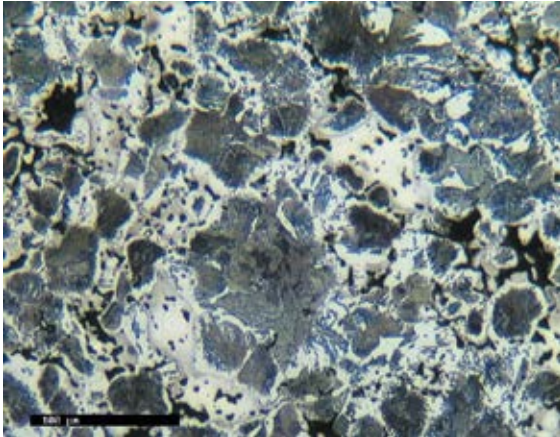


Figure 1.57 ASC100.29 + 3% Ni + 0.5% C, sintered at 1120°C for 30 minutes.

During sintering the nickel atoms diffuse into the iron lattice and vice versa: the iron atoms diffuse into the nickel particles. A nickel and iron gradient will be present in the areas around the nickel particle. The highest nickel concentration will be found after sintering in the center of the original nickel particle.

As nickel is austenite stabiliser, the areas richer in nickel will be austenitic. If carbon is present in the material, small amounts of martensite can be observed around austenite. Martensite forms in the areas where the amount of nickel is high, but not high enough to form austenite. The areas which have not been reached by the nickel atoms will have a ferritic structure if no carbon is present, and a ferritic-pearlitic structure if carbon is present in the material. The relative amounts of pearlite, ferrite and martensite depend on the carbon content.

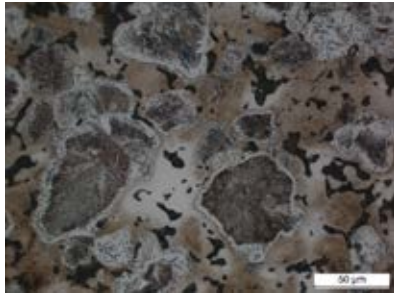
As already stated in the case of copper, a more homogeneous nickel distribution can be obtained by increasing the sintering time and/or the sintering temperature. In the case of an iron-nickel-carbon alloy, the amount of austenite decreases while the amount of martensite increases (if e.g. the sintering temperature is increased).

1.4.7.4 Fe-Cu-Ni-Mo-C

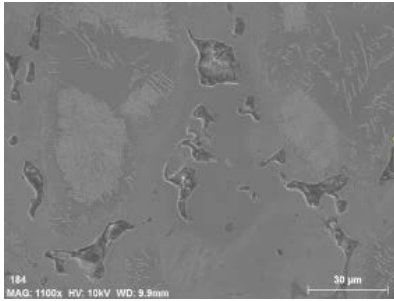
PM steels are often alloyed with copper, nickel, molybdenum and carbon. In order to prevent demixing, the alloying elements are often diffusion-bonded to the iron particles, as for example in the case of Distaloy® AE (4% Ni, 1.5% Cu, 0.5% Mo). Distaloy AE + 0.5% C is now examined in order to understand the relationship between microstructure and distribution of the alloying elements Ni, Cu, Mo and C.

The microstructure of Distaloy AE + 0.5% C sintered at 1120°C for 30 minutes is reported in *figure 1.59a*. The material was cooled at a rate of approximately 1°C/second. Martensite, austenite, ferrite, bainite and pearlite can be observed.

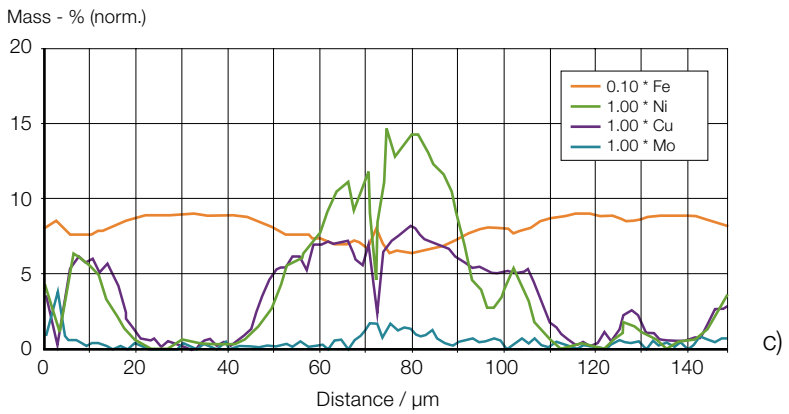
Figure 1.58 shows Ni and Cu distribution after sintering at 1120°C for 30 minutes. Areas with high Cu and Ni content can be observed. The distribution of Mo is difficult to study for two main reasons: (a) the amount of Mo is relatively small in this material, (b) Mo diffuses faster in the Fe lattice, compared with Ni and Cu, which gives a more homogenous distribution of Mo.



a)



b)



c)

Figure 1.58 Distalloy AE + 0.5% C, sintered at 1120°C for 30 minutes.

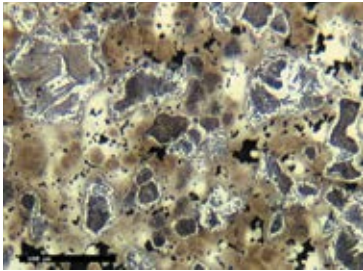
(a) LOM image.

(b) Same as in (a) but SEM image.

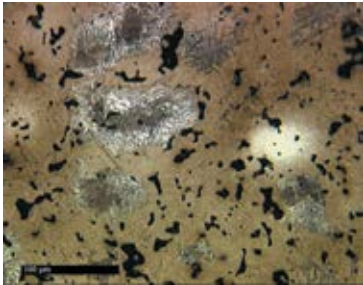
(c) Fe, Cu, Mo and Ni distribution along the line indicated in (b).

Note that (a) and (b) do not have the same magnification.

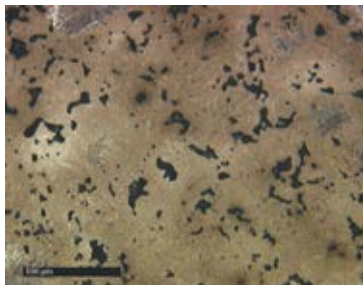
During sintering Ni atoms diffuse from the Ni particles into the Fe lattice and vice versa: Fe atoms diffuse from the iron lattice into the Ni particles. A gradient in Ni concentration is present in the material due to the slow diffusion rate of this alloying element. The highest Ni concentration (around 30%) is found in the austenite phase which corresponds largely to the original Ni particles. *Figure 1.59* shows that a very long time is needed to obtain a homogeneous Ni distribution when sintering at 1120°C. Austenite areas rich in Ni are still present after sintering for 4h at 1120°C.



a)



b)



c)

Figure 1.59 Distaloy® AE + 0.5% C after sintering for (a) 30 minutes, (b) 4h and (c) 16h, respectively at 1120°C.

Cu is more homogeneously distributed if compared with Ni, after sintering at 1120°C for 30 minutes. Highest Cu concentration approximately 5-7% is found in the austenite areas, as shown in *figure 1.58*. Copper distribution is more homogeneous compared with Ni, due to the fact that copper melts at the sintering temperature. Melted copper is pulled by capillary forces between both the iron powder particles and the grain boundaries. From there the copper atoms diffuse into the Fe lattice, as described in Section 1.3.4.2.

Mo is more homogeneously distributed than Ni and Cu, due to its faster diffusion rate in the Fe lattice. Even though the Mo distribution is difficult to study, a slightly higher Mo content has been found in the bainitic areas located around the pearlitic areas always when sintering at 1120°C for 30 minutes.

The rate of carbon diffusion is much faster than that for Ni, Cu and Mo. Therefore less than 30 minutes is sufficient for carbon to dissolve and achieve a homogeneous distribution at 1120°C.

The concentration of alloying elements is highest at the surface of the original iron powder particles. These areas will therefore transform into martensite during cooling from the sintering temperature. An extended time is needed for substitutional alloying element to reach the centre of the original iron powder particles. Therefore the longer the distance from the surface of the original Fe particle, the lower the amount of Ni, Cu and Mo. Due to the lower amount of alloying element, a mixture of bainite, pearlite and very small quantities of ferrite form.

The diffusion rate of Ni, Cu and Mo increases when increasing the sintering temperature, which results in a more homogeneous distribution of these alloying elements in the material. The quantity of martensite increases, while the amount of austenite, pearlite and bainite decreases. *Figure 1.60* shows the microstructure of Distaloy® AE + 0.5% C sintered at 1250°C for 30 minutes.

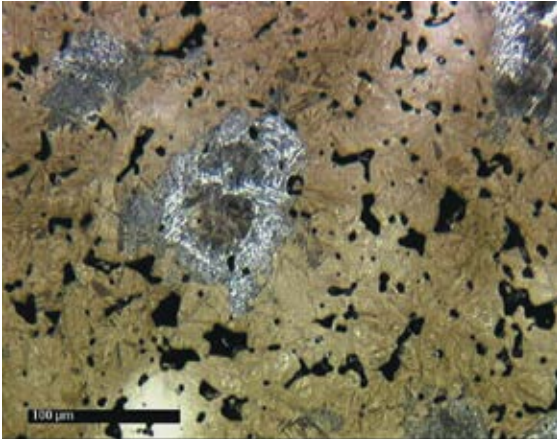


Figure 1.60 Distaloy® AE + 0.5% C sintered at 1250°C for 30 minutes.

1.4.7.5 Fe-P

In powder metallurgy phosphorous is normally added to the base iron powder as Fe_3P . The most widely used Fe-P alloys contain between 0.3% to 0.60% phosphorous.

The diffusion rate of phosphorous in the iron lattice is lower than that of carbon, but higher than that of Mo, Cu, and Ni. The reasons for this are: a) at 1050°C a liquid phase forms, due to the eutectic reaction $\text{Fe-}\alpha + \text{Fe}_3\text{P} \rightarrow \text{Liquid}$ (see figure 1.20), and b) phosphorous stabilises ferrite.

During sintering at 1120°C, the P concentration at the surface of the iron powder particles temporarily exceeds 2.6 wt.% and the particles melt superficially. The liquid phase is pulled by capillary forces between the iron powder particles. The transport of both phosphorous and iron atoms in the liquid phase is faster than in the solid phase. As phosphorous diffuses deeper into the iron particles, its concentration at the surface of the iron particles drops below 2.6% and the liquid phase disappears. In addition, surface regions of iron particles with phosphorous concentrations of between 2.6 and 0.5 wt.% change from austenite to ferrite. As described in Section 1.4.5, the diffusion rate in Fe- α (BCC) is much larger than in Fe- γ (FCC).

Figure 1.61 shows the microstructure of ASC100.29 + 0.45% P sintered at 1120°C for 30 minutes. An entirely ferritic structure can be observed.

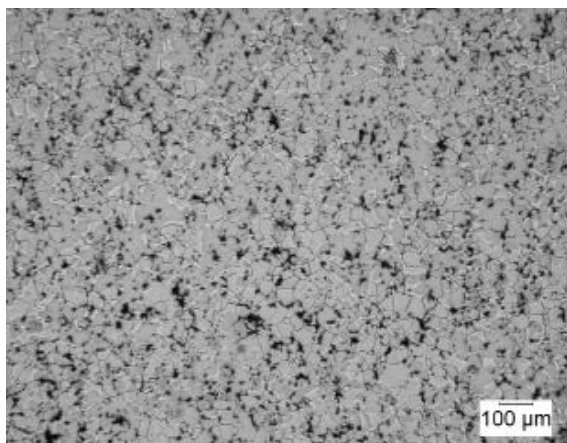


Figure 1.61 ASC100.29 + 0.45% P sintered at 1120°C for 30 minutes.

Studies conducted with P-alloyed materials have revealed that ferrite has two different P contents: 0.15 and 0.6% P respectively. The areas with high and low phosphorous content can be observed in a metallic microscope with samples etched in 4% Nital and defocused (*figure 1.62*). The areas with low P content appear as a light phase with an heterogeneous surface structure and clear boundaries between the ferrite grains, while the areas with high P content appear dark and flat. The ferrite grain boundaries in the P-rich areas can be seen only in high magnification*.

According to the Fe-P phase diagram (*see figure 1.20*), both ferrite and austenite are present at the sintering temperature (1120°C) when P is added in the range 0.3-0.6%. The P content is much higher in ferrite than in austenite. As the P distribution changes only slightly during cooling, two phases, one with low and one with high P content, are found at room temperature.

* "Brittleness in Phosphorous Alloyed Sintered Steels"

Ulla Gustavsson, Per Johansson. Swedish Institute for Metals Research, Höganäs AB, IM-2173.

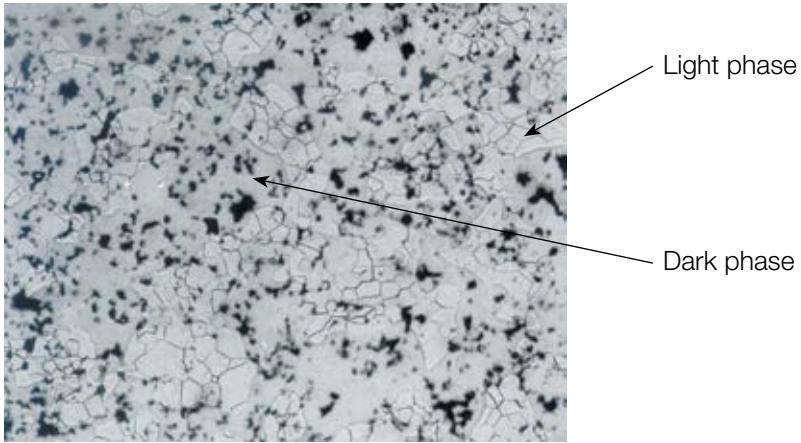


Figure 1.62 Areas with low and high phosphorous content appear as light (low) and dark (high) phases in this micrograph.

The presence of a liquid phase and mostly ferrite at the sintering temperature increases the sintering rate. This results in a spheroidisation of the pores. See *figures 1.63 and 1.64*, where the pore structure of ASC100.29 with and without phosphorous additions is compared.

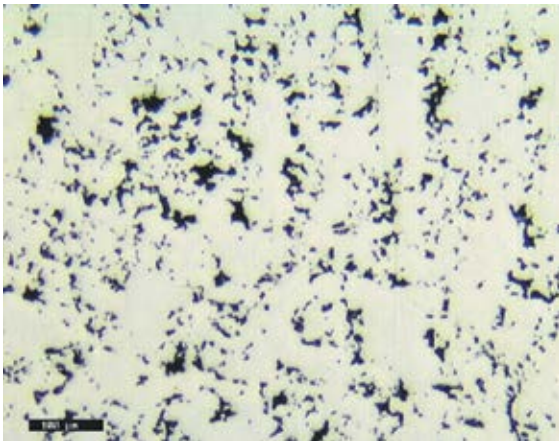


Figure 1.63 ASC100.29, compacting pressure 600 MPa, sintering at 1120°C for 30 minutes.

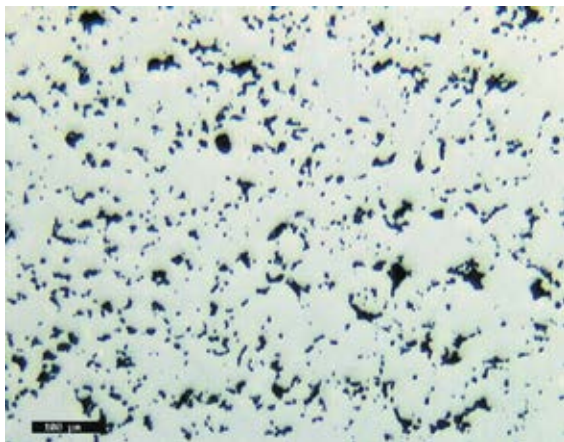


Figure 1.64 ASC100.29 + 0.45% P, compacting pressure 600 MPa, sintering at 1120°C for 30 minutes.

1.5 Mechanical Properties and Microstructures

This section will deal exclusively with relationships between the microstructures and mechanical properties of sintered steels. Thus attention is now focused on the performance (or functional) properties of sintered steels. The introduction below briefly describes the major microstructural components and their relationship to the performance from a general point of view. Following this, various typical structures are analysed and discussed in regard to mechanical properties.

1.5.1 Introduction

In the sections above it has been shown how structures develop and what factors determine the amount and distribution of different phases in PM materials. In other words: their thermal and mechanical “history”, chemical composition and the diffusion paths of the elements present. The “history” of a material can be examined in its microstructure, but micrographs can also be used to predict, mostly qualitatively, the functional properties of sintered steels.

As mentioned, this section deals with the influence of microstructure on mechanical properties. Keep in mind that porosity has a great influence on performance, since pores cannot carry loads and they may act as crack initiators. In *figure 1.65*, the connection between process parameters, “history”, microstructure and performance is shown.

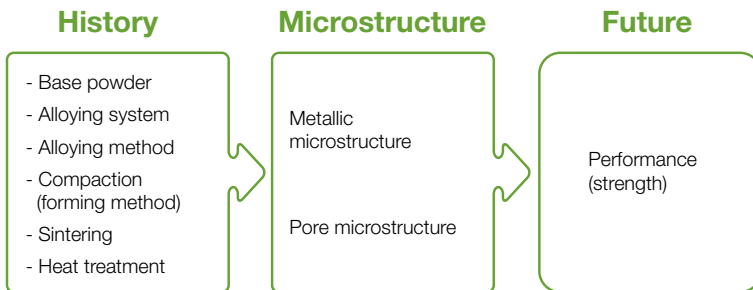


Figure 1.65 Connection between history, microstructure and performance of PM materials.

What constitutes the microstructure and which constituents define the performance of a material? In order to answer the first question one has to know the appearance of different structures and how they are classified. This is dealt with in other sections in this handbook. The second question is dealt with in the following. Performance is how a material responds to mechanical treatment (in its application environment) and is a function of:

- stress state (defined by geometry of the component and load conditions)
- strain rate
- temperature

These “macroscopical” conditions can be translated into microstructural terms. From Höganäs Handbook Vol. 1*, and other literature**, it is known that the main deformation mechanism in metals is dislocation movements. Consequently, the main methods of obtaining greater strength and performance in a material depend upon preventing dislocation movements. In mechanical metallurgy, or physical metallurgy, these methods are called hardening mechanisms. Some of the most important *hardening mechanisms* are presented here. In the following text, strength means the ultimate tensile strength if no other defining qualities are mentioned.

1.5.2 Hardening mechanisms

1.5.2.1 Grain boundary hardening

The more grains (NB not particles!) per volume in a structure (i.e. less average grain diameter) the more obstacles for dislocation movements, hence the higher strength of the material. This is referred to as grain boundary hardening. Thus, a fine grain structure has higher strength than a coarse one.

1.5.2.2 Precipitation hardening

If secondary phases are present in a structure, these can also prevent dislocation movements. A more finely dispersed secondary phase, or phases, (i.e. smaller average diameters of the secondary phase regions and less distances between these regions) gives higher strength. This is often referred to as *precipitation hardening*. A fine dispersed structure thus has higher strength than a coarse one.

* “Höganäs Handbook for Sintered Components”, No 1-3. Höganäs 2013.

** “Mechanical Metallurgy”, George E. Dieter McGraw-Hill Book Company, 1988 (ISBN 0-07-100406-8).

1.5.2.3 Solid solution hardening

The solid solution between elements in an alloy gives rise to a microscopic tension in the crystal lattice which obstruct dislocation movements. This is in fact the case for all hardening mechanisms; they create a tension, a disturbance, in the crystal lattice. As in the case of precipitation hardening (see above), the distance between and frequency of these disturbances, in this case “foreign” atoms in the mother lattice, determine the strength.

One distinguishes between interstitial and substitutional solution. Interstitial solution describes the situation e.g. with C in Fe (alloying atoms can fit between the atoms in the mother lattice). Substitutional solution describes the situation e.g. with Mo in Fe (alloying atoms substitute atoms of the base material).

This hardening mechanism cannot easily be spotted in a microstructure. When analysing the structure it is therefore important to know the approximate relative diffusion rates of the different added elements in the powder mix in order to know what kind of concentration gradients might be present in the structure, (see figure 1.48). The concentration gradients will result in changes in hardness/strength.

1.5.2.4 Deformation hardening

As a metal deforms, dislocations slide, multiply, get entangled, and hinder further deformation. Hence dislocations are both a deformation mechanism and a way of stopping deformation. Or more clearly, they increase the flow stress (i.e. the stress required to further deform the material).

In normal Light Optical Microscopy (LOM) dislocations cannot be spotted. Other methods are needed, such as Transmission Electron Microscopy (TEM). In this handbook only LOM-micrographs are considered and therefore this hardening mechanism is not revealed by the microstructure. Deformation hardening is of limited importance for sintered steels as these are often used as-sintered or as-heat treated. The deformation occurring during sizing and coining of sintered steels parts is normally very limited and thus has a minor effect on mechanical properties.

1.5.3 Relative strength/hardness of different phases and structures

Briefly, structures mean geometrical separable regions of a micrograph, which are built up by one or more phases. Hence pearlite is a structure built up by two phases, ferrite and cementite, in a characteristic geometrical pattern (lamellas). Note that bainite also is a structure of ferrite and carbides (mostly cementite), but with other geometrical properties than pearlite.

HV0.05

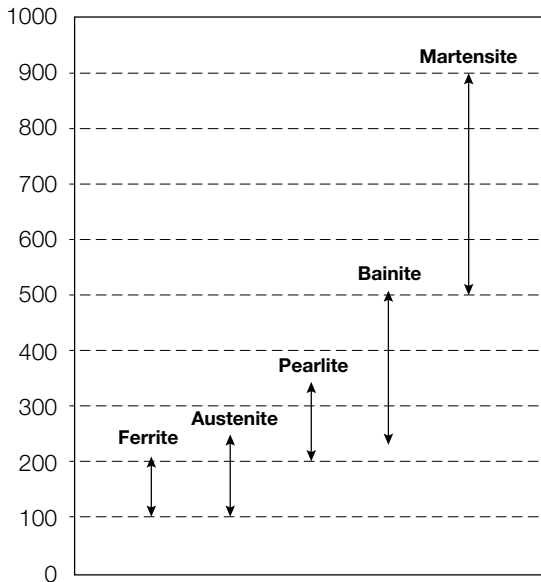


Figure 1.66. Micro hardness range of different phases and structures measured for a great number of alloying systems.

The different transformation structures of steel (Fe-base alloys) have different strengths/hardness, depending on above mentioned hardening mechanisms (see also Höganäs Handbook for Sintered Components Vol. 1, Chapter 1.7*).

* "Höganäs Handbook for Sintered Components", No 1-3. Höganäs 2013.

In *figure 1.66*, the micro hardness range (HV0.05) for the different structures have been measured for a large number of alloying systems. This means that the data below is applicable for sintered steels based on different pure iron powders with admixed alloying elements such as graphite, copper, nickel and phosphorous, but also for prealloyed steel powders and diffusion alloyed grades with various alloying elements. Sintering conditions are between 30-60 minutes at 1120-1250°C in various sintering atmospheres.

It is obvious that ferrite is the “softest” phase and martensite the hardest phase (or structure). Martensite is a phase but when tempered small carbides precipitate in the martensite matrix, one can call martensite a structure.

The amount and distribution of the different structures and phases, and the morphology or microstructure, define the mechanical properties of a material.

1.5.4 Fe-C

In *figure 1.67* two PM steels, ASC100.29 and ASC100.29 + 0.5% C, are shown. In the C-containing material pearlite (lamellar structure), ferrite (bright) and pores (black) can be observed. Ferrite and a certain fraction of porosity can be observed in pure ASC100.29. Ferrite grain boundaries are clearly seen both in the C-containing material and in pure ASC100.29.

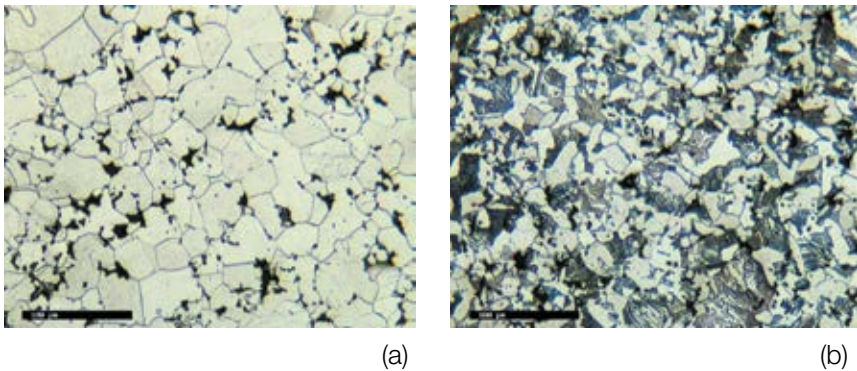


Figure 1.67 Microstructure of sintered (a) Fe and (b) Fe-C.

The effect of carbon in the structure is thus not only a solid solution strengthening of the ferrite, as interstitial dissolved carbon, but also a “precipitation hardening” by the pearlite regions. The ferrite cannot dissolve very high amounts of carbon (see the Fe-C phase-diagram in Section 1.2.2.4), which is why the contribution of the pearlite-structure to the higher strength of the Fe-C-material is dominating. The higher fraction of carbon, the more pearlite and hence higher strength. The grains are also smaller in the iron-carbon material. This is due to the dissolved carbon, which hinders the grain growth in a similar way to dislocation movements, at the sintering temperature (1120°C). At this temperature the structure is completely austenitic and can dissolve much carbon. (The solubility of carbon in austenite is approximately 1.8%.)

Pure ASC100.29 without any additives has a tensile strength of approximately 190 MPa at a density level around 7.0 g/cc. For ASC100.29 + 0.5% C, the value is higher, around 310 MPa.

1.5.5 Fe-Cu and Fe-Cu-C

Copper is a very common alloying element in PM Steels and the addition can be made with either a variety of elemental copper grades or copper “carriers” such as

- elemental additions with different particle sizes (e.g. Cu-100, Cu-200)
- partially prealloyed alloys or master alloys (e.g. Distaloy® AE, Distaloy® Cu)
- fully prealloyed master alloys (e.g. Astaloy™ 20 Cu)

The sintered microstructure in copper steels is very dependant upon the copper source. In *figure 1.68* the addition of elemental copper is illustrated. Addition of different Cu-master alloys to PM steels and their effect on the microstructure is illustrated in the metallographic atlas (see Chapter 2).

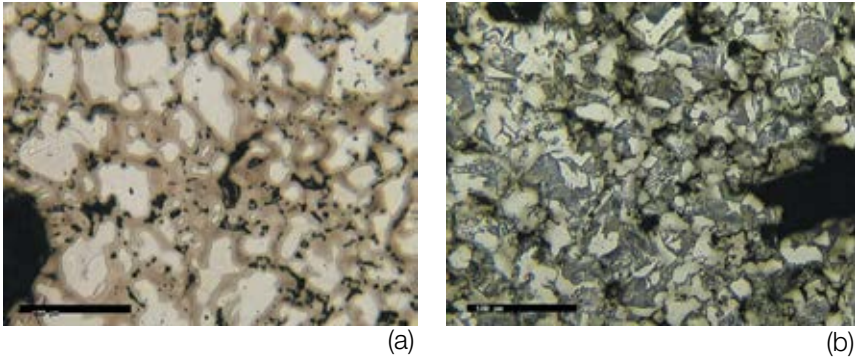


Figure 1.68 Microstructure of sintered (a) Fe-Cu and (b) Fe-Cu-C.

The effect of elemental Cu addition can be seen in *figure 1.68*. *Figure 1.68a* shows ASC100.29 + 2% Cu and *figure 1.68b* ASC100.29 + 2% Cu + 0.5% C. *Figure 1.68a* has bright areas surrounded by darker borders, where the borders are copper rich ferrite. If the sintering time is increased, the width of the borders should increase as is expected due to the longer time required for diffusion processes to occur.

In the present structure copper is completely dissolved in the ferrite and the main strengthening mechanism is solid solution hardening. Here it is obvious that a concentration gradient is present giving a strong skeletal structure of copper rich ferrite around the softer original ferrite grains.

After melting, copper infiltrates the structure along the grain boundaries during sintering, which explains the swelling behaviour of copper. That is why grain boundaries are hard to separate from particle to particle contacts.

The material in *figure 1.68a* has a tensile strength of approximately 300 MPa compared with 190 MPa for a copper-free material, as in *figure 1.67a*.

Figure 1.68b is a combination of skeletal copper-rich ferrite and areas of pearlite in the centre of the original particles. The pearlite is somewhat degenerated and not as regular as normal “text book” examples due to the disturbance from copper. Adding the pearlite and the precipitation hardening to the skeletal copper rich ferrite increases the tensile strength to approximately 500 MPa at this density level.

1.5.6 Fe-P

Phosphorous creates a liquid phase, as copper, during normal sintering conditions. The difference in microstructure is however significant. Unlike the copper in low concentrations, phosphorous creates shrinkage due to sintering in the ferrite phase. The P-diffusion rate is not as high as for carbon but still fast enough at normal sintering times and temperatures to assure a good distribution of phosphorous in the material.

Figure 1.69a shows the microstructure of ASC100.29 + 0.45% P. A homogeneous ferrite structure is observed. In reality, one low-phosphorous phase and a high-phosphorous phase are present containing 0.15% and 0.60% P, respectively*. The major strengthening mechanism for this sintered steel is thus the solid solution strengthening of ferrite. It can also be seen that the pores are much more round (compared with e.g. *figure 1.67a*) which also contributes to the strength. A tensile strength of approximately 400 MPa is achieved when 0.45% P is added to iron.

Once again, when adding carbon, the strength increases due to dispersion hardening. *Figure 1.69b* shows the microstructure of ASC100.29 + 0.45% P + 0.5% C. Ferrite (bright areas) and pearlite (greyish, lamellae areas) are observed. The strength is around 500 MPa.

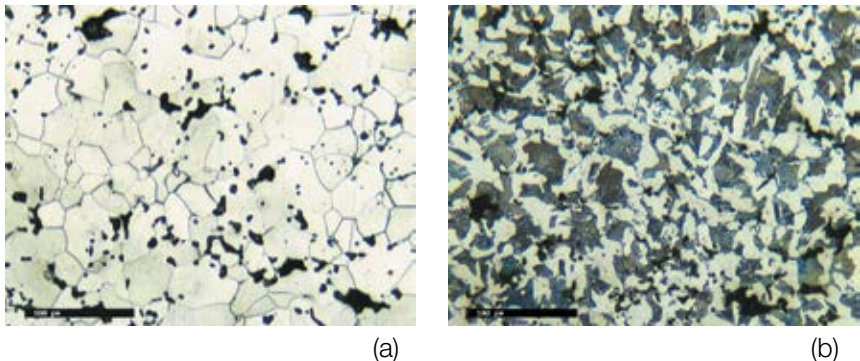


Figure 1.69 Microstructure of sintered (a) Fe-P and (b) Fe-P-C.

* "Brittleness in Phosphorous Alloyed Sintered Steels"

Ulla Gustavsson, Per Johansson. Swedish Institute for Metals Research, Höganäs AB, IM-2173.

1.5.7 Prealloyed structures: Fe-Mo, Fe-Cr-Mo

Instead of admixing alloying elements, it can be feasible to homogenise an alloying element in the molten state before atomisation takes place. The result is a base powder with lower compressibility but with increased hardenability, which can be very useful. Powder grades like Astaloy™ Mo and Astaloy CrM® are good examples of these materials. The resulting structures are homogenous and contain bainite and martensite, depending on carbon content and other alloying elements and sintering conditions. Most often the structures are completely bainitic as is shown in *figure 1.70* (Astaloy Mo + 0.5% C). The strength of this material is approximately 500 MPa.

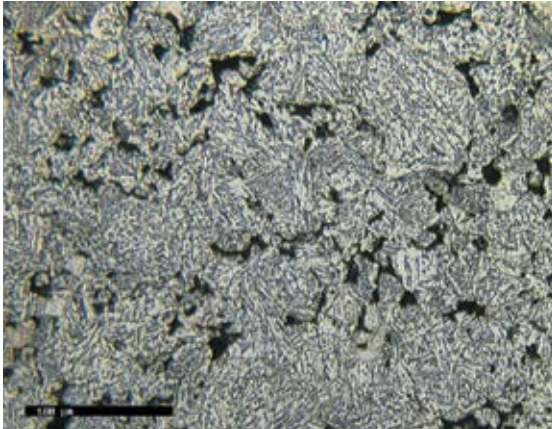


Figure 1.70 Microstructure of sintered Astaloy Mo + 0.5% C.

1.5.8 Heterogeneous and Homogenous Structures: Fe-Ni-Cu-Mo-C

As seen in the sections above, the strength of PM steels is controlled by the “edges” of the pores (i.e. the skeletal structure) and the hardness/strength in the centre of the original particles.

Heterogeneous structures, like diffusion alloyed materials, have remarkably high impact strength compared with homogenous materials, at both low and high density levels*. In *figure 1.71* two heterogeneous microstructures are shown.

* Jens Rasmus, Monica Carlsson, Anne Larsson-Westberg, Höganäs AB, 1999.

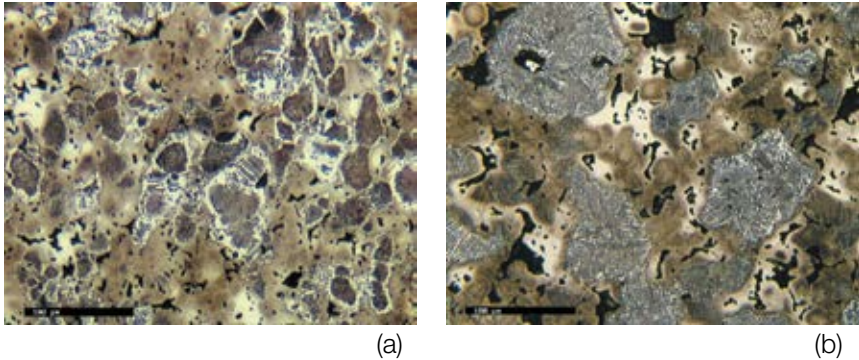


Figure 1.71 Microstructure of sintered (a) Distaloy AE + 0.5% C and (b) Distaloy HP + 0.5% C.

Figure 1.71a shows Distaloy[®] AE admixed with 0.5% C. The pores are black and in the center of the original particles it is possible to spot pearlite (the somewhat degenerated grey areas). A brown and white spotted area is embedding the pearlite islands, giving skeletal reinforcement to the structure. The brown regions are copper and nickel-rich martensite, and the white areas are nickel-rich austenite.

Austenite increases the toughness of the material (and the impact energy). At low Ni concentrations the austenite can transform to martensite if the crystal is deformed, and at higher Ni concentrations the strain-rate hardening properties of austenite will hinder further deformation. Both low and high Ni concentrations are present in the structure. The penetration depth, into the iron particles, can be seen in the structure and this is easily explained by “relative diffusion rates” in *figure 1.49*. Nickel has a low diffusion rate in iron and the nickel-rich areas are not as big as the copper rich-regions, for example. Molybdenum is not easy to detect, but just around the pearlite areas a border of molybdenum-rich bainite is present.

Distaloy AE + 0.5% C has a tensile strength of 720 MPa. If the base material, ASC100.29, is changed to a prealloyed material like Astaloy[™] Mo, even higher strengths are possible. Distaloy HP (**H**igh **P**erformance) is such a material, with 4% Ni and 2% Cu diffusion bonded to Astaloy Mo (1.5% Mo-steel). In *figure 1.71b* 0.5% C has been admixed. Distaloy HP has a tensile strength of approximately 1000 MPa despite the lower density compared with Distaloy AE.

Distaloy® HP represents a very high performance material having the combined benefits of fully prealloyed and diffusion alloyed elements. The toughness and strength of the austenite-martensite skeletal structure embeds strong bainitic islands.

1.5.9 Heat treated materials

Heat treatment here means post-sintering treatments including case hardening, etc. The effect of a case-hardening operation is normally carburising, followed by quenching, resulting in a more or less martensitic structure at the surface of the heat treated components. *Figure 1.72* shows two similar materials that have been case hardened in a carburising atmosphere for 40 minutes, then quenched and tempered.

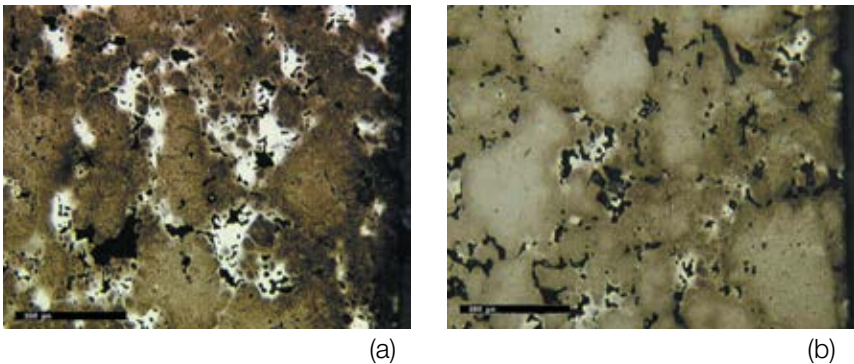


Figure 1.72 Microstructure of case hardened (a) Distaloy AE and (b) Distaloy AB.

It is obvious that the amount of “white spots” is larger in Distaloy® AE (*figure 1.72a*) compared with Distaloy® AB (*figure 1.72b*). This is explained by the lower nickel content of Distaloy AB (1.75% Ni). With the arguments from Chapter 1.5.6, the structure in *figure 1.72a*, has greater toughness than *figure 1.72b*. Distaloy AB is harder but slightly more brittle since the martensite fraction is higher.

Metallographic Atlas

2.1	Sponge Iron Powder.....	101
2.2	Atomised Iron Powder.....	125
2.3	Diffusion Alloyed Grades.....	143
2.4	Pre-alloyed Powder.....	159
2.5	Stainless Steel Powder.....	173
2.6	Continuous Cooling Transformation (CCT)...	179
2.7	Heat Treatment.....	247
2.8	Index.....	264

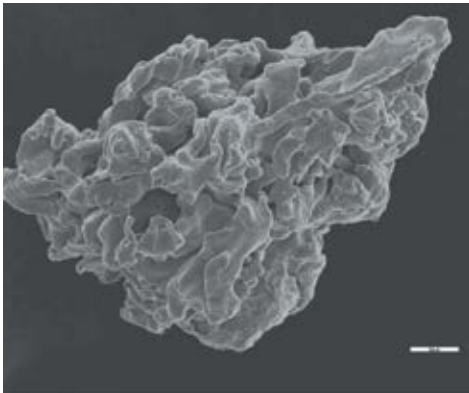


Index

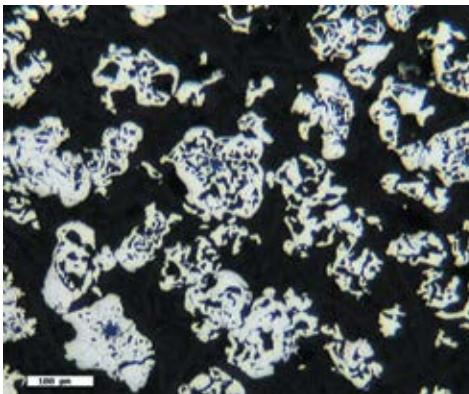
2.1.1	MH80.23	101
2.1.2	NC100.24	108
2.1.3	SC100.26	119

2.1. Sponge Iron Powder

2.1.1 MH80.23



SEM image

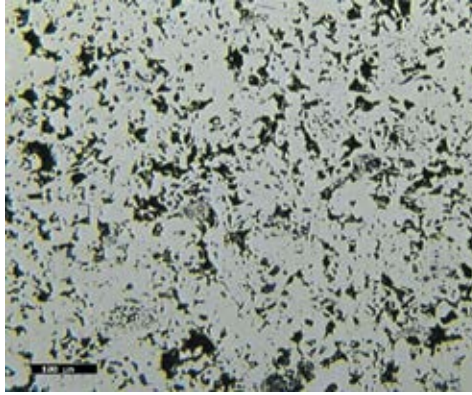


LOM image



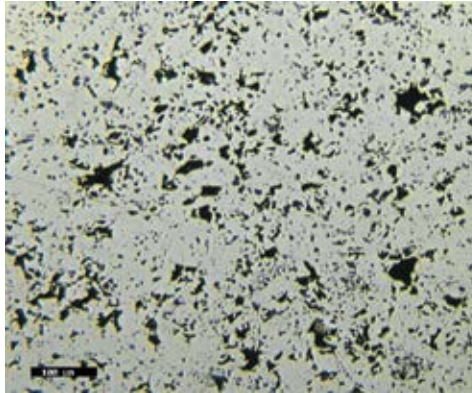
0% C

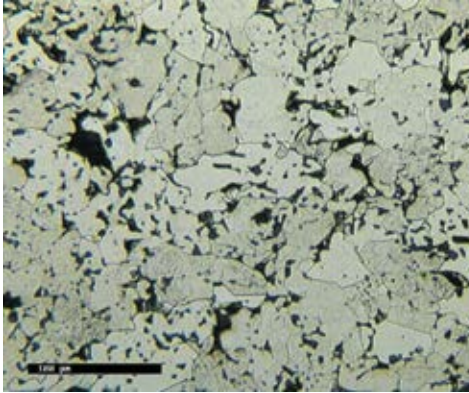
1050°C, 30 minutes
Unetched



0% C

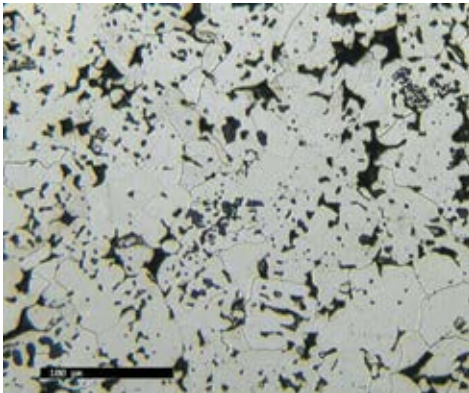
1120°C, 30 minutes
Unetched



**0% C**

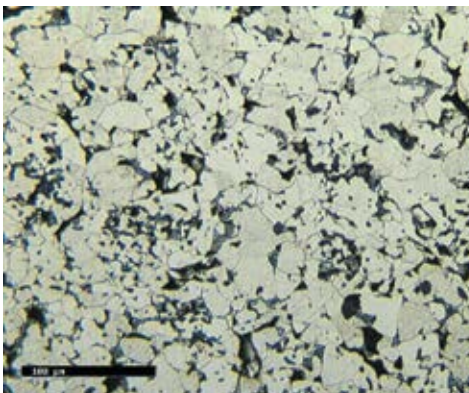
1050°C, 30 minutes

Etched: Nital

**0% C**

1120°C, 30 minutes

Etched: Nital

**0.2% C**

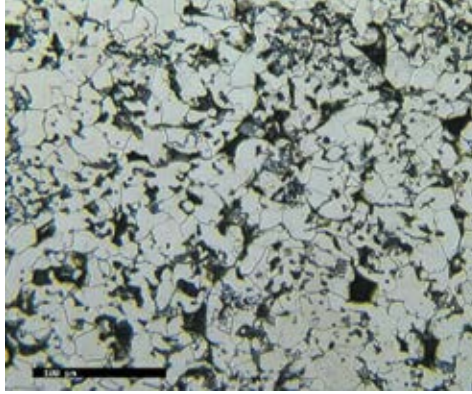
1050°C, 30 minutes

Etched: Nital

0.2% C

1120°C, 30 minutes

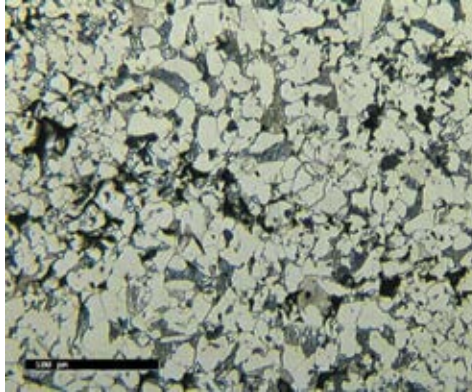
Etched: Nital



0.5% C

1050°C, 30 minutes

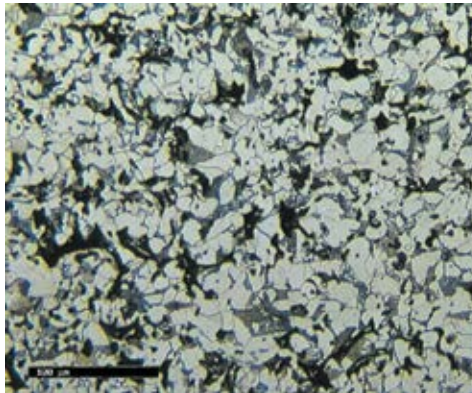
Etched: Nital

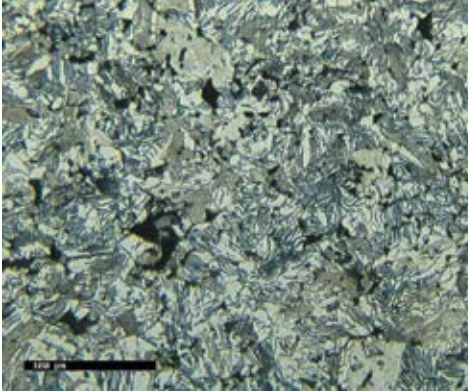


0.5% C

1120°C, 30 minutes

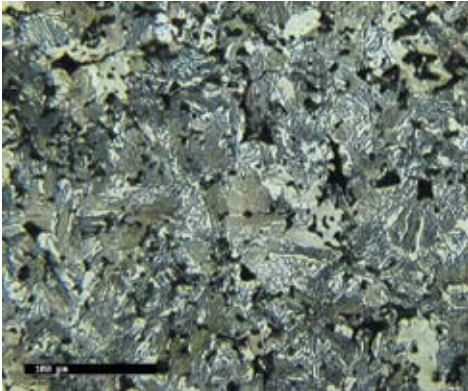
Etched: Nital



**1% C**

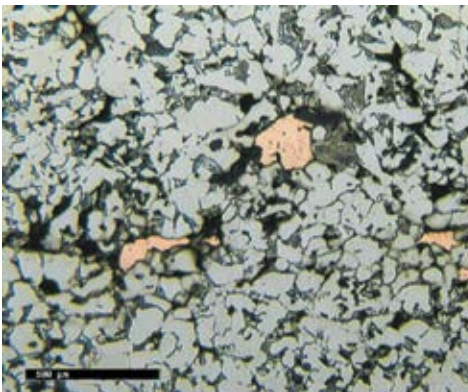
1050°C, 30 minutes

Etched: Nital

**1% C**

1120°C, 30 minutes

Etched: Nital

**2% Cu (-100) +****0.5% C**

1050°C, 30 minutes

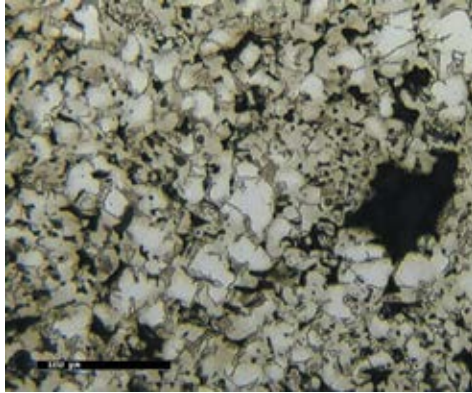
Etched: Nital

2% Cu (-100)

+ 0.5% C

1120°C, 30 minutes

Etched: Nital

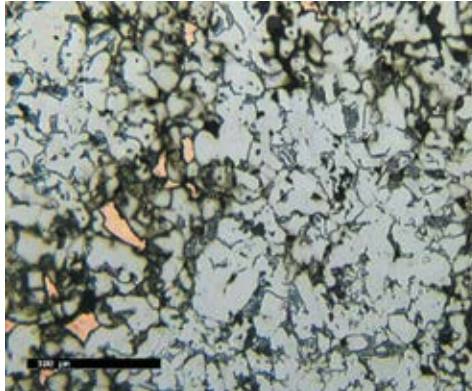


2% Cu (Distaloy® MH)

+ 0.5% C

1050°C, 30 minutes

Etched: Nital

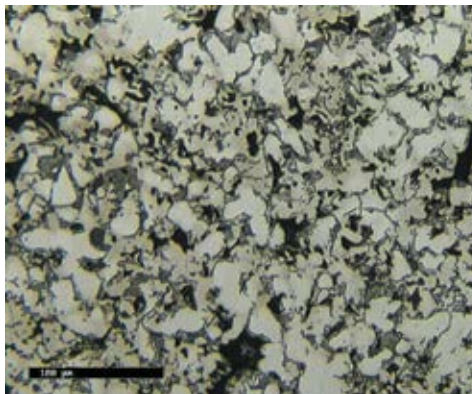


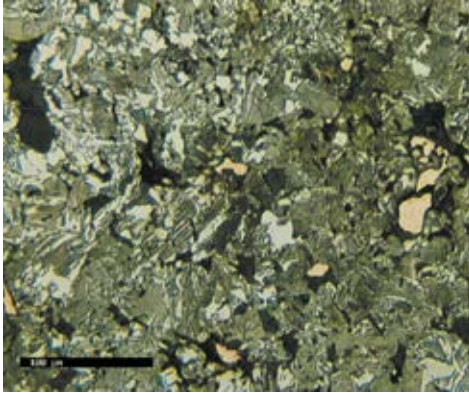
2% Cu (Distaloy MH)

+ 0.5% C

1120°C, 30 minutes

Etched: Nital



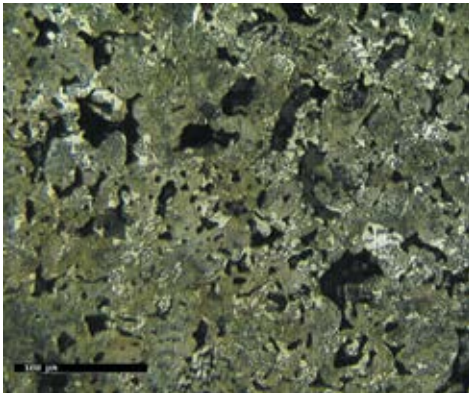


2% Cu (Distalloy Cu)

+ 0.8% C

1050°C, 30 minutes

Etched: Nital



2% Cu (Distalloy Cu)

+ 0.8% C

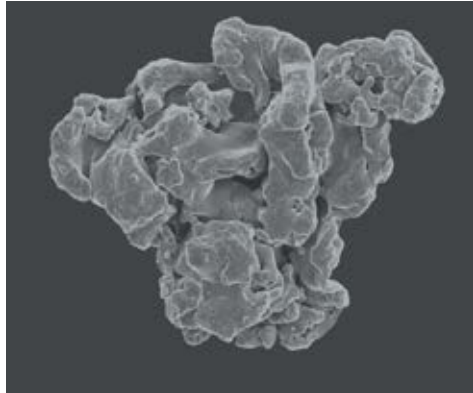
1120°C, 30 minutes

Etched: Nital

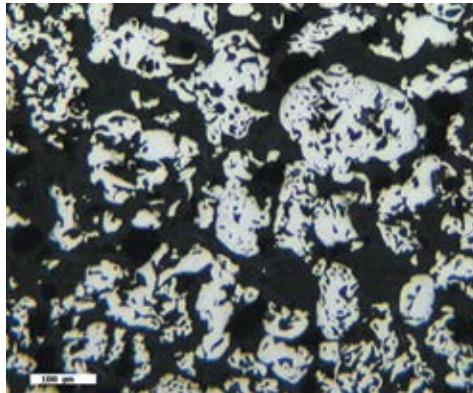


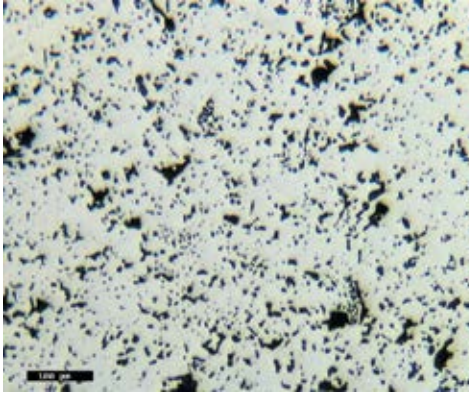
2.1.2 NC100.24

SEM image



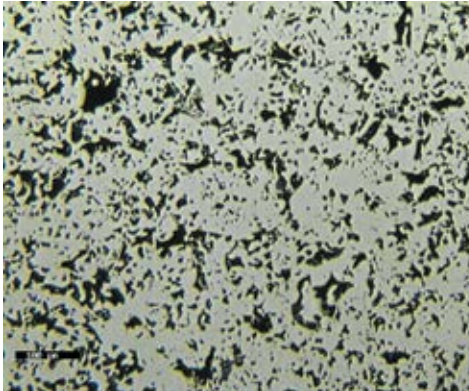
LOM image



**0% C**

1130°C, 30 minutes

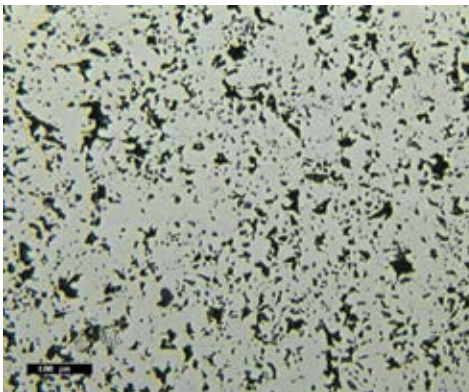
Unetched

**0.5% C**

1120°C, 30 minutes

Density: 6.2g/cm³

Unetched

**0.5% C**

1120°C, 30 minutes

Density: 6.65g/cm³

Unetched

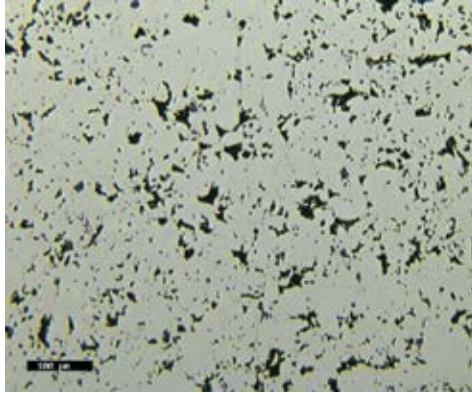


0.5% C

1120°C, 30 minutes

Density: 7.02g/cm³

Unetched

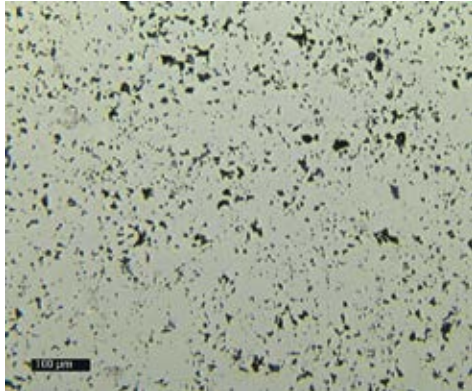


0.5% C

1120°C, 30 minutes

Density: 7.2g/cm³

Unetched

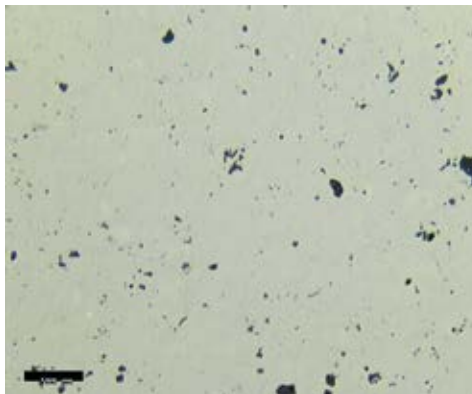


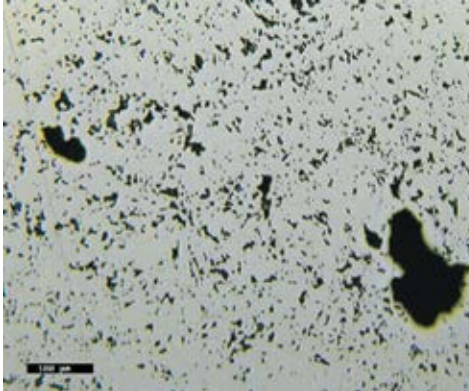
0.5% C

1120°C, 30 minutes

Density: 7.8g/cm³

Unetched

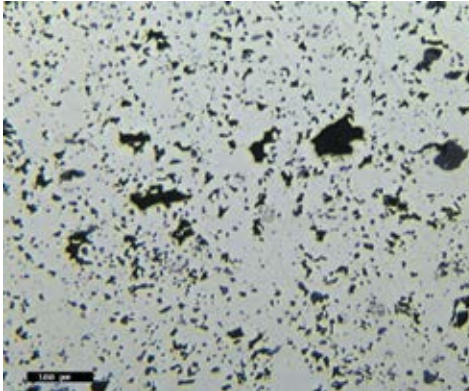




2% Cu (-100)

1120°C, 30 minutes

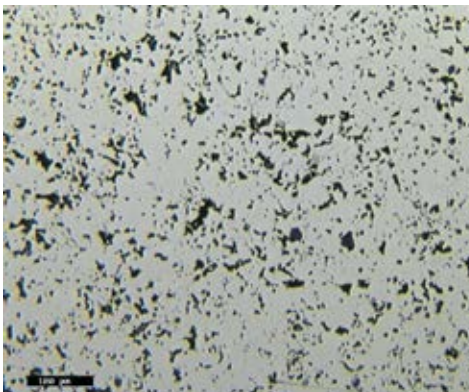
Unetched



2% Cu (-200)

1120°C, 30 minutes

Unetched



2% Cu (Distaloy® Cu)

1120°C, 30 minutes

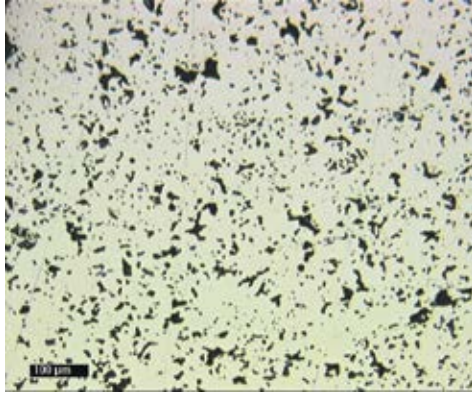
Unetched

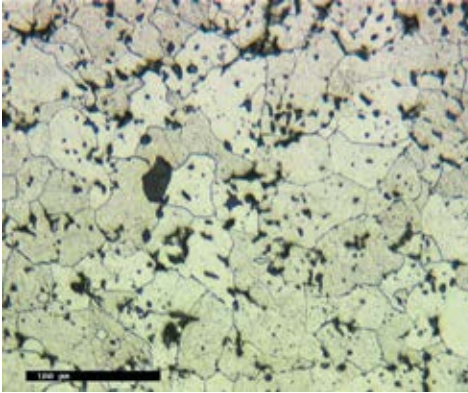


0.45% P

1120°C, 30 minutes

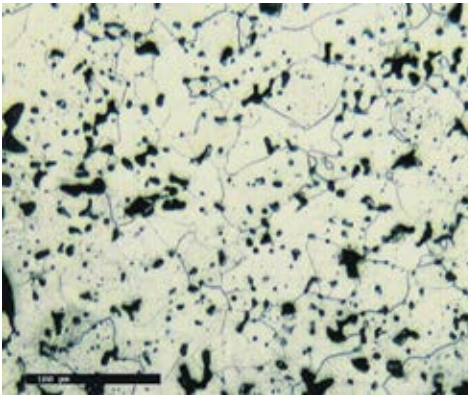
Unetched



**0% C**

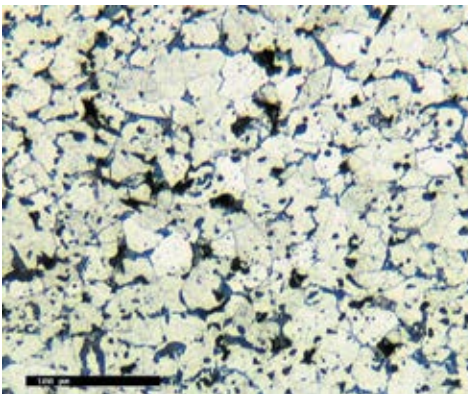
1120°C, 30 minutes

Etched: Nital

**0% C**

1250°C, 30 minutes

Etched: Nital

**0.2% C**

1120°C, 30 minutes

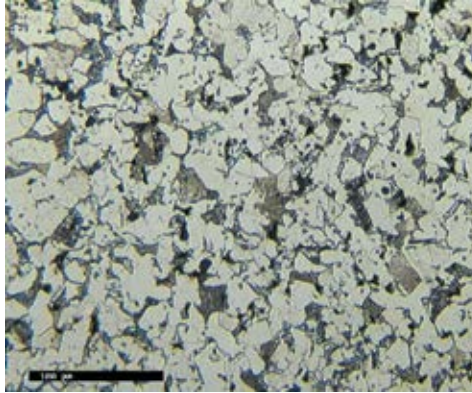
Etched: Nital



0.5% C

1120°C, 30 minutes

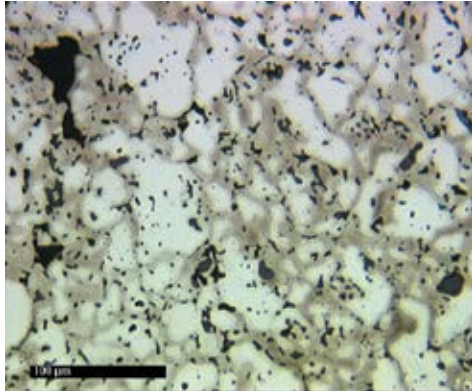
Etched: Nital



2% Cu (-100)

1120°C, 30 minutes

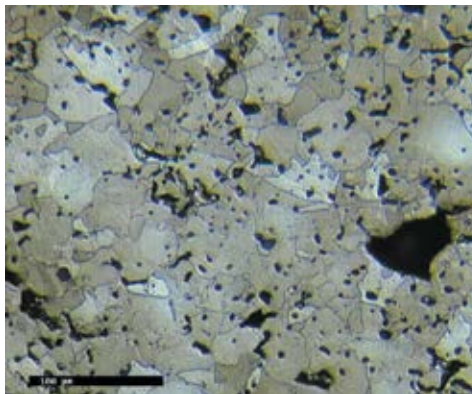
Etched: Nital

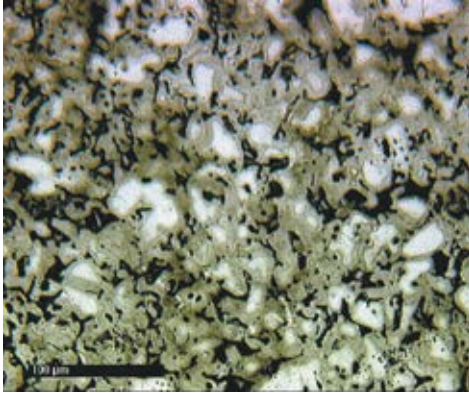


2% Cu (-100)

1250°C, 30 minutes

Etched: Nital

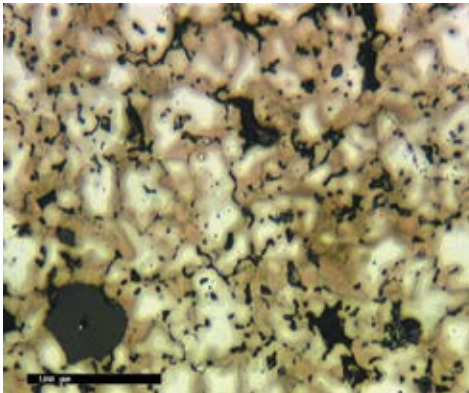




2% Cu (Distaloy® Cu)

1120°C, 30 minutes

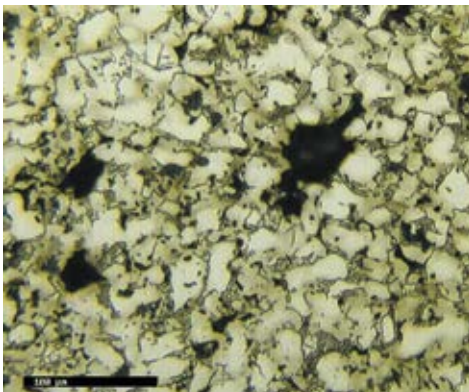
Etched: Nital



4% Cu (-100)

1120°C, 30 minutes

Etched: Nital



2% Cu (-100)

+ 0.4% C

1120°C, 30 minutes

Etched: Nital

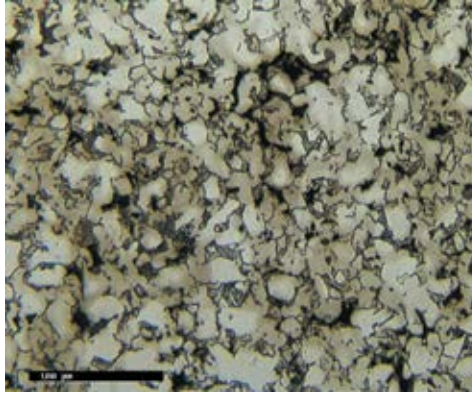


2% Cu (Distaloy® Cu)

+ 0.4% C

1120°C, 30 minutes

Etched: Nital

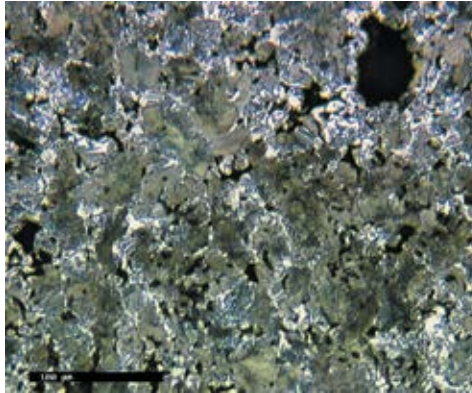


2% Cu (-100)

+ 0.8% C

1120°C, 30 minutes

Etched: Nital

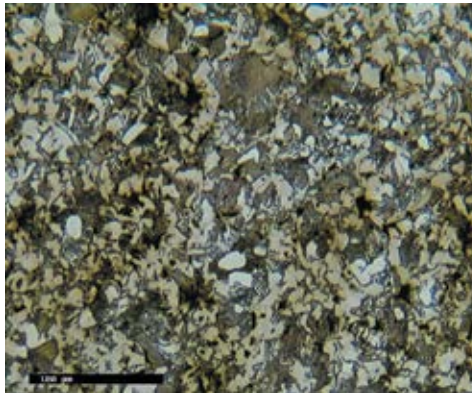


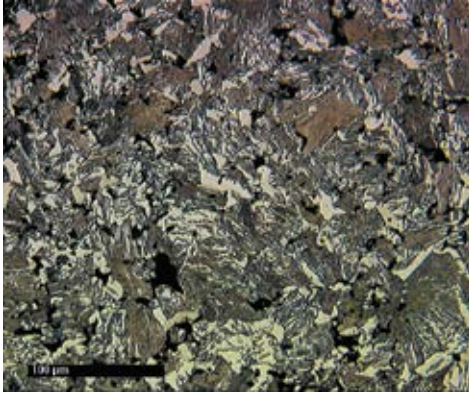
2% Cu (Distaloy Cu)

+ 0.7% C

1120°C, 30 minutes

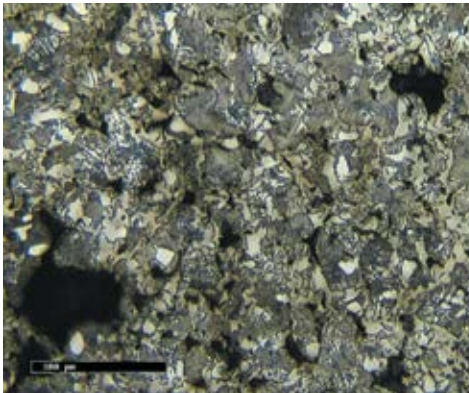
Etched: Nital



**0.8% C**

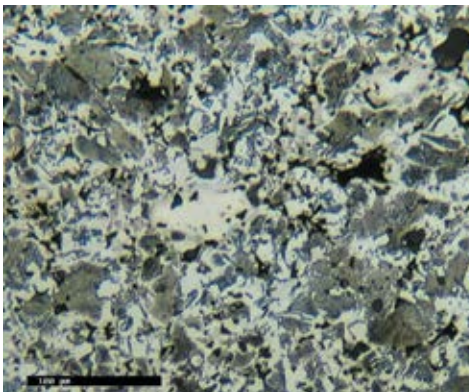
1120°C, 30 minutes

Etched: Nital

**3% Cu (-100)****+ 0.8% C**

1120°C, 30 minutes

Etched: Nital

**3% Ni + 0.6% C**

1120°C, 30 minutes

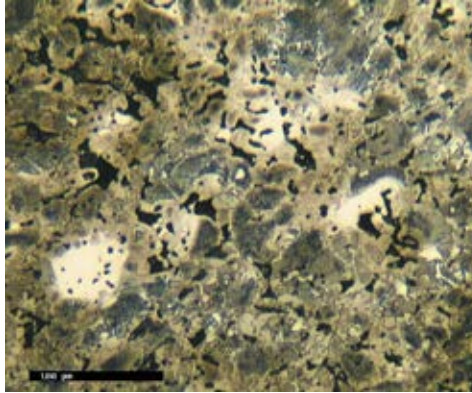
Etched: Picral



**2.5% Cu (-100)
+ 2.5% Ni + 0.6% C**

1120°C, 30 minutes

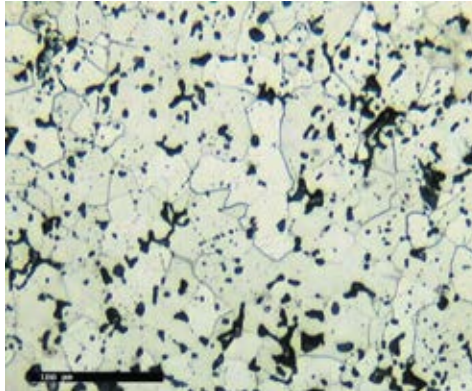
Etched: Picral



0.45% P

1120°C, 30 minutes

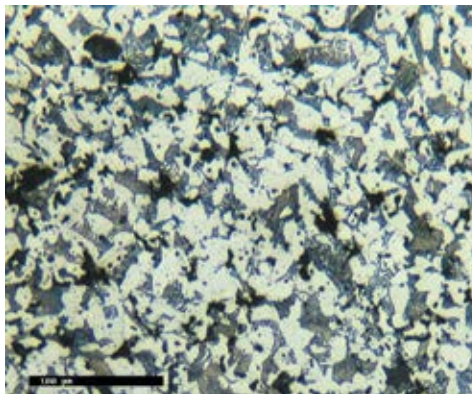
Etched: Nital



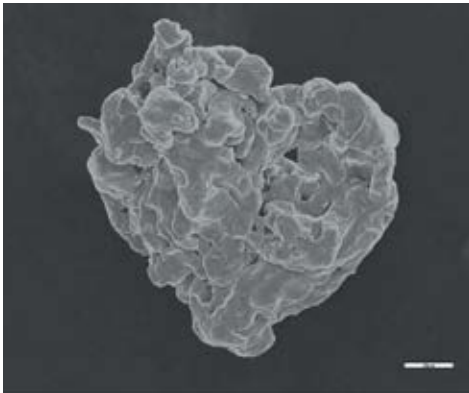
0.45% P + 0.5% C

1120°C, 30 minutes

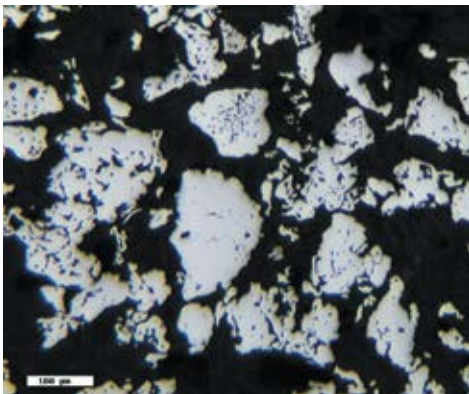
Etched: Nital



2.1.3 SC100.26



SEM image



LOM image

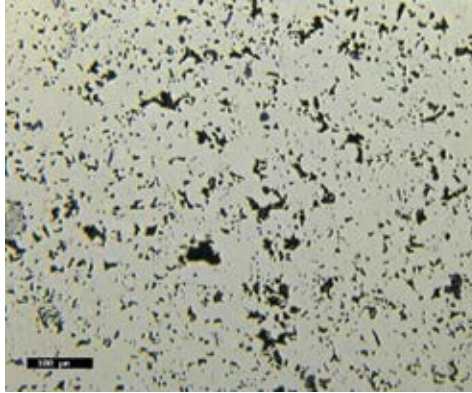


0.5% C

1120°C, 30 minutes

Density: 6.8 g/cm³

Unetched

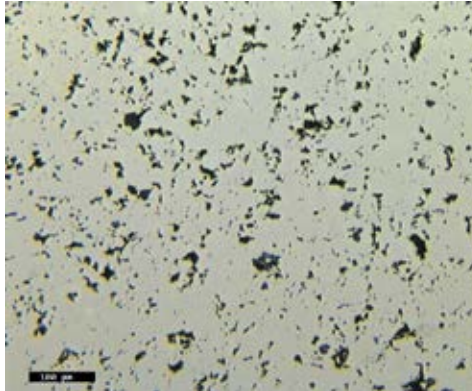


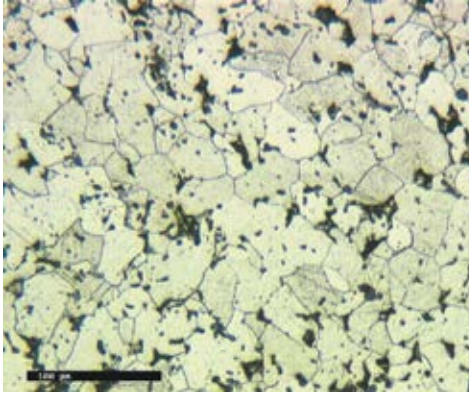
0.5% C

1120°C, 30 minutes

Density: 7.15 g/cm³

Unetched

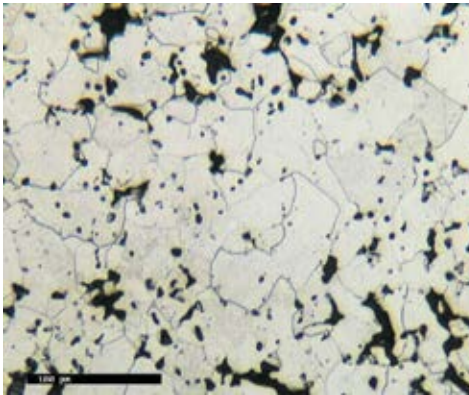




0% C

1120°C, 30 minutes

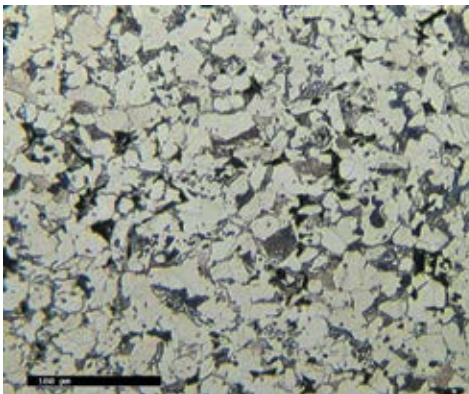
Etched: Nital



0% C

1250°C, 30 minutes

Etched: Nital



0.5% C

1120°C, 30 minutes

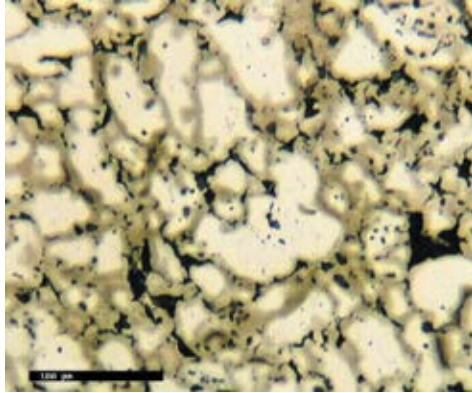
Etched: Nital



2% Cu (-100)

1120°C, 30 minutes

Etched: Picral

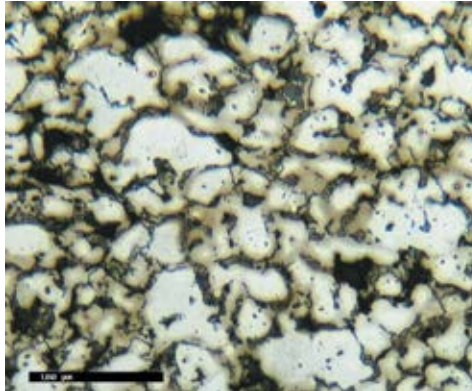


2% Cu (-100)

+ 0.2% C

1120°C, 30 minutes

Etched: Picral

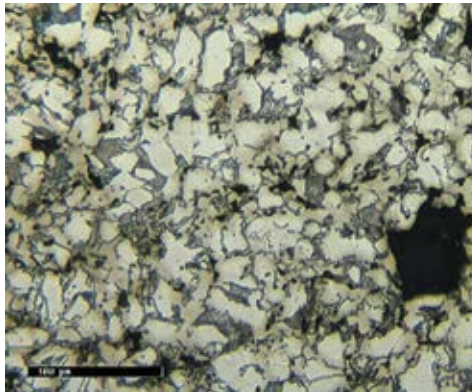


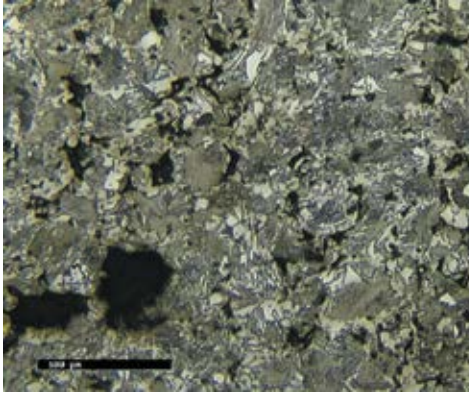
2% Cu (-100)

+ 0.5% C

1120°C, 30 minutes

Etched: Picral



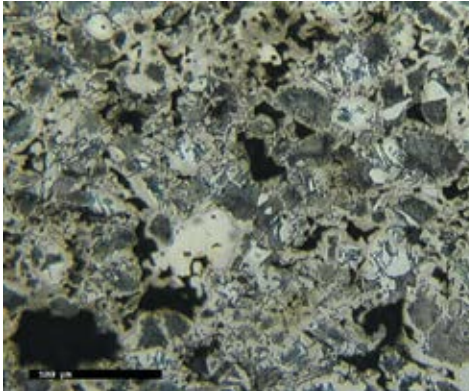


2% Cu (-100)

+ 0.8% C

1120°C, 30 minutes

Etched: Picral



2% Cu (-100)

+ 2.5% Ni + 0.6% C

1120°C, 30 minutes

Etched: Picral



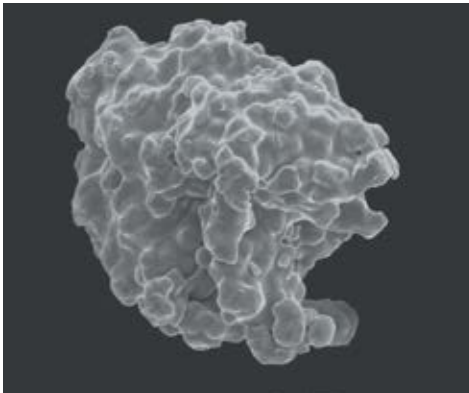


Index

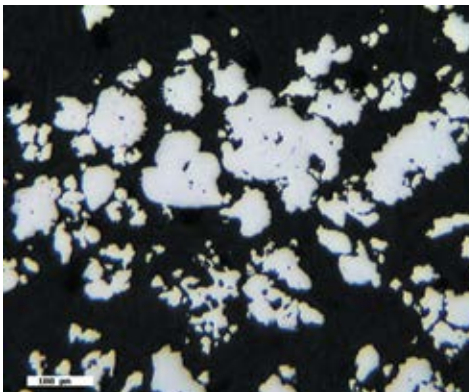
2.2.1 **ASC100.29** **125**

2.2 Atomised Iron Powder

2.2.1 ASC100.29



SEM image

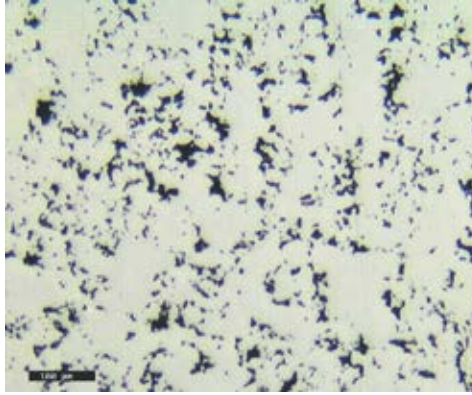


LOM image



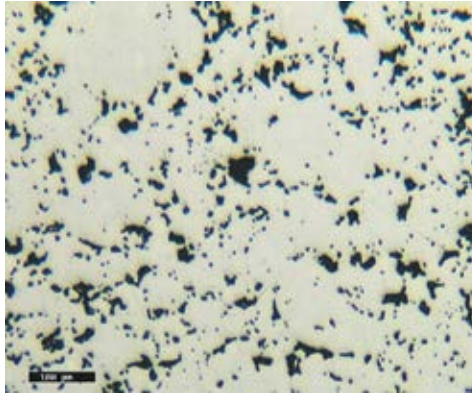
0% C

1120°C, 30 minutes
Unetched



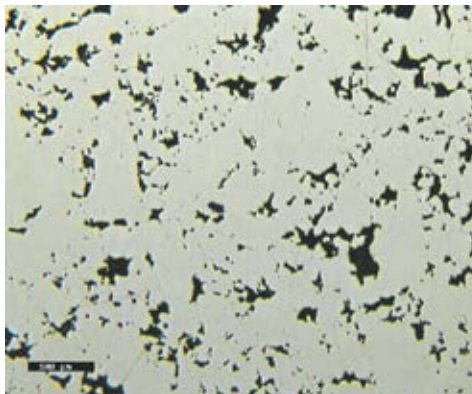
0% C

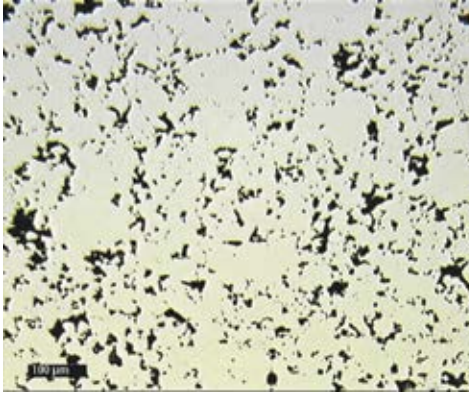
1250°C, 30 minutes
Unetched



0.5% C

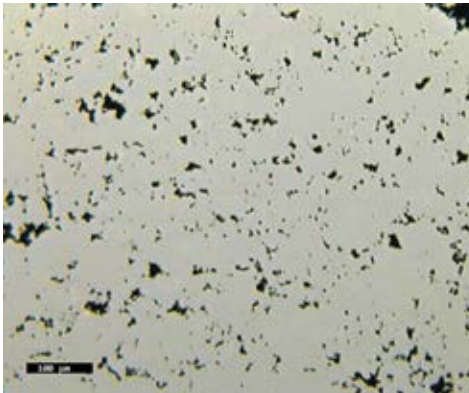
1120°C, 30 minutes
Density: 6.82 g/cm³
Unetched





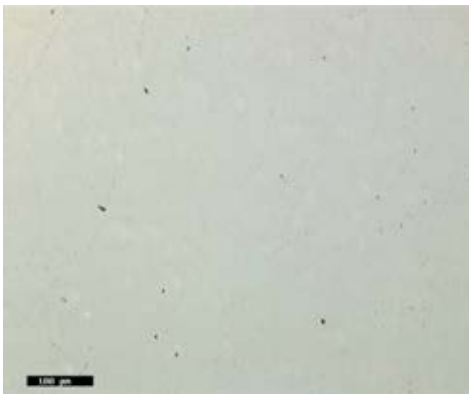
0.5% C

1120°C, 30 minutes
 Density: 7.07 g/cm³
 Unetched



0.5% C

1120°C, 30 minutes
 Density: 7.38 g/cm³
 Unetched



0.5% C

1120°C, 30 minutes
 Density: 7.85 g/cm³
 Unetched



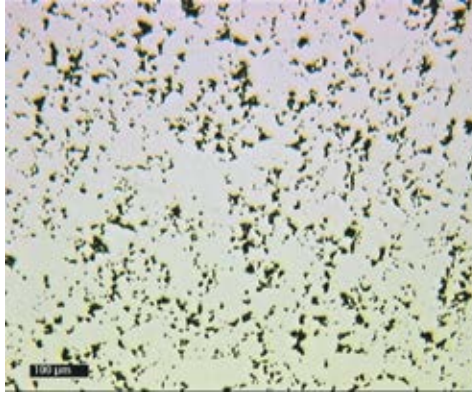
0.5% C

Warm compacted

1120°C, 30 minutes

Density: 7.2 g/cm³

Unetched



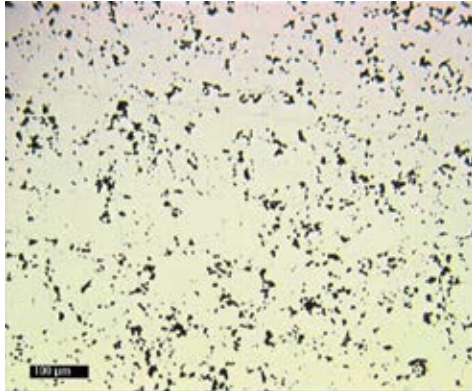
0.5% C

Warm compacted

1120°C, 30 minutes

Density: 7.35 g/cm³

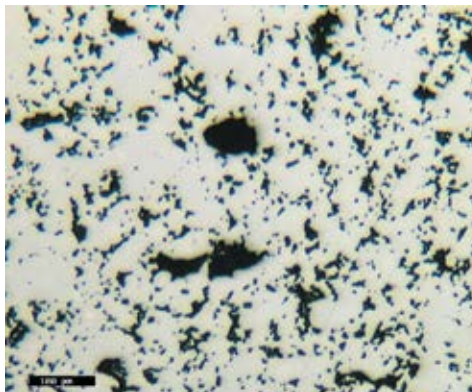
Unetched

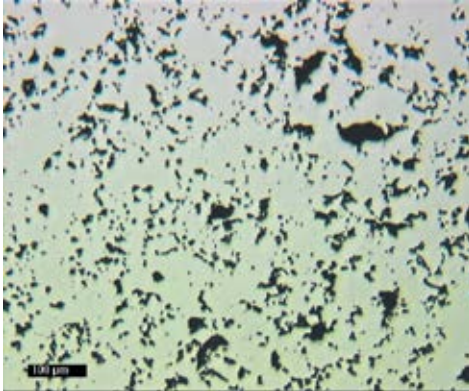


2% Cu (-100)

1120°C, 30 minutes

Unetched

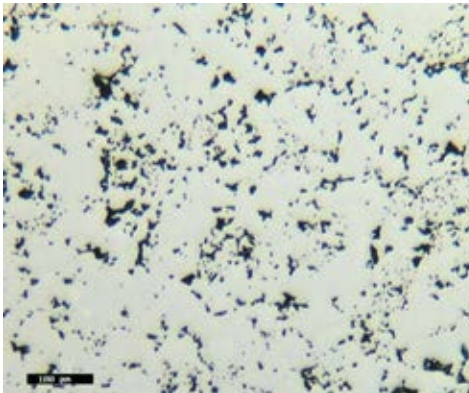




2% Cu (-200)

1120°C, 30 minutes

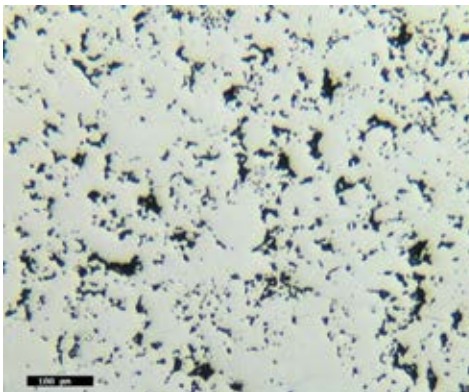
Unetched



2% Cu (Distaloy® Cu)

1120°C, 30 minutes

Unetched



2% Cu (Astaloy™ 20 Cu)

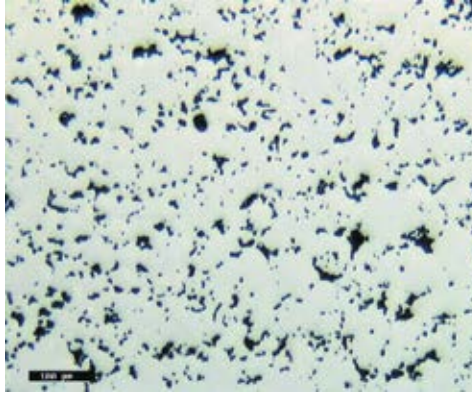
1120°C, 30 minutes

Unetched



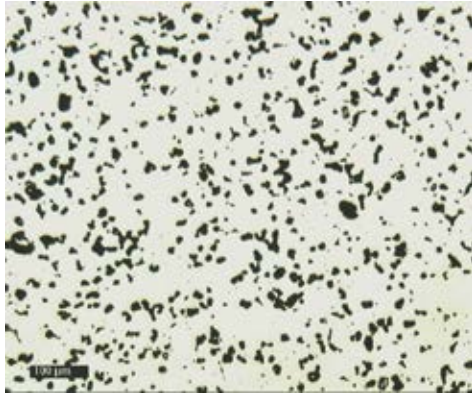
0.45% P

1120°C, 30 minutes
Unetched



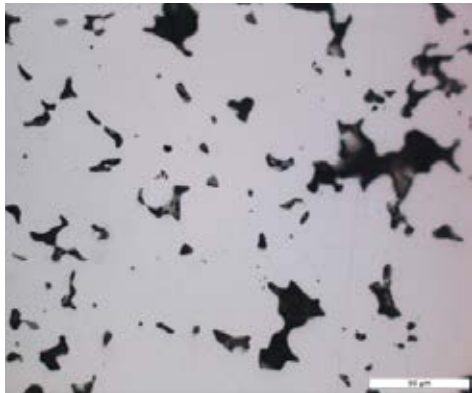
0.45% P

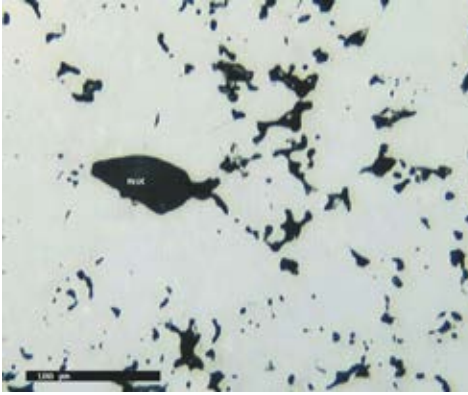
1250°C, 30 minutes
Unetched



0.5% MnS-E

1120°C, 30 minutes
Unetched





0.5% MnX

1120°C, 30 minutes

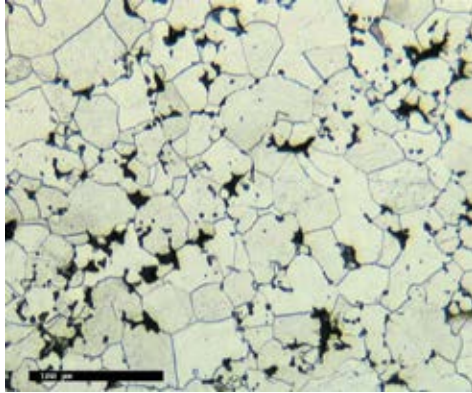
Unetched



0% C

1120°C, 30 minutes

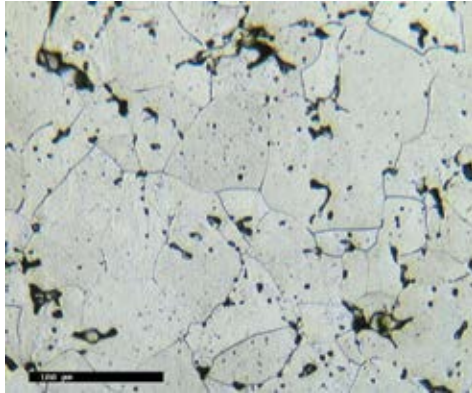
Etched: Nital



0% C

1250°C, 30 minutes

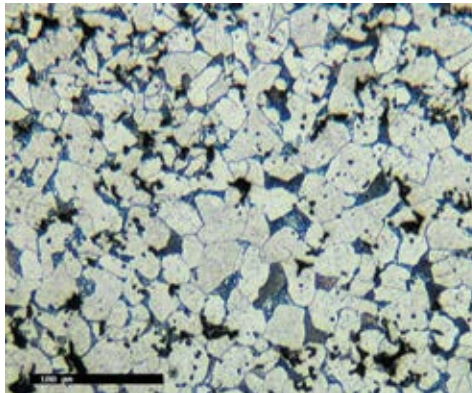
Etched: Nital

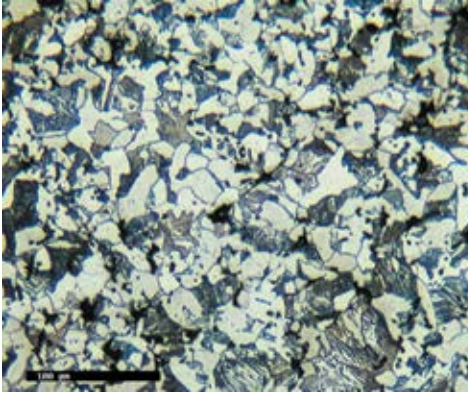


0.2% C

1120°C, 30 minutes

Etched: Nital

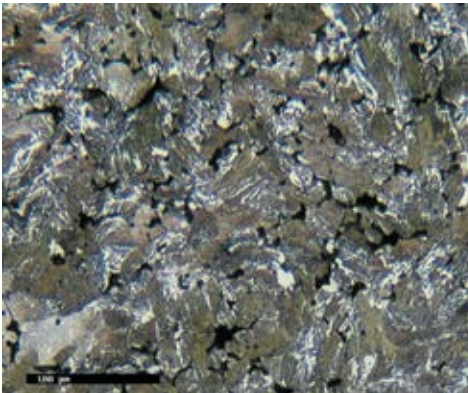




0.5% C

1120°C, 30 minutes

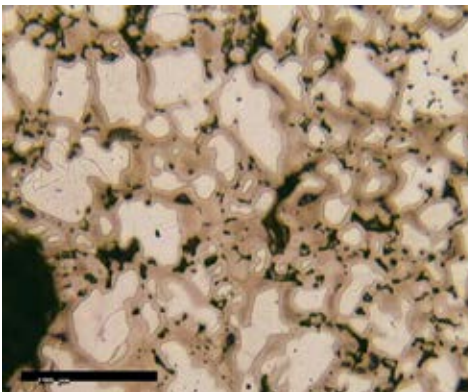
Etched: Nital



0.8% C

1120°C, 30 minutes

Etched: Nital



2% Cu (-100)

1120°C, 30 minutes

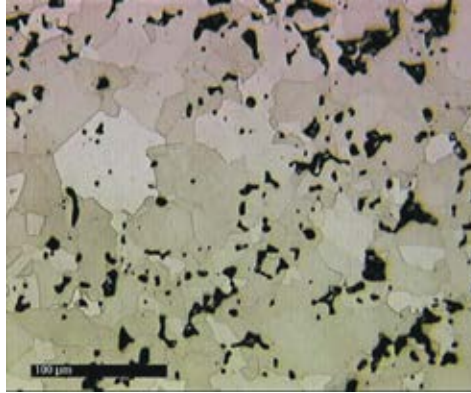
Etched: Picral



2% Cu (-100)

1250°C, 30 minutes

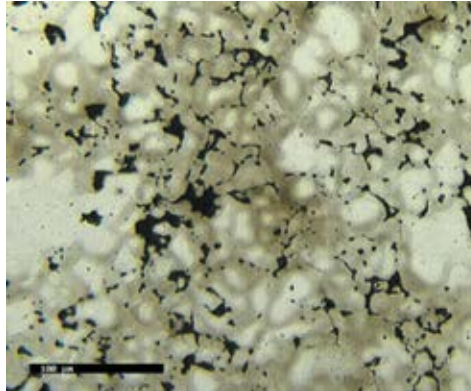
Etched: Picral



2% Cu (Distaloy® Cu)

1120°C, 30 minutes

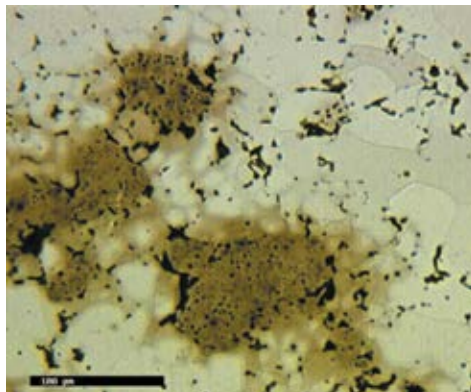
Etched: Picral

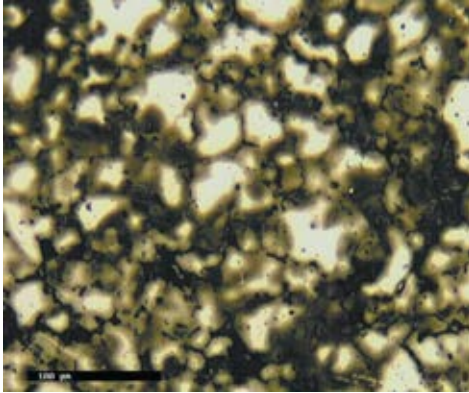


**2% Cu
(Astaloy™ 20 Cu)**

1120°C, 30 minutes

Etched: Picral

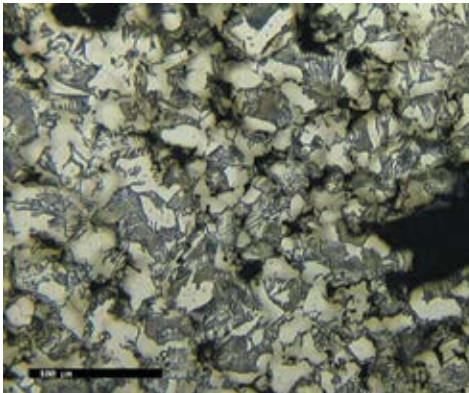




4% Cu (-100)

1120°C, 30 minutes

Etched: Picral

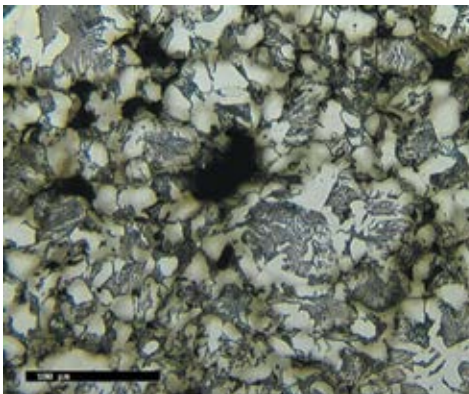


4% Cu (-100)

+ 0.5% C

1120°C, 30 minutes

Etched: Picral



2% Cu (-200)

+ 0.5% C

1120°C, 30 minutes

Etched: Picral

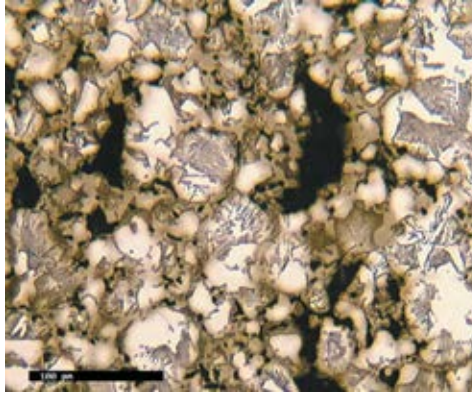


3% Cu (-100)

+ 0.5% C

1120°C, 30 minutes

Etched: Picral

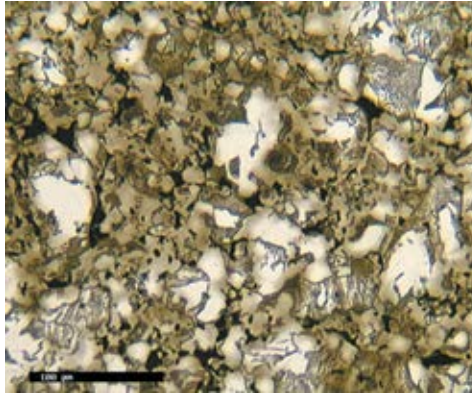


3% Cu (Distaloy® Cu)

+ 0.5% C

1120°C, 30 minutes

Etched: Picral

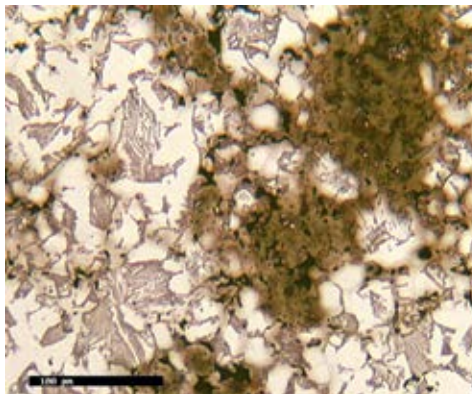


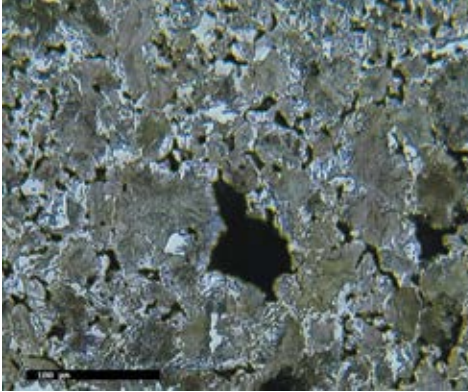
**4% Cu
(Astaloy™ 20 Cu)**

+ 0.5% C

1120°C, 30 minutes

Etched: Picral



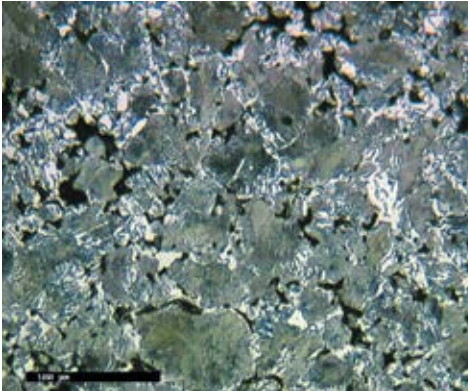


2% Cu (-100)

+ 0.8% C

1120°C, 30 minutes

Etched: Picral

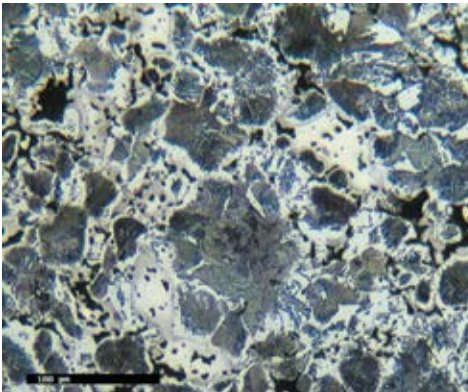


3% Cu (Distaloy® Cu)

+ 0.8% C

1120°C, 30 minutes

Etched: Picral



3% Ni + 0.6% C

1120°C, 30 minutes

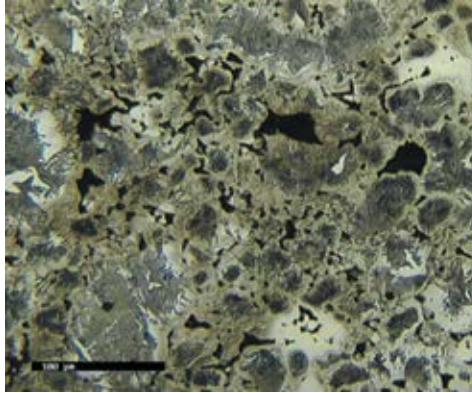
Etched: Picral



**2.2% Cu (-100)
+ 2.5% Ni + 0.6% C**

1120°C, 30 minutes

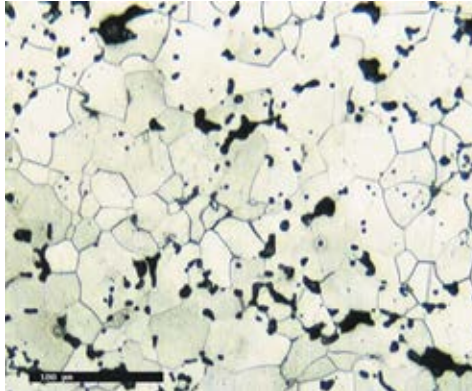
Etched: Picral



0.45% P

1120°C, 30 minutes

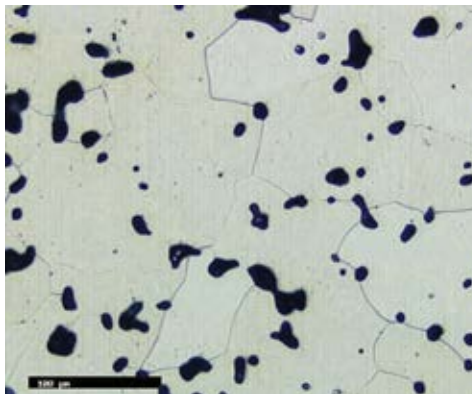
Etched: Nital

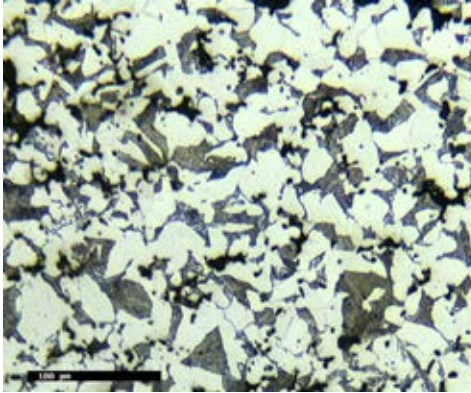


0.45% P

1250°C, 30 minutes

Etched: Nital

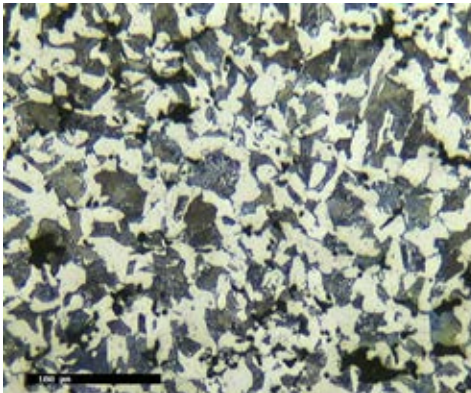




0.45% P + 0.3% C

1120°C, 30 minutes

Etched: Nital



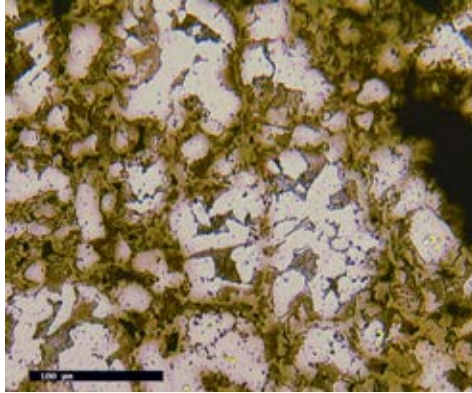
0.45% P + 0.5% C

1120°C, 30 minutes

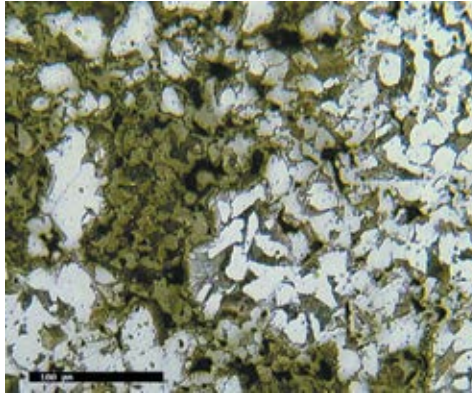
Etched: Nital



2% Cu (-100)
+ 0.45% P + 0.2% C
1120°C, 30 minutes
Etched: Picral



2% Cu
(Astaloy™ 20 Cu)
+ 0.45% P + 0.2% C
1120°C, 30 minutes
Etched: Picral

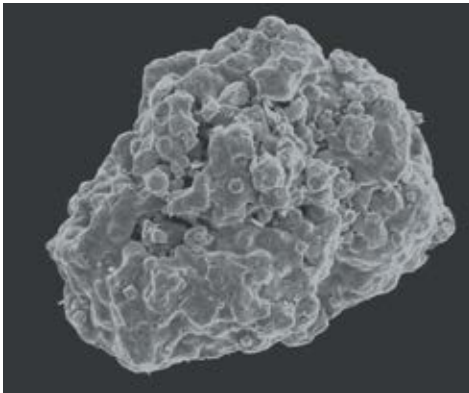


Index

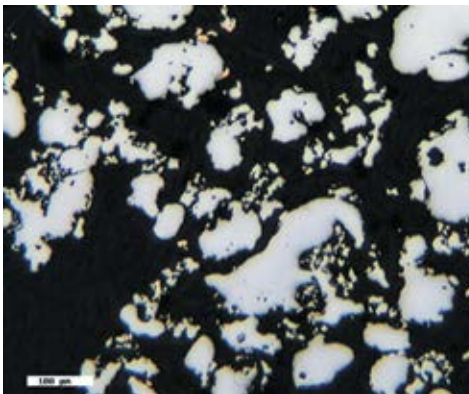
2.3.1	Distaloy® AE	143
2.3.2	Distaloy AB	149
2.3.3	Distaloy AQ	150
2.3.4	Distaloy SA	151
2.3.5	Distaloy DC	152
2.3.6	Distaloy DH	154
2.3.7	Distaloy HP	156

2.3 Diffusion Alloyed Grades

2.3.1 Distaloy[®] AE



SEM image

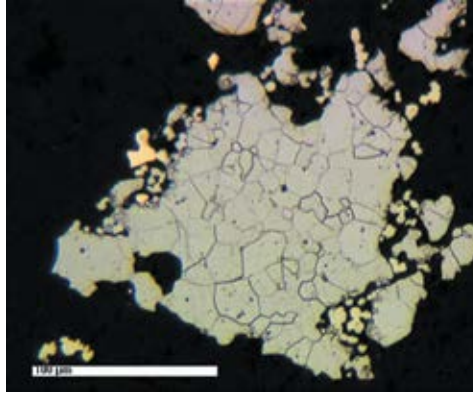


LOM image



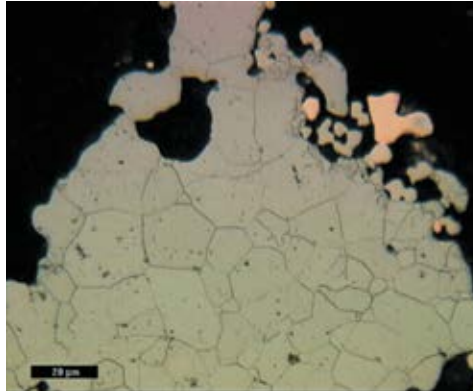
LOM image

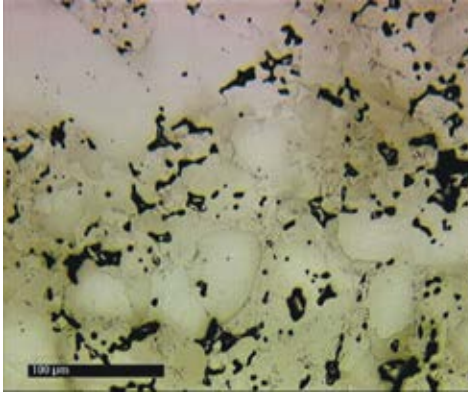
Etched: Nital



LOM image

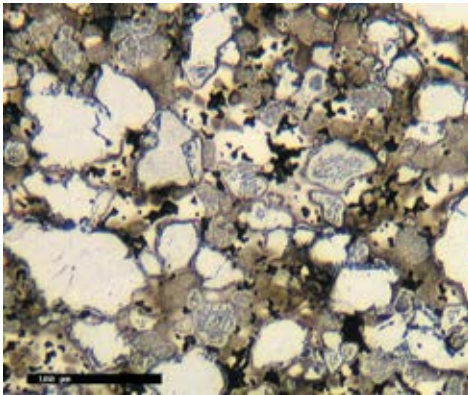
Etched: Nital



**0% C**

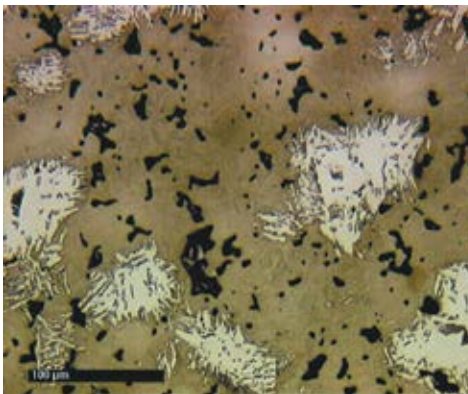
1120°C, 30 minutes

Etched: Picral

**0.2% C**

1120°C, 30 minutes

Etched: Picral

**0.3% C**

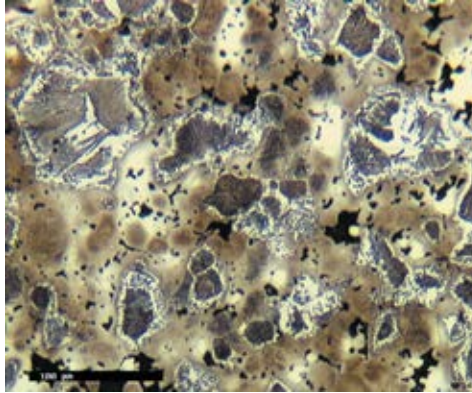
1250°C, 30 minutes

Etched: Picral



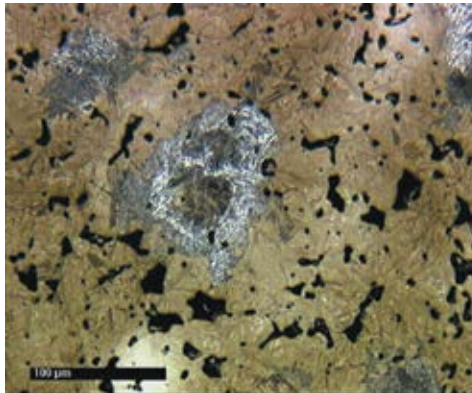
0.5% C

1120°C, 30 minutes
Etched: Picral



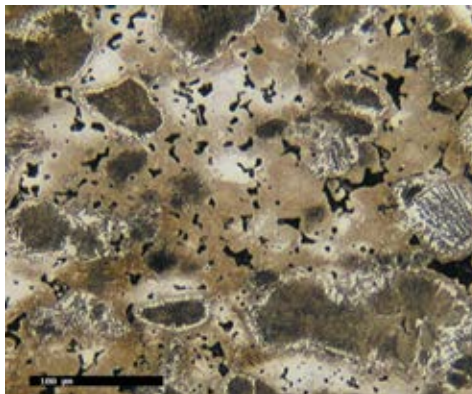
0.5% C

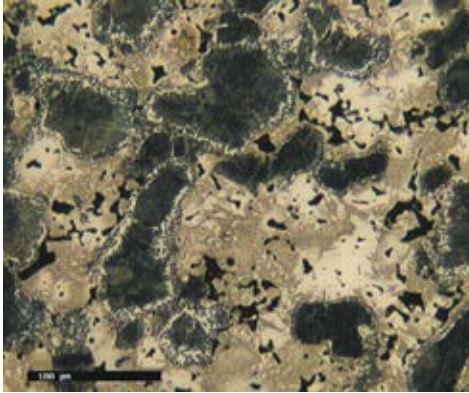
1250°C, 30 minutes
Etched: Picral



0.8% C

1120°C, 30 minutes
Etched: Picral

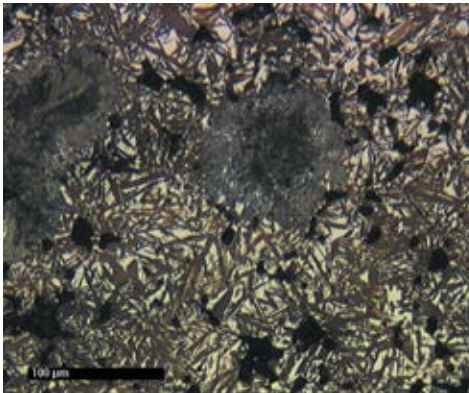




1% C

1120°C, 30 minutes

Etched: Picral



1% C

1250°C, 30 minutes

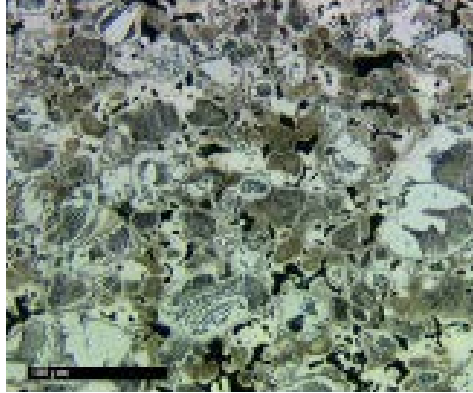
Etched: Picral



0.45% C

1120°C, 15 minutes

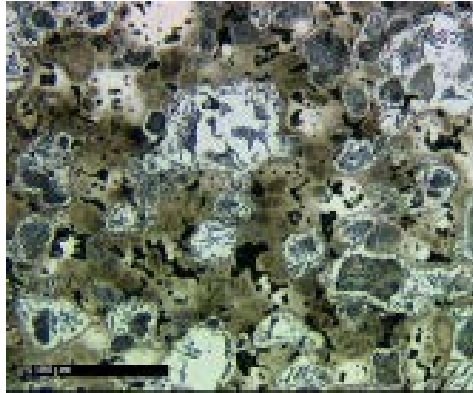
Etched: Picral



0.45% C

1120°C, 30 minutes

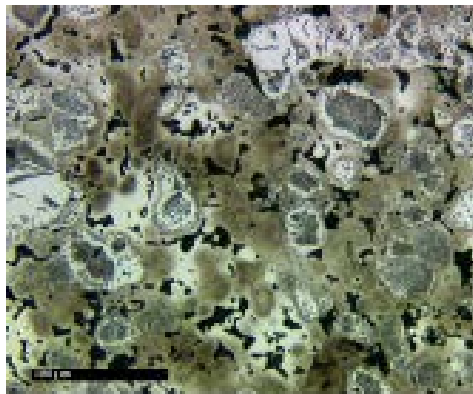
Etched: Picral



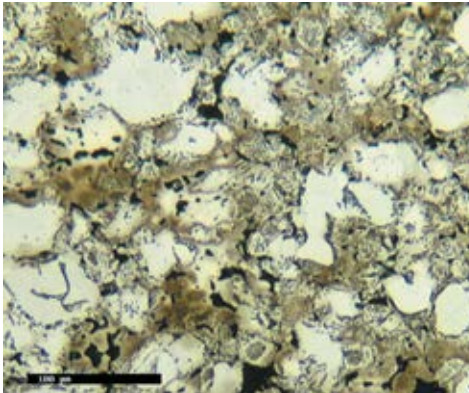
0.45% C

1120°C, 45 minutes

Etched: Picral



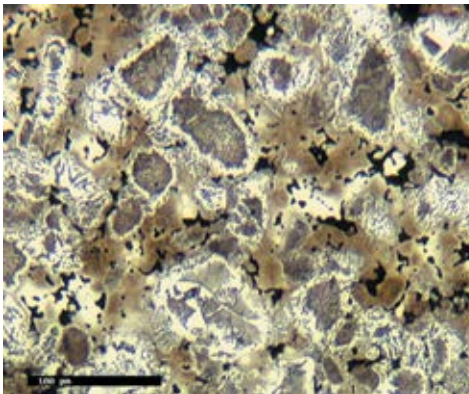
2.3.2 Distaloy[®] AB



0.2% C

1120°C, 30 minutes

Etched: Picral



0.5% C

1120°C, 30 minutes

Etched: Picral

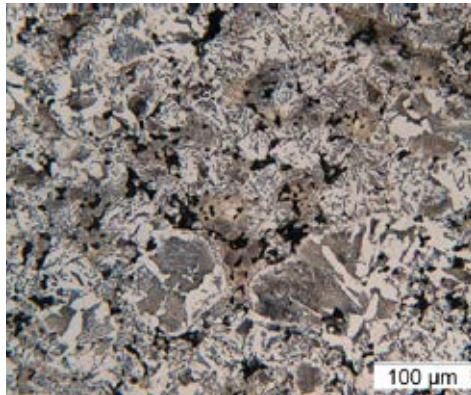


2.3.3 Distaloy® AQ

0.6% C

1120°C, 30 minutes

Etched: Picral

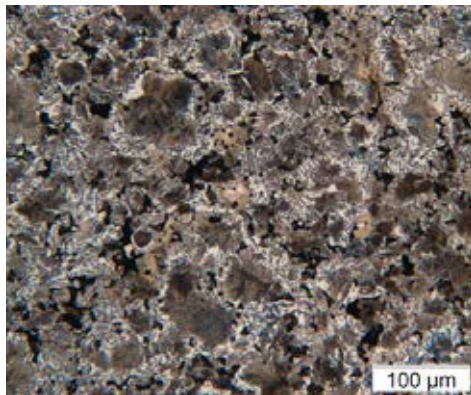


.....

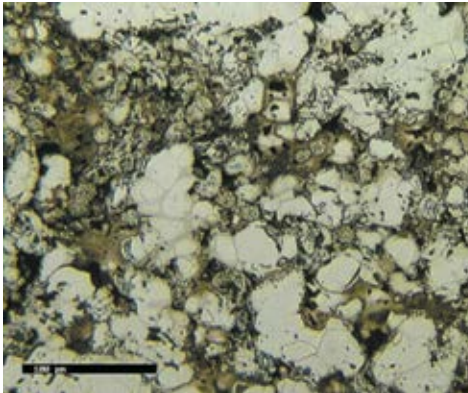
0.8% C

1120°C, 30 minutes

Etched: Picral



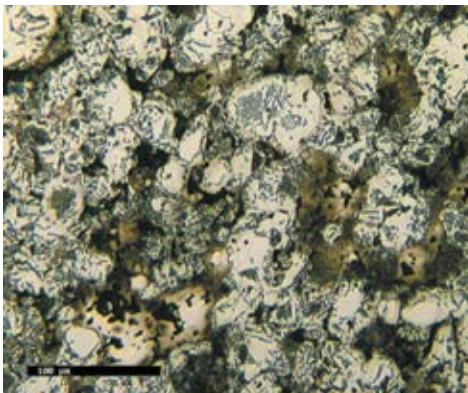
2.3.4 Distaloy® SA



0.2% C

1120°C, 30 minutes

Etched: Picral



0.5% C

1120°C, 30 minutes

Etched: Picral

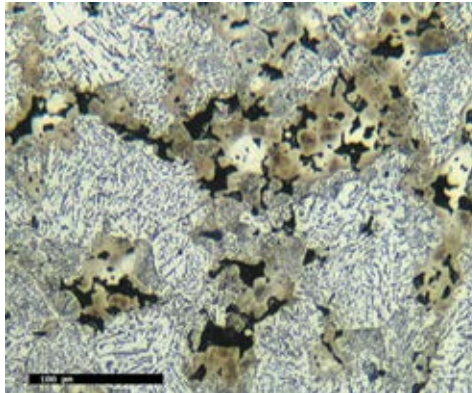


2.3.5 Distaloy® DC (Dimensional Control)

0.2% C

1120°C, 30 minutes

Etched: Picral

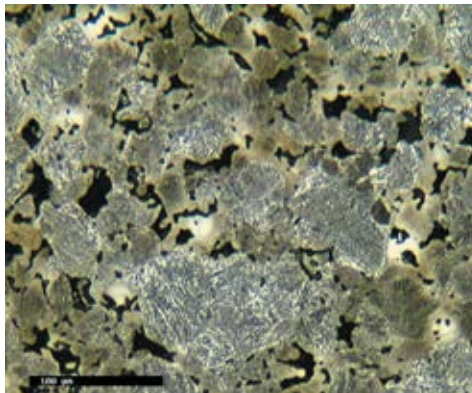


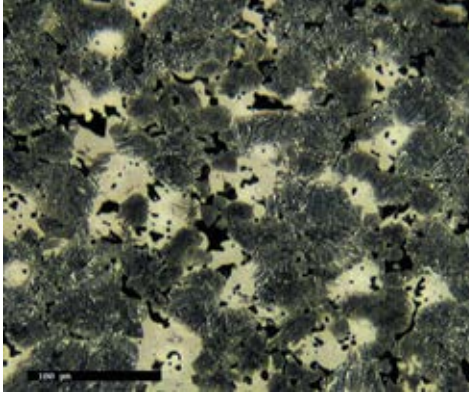
.....

0.5% C

1120°C, 30 minutes

Etched: Picral





0.8% C

1120°C, 30 minutes

Etched: Picral

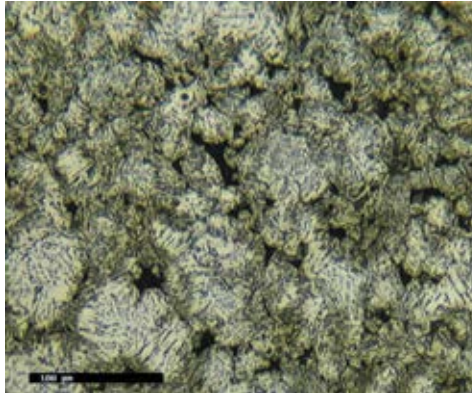


2.3.6 Distaloy® DH (Direct Hardening)

0.2% C

1120°C, 30 minutes

Etched: Picral

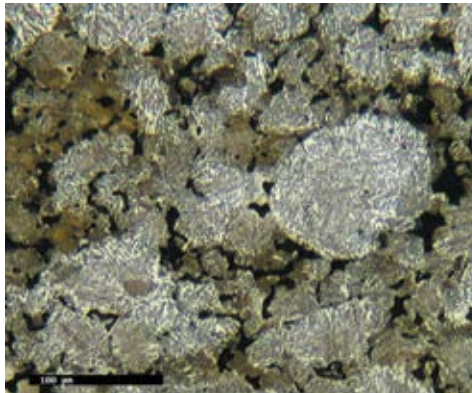


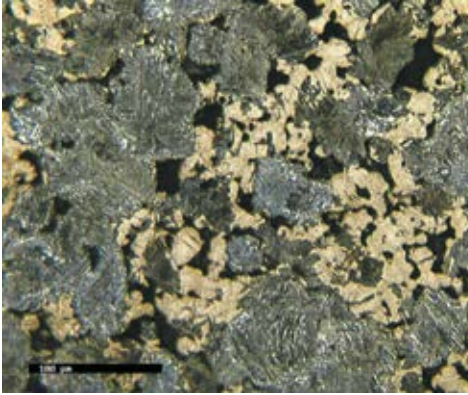
.....

0.5% C

1120°C, 30 minutes

Etched: Picral





0.8% C

1120°C, 30 minutes

Etched: Picral

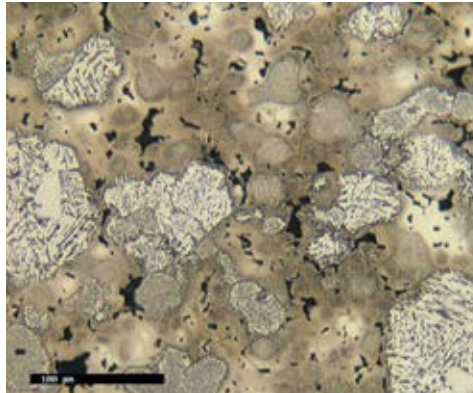


2.3.7 Distaloy® HP (High Performance)

0.2% C

1120°C, 30 minutes

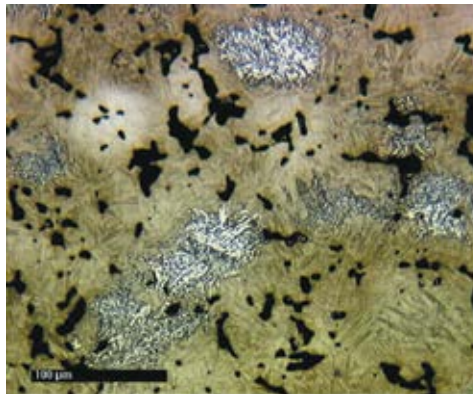
Etched: Picral

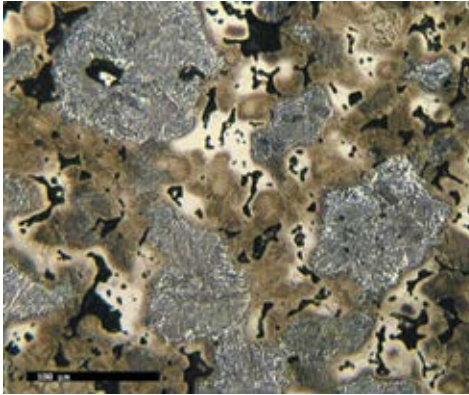


0.3% C

1250°C, 30 minutes

Etched: Picral

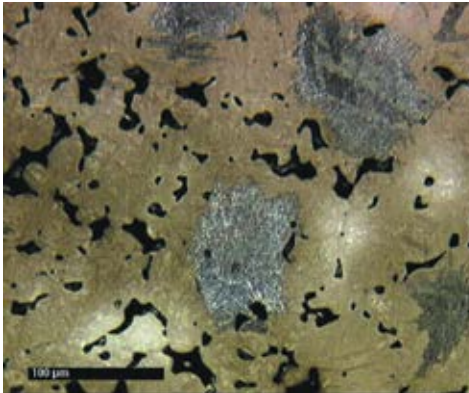




0.5% C

1120°C, 30 minutes

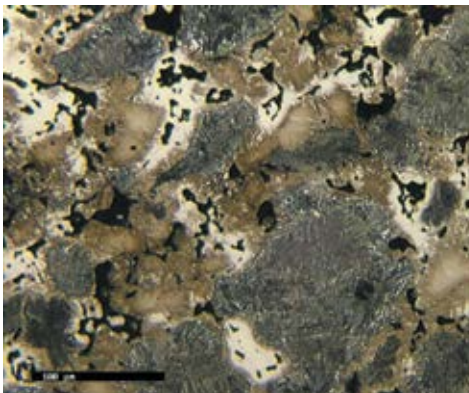
Etched: Picral



0.5% C

1250°C, 30 minutes

Etched: Picral



0.8% C

1120°C, 30 minutes

Etched: Picral



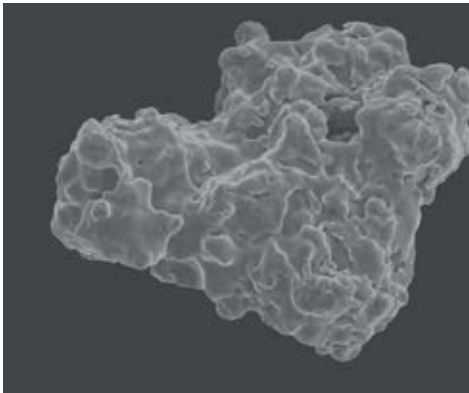


Index

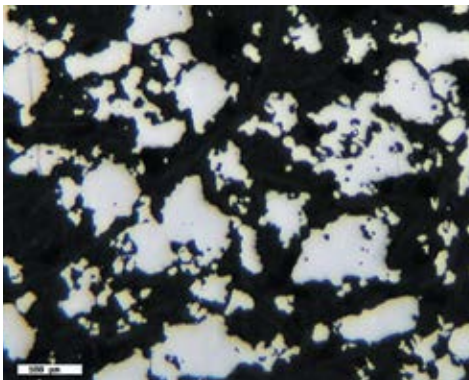
2.4.1	Astaloy™ Mo	159
2.4.2	Astaloy 85 Mo.	163
2.4.3	Astaloy A.	165
2.4.4	Astaloy CrA.	167
2.4.5	Astaloy CrM®	170

2.4 Pre-alloyed Powder

2.4.1 Astaloy™ Mo



SEM image



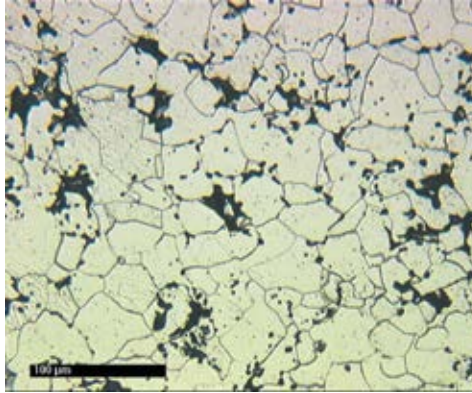
LOM image



0% C

1120°C, 30 minutes

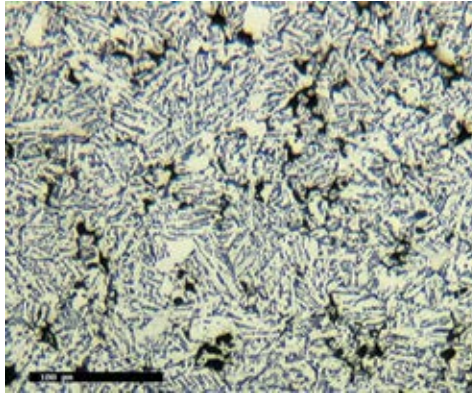
Etched: Nital



0.2% C

1120°C, 30 minutes

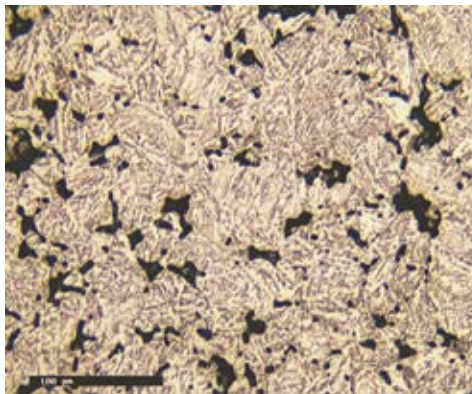
Etched: Nital

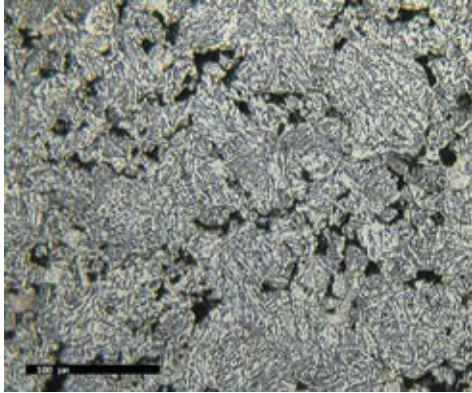


0.2% C

1250°C, 30 minutes

Etched: Nital

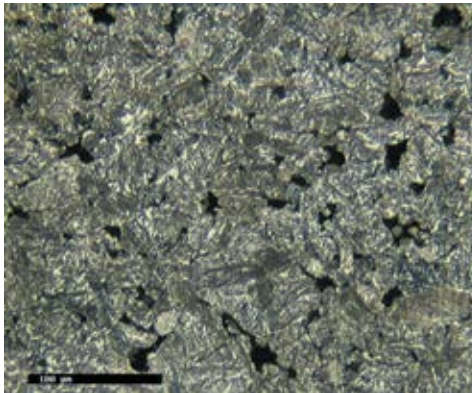




0.5% C

1120°C, 30 minutes

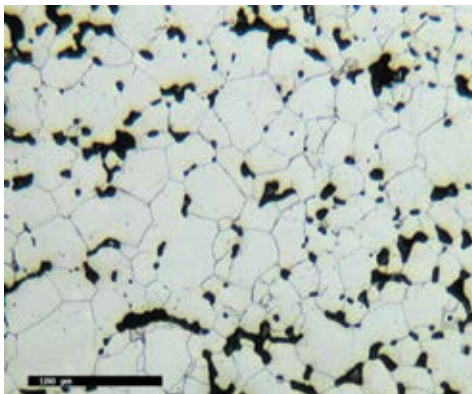
Etched: Nital



0.8% C

1120°C, 30 minutes

Etched: Nital



0.5% P

1120°C, 30 minutes

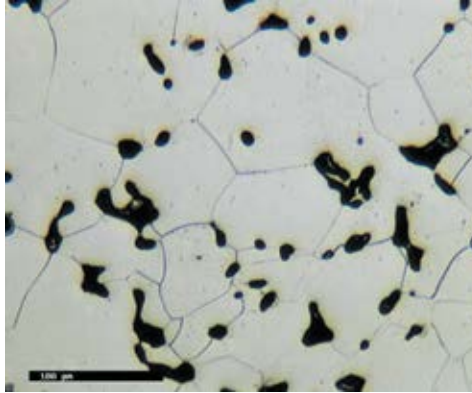
Etched: Nital



0.5% P

1250°C, 30 minutes

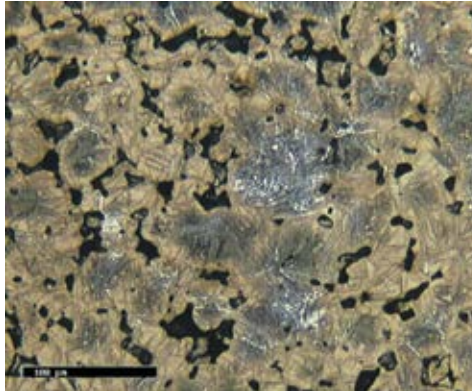
Etched: Nital



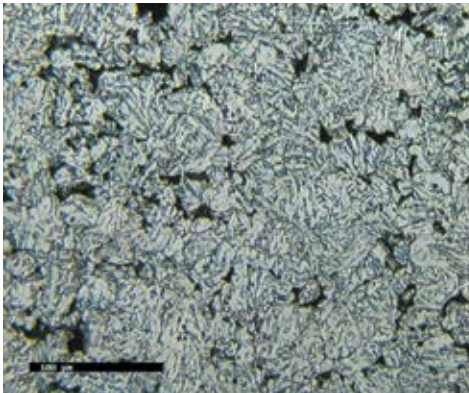
**0.45% P + 2% Cu
(-100) + 0.5% C**

1120°C, 30 minutes

Etched: Nital



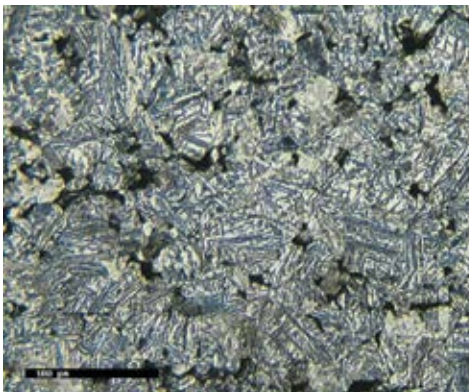
2.4.2 Astaloy™ 85 Mo



0.5% C

1120°C, 30 minutes

Etched: Nital



0.8% C

1120°C, 30 minutes

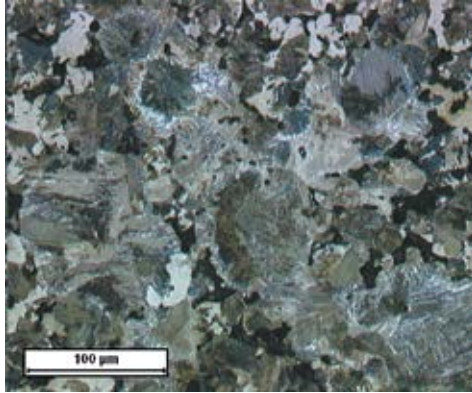
Etched: Nital



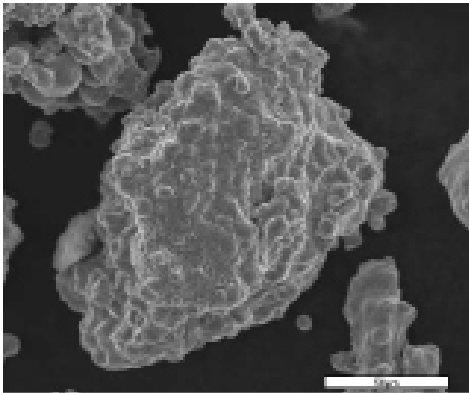
2% Cu (-100) + 0.8% C

1120°C, 30 minutes

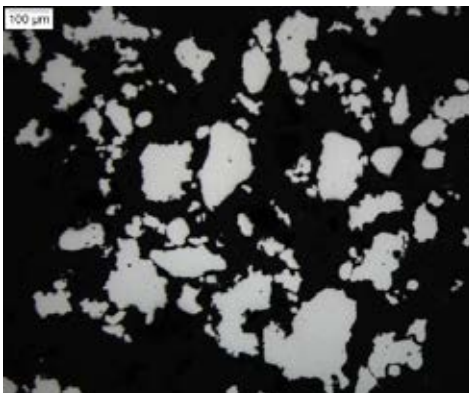
Etched: Nital



2.4.3 Astaloy™ A



SEM image



LOM image



0.5% C

1120°C, 30 minutes

Etched: Nital



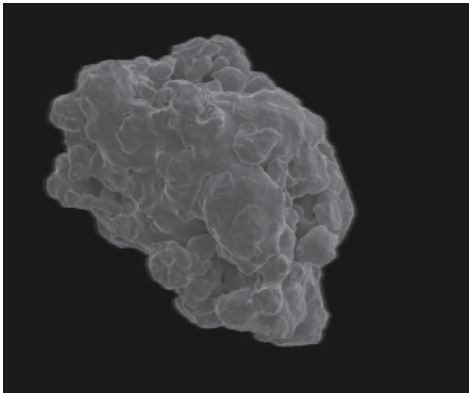
0.8% C

1120°C, 30 minutes

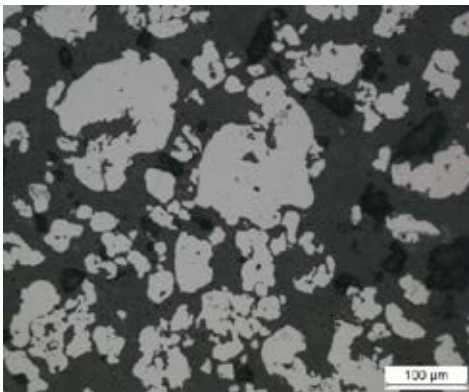
Etched: Nital



2.4.4 Astaloy™ CrA



SEM image

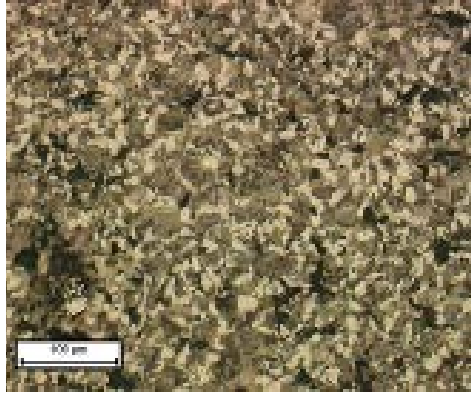


LOM image



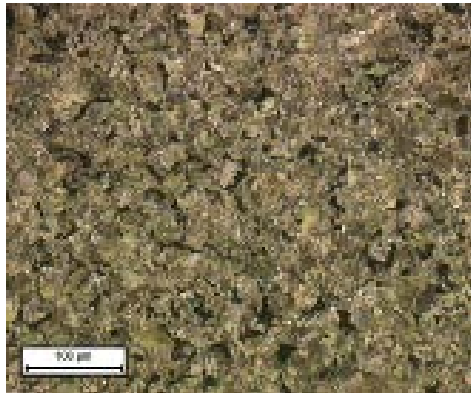
0.4% C

1120°C, 30 minutes
Etched: Nital + Picral



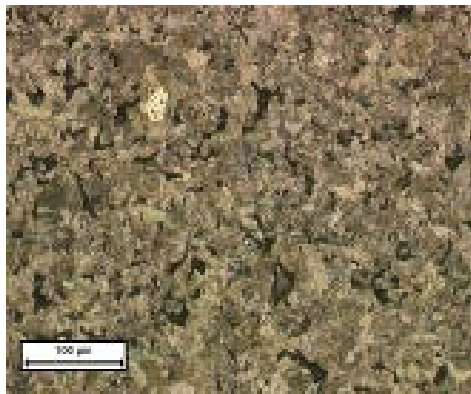
0.6% C

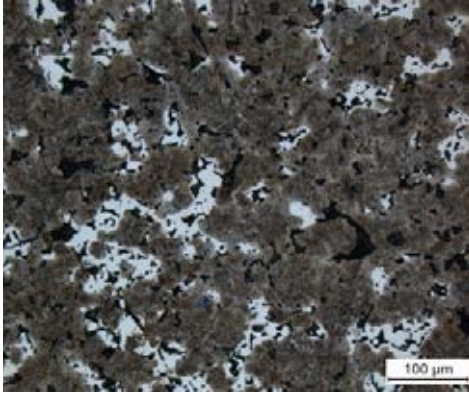
1120°C, 30 minutes
Etched: Nital + Picral



0.8% C

1120°C, 30 minutes
Etched: Nital + Picral

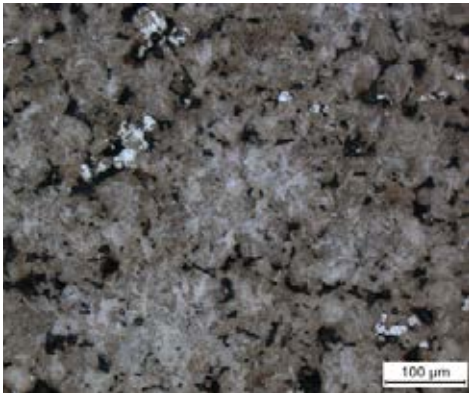




2% Ni + 0.6% C

1120°C, 30 minutes

Etched: Nital + Picral



2% Cu + 0.6% C

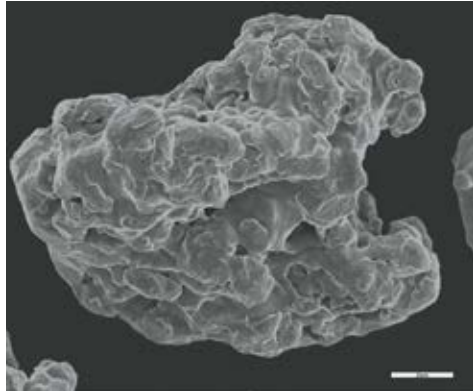
1120°C, 30 minutes

Etched: Nital + Picral

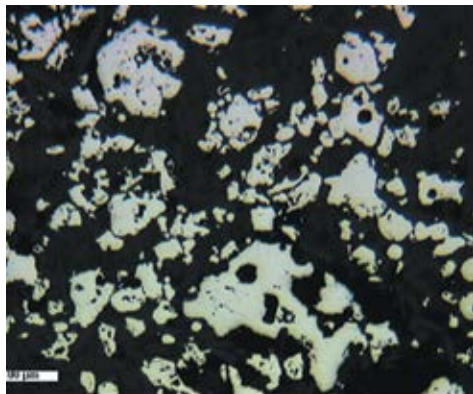


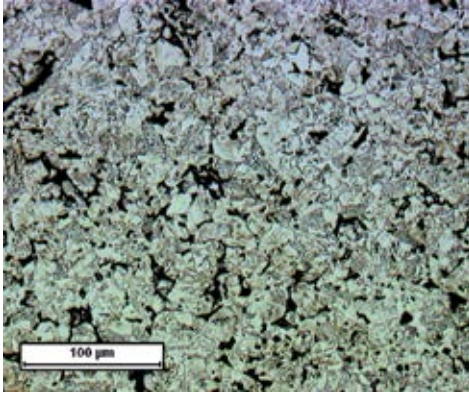
2.4.5 Astaloy CrM[®]

SEM image



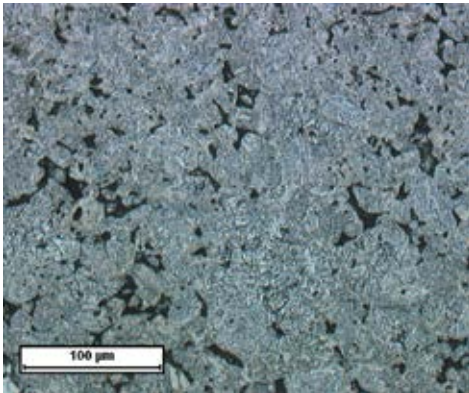
LOM image



**0.1% C**

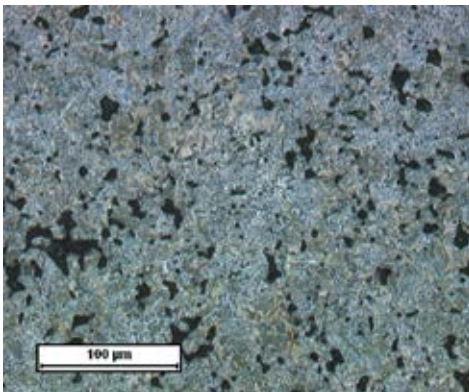
1120°C, 30 minutes

Etched: Nital + Picral

**0.3% C**

1120°C, 30 minutes

Etched: Nital + Picral

**0.4% C**

1120°C, 30 minutes

Etched: Nital + Picral



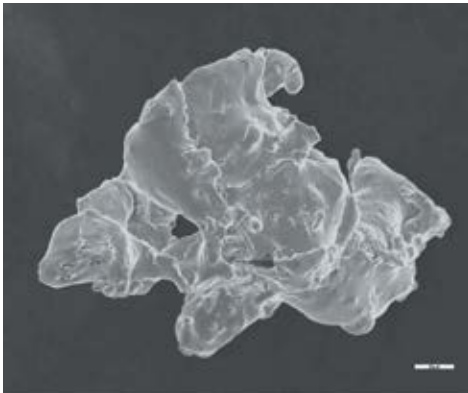


Index

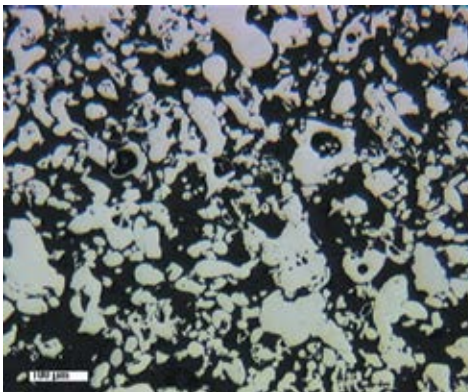
2.5.1	316L.....	173
2.5.2	410L.....	175

2.5 Stainless Steel Powder

2.5.1 316L



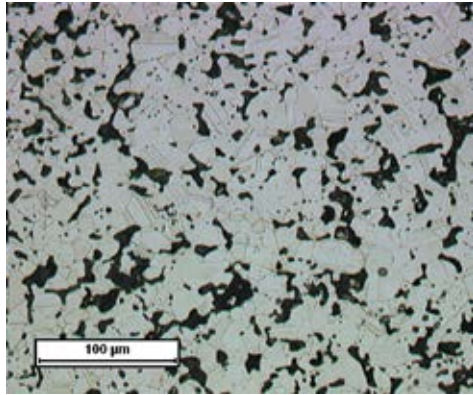
SEM image



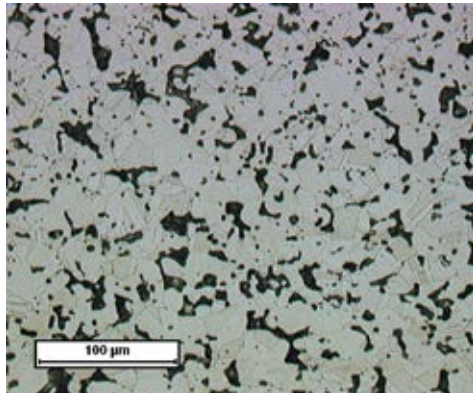
LOM image



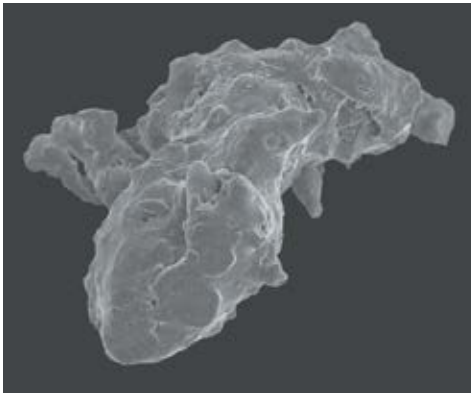
1120°C, 30 minutes
Etched: Glyceregia



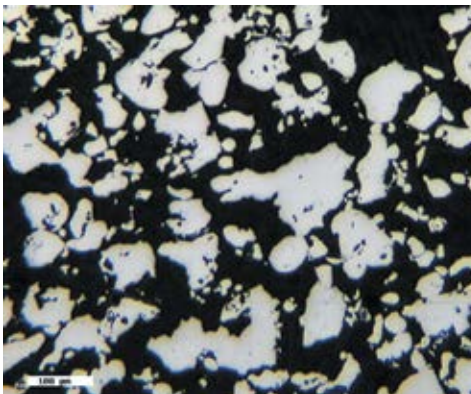
1250°C, 30 minutes
Etched: Glyceregia



2.5.2 410L



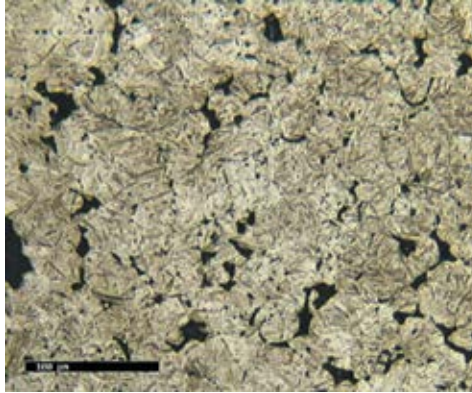
SEM image



LOM image

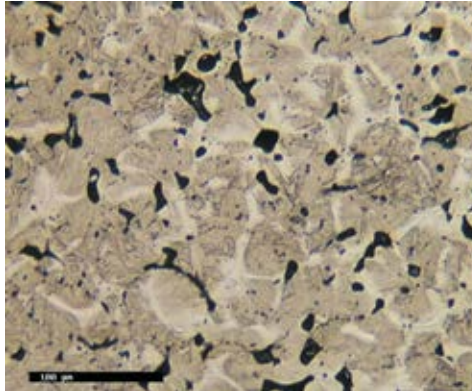


1120°C, 30 minutes
Etched: 3.3



.....

1250°C, 30 minutes
Etched: 3.3



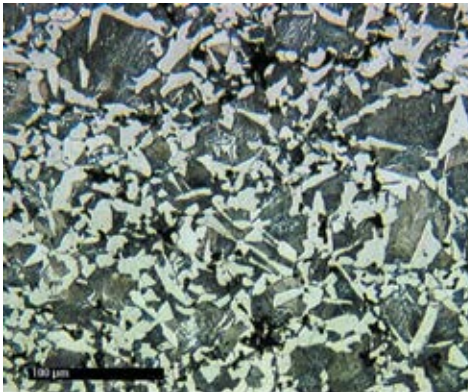
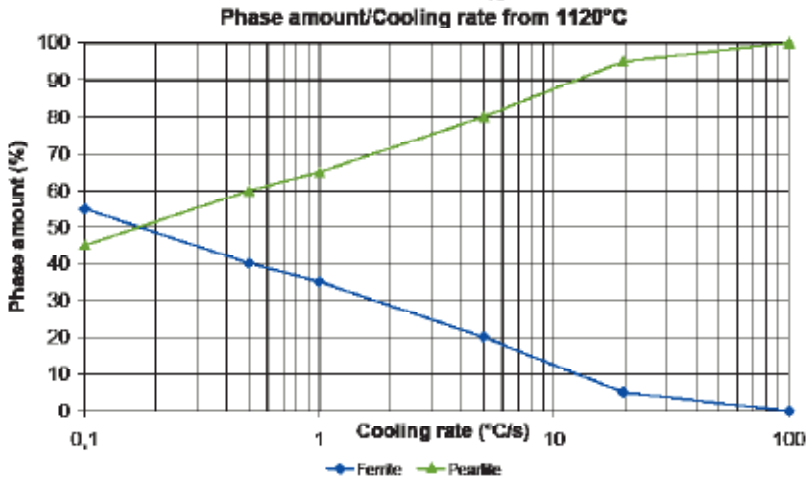
.....

Index

2.6.1	ASC100.29 + 0.5% C	179
2.6.2	ASC100.29 + 2% Cu (-100) + 0.5% C	182
2.6.3	Distaloy® AB + 0.5% C	185
2.6.4	Distaloy AB + 0.8% C	188
2.6.5	Distaloy AE + 0.5% C	191
2.6.6	Distaloy AE + 0.8% C	194
2.6.7	Distaloy HP + 0.5% C	197
2.6.8	Distaloy DC + 0.5% C	200
2.6.9	Distaloy DH + 0.4% C	203
2.6.10	Distaloy DH + 0.5% C	206
2.6.11	Distaloy DH + 0.6% C	209
2.6.12	Astaloy™ Mo + 0.4% C	212
2.6.13	Astaloy Mo + 0.6% C	215
2.6.14	Astaloy 85 Mo + 0.8% C	218
2.6.15	Astaloy 85 Mo + 2% Cu (-100) + 0.8% C	221
2.6.16	Astaloy A + 2% Cu (-100) + 0.6% C	224
2.6.17	Astaloy CrA + 0.8% C	227
2.6.18	Astaloy CrA + 2% Cu + 0.6% C	230
2.6.19	Astaloy CrA + 2% Ni + 0.6% C	233
2.6.20	Astaloy CrM® + 0.3% C	236
2.6.21	Astaloy CrM + 0.4% C	239
2.6.22	Astaloy CrM + 0.5% C	242

2.6 Continuous Cooling Transformation (CCT)

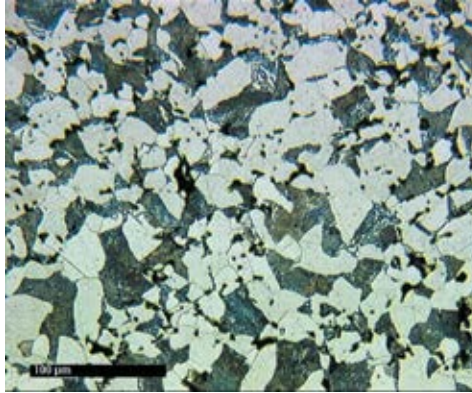
2.6.1 ASC100.29 + 0.5% C



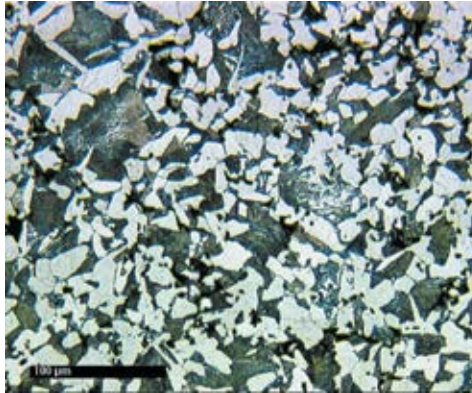
Cooling rate

1°C/second

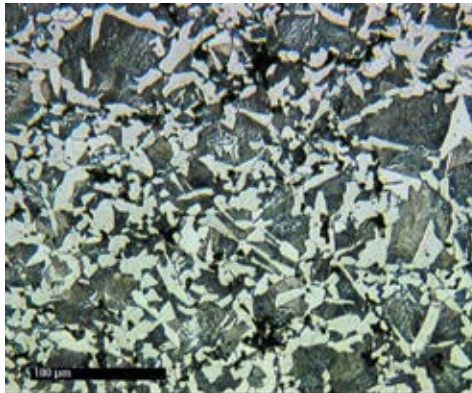
0.1°C/second



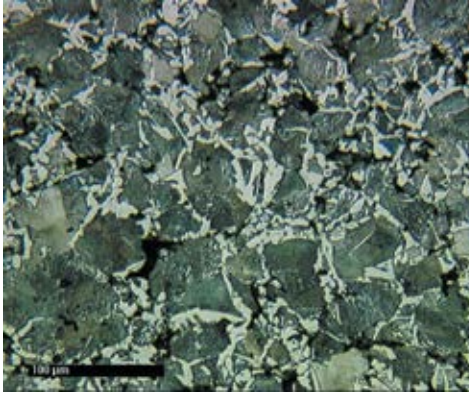
0.5°C/second



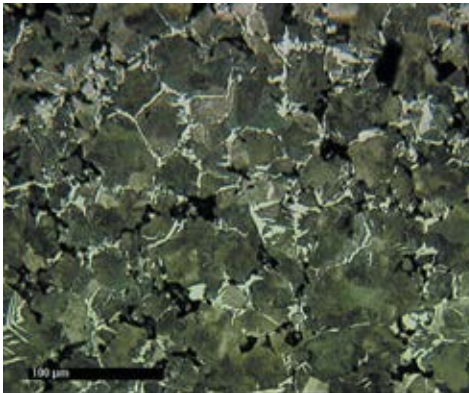
1°C/second



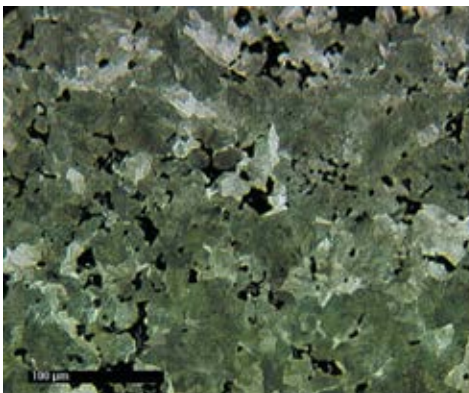
ASC100.29 + 0.5% C



5°C/second



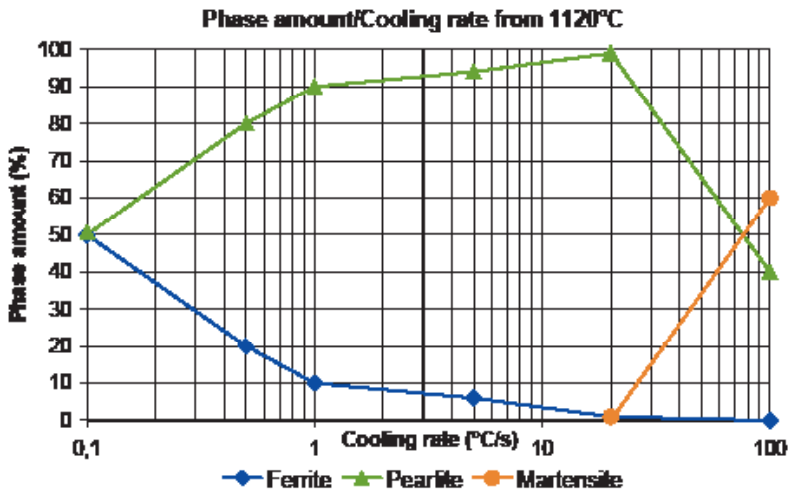
20°C/second



100°C/second

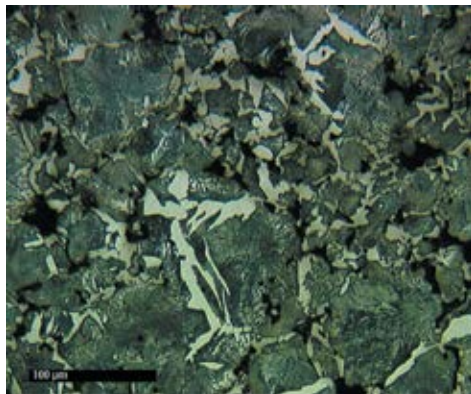


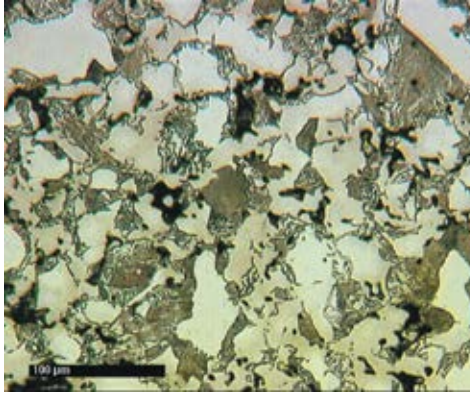
2.6.2 ASC100.29 + 2% Cu (-100) + 0.5% C



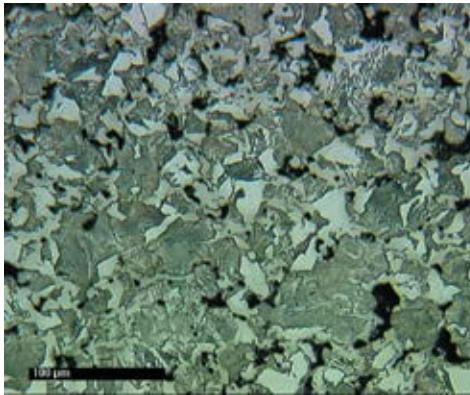
Cooling rate

1°C/second

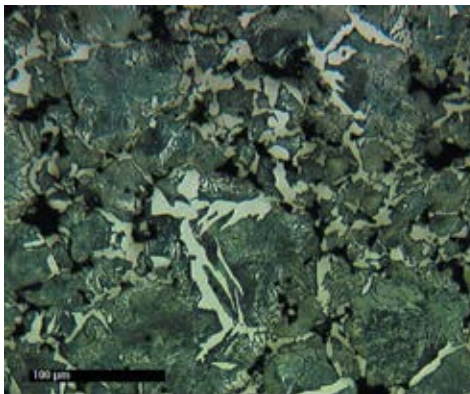




0.1°C/second



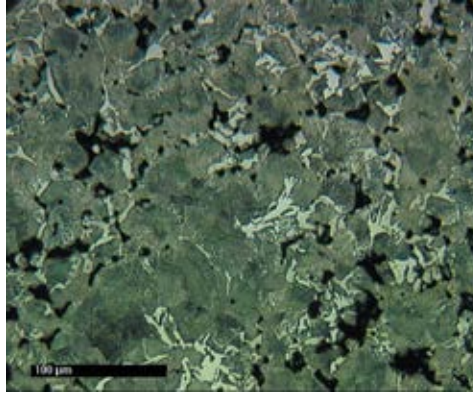
0.5°C/second



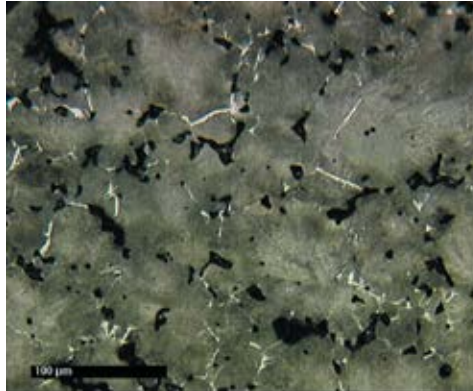
1°C/second



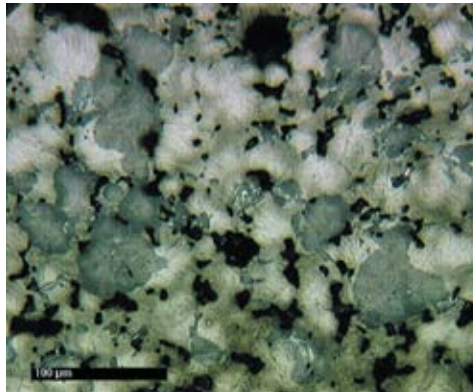
5°C/second



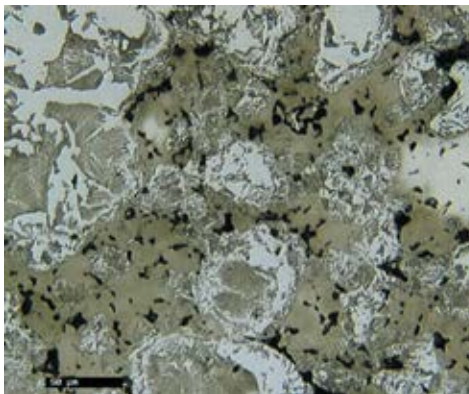
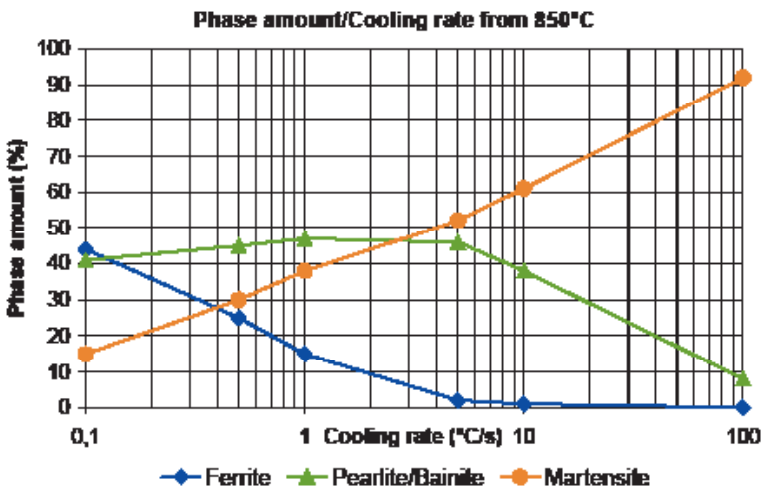
20°C/second



100°C/second



2.6.3 Distaloy® AB + 0.5% C

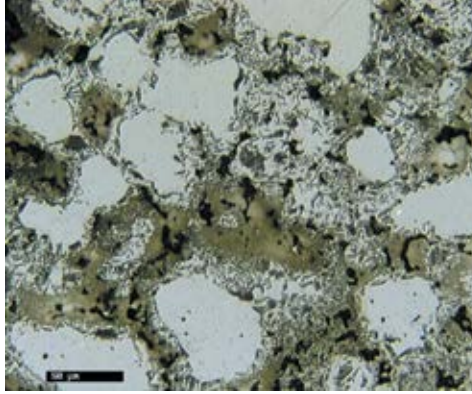


Cooling rate

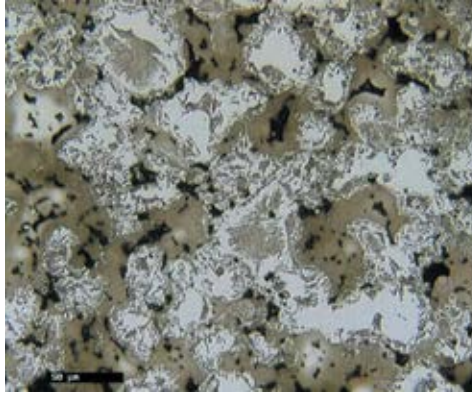
1°C/second



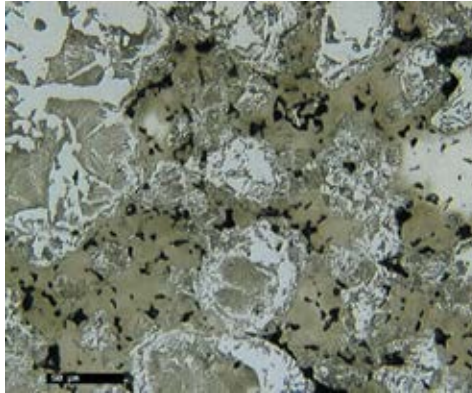
0.1°C/second



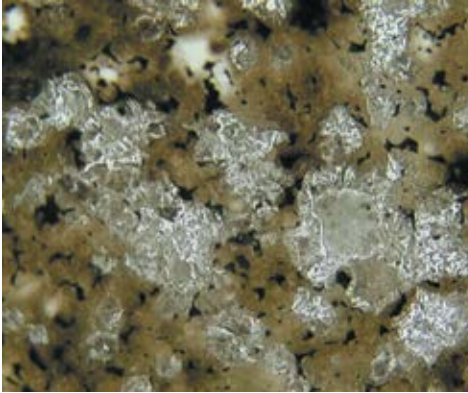
0.5°C/second



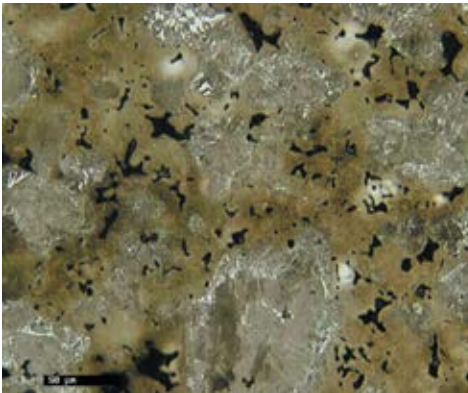
1°C/second



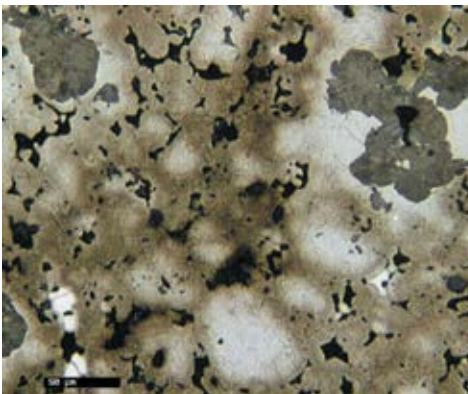
Distaloy AB + 0.5% C



5°C/second



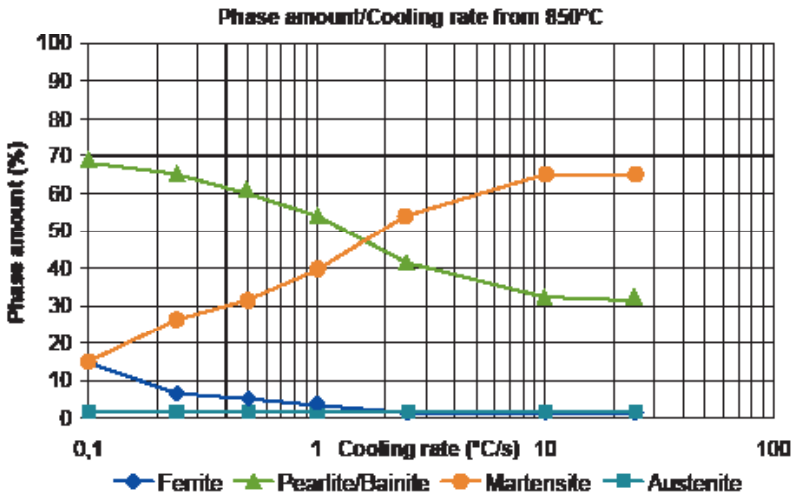
20°C/second



100°C/second

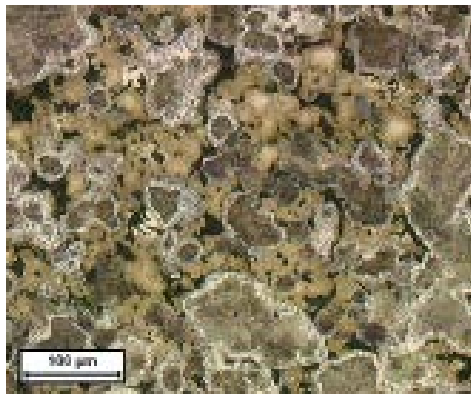


2.6.4 Distaloy® AB + 0.8% C

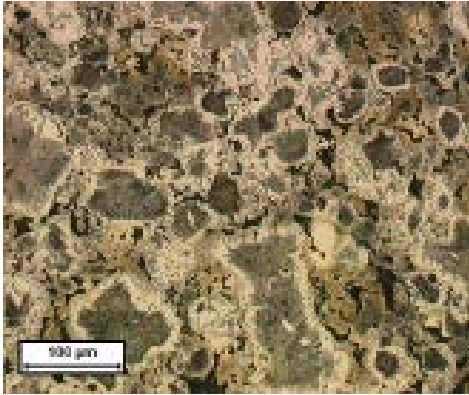


Cooling rate

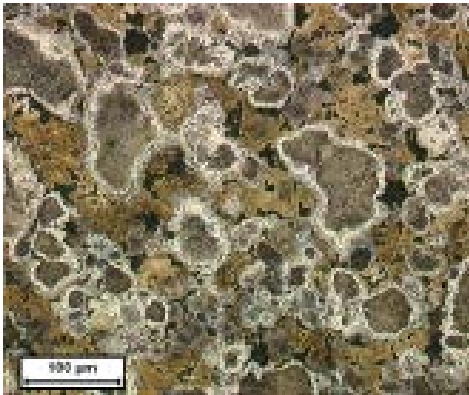
1°C/second



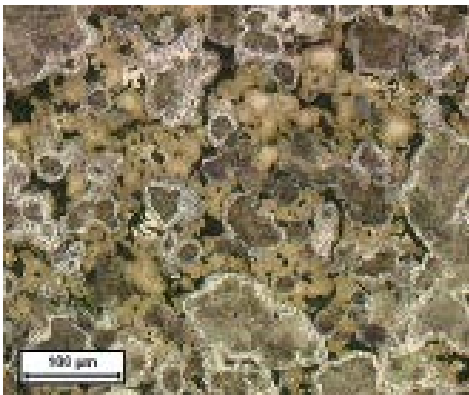
Distaloy AB + 0.8% C



0.1°C/second



0.5°C/second

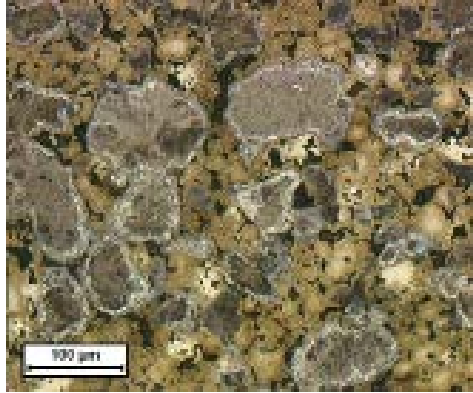


1°C/second

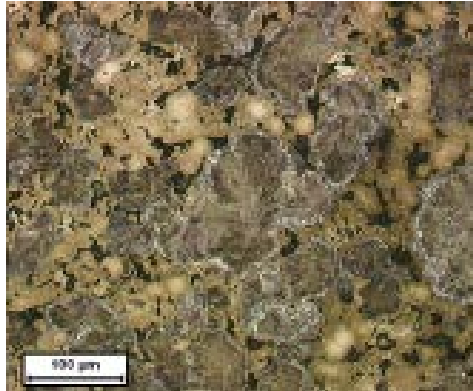


Distaloy AB + 0.8% C

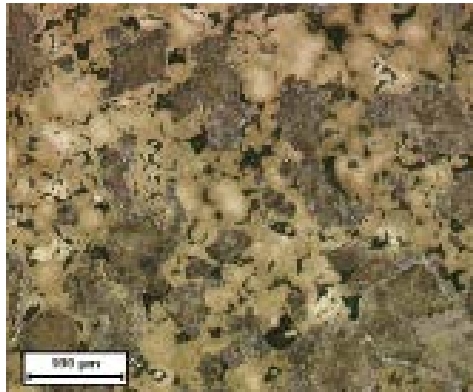
2.5°C/second



10°C/second

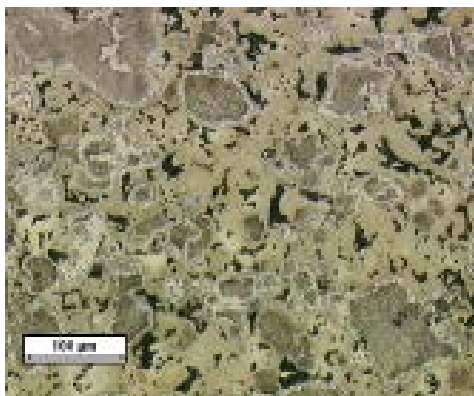
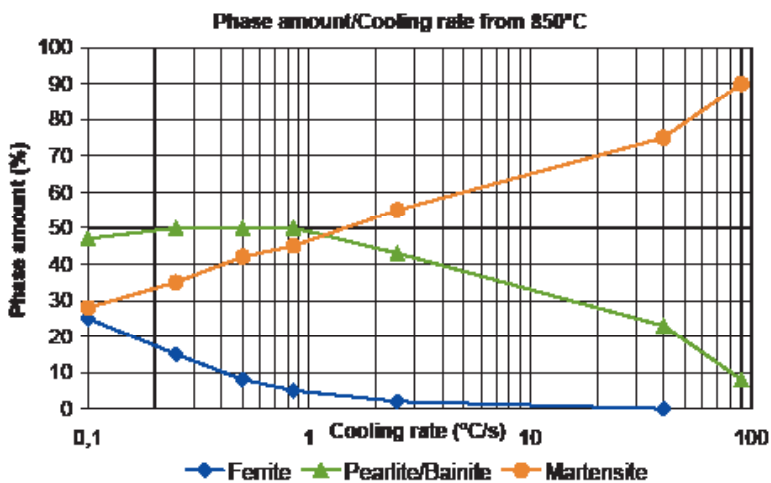


25°C/second



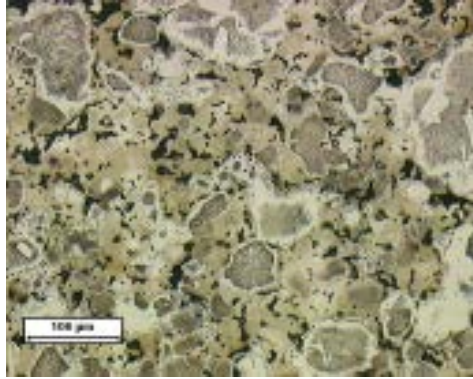
Distaloy AB + 0.8% C

2.6.5 Distaloy® AE + 0.5% C

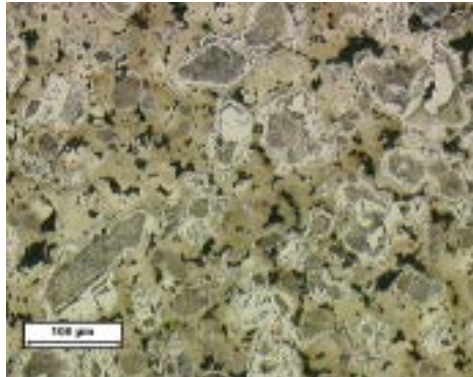


Cooling rate
1°C/second

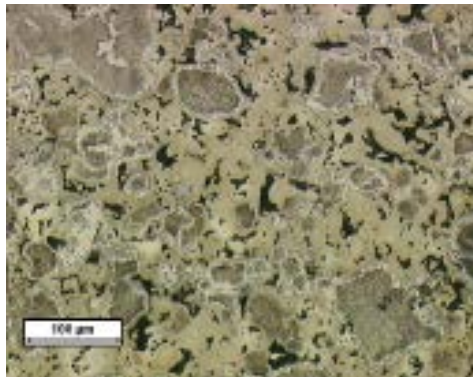
0.1°C/second

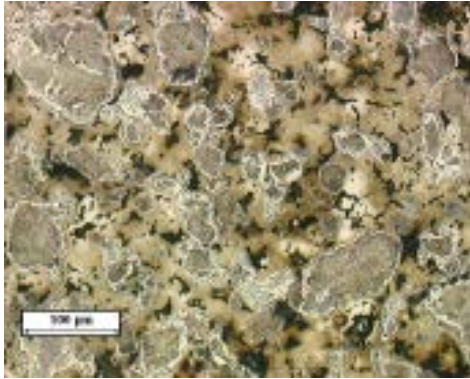


0.5°C/second

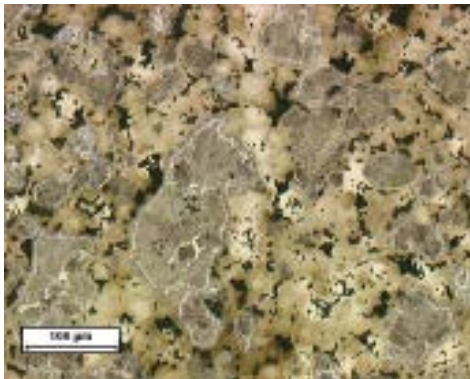


1°C/second

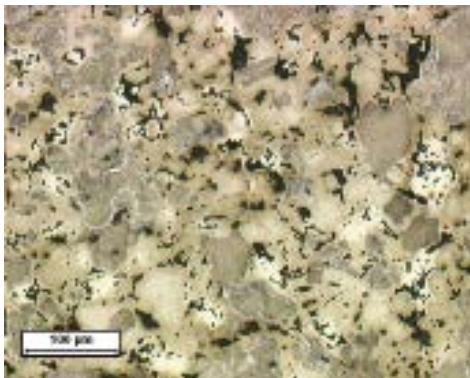




2.5°C/second



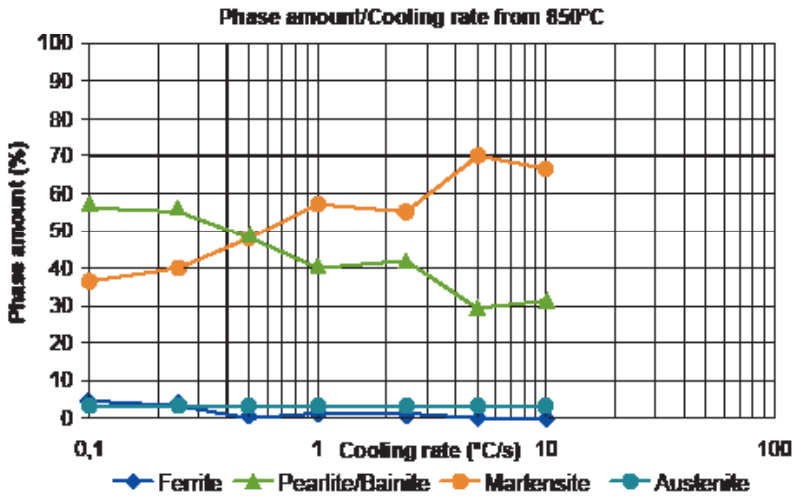
5°C/second



10°C/second

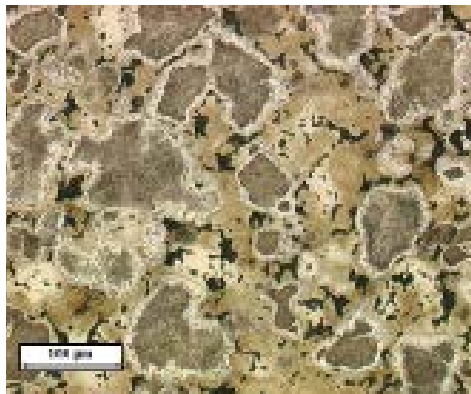


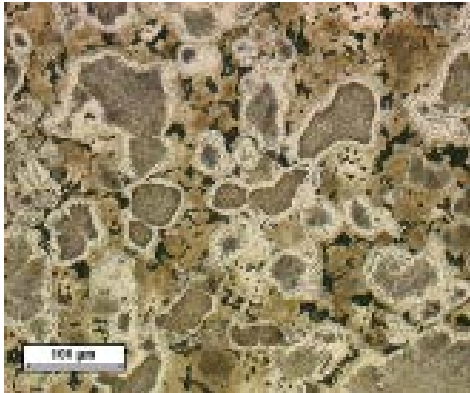
2.6.6 Distaloy® AE + 0.8% C



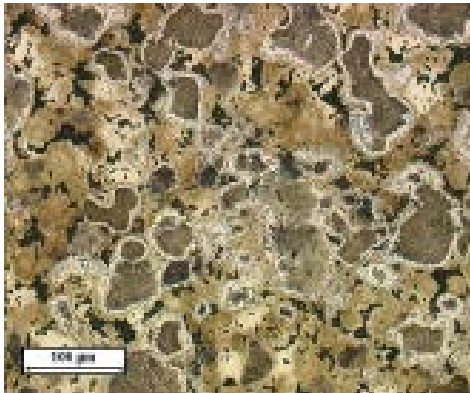
Cooling rate

0.5°C/second

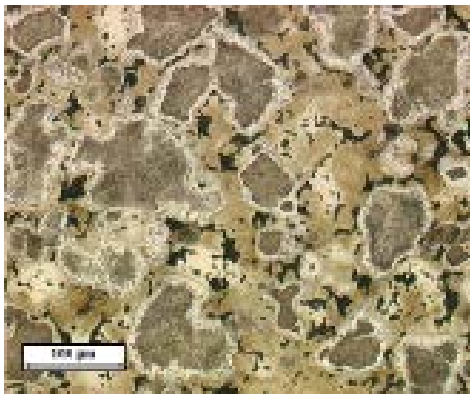




0.1°C/second



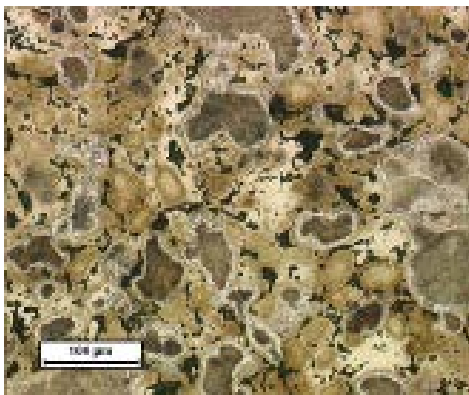
0.25°C/second



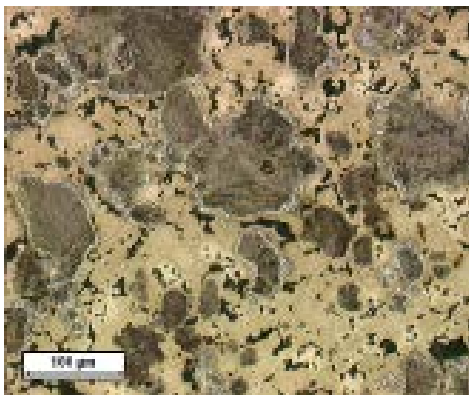
0.5°C/second



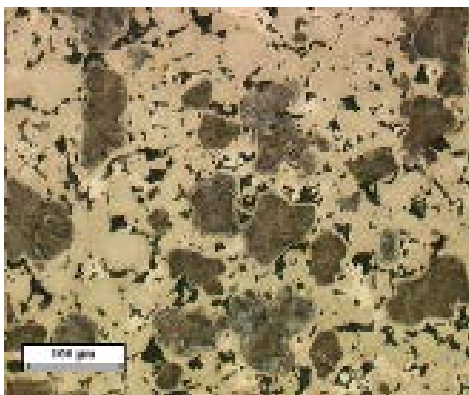
1°C/second



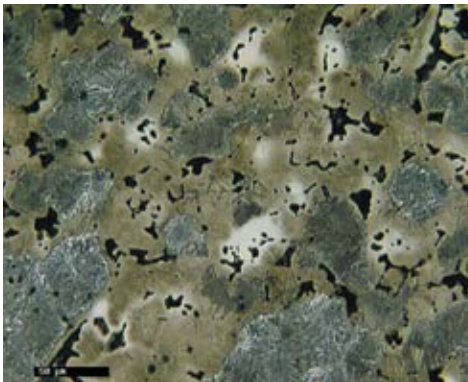
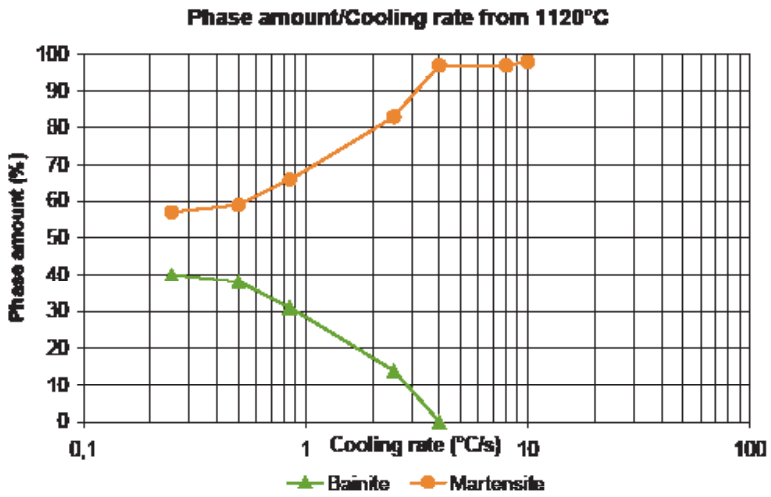
2.5°C/second



5°C/second



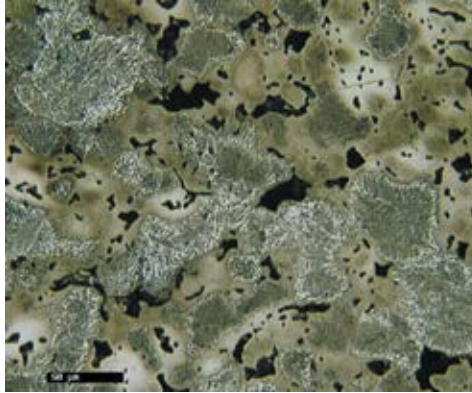
2.6.7 Distaloy® HP + 0.5% C



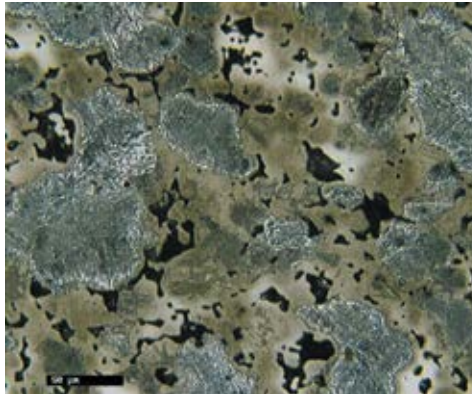
Cooling rate

0.85°C/second

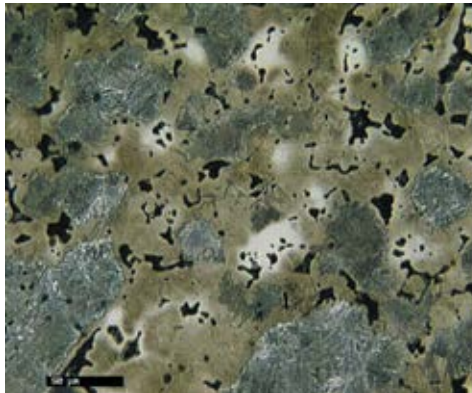
0.25°C/second



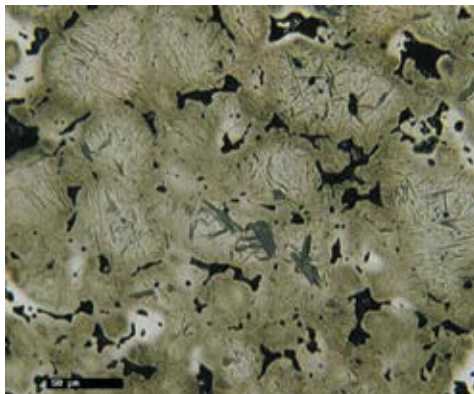
0.5°C/second



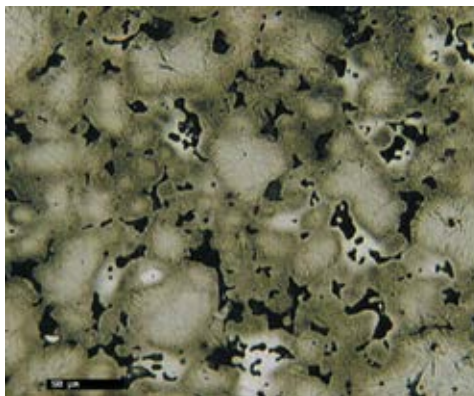
0.85°C/second



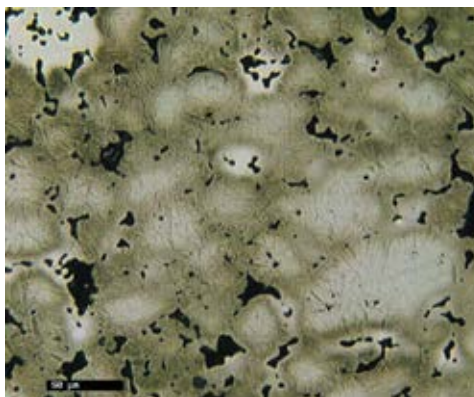
Distaloy HP + 0.5% C



4°C/second



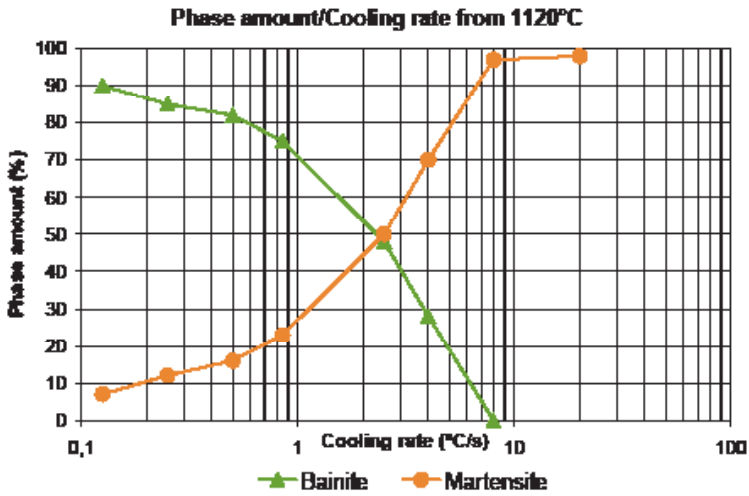
8°C/second



64°C/second

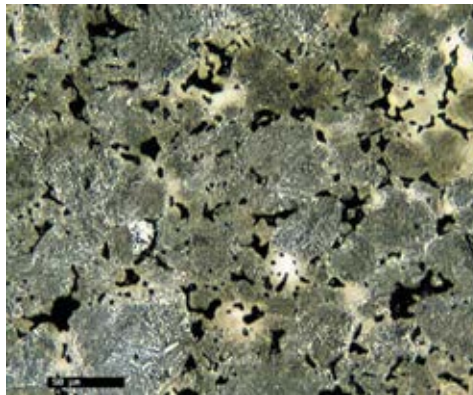


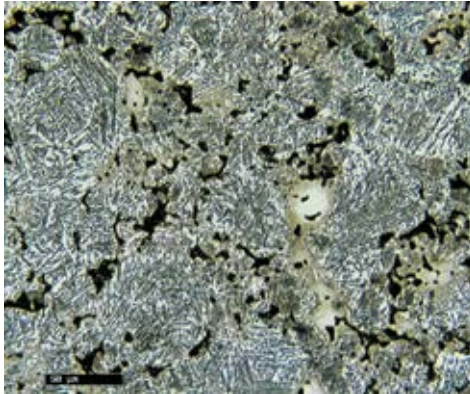
2.6.8 Distaloy® DC + 0.5% C



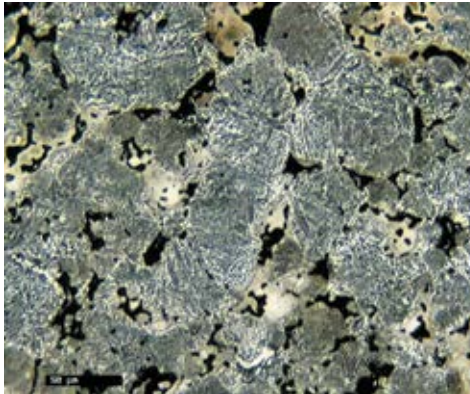
Cooling rate

0.85°C/second

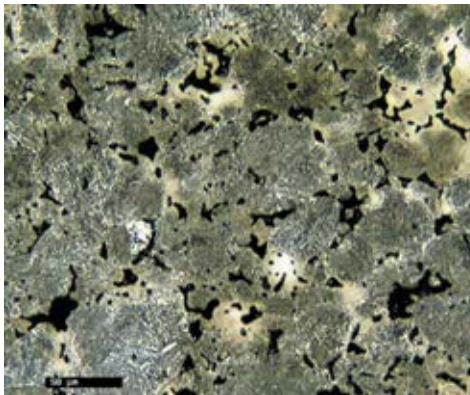




0.125°C/second



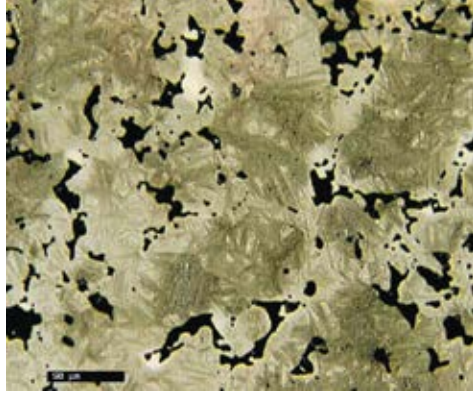
0.5°C/second



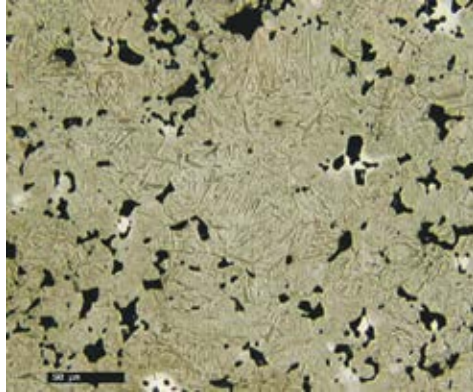
0.85°C/second



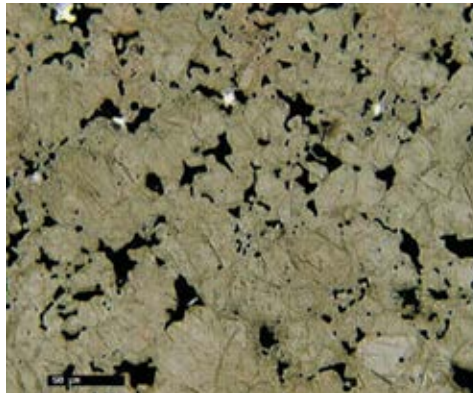
4°C/second



8°C/second

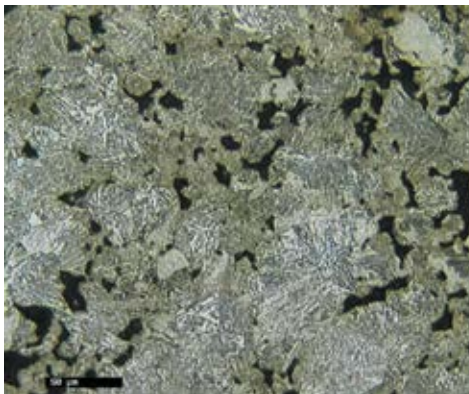
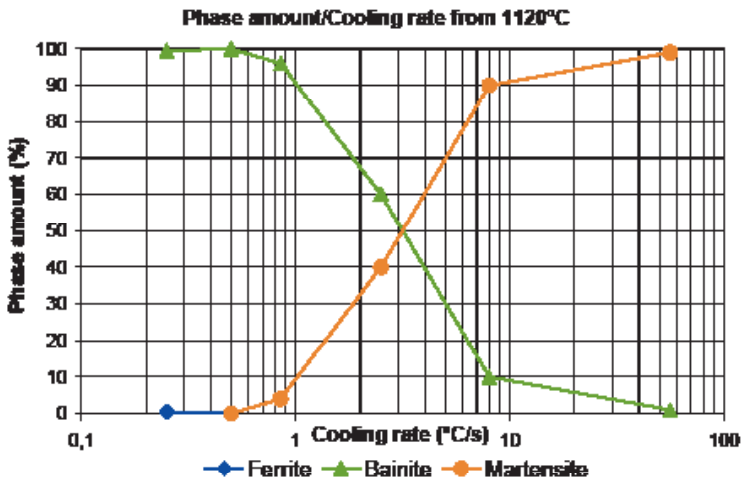


70°C/second



Distaloy DC + 0.5% C

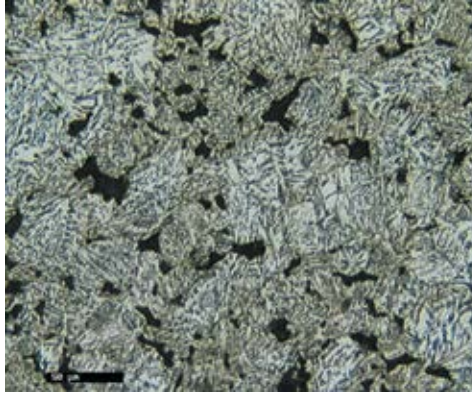
2.6.9 Distaloy® DH + 0.4% C



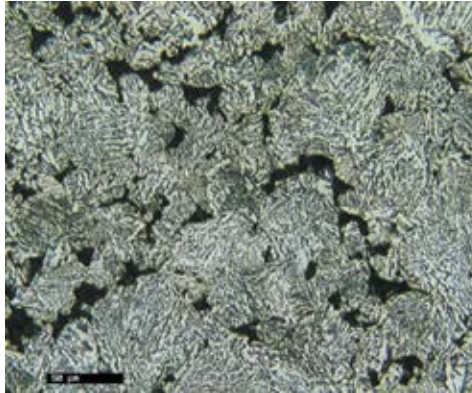
Cooling rate

0.85°C/second

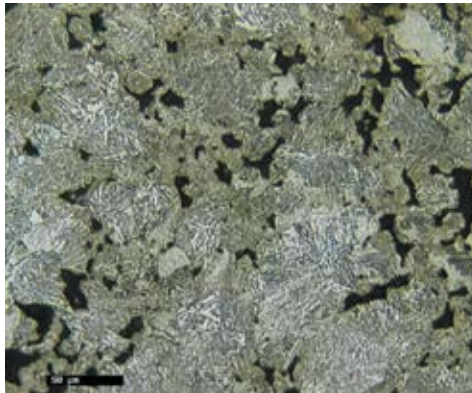
0.25°C/second



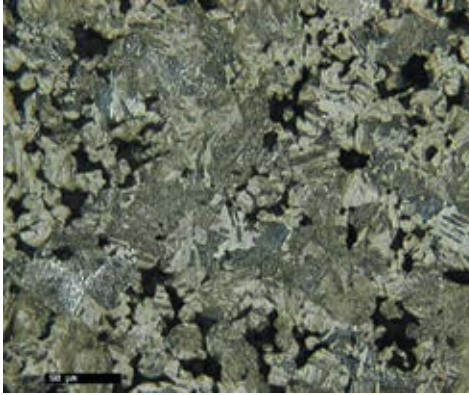
0.5°C/second



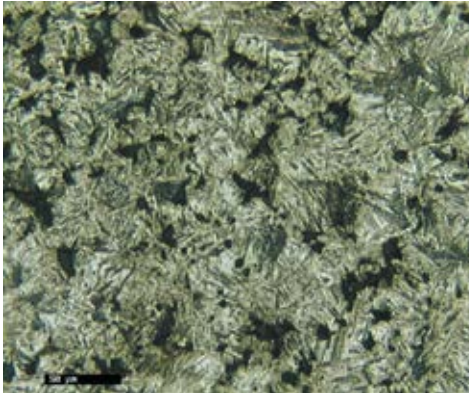
0.85°C/second



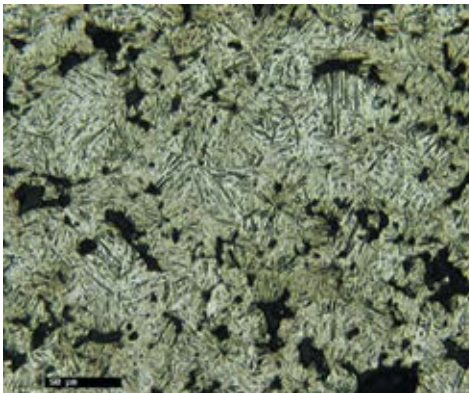
Distaloy DH + 0.4% C



2.5°C/second



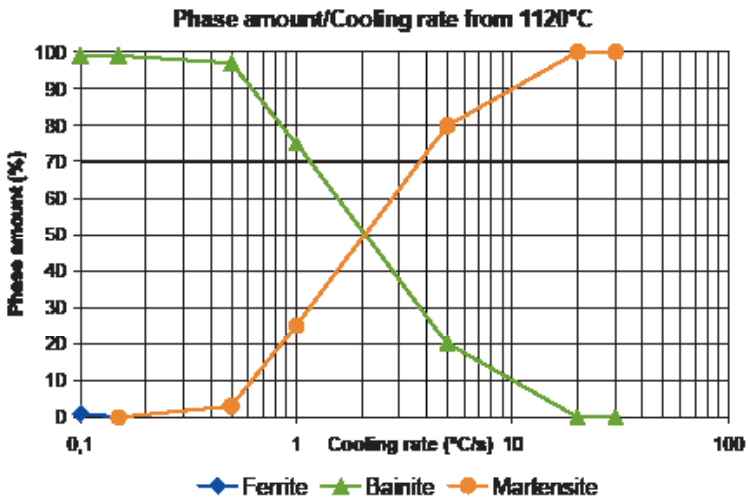
8°C/second



56°C/second

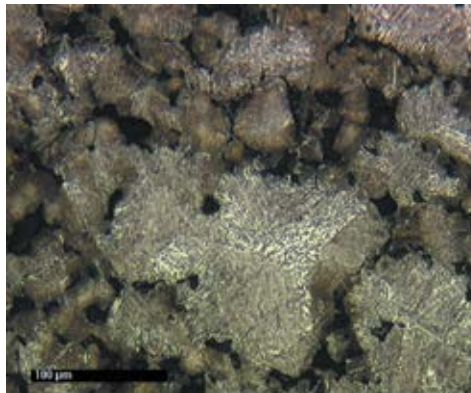


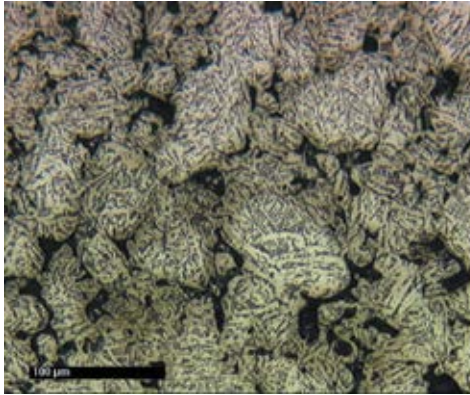
2.6.10 Distaloy® DH + 0.5% C



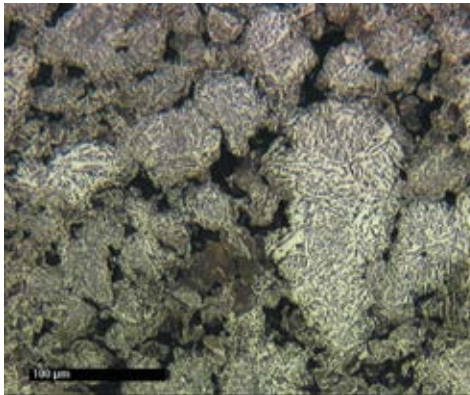
Cooling rate

1°C/second

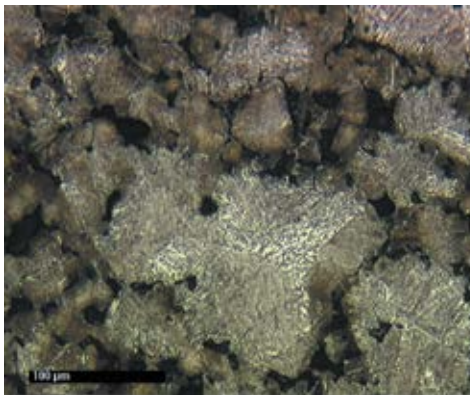




0.1°C/second



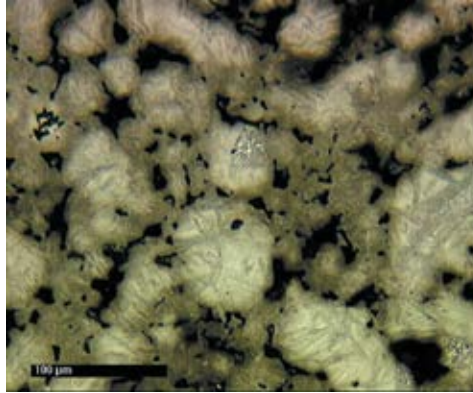
0.5°C/second



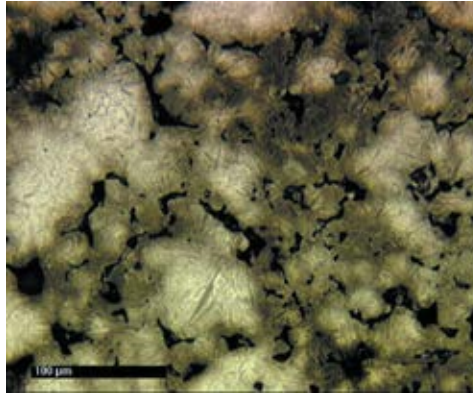
1°C/second



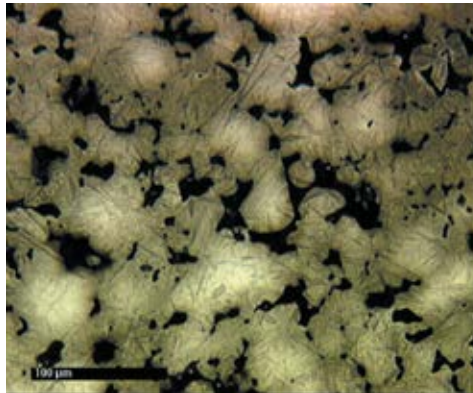
5°C/second



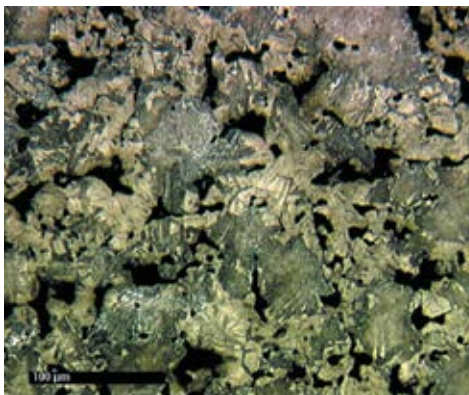
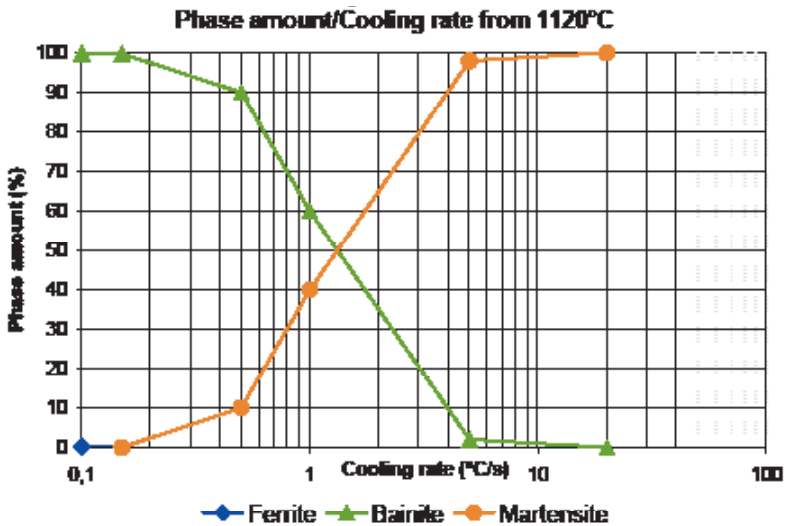
20°C/second



100°C/second

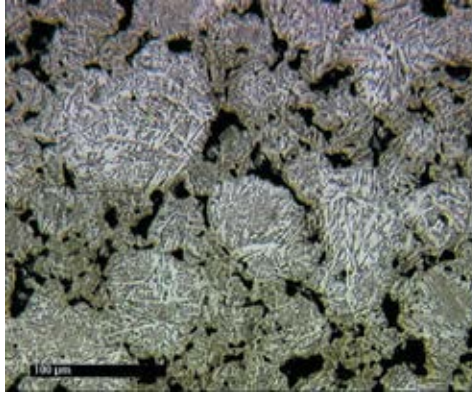


2.6.11 Distaloy® DH + 0.6% C

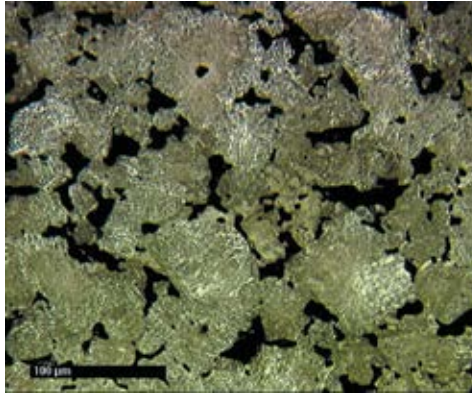


Cooling rate
1°C/second

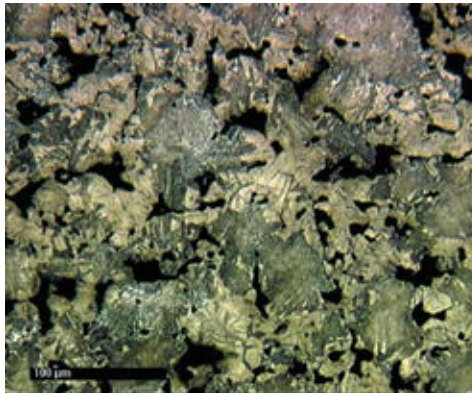
0.1°C/second

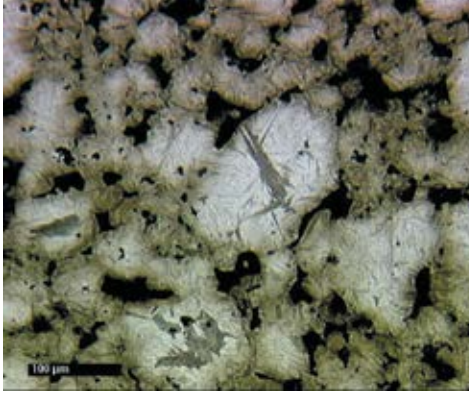


0.5°C/second

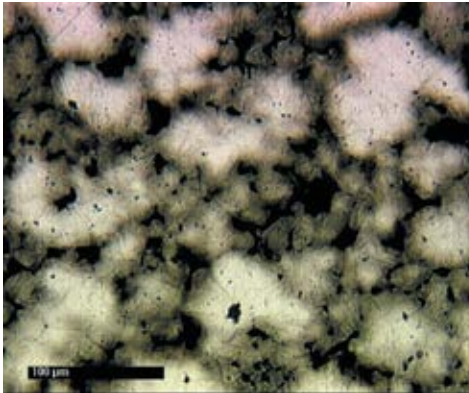


1°C/second

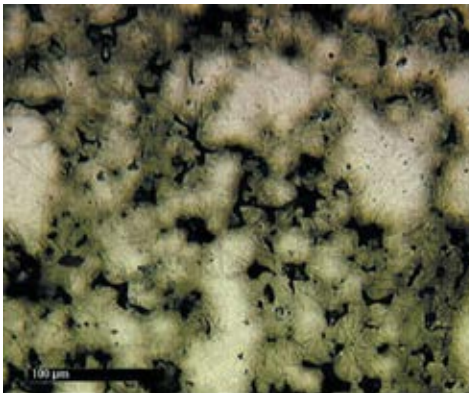




5°C/second



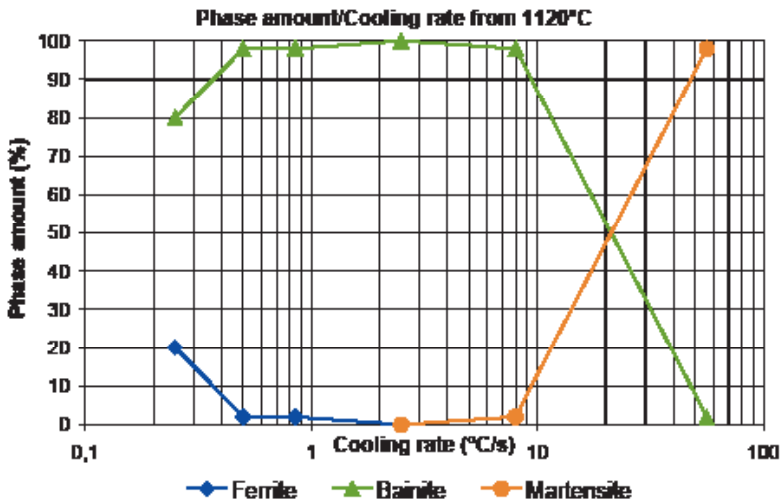
20°C/second



100°C/second

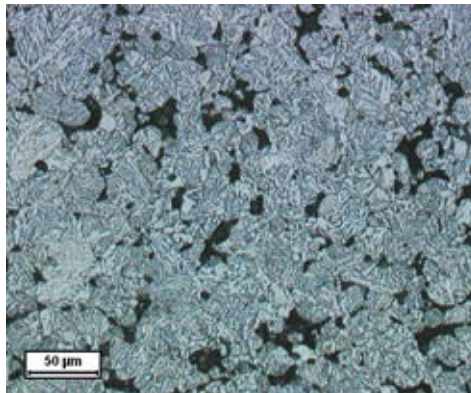


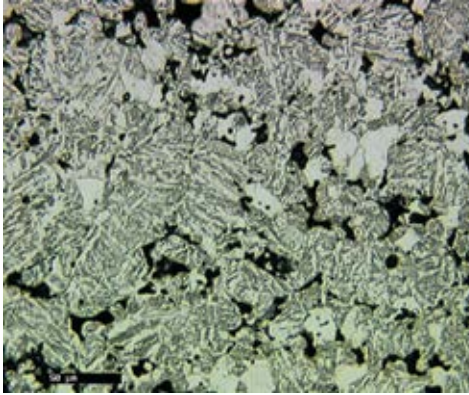
2.6.12 Astaloy™ Mo + 0.4% C



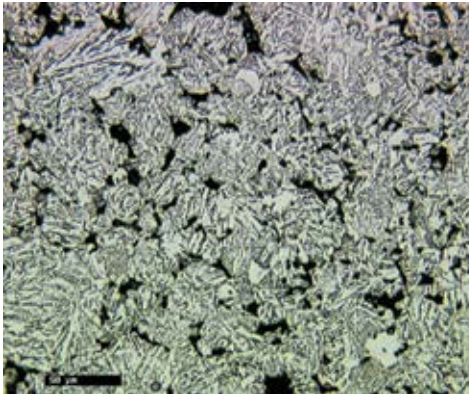
Cooling rate

0.85°C/second

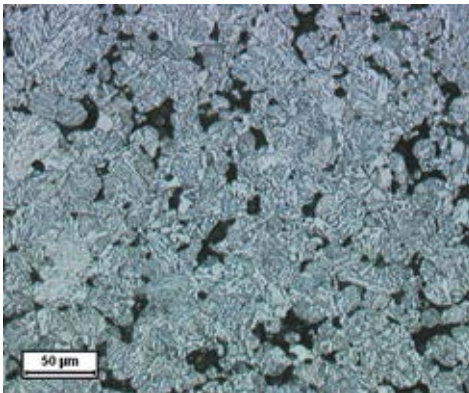




0.25°C/second



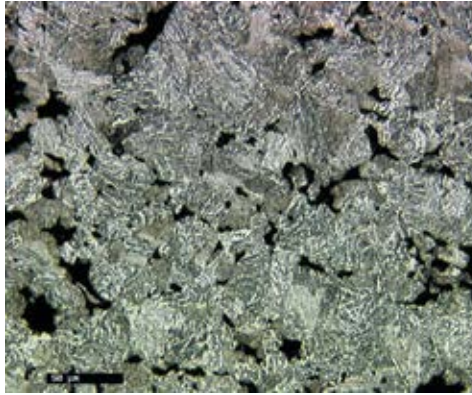
0.5°C/second



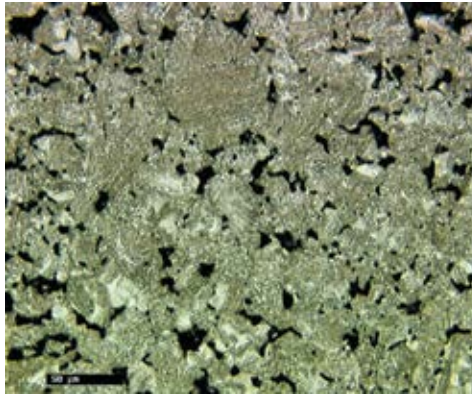
0.85°C/second



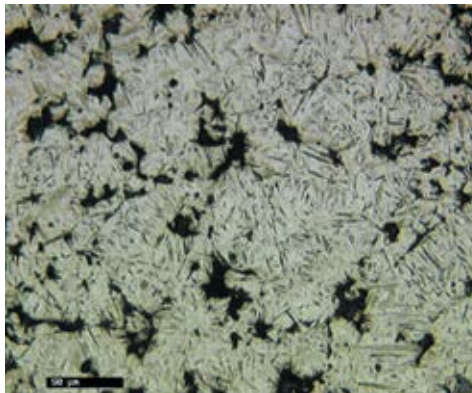
2.5°C/second



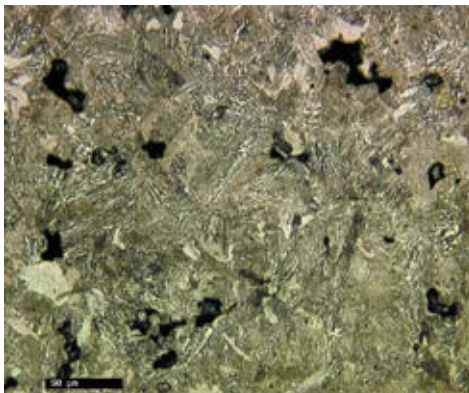
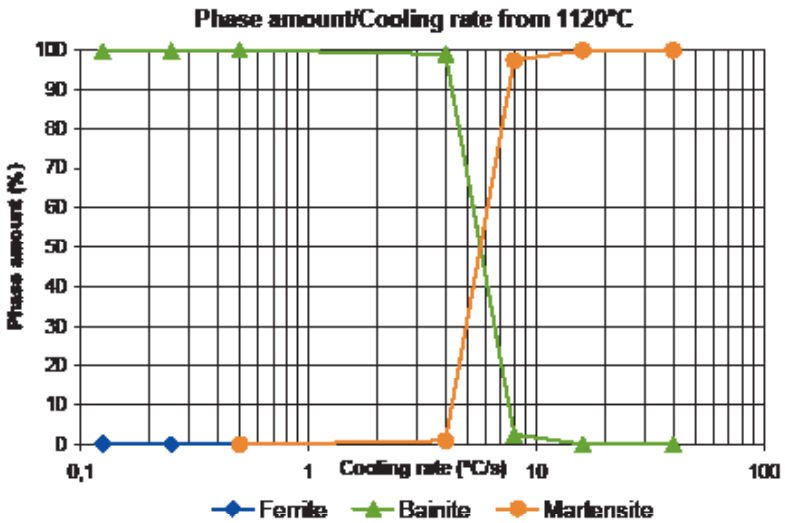
8°C/second



56°C/second



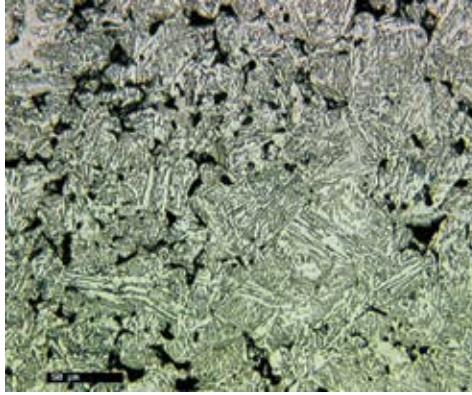
2.6.13 Astaloy™ Mo + 0.6% C



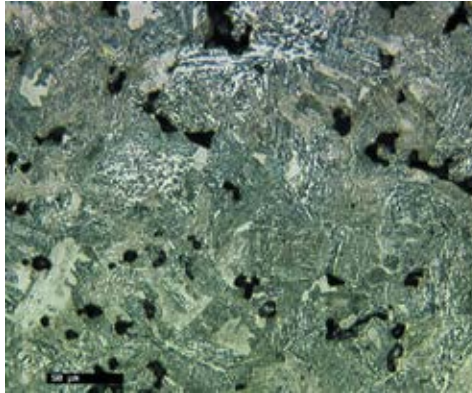
Cooling rate

0.85°C/second

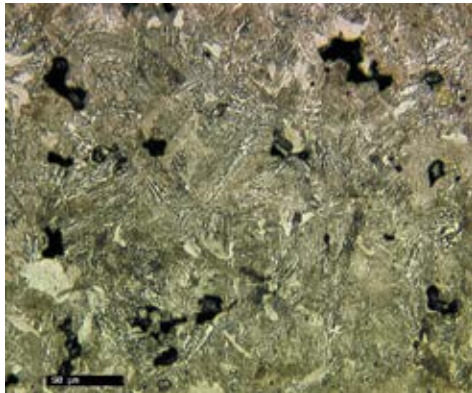
0.25°C/second

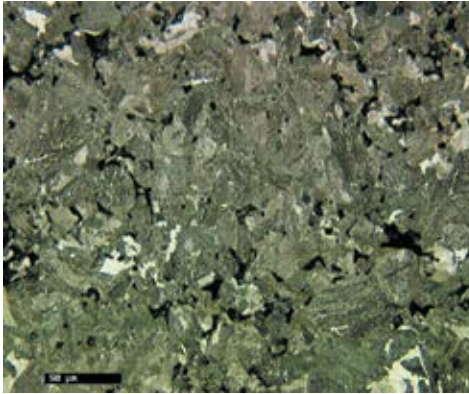


0.5°C/second

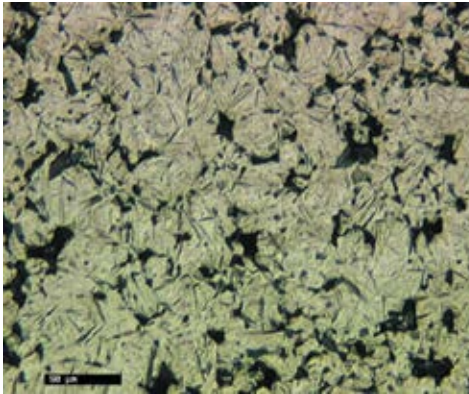


0.85°C/second

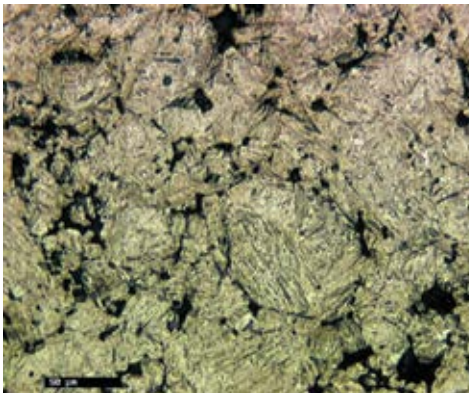




2.5°C/second



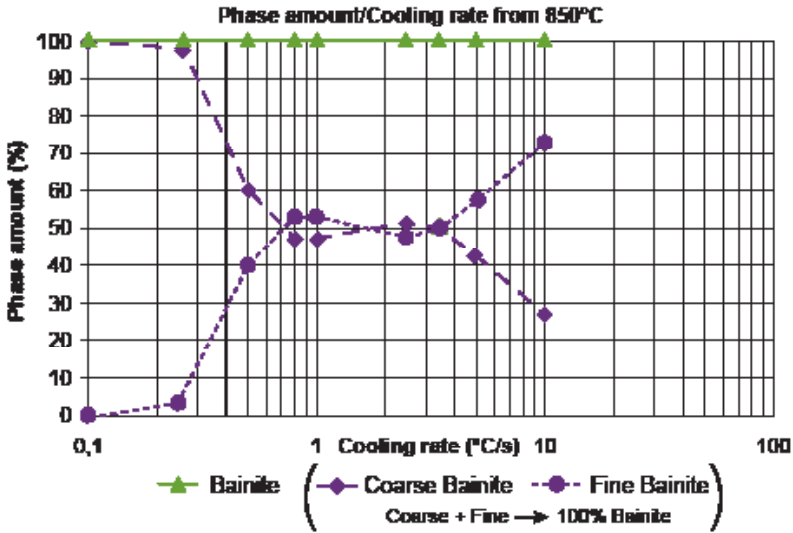
8°C/second



40°C/second



2.6.14 Astaloy™ 85 Mo + 0.8% C



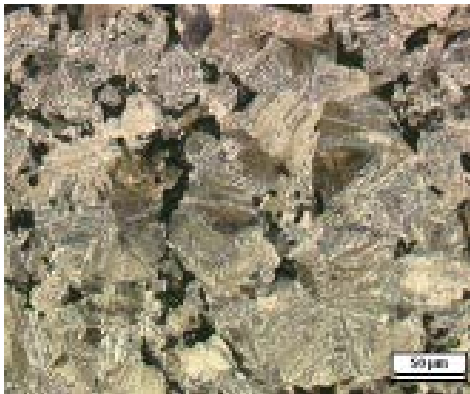
Cooling rate

0.5°C/second





0.1°C/second



0.25°C/second



0.5°C/second



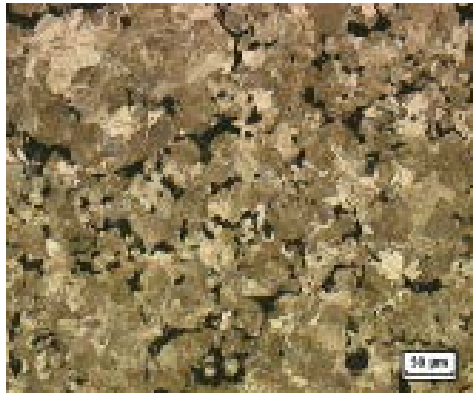
1°C/second



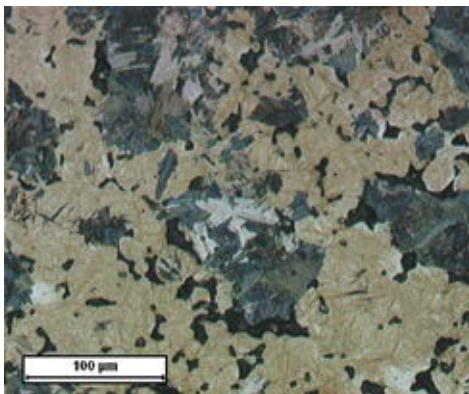
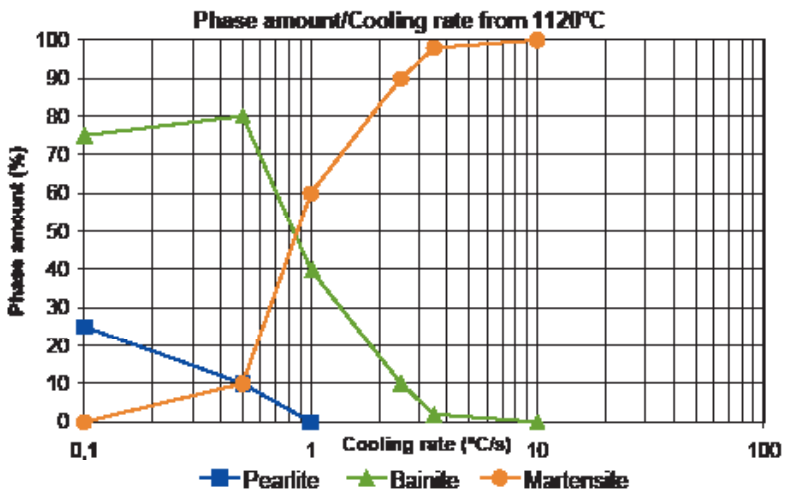
2.5°C/second



10°C/second

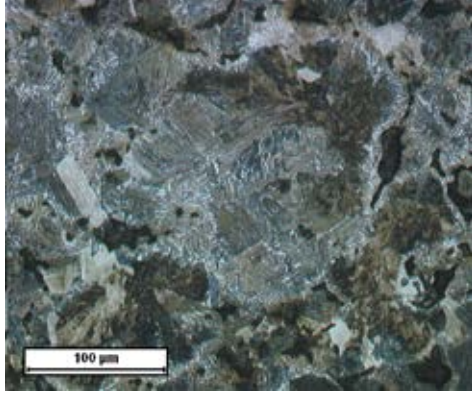


2.6.15 Astaloy™ 85 Mo + 2% Cu (-100) + 0.8% C

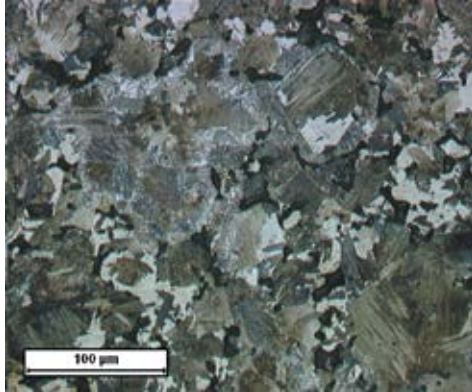


Cooling rate
1°C/second

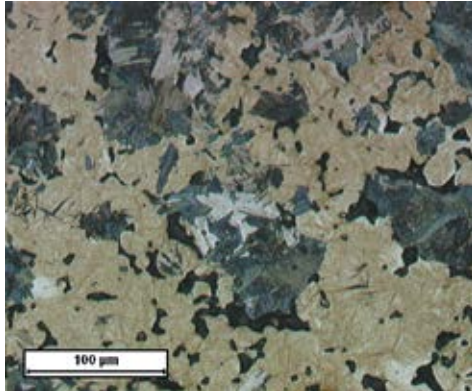
0.25°C/second

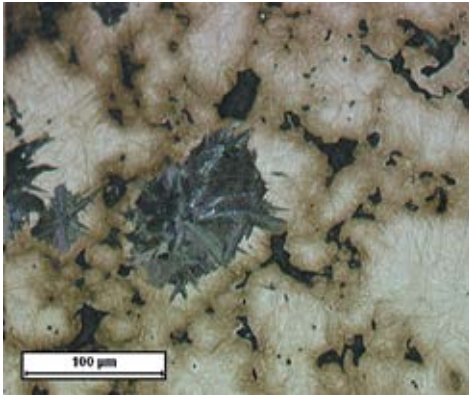


0.5°C/second

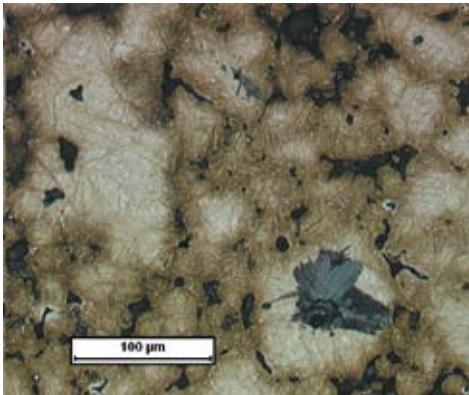


1°C/second

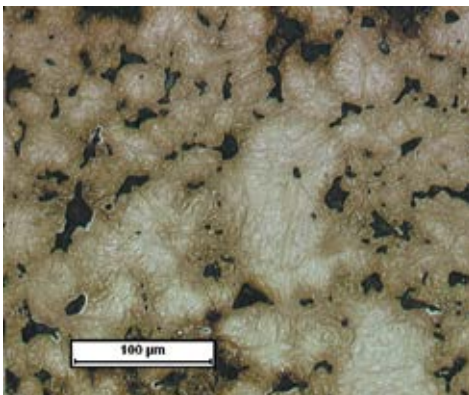




2.5°C/second



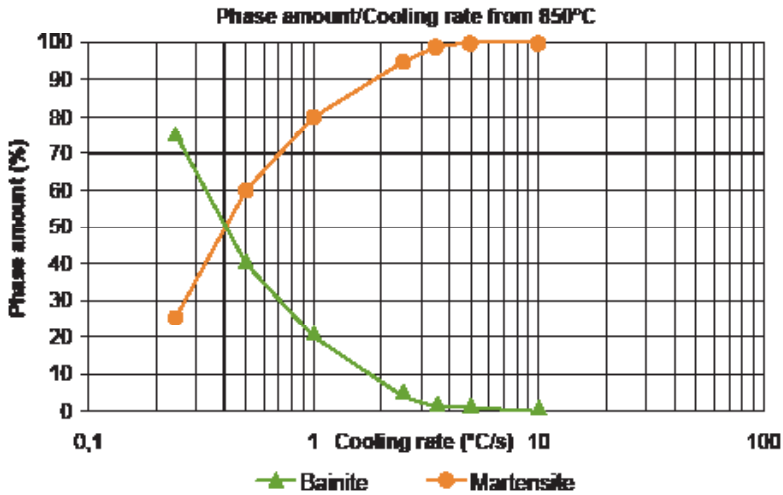
3.5°C/second



10°C/second

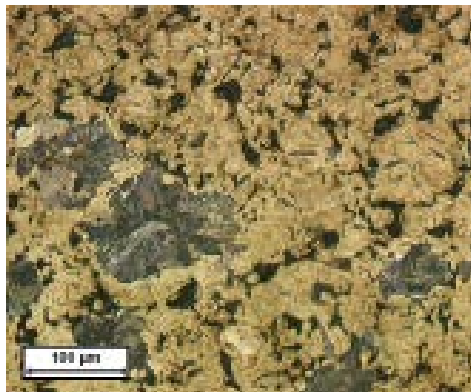


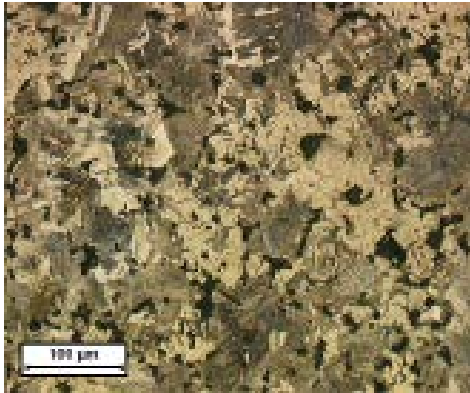
2.6.16 Astaloy™ A + 2% Cu (-100) + 0.6% C



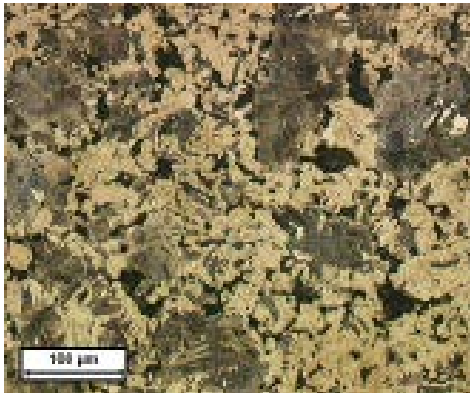
Cooling rate

1°C/second





0.25°C/second



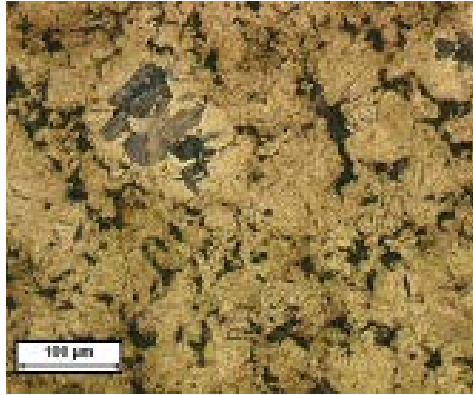
0.5°C/second



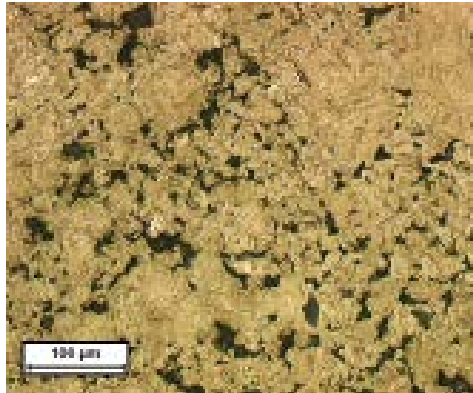
1°C/second



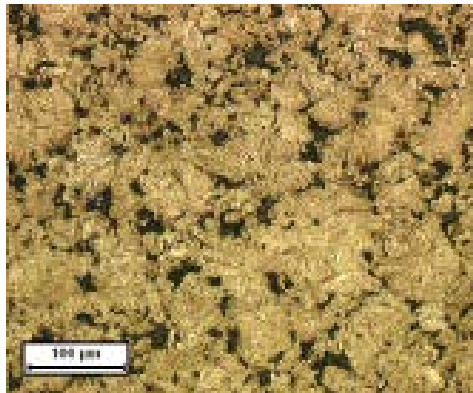
2.5°C/second



5°C/second

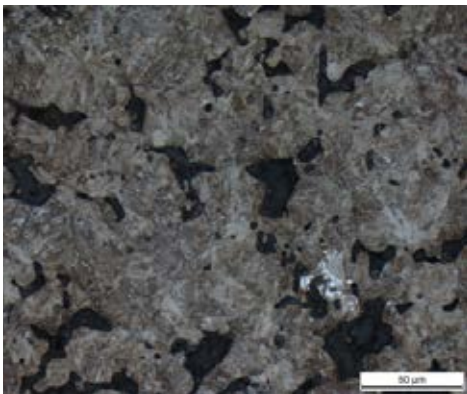
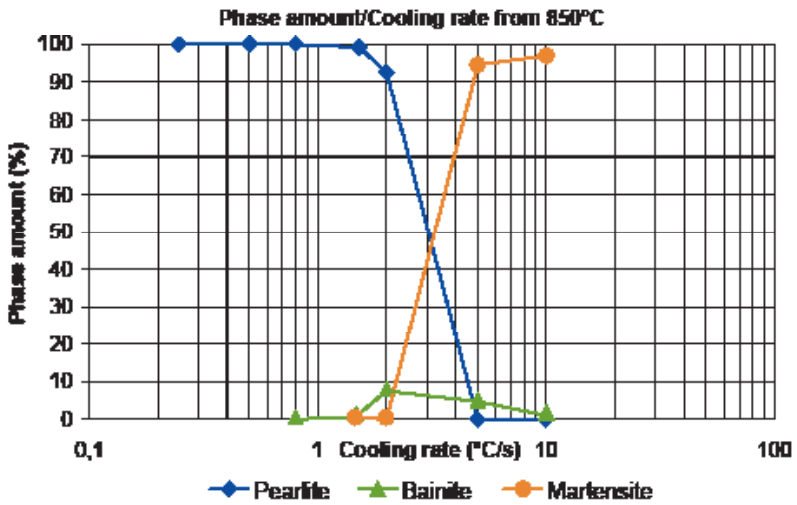


10°C/second



Astloy A + 2% Cu (-100) + 0.6% C

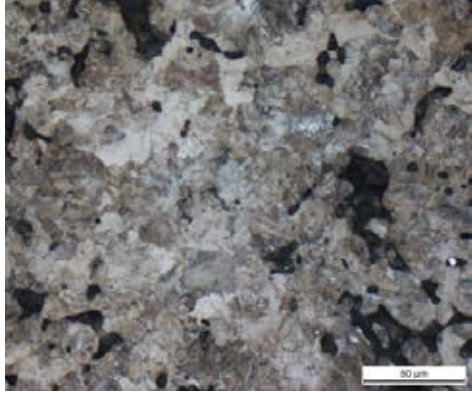
2.6.17 Astaloy™ CrA + 0.8% C



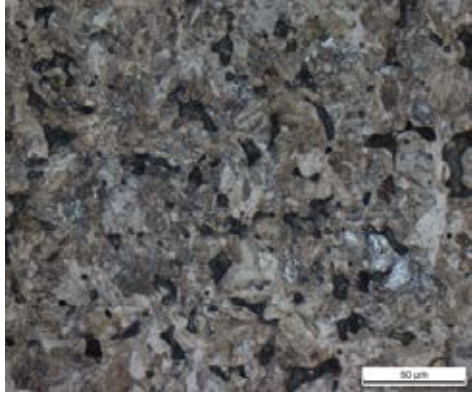
Cooling rate

1.5°C/second

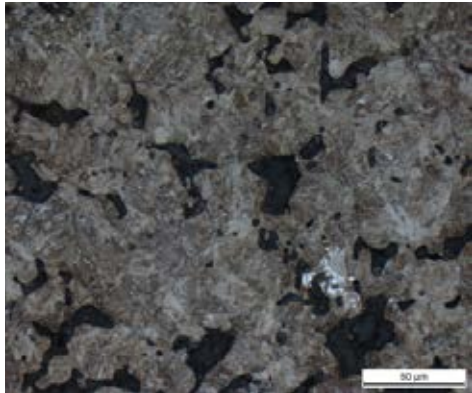
0.1°C/second



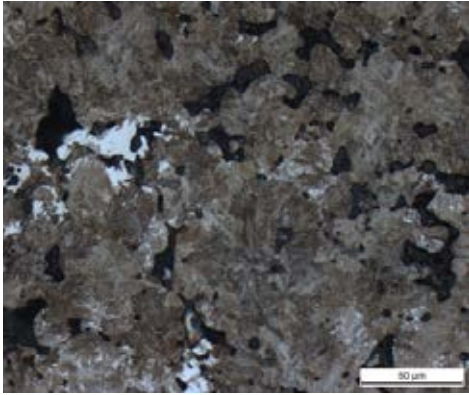
0.5°C/second



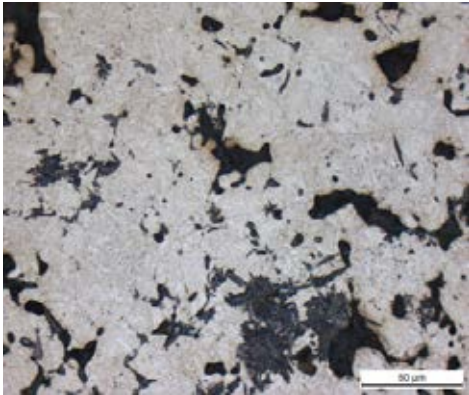
1.5°C/second



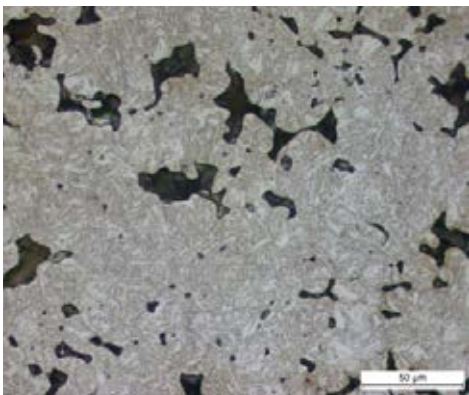
Astaloy CrA + 0.8% C



2°C/second



5°C/second

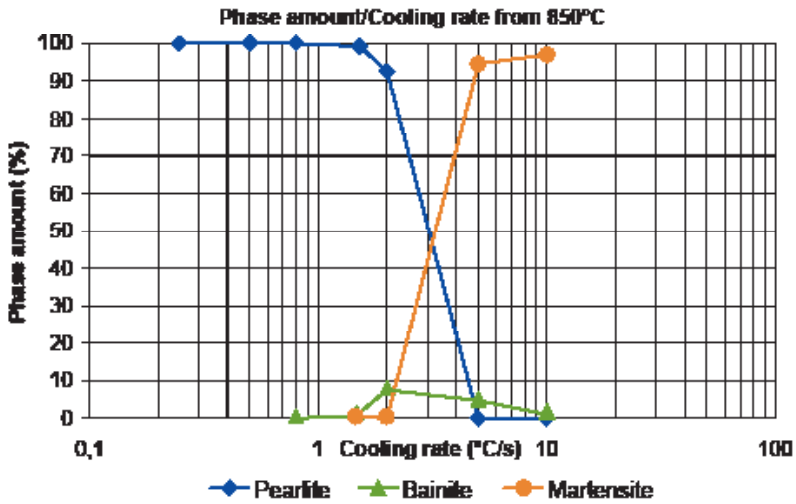


10°C/second



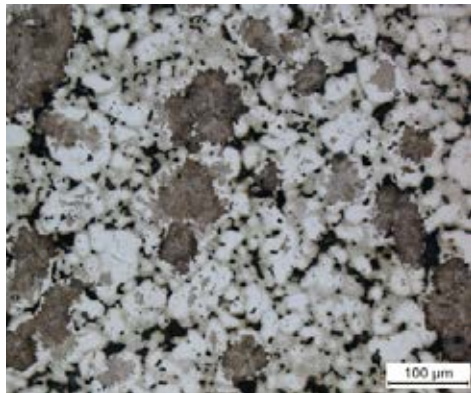
Astaloy CrA + 0.8% C

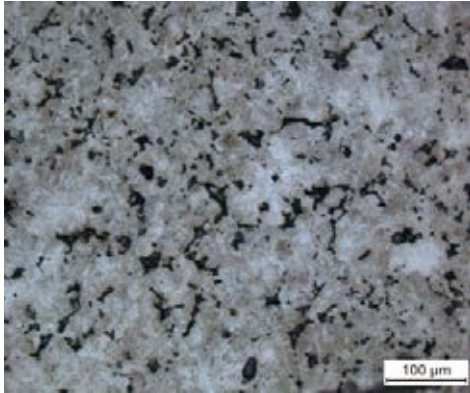
2.6.18 Astaloy™ CrA + 2% Cu + 0.6% C



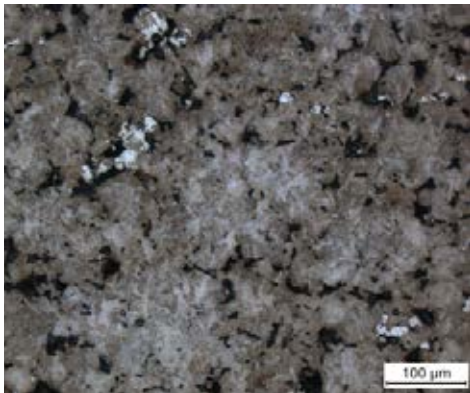
Cooling rate

1.5°C/second

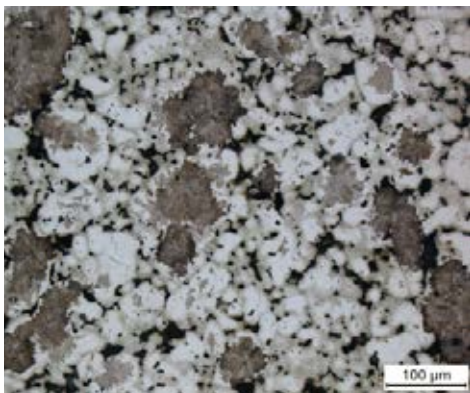




0.25°C/second



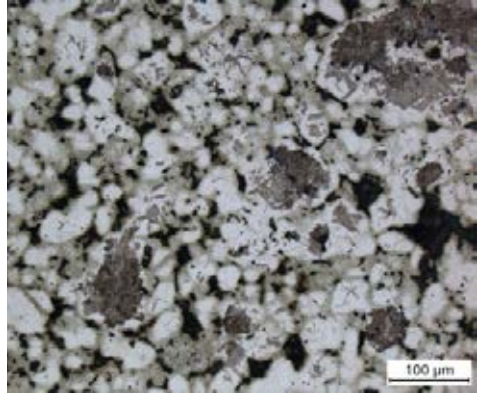
0.5°C/second



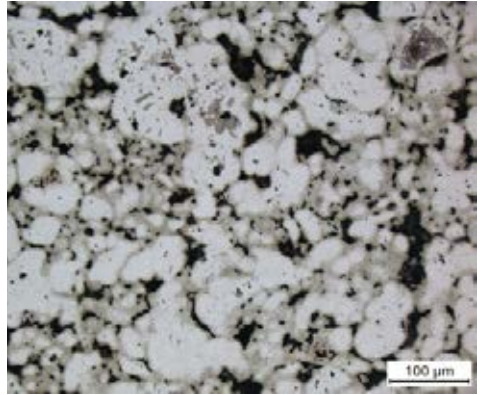
1.5°C/second



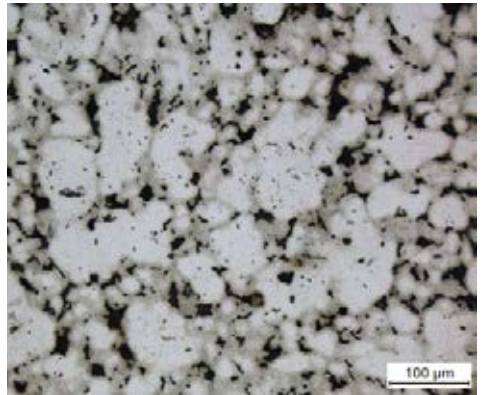
2°C/second



5°C/second

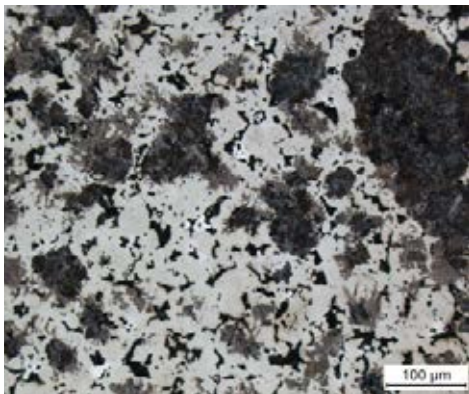
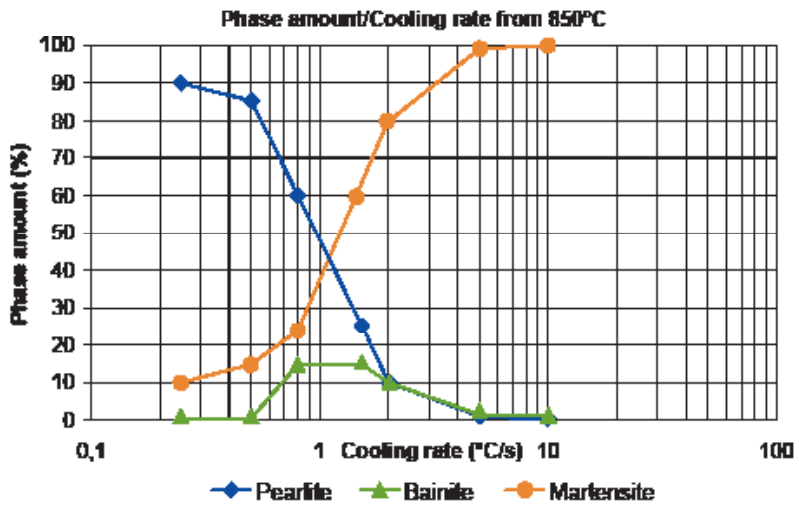


10°C/second



Astloy CrA + 2% Cu + 0.6% C

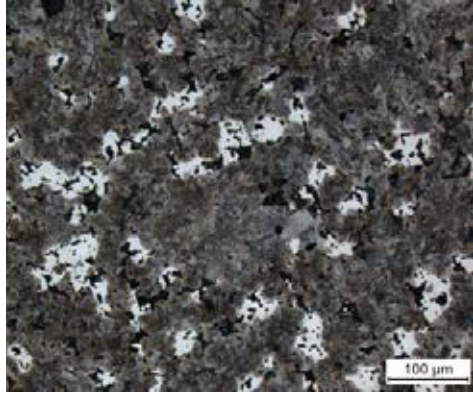
2.6.19 Astaloy™ CrA + 2% Ni + 0.6% C



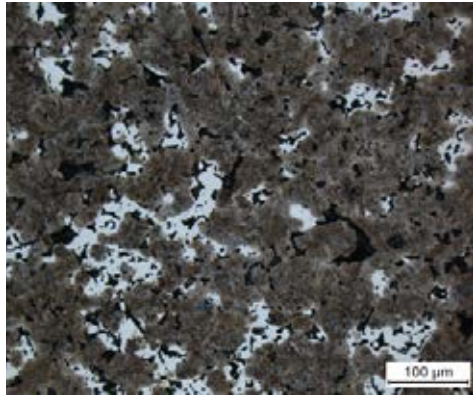
Cooling rate

1.5°C/second

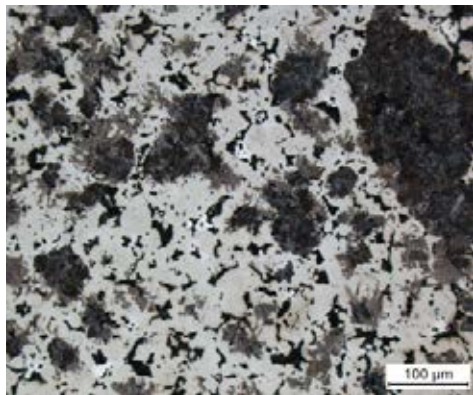
0.25°C/second



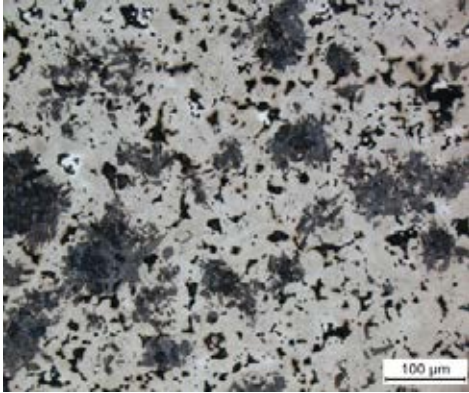
0.5°C/second



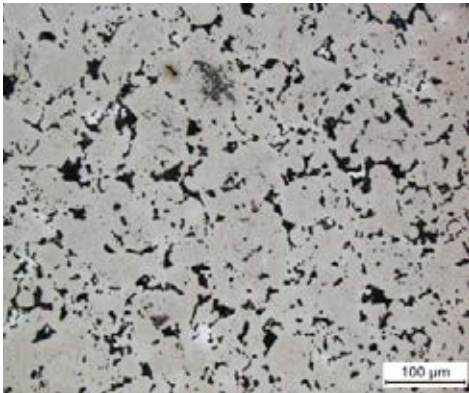
1.5°C/second



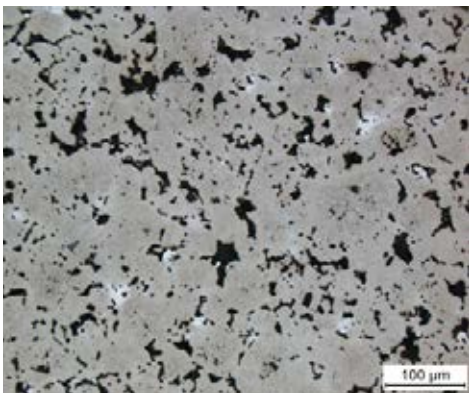
Astaloy CrA + 2% Ni + 0.6% C



2°C/second



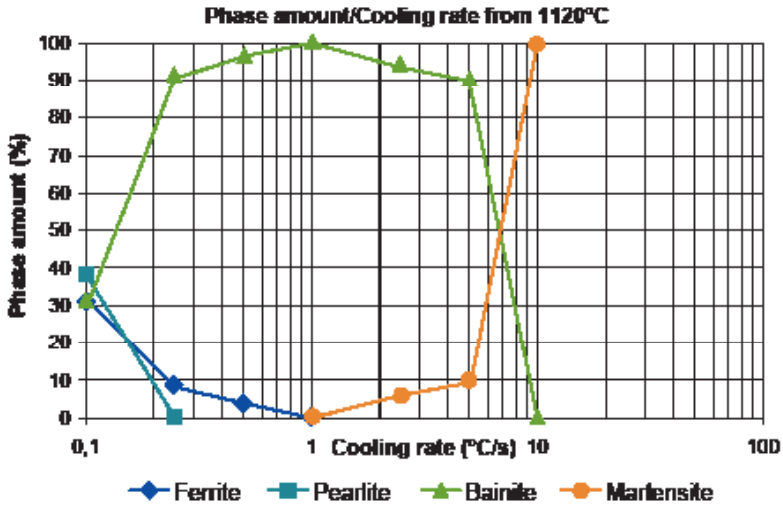
5°C/second



10°C/second

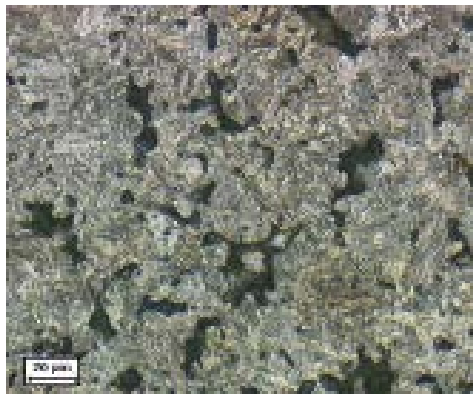


2.6.20 Astaloy™ CrM + 0.3% C



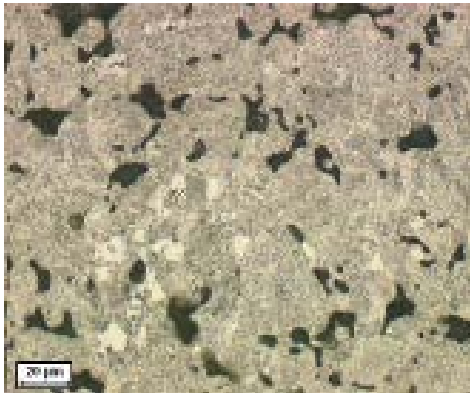
Cooling rate

1°C/second

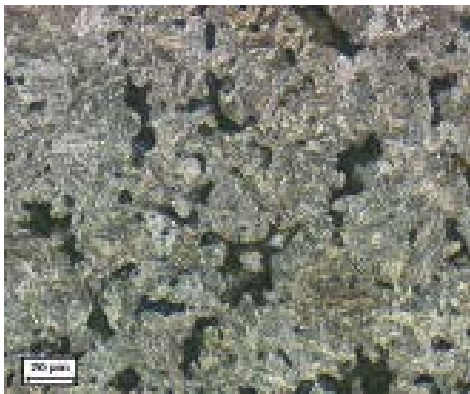




0.1°C/second



0.5°C/second



1°C/second



Astaloy CrM + 0.3% C

2.5°C/second



5°C/second

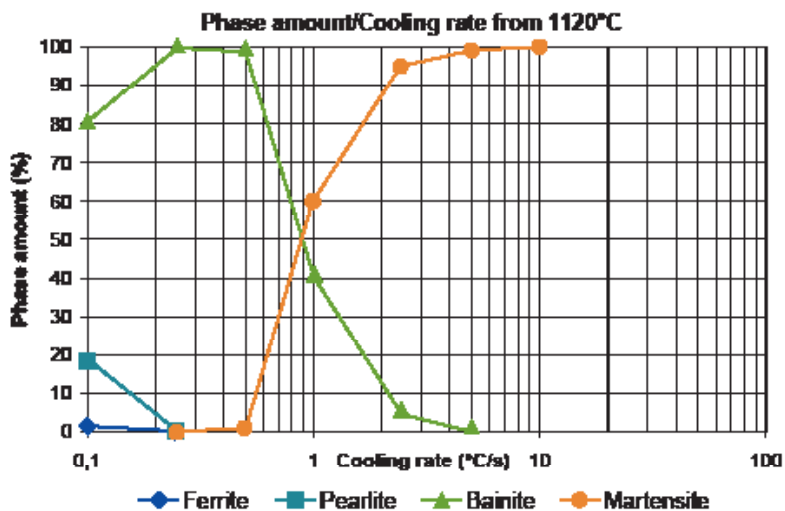


10°C/second



Astaloy CrM + 0.3% C

2.6.21 Astaloy CrM® + 0.4% C



Cooling rate

1°C/second

0.1°C/second



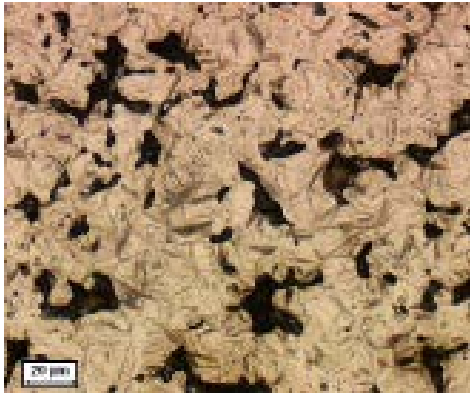
0.5°C/second



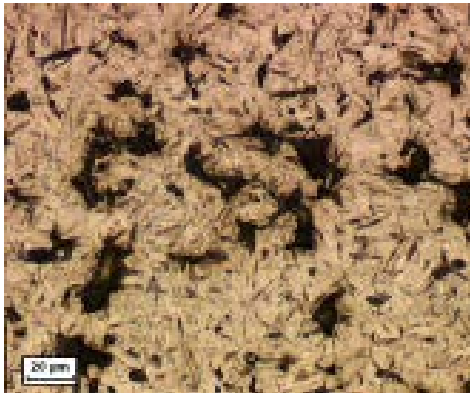
1°C/second



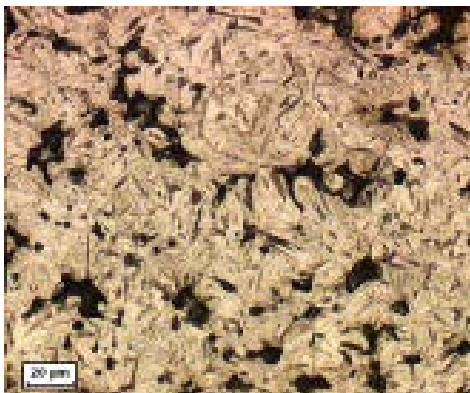
Astaloy CrM + 0.4% C



2.5°C/second



5°C/second

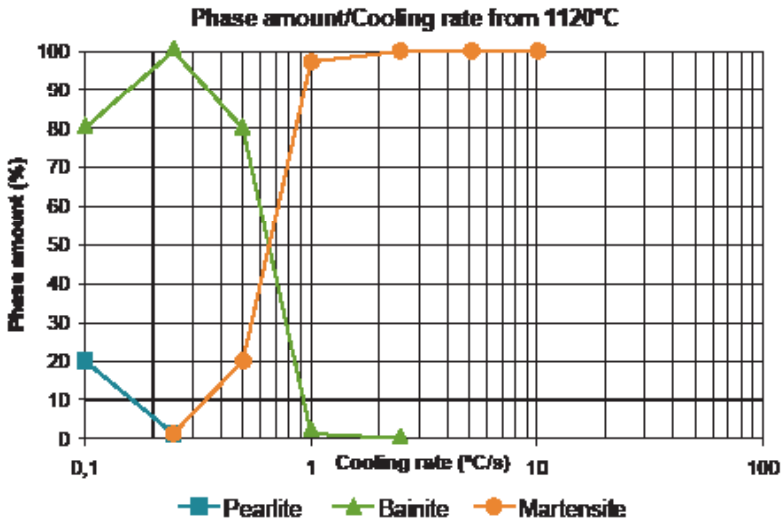


10°C/second



Astaloy CrM + 0.4% C

2.6.22 Astaloy™ CrM + 0.5% C



Cooling rate

1°C/second





0.1°C/second



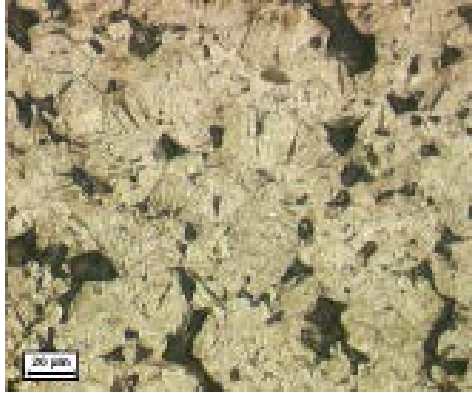
0.5°C/second



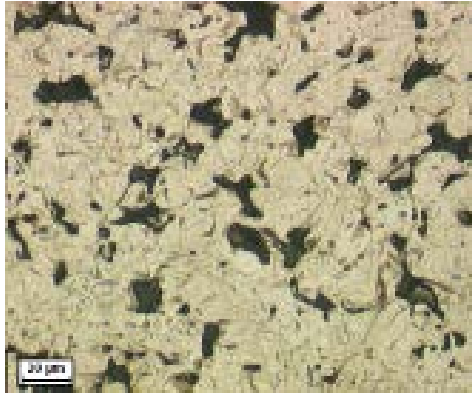
1°C/second



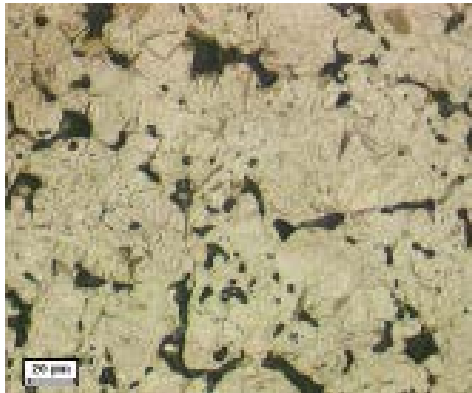
2.5°C/second



5°C/second



10°C/second



Astloy CrM + 0.5% C

**Index**

2.7.1	Distaloy® AQ	248
2.7.2	Distaloy AB	251
2.7.3	Distaloy AE	253
2.7.4	Distaloy HP	255
2.7.5	Astaloy™ Mo	257
2.7.6	Astaloy CrM®	259
2.7.7	Astaloy CrA	263

2.7 Heat Treatment



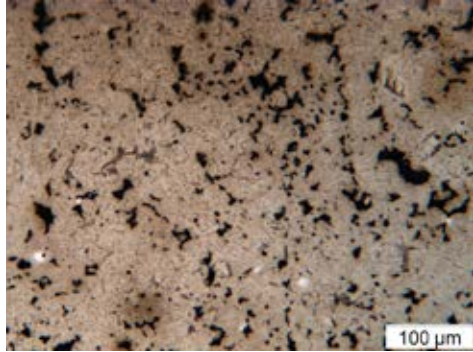
2.7.1 Distaloy® AQ

Through hardened

Surface

Ø 25 mm

Height 20 mm

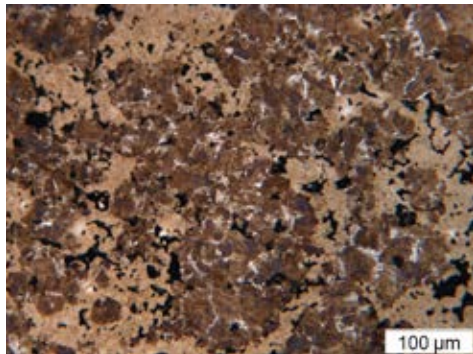


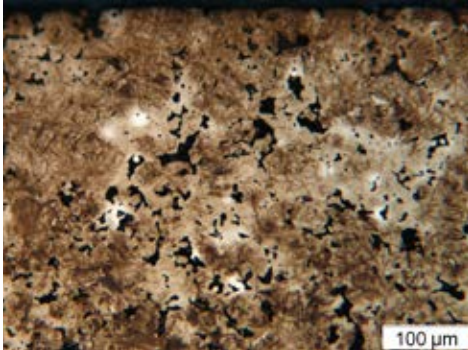
Through hardened

Centre

Ø 25 mm

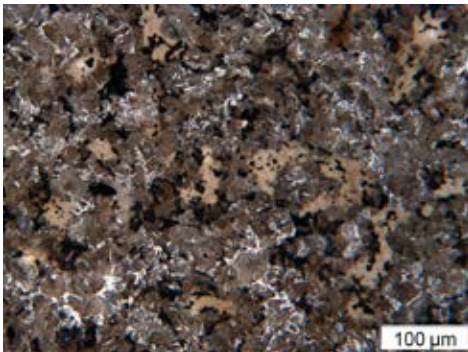
Height 20 mm





Through hardened

Surface
Ø 64 mm
Height 35 mm



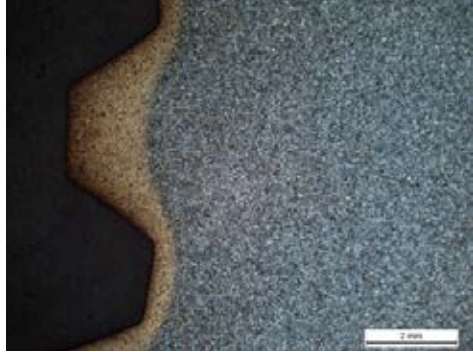
Through hardened

Centre
Ø 64 mm
Height 35 mm



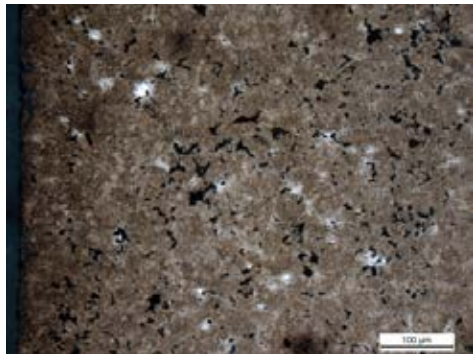
Induction hardened

Overview



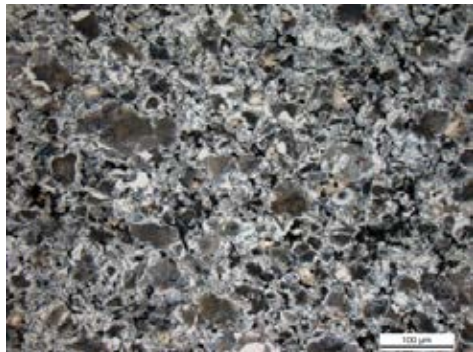
Induction hardened

Surface

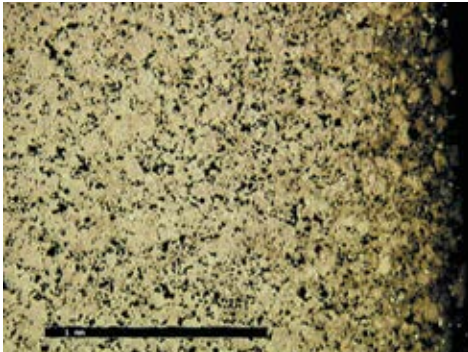


Induction hardened

Centre

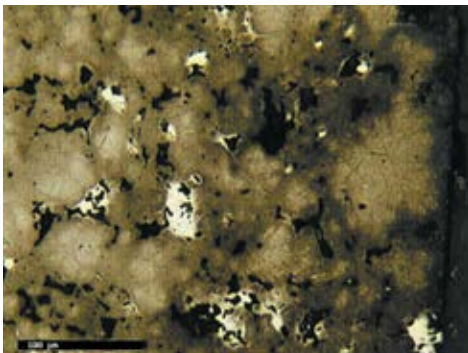


2.7.2 Distaloy® AB



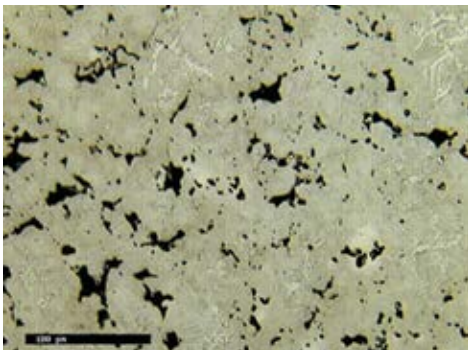
Case hardened

Overview



Case hardened

Surface



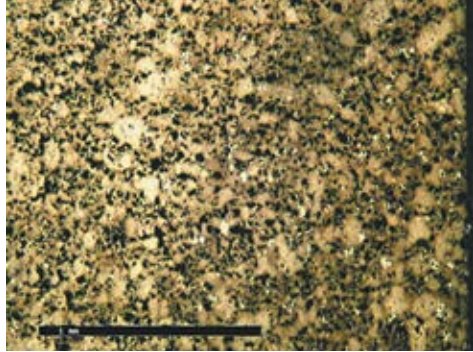
Case hardened

Centre



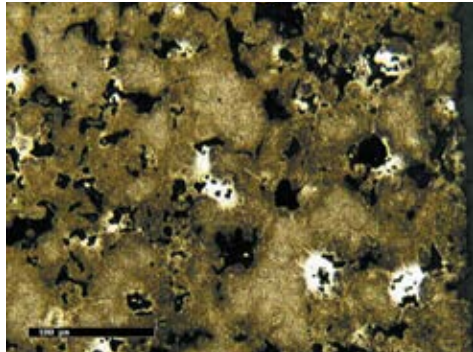
Through hardened

Overview



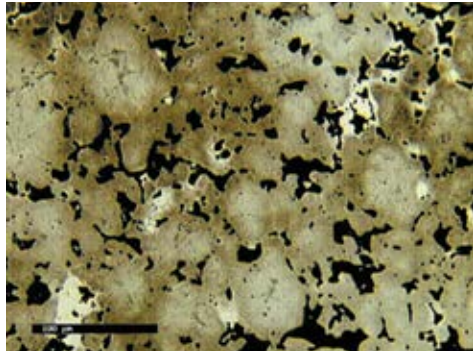
Through hardened

Surface

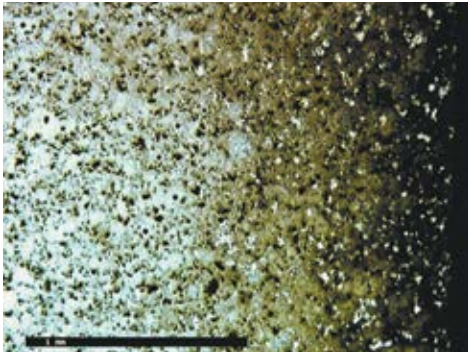


Through hardened

Centre

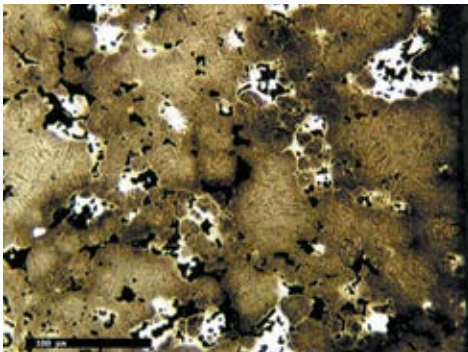


2.7.3 Distaloy® AE



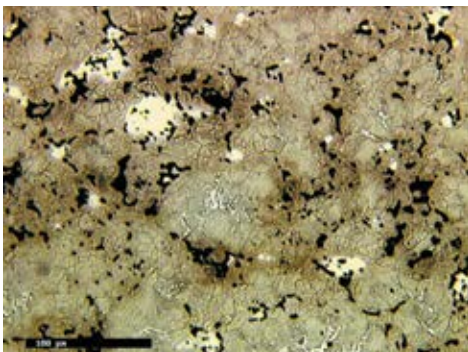
Case hardened

Overview



Case hardened

Surface



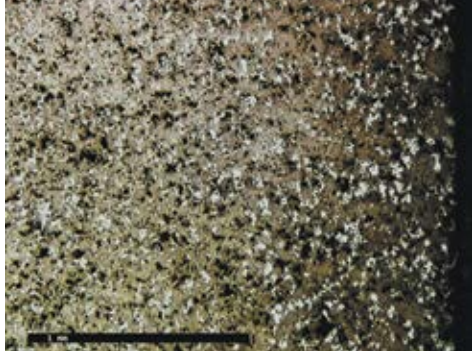
Case hardened

Centre



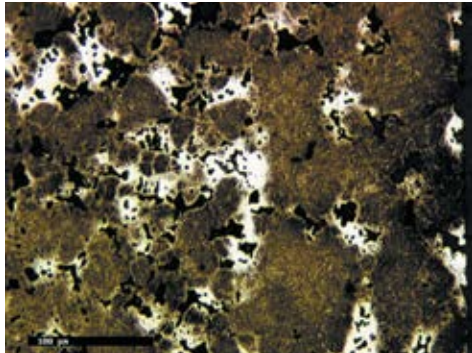
Through hardened

Overview



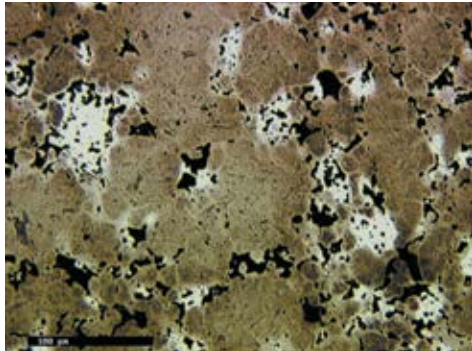
Through hardened

Surface

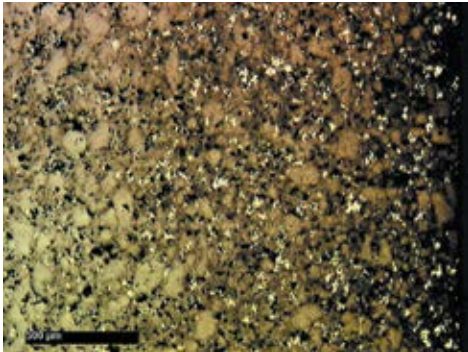


Through hardened

Centre

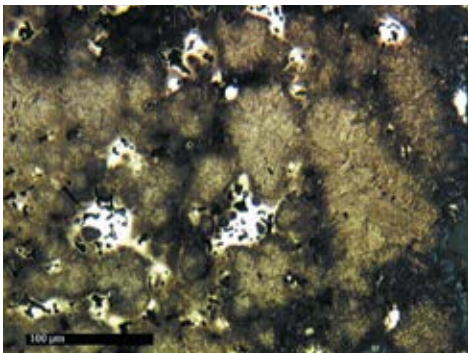


2.7.4 Distaloy® HP



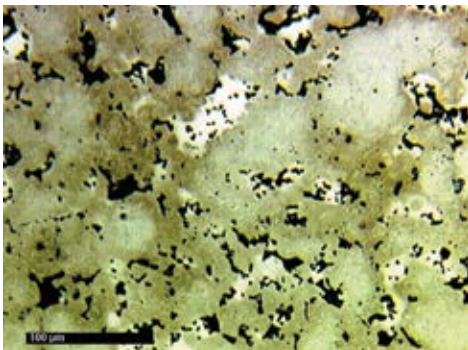
Case hardened

Overview



Case hardened

Surface



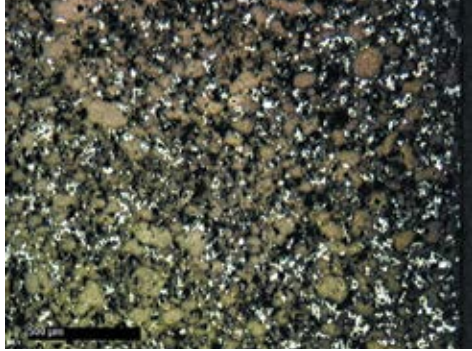
Case hardened

Centre



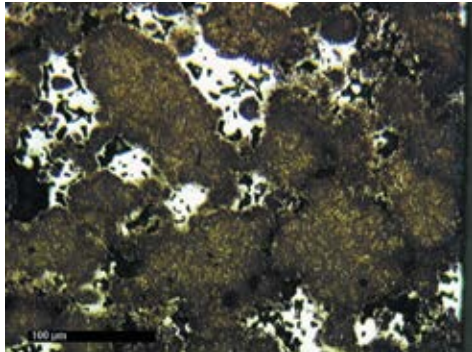
Through hardened

Overview



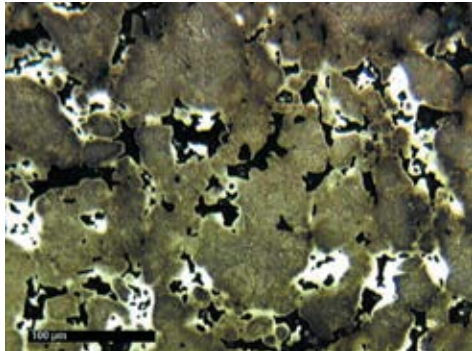
Through hardened

Surface

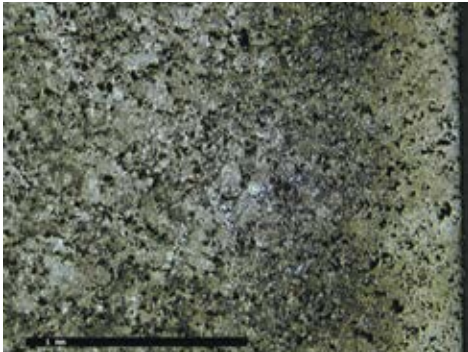


Through hardened

Centre

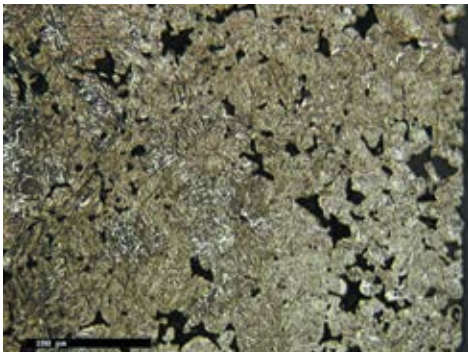


2.7.5 Astaloy™ Mo



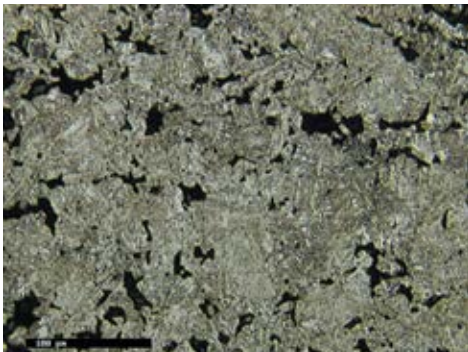
Case hardened

Overview



Case hardened

Surface



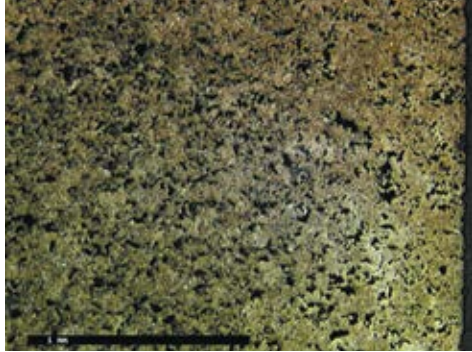
Case hardened

Centre



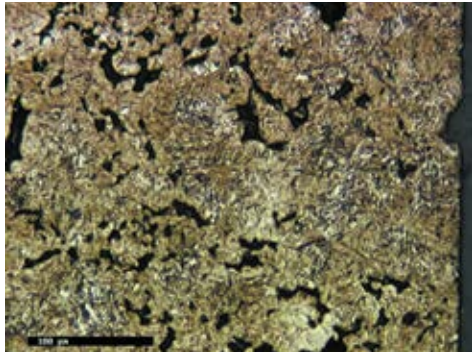
Through hardened

Overview



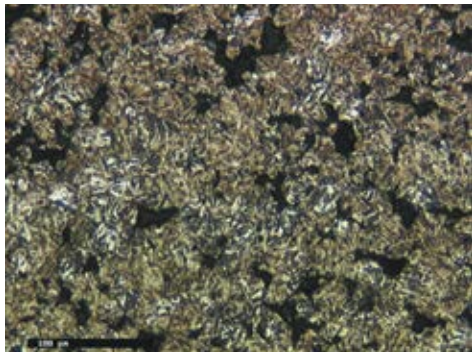
Through hardened

Surface

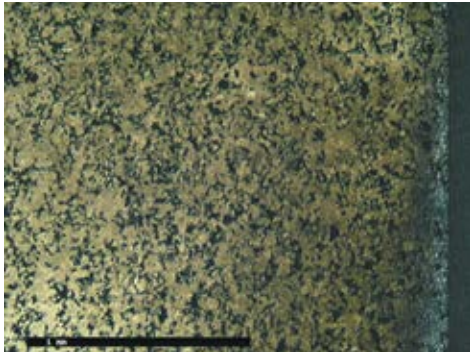


Through hardened

Centre

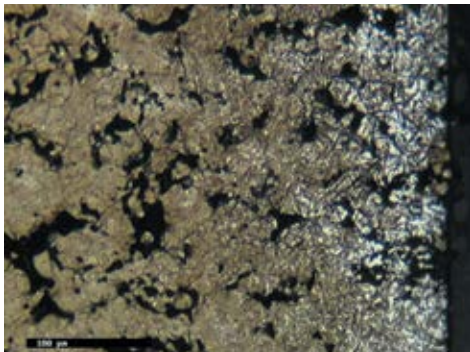


2.7.6 Astaloy CrM®



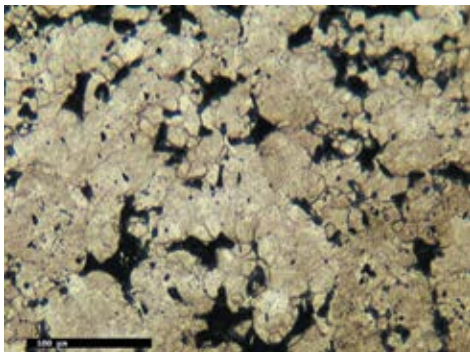
Case hardened

Overview



Case hardened

Surface



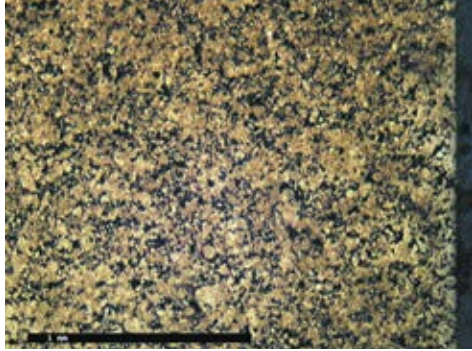
Case hardened

Centre



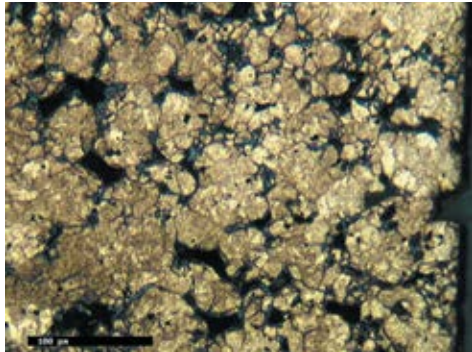
Through hardened

Overview



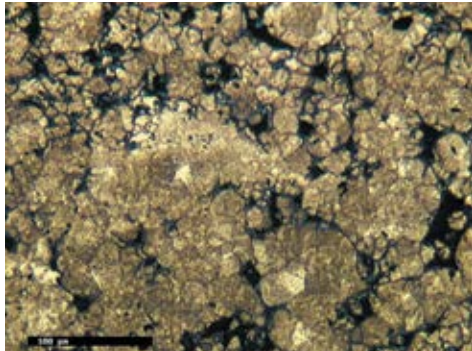
Through hardened

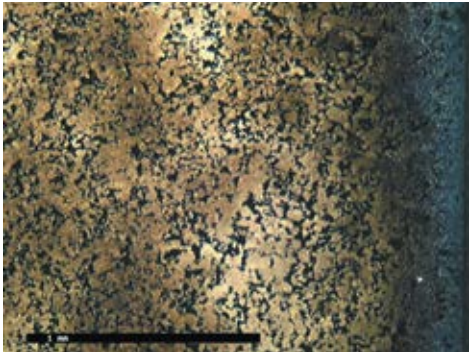
Surface



Through hardened

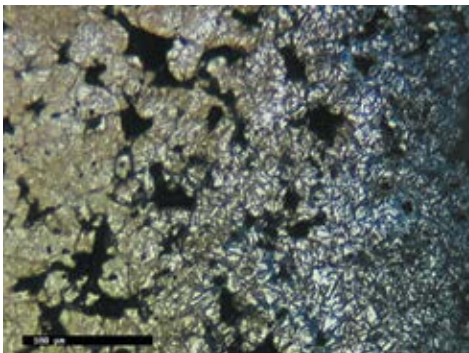
Centre





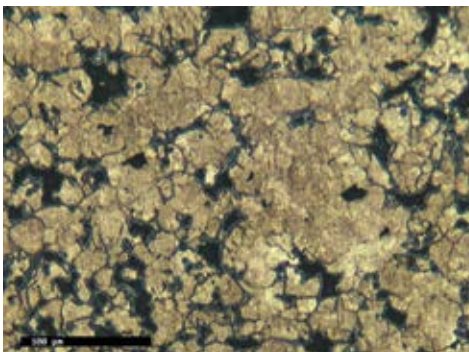
Carbonitrided

Overview



Carbonitrided

Surface



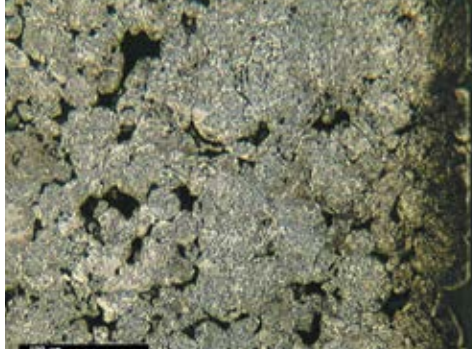
Carbonitrided

Centre



Plasmanitrided

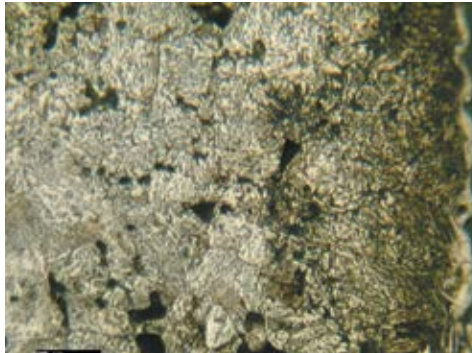
Overview



.....

Plasmanitrided

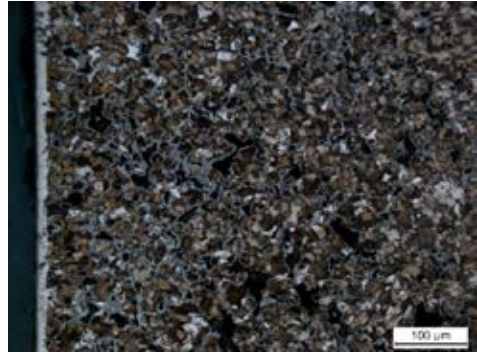
Surface



2.7.7 Astaloy™ CrA

Steam treated + Nitrocarburised

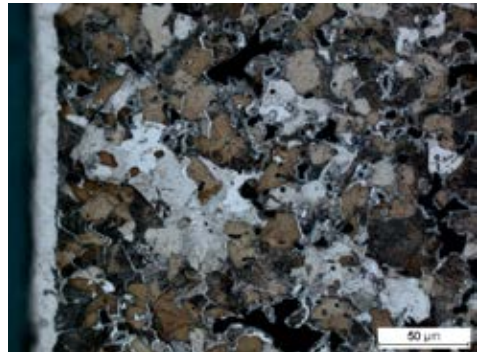
Overview



.....

Steam treated + Nitrocarburised

Surface



Index

Numerics

316L.....173

1120°C, 30 min Etched: Glyceregia...174

1250°C, 30 min Etched: Glyceregia...174

LOM image173

SEM image.....173

410L.....175

1120°C, 30 min Etched: 3.3176

1250°C, 30 min Etched: 3.3176

LOM image175

SEM image.....175

A

ASC100.29.....125

• 0.2% C 1120°C, 30 min

Etched: Nital132

• 0.5% C 1120°C, 30 min

Density: 6.82 g/cm³ Unetched126

• 0.5% C 1120°C, 30 min

Density: 7.07 g/cm³ Unetched127

• 0.5% C 1120°C, 30 min

Density: 7.38 g/cm³ Unetched127

• 0.5% C 1120°C, 30 min

Density: 7.85 g/cm³ Unetched127

• 0.5% C 1120°C, 30 min

Etched: Nital133

• 0.5% C Warm compacted 1120°C,

30 min Density: 7.2 g/cm³ Unetched . .128

• 0.5% C Warm compacted 1120°C,

30 min Density: 7.35 g/cm³ Unetched .128

• 0.5% MnS-E 1120°C, 30 min

Unetched.130

• 0.5% MnX 1120°C, 30 min

Unetched.131

• 0.8% C 1120°C, 30 min

Etched: Nital133

• 0.45% P + 0.3% C 1120°C,

30 min Etched: Nital139

• 0.45% P + 0.5% C 1120°C,

30 min Etched: Nital139

• 0.45% P 1120°C, 30 min

Etched: Nital138

• 0.45% P 1120°C, 30 min Unetched . .130

• 0.45% P 1250°C, 30 min

Etched: Nital138

• 0.45% P 1250°C, 30 min Unetched . 130

• 0% C 1120°C, 30 min

Etched: Nital132

• 0% C 1120°C, 30 min Unetched . . .126

• 0% C 1250°C, 30 min Etched: Nital .132

• 0% C 1250°C, 30 min Unetched126

• 2.2% Cu (-100) + 2.5% Ni + 0.6% C

1120°C, 30 min Etched: Picral138

• 2% C (-100) 1120°C, 30 min

Unetched.128

• 2% C (-200) 1120°C, 30 min

Unetched.129

• 2% C (Astaloy™ 20 Cu) 1120°C,

30 min Unetched129

• 2% C (Distaloy® Cu) 1120°C,

30 min Unetched129

• 2% Cu (-100) + 0.8% C 1120°C,

30 min Etched: Picral137

• 2% Cu (-100) + 0.45% P + 0.2% C

1120°C, 30 min Etched: Picral140

• 2% Cu (-100) 1120°C, 30 min

Etched: Picral133

• 2% Cu (-100) 1250°C, 30 min

Etched: Picral134

• 2% Cu (-200) + 0.5% C 1120°C,

30 min Etched: Picral135

• 2% Cu (Astaloy™ 20 Cu) + 0.45% P +

0.2% C 1120°C, 30 min

Etched: Picral140

• 2% Cu (Astaloy™ 20 Cu) 1120°C,

30 min Etched: Picral134

• 2% Cu (Distaloy® Cu) 1120°C,

30 min Etched: Picral134

• 3% Cu (-100) + 0.5% C 1120°C,

30 min Etched: Picral136

• 3% Cu (Distaloy® Cu) + 0.5% C

1120°C, 30 min Etched: Picral136

• 3% Cu (Distaloy® Cu) + 0.8% C

1120°C, 30 min Etched: Picral137

• 3% Ni + 0.6% C 1120°C, 30 min

Etched: Picral137

• 4% Cu (-100) + 0.5% C 1120°C,

- 30 min Etched: Picral 135
- 4% Cu (-100) 1120°C, 30 min
- Etched: Picral 135
- 4% Cu (Astaloy™ 20 Cu) + 0.5% C
- 1120°C, 30 min Etched: Picral 136
- LOM image 125
- SEM image 125
- Astaloy™ 85 Mo 163**
- 0.5% C 1120°C, 30 min
- Etched: Nital 163
- 0.8% C 1120°C, 30 min
- Etched: Nital 163
- 2% Cu (-100) + 0.8% C 1120°C,
- 30 min Etched: Nital 164
- Astaloy™ A 165**
- 0.5% C 1120°C, 30 min
- Etched: Nital 166
- 0.8% C 1120°C, 30 min
- Etched: Nital 166
- LOM image 165
- SEM image 165
- Astaloy™ CrA 167**
- 0.4% C 1120°C, 30 min
- Etched: Nital + Picral 168
- 0.6% C 1120°C, 30 min
- Etched: Nital + Picral 168
- 0.8% C 1120°C, 30 min
- Etched: Nital + Picral 168
- 2% Ni + 0.6% C, 1120°C, 30 min
- Etched: Nital + Picral 169
- 2% Cu + 0.6% C, 1120°C, 30 min
- Etched: Nital + Picral 169
- LOM image 167
- SEM image 167
- Astaloy CrM® 170**
- 0.1% C 1120°C, 30 min
- Etched: Nital + Picral 171
- 0.3% C 1120°C, 30 min
- Etched: Nital + Picral 171
- 0.4% C 1120°C, 30 min
- Etched: Nital + Picral 171
- LOM image 170
- SEM image 170
- Astaloy™ Mo 159**
- 0.2% C 1120°C, 30 min
- Etched: Nital 160
- 0.2% C 1250°C, 30 min
- Etched: Nital 160
- 0.5% C 1120°C, 30 min
- Etched: Nital 161
- 0.5% P 1120°C, 30 min
- Etched: Nital 161
- 0.5% P 1250°C, 30 min
- Etched: Nital 162
- 0.8% C 1120°C, 30 min
- Etched: Nital 161
- 0.45% P + 2% Cu (-100) + 0.5% C
- 1120°C, 30 min Etched: Nital 162
- 0% C 1120°C, 30 min
- Etched: Nital 160
- LOM image 159
- SEM image 159
- C**
- CCT 179**
- ASC100.29 + 0.5% C 179
- 0.1°C/second 180
 - 0.5°C/second 180
 - 1°C/second 180
 - 5°C/second 181
 - 20°C/second 181
 - 100°C/second 181
 - Cooling rate 1°C/second 179
- ASC100.29 + 2% Cu (-100) + 0.5% C 182
- 0.1°C/second 183
 - 0.5°C/second 183
 - 1°C/second 183
 - 5°C/second 184
 - 20°C/second 184
 - 100°C/second 184
 - Cooling rate 1°C/second 182
- Astaloy™ 85 Mo + 0.8% C 218
- 0.1°C/second 219
 - 0.25°C/second 219
 - 0.5°C/second 219
 - 1°C/second 220
 - 2.5°C/second 220
 - 10°C/second 220
 - Cooling rate 0.5°C/second 218
- Astaloy™ 85 Mo + 2% Cu(-100) +
- 0.8% C 221
 - 0.25°C/second 222
 - 0.5°C/second 222

1°C/second	222	0.5°C/second	240
2.5°C/second	223	1°C/second	240
3.5°C/second	223	2.5°C/second	241
10°C/second	223	5°C/second	241
Cooling rate 1°C/second	221	10°C/second	241
Astaloy™ A + 0.6% C	224	Cooling rate 1°C/second	239
0.1°C/second	228	Astaloy™ CrM + 0.5% C	242
0.5°C/second	228	0.1°C/second	243
1.5°C/second	228	0.5°C/second	243
2°C/second	229	1°C/second	243
5°C/second	229	2.5°C/second	244
10°C/second	229	12°C/second	244
Cooling rate 1°C/second	224	25°C/second	244
Astaloy™ CrA + 0.8% C	227	Cooling rate 1°C/second	242
0.1°C/second	228	Astaloy™ Mo + 0.4% C	212
0.5°C/second	228	0.25°C/second	213
1.5°C/second	228	0.5°C/second	213
2°C/second	229	0.85°C/second	213
5°C/second	229	2.5°C/second	214
10°C/second	229	8°C/second	214
Cooling rate 1.5°C/second	227	56°C/second	214
Astaloy™ CrA + 2% Cu + 0.6% C	230	Cooling rate 0.85°C/second	212
0.25°C/second	231	Astaloy™ Mo + 0.6% C	215
0.5°C/second	231	0.25°C/second	216
1.5°C/second	231	0.5°C/second	216
2°C/second	232	0.85°C/second	216
5°C/second	232	2.5°C/second	217
10°C/second	232	8°C/second	217
Cooling rate 1.5°C/second	230	40°C/second	217
Astaloy™ CrA + 2% Ni + 0.6% C	233	Cooling rate 0.85°C/second	215
0.25°C/second	234	Distaloy® AB + 0.5% C	185
0.5°C/second	234	0.1°C/second	186
1.5°C/second	234	0.5°C/second	186
2°C/second	235	1°C/second	186
5°C/second	235	5°C/second	187
10°C/second	235	20°C/second	187
Cooling rate 1.5°C/second	233	100°C/second	187
Astaloy CrM® + 0.3% C	236	Cooling rate 1°C/second	185
0.1°C/second	237	Distaloy® AB + 0.8% C	188
0.5°C/second	237	0.1°C/second	189
1°C/second	237	0.5°C/second	189
2.5°C/second	238	1°C/second	189
5°C/second	238	2.5°C/second	190
10°C/second	238	10°C/second	190
Cooling rate 1°C/second	236	25°C/second	190
Astaloy CrM® + 0.4% C	239	Cooling rate 1°C/second	188
0.1°C/second	240		

Distaloy® AE + 0.5% C	191	Distaloy® HP + 0.5% C	197
0.1°C/second	192	0.25°C/second	198
0.5°C/second	192	0.5°C/second	198
1°C/second	192	0.85°C/second	198
2.5°C/second	193	4°C/second	199
5°C/second	193	8°C/second	199
10°C/second	193	64°C/second	199
Cooling rate 1°C/second	191	Cooling rate 0.85°C/second	197
Distaloy® AE + 0.8% C	194		
0.1°C/second	195		
0.25°C/second	195		
0.5°C/second	195		
1°C/second	196		
2.5°C/second	196		
5°C/second	196		
Cooling rate 0.5°C/second	194		
Distaloy® DC + 0.5% C	200		
0.125°C/second	201		
0.5°C/second	201		
0.85°C/second	201		
4°C/second	202		
8°C/second	202		
70°C/second	202		
Cooling rate 0.85°C/second	200		
Distaloy® DH + 0.4% C	203		
0.25°C/second	204		
0.5°C/second	204		
0.85°C/second	204		
2.5°C/second	205		
8°C/second	205		
56°C/second	205		
Cooling rate 0.85°C/second	203		
Distaloy® DH + 0.5% C	206		
0.1°C/second	207		
0.5°C/second	207		
1°C/second	207		
5°C/second	208		
20°C/second	208		
100°C/second	208		
Cooling rate 1°C/second	206		
Distaloy® DH + 0.6% C	209		
0.1°C/second	210		
0.5°C/second	210		
1°C/second	210		
5°C/second	211		
20°C/second	211		
100°C/second	211		
Cooling rate 1°C/second	209		
		D	
		Distaloy® AB	149
		• 0.2% C 1120°C, 30 min	
		Etched: Picral	149
		• 0.5% C 1120°C, 30 min	
		Etched: Picral	149
		Distaloy® AE	143
		• 0.2% C 1120°C, 30 min	
		Etched: Picral	145
		• 0.3% C 1250°C, 30 min	
		Etched: Picral	145
		• 0.45% C 1120°C, 15 min	
		Etched: Picral	148
		• 0.45% C 1120°C, 30 min	
		Etched: Picral	148
		• 0.45% C 1120°C, 45 min	
		Etched: Picral	148
		• 0.5% C 1120°C, 30 min	
		Etched: Picral	146
		• 0.5% C 1250°C, 30 min	
		Etched: Picral	146
		• 0.8% C 1120°C, 30 min	
		Etched: Picral	146
		• 0% C 1120°C, 30 min	
		Etched: Picral	145
		• 1% C 1120°C, 30 min	
		Etched: Picral	147
		• 1% C 1250°C, 30 min	
		Etched: Picral	147
		LOM image	143
		LOM image Etched: Nital	144
		SEM image	143
		Distaloy® AQ	150
		• 0.6% C 1120°C, 30 min	
		Etched: Picral	150
		• 0.8% C 1120°C, 30 min	
		Etched: Picral	150

Distaloy® DC	152
• 0.2% C 1120°C, 30 min	
Etched: Picral	152
• 0.5% C 1120°C, 30 min	
Etched: Picral	152
• 0.8% C 1120°C, 30 min	
Etched: Picral	152
Distaloy® DH	154
• 0.2% C 1120°C, 30 min	
Etched: Picral	154
• 0.5% C 1120°C, 30 min	
Etched: Picral	154
• 0.8% C 1120°C, 30 min	
Etched: Picral	155
Distaloy® HP	156
• 0.2% C 1120°C, 30 min	
Etched: Picral	156
• 0.3% C 1120°C, 30 min	
Etched: Picral	156
• 0.5% C 1120°C, 30 min	
Etched: Picral	157
• 0.5% C 1250°C, 30 min	
Etched: Picral	157
• 0.8% C 1120°C, 30 min	
Etched: Picral	157

H

Heat Treatment	247
Astaloy™ CrA	263
Steam treated + Nitrocarburised	
Overview	263
Steam treated + Nitrocarburised	
Surface	263
Astaloy CrM®	259
Carbonitrided Centre	261
Carbonitrided Overview	261
Carbonitrided Surface	261
Case hardened Centre	259
Case hardened Overview	259
Case hardened Surface	259
Plasmanitrided Overview	262
Plasmanitrided Surface	262
Through hardened Centre	260
Through hardened Overview	260
Through hardened Surface	260

Astaloy™ Mo	257
Case hardened Centre	257
Case hardened Overview	257
Case hardened Surface	257
Through hardened Centre	258
Through hardened Overview	258
Through hardened Surface	258
Distaloy® AB	251
Case hardened Centre	251
Case hardened Overview	251
Case hardened Surface	251
Through hardened Centre	252
Through hardened Overview	252
Through hardened Surface	252
Distaloy® AE	253
Case hardened Centre	253
Case hardened Overview	253
Case hardened Surface	253
Through hardened Centre	254
Through hardened Overview	254
Through hardened Surface	254
Distaloy® AQ	248
Through hardened Surface	
Ø 25mm	248
Through hardened Centre	
Ø 25mm	248
Through hardened Surface	
Ø 64mm	249
Through hardened Centre	
Ø 64mm	249
Induction hardened Centre	250
Induction hardened Overview	250
Induction hardened Surface	250
Distaloy® HP	255
Case hardened Centre	255
Case hardened Overview	255
Case hardened Surface	255
Through hardened Centre	256
Through hardened Overview	256
Through hardened Surface	256

M

MH80.23	101
0.2% C 1050°C, 30 min Etched: Nital	103
0.2% C 1120°C, 30 min Etched: Nital	104
0.5% C 1050°C, 30 min Etched: Nital	104

0.5% C 1120°C, 30 min Etched: Nital . 104
 0% C 1050°C, 30 min Etched: Nital . . 103
 0% C 1050°C, 30 min Unetched 102
 0% C 1120°C, 30 min Etched: Nital . . 103
 0% C 1120°C, 30 min Unetched 102
 1% C 1050°C, 30 min Etched: Nital . . 105
 1% C 1120°C, 30 min Etched: Nital . . 105
 • 2% Cu (-100) + 0.5% C 1050°C,
 30 min Etched: Nital 105
 • 2% Cu (-100) + 0.5% C 1120°C,
 30 min Etched: Nital 106
 • 2% Cu (Distaloy[®] Cu) + 0.8% C
 1050°C, 30 min Etched: Nital 107
 • 2% Cu (Distaloy[®] Cu) + 0.8% C
 1120°C, 30 min Etched: Nital 107
 • 2% Cu (Distaloy[®] MH) + 0.5% C
 1050°C, 30 min Etched: Nital 106
 • 2% Cu (Distaloy[®] MH) + 0.5% C
 1120°C, 30 min Etched: Nital 106
 LOM image 101
 SEM image 101

N
NC100.24 108

• 0.2% C 1120°C, 30 min
 Etched: Nital 113
 • 0.5% C 1120°C, 30 min
 Density: 6.2g/cm³ Unetched 109
 • 0.5% C 1120°C, 30 min
 Density: 6.65g/cm³ Unetched 109
 • 0.5% C 1120°C, 30 min
 Density: 7.02g/cm³ Unetched 110
 • 0.5% C 1120°C, 30 min
 Density: 7.2g/cm³ Unetched 110
 • 0.5% C 1120°C, 30 min
 Density: 7.8g/cm³ Unetched 110
 • 0.5% C 1120°C, 30 min
 Etched: Nital 114
 • 0.8% C 1120°C, 30 min
 Etched Nital 117
 • 0.45% P + 0.5% C 1120°C, 30 min
 Etched: Nital 118
 • 0.45% P 1120°C, 30 min
 Etched: Nital 118
 • 0.45% P 1120°C, 30 min
 Unetched 112

• 0% C 1120°C, 30 min
 Etched: Nital 113
 • 0% C 1130°C, 30 min
 Unetched 109
 • 0% C 1250°C, 30 min
 Etched: Nital 113
 • 2.5% Cu (-100) + 2.5% Ni + 0.6% C
 1120°C, 30 min Etched: Picral 118
 • 2% Cu (-100) + 0.4% C 1120°C,
 30 min Etched: Nital 115
 • 2% Cu (-100) + 0.8% C 1120°C,
 30 min Etched Nital 116
 • 2% Cu (-100) 1120°C, 30 min
 Etched: Nital 114
 • 2% Cu (-100) 1120°C, 30 min
 Unetched 111
 • 2% Cu (-100) 1250°C, 30 min
 Etched: Nital 114
 • 2% Cu (-200) 1120°C, 30 min
 Unetched 111
 • 2% Cu (Distaloy[®] Cu) + 0.4% C
 1120°C, 30 min Etched Nital 116
 • 2% Cu (Distaloy[®] Cu) + 0.7% C
 1120°C, 30 min Etched Nital 116
 • 2% Cu (Distaloy[®] Cu) 1120°C,
 30 min Etched: Nital 115
 • 2% Cu (Distaloy[®] Cu) 1120°C,
 30 min Unetched 111
 • 3% Cu (-100) + 0.8% C 1120°C,
 30 min Etched: Nital 117
 • 3% Ni + 0.6% C 1120°C, 30 min
 Etched: Picral 117
 • 4% Cu (-100) 1120°C, 30 min
 Etched: Nital 115
 LOM image 108
 SEM image 108

S
SC100.26 119

• 0.5% C 1120°C, 30 min
 Density: 6.8 g/cm³ Unetched 120
 • 0.5% C 1120°C, 30 min
 Density: 7.15 g/cm³ Unetched 120
 • 0.5% C 1120°C, 30 min
 Etched: Nital 121
 • 0% C 1120°C, 30 min
 Etched: Nital 121

- 0% C 1250°C, 30 min
Etched: Nital 121
- 2% Cu (-100) + 0.2% C 1120°C,
30 min Etched: Picral 122
- 2% Cu (-100) + 0.5% C 1120°C,
30 min Etched: Picral 122
- 2% Cu (-100) + 0.8% C 1120°C,
30 min Etched: Picral 123
- 2% Cu (-100) + 2.5% Ni + 0.6% C
1120°C, 30 min Etched: Picral 123
- 2% Cu (-100) 1120°C, 30 min
Etched: Picral 122
- LOM image 119
- SEM image 119

Metallographic Sample Preparation

3.1	General Considerations	274
3.2	Cutting	276
3.3	Mounting	277
3.4	Mechanical Preparation	278
3.5	Etching	280

3.1 General Considerations

The aim of metallographic sample preparation is to reveal the true structure of the material being investigated. The major difference between PM and wrought metal materials is that the porosity of PM materials must be considered during sample preparation. Careful metallographic preparation is important because the amount and shape of the pores in an observed sample should reveal a true picture of the material being sampled.

During metallographic preparation of most sintered specimens, the pores become smeared during grinding and rough polishing. Proper polishing will open the smeared pores and reveal their true shapes and distribution. Showing an accurate amount of porosity is necessary to observe the density variation within a sample.

Figures 3.1-3.4 show the effect of grinding and polishing on pore opening. The material used for this sample was a compacted and sintered component made from ASC100.29 (without carbon) and with a density of 7.2 g/cm^3 .

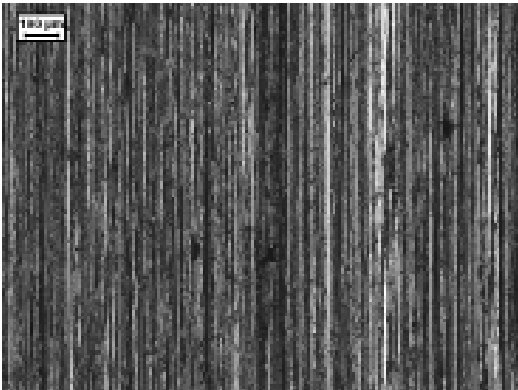


Figure 3.1. After grinding with 180 paper.

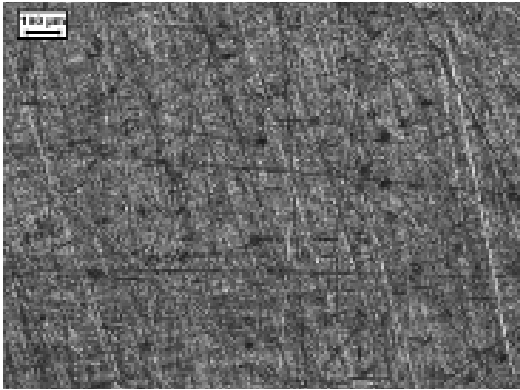


Figure 3.2. Fine grinding with $9\mu\text{m}$ DP (Diamond polishing).

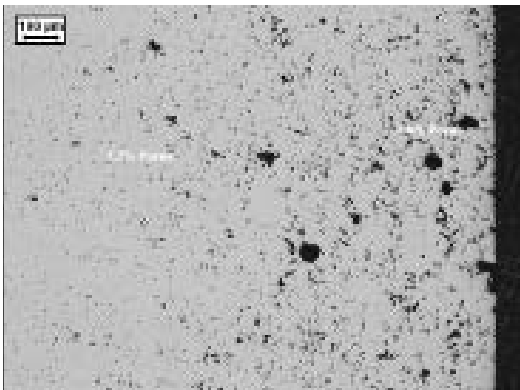


Figure 3.3. Polished for two minutes with $3\mu\text{m}$ DP.

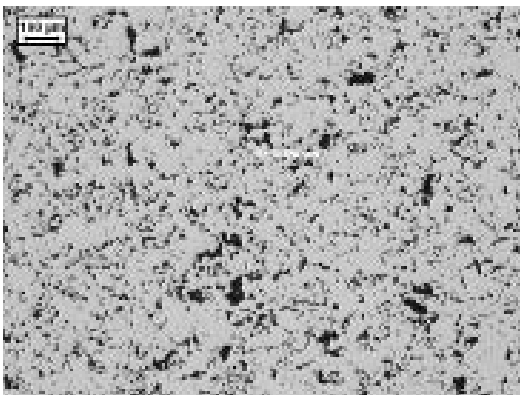


Figure 3.4. Polished for eight minutes with $3\mu\text{m}$ DP and 20 seconds with $1\mu\text{m}$ DP.

3.2 Cutting

Because of the difficulty in opening all the pores in a PM part, the use of smaller sections is recommended. An easy polished specimen will measure less than 15 x 15 mm.

A soft abrasive wheel that breaks down easily will control overheating during cutting. A substantial flow of water correctly striking the interface between the wheel and the part is also required. Rust inhibitor should be added to recirculated water. The choice of wheel depends of the material to be cut. Hard bakelite/ Al_2O_3 wheels are recommended for soft materials and soft bakelite/ Al_2O_3 wheels for harder material.

After cutting, water and rust inhibitor, as well as oil from heat treatment and machining, must be removed from the specimen with acetone. If the specimen contains a lot of oil it may be necessary to use washing with Soxhlet. A solvent such as toluene or acetone is placed in a flask and the specimens to be cleaned are placed in the siphon cup inside the flask. A cold-water line is connected to the condenser coil and the flask is heated to the boiling temperature of the solvent. The solvent evaporates, and when the vapour contacts the cold condensing coil, it drips into the siphon cup and onto the specimens.

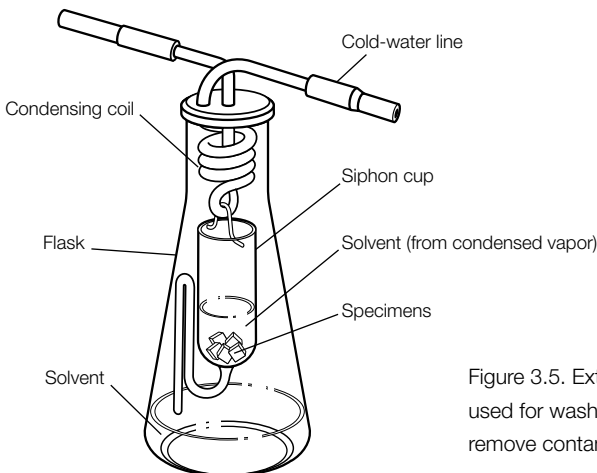


Figure 3.5. Extractor-condenser used for washing PM specimens to remove contaminants from pores.

3.3 Mounting

Depending on the number of samples and the quality required, both cold mounting and hot mounting techniques have certain advantages. The best results are achieved when samples are free from grease and other contaminants. This ensures good adhesion of resin to each sample.

3.3.1 Cold vacuum mounting

Cold mounting in a vacuum is required for **green specimens** and samples taken from **magnetic applications**. All pores connected to the surface require special procedures that include the use of epoxy resin and vacuum impregnation. The specimens are put in a cup and air is evacuated in a vacuum chamber for at least 15 minutes. When evacuation is completed, resin is carefully poured over the specimens. The specimens are then cured at 70°C for 1-2 hours.

3.3.2 Hot compression mounting

Hot compression mounting is used with **sintered and heat-treated** specimens. The sample is put in the mounting press and 1/3 of resin with glass fibre is added first and then 2/3 of bakelite. The sample is processed under high pressure both during the heating and cooling cycles. This results in the least shrinkage and helps to maintain good adhesion between the resin and the sample.

Hot compression mounting can also be used with **metallic powders**. It is possible to reach a good result with hot mounting of powder particles if a resin with fine particle size is used. Mix 1-2 ml of the powder with 5 ml of a fine-particle resin in a small container. Pour the powder mix in the mounting press, add 5 ml bakelite on top, and process as above.

3.4 Mechanical Preparation

Mechanical preparation is the most common method of preparing metallographic samples of sintered and heat-treated materials for microscopic examination. Abrasive particles are used in successively finer steps in order to remove undesired material from the sample surface, until the required result is reached. Mechanical preparation is divided into two operations: **grinding** and **polishing**.

3.4.1 Grinding

The first step in mechanical material removal is called grinding. Proper grinding removes damaged or deformed surface material, while introducing only limited amounts of new deformation. The aim is to reach a plane surface while creating minimal damage that can be removed easily during polishing, in the shortest possible time. Grinding consists of two separate processes: Plane grinding and fine grinding.

Plane grinding

Plane grinding ensures that the surface of all specimens are similar and in the same level or plane. Relatively coarse fixed abrasive particles are used to remove material quickly. SiC papers or Al_2O_3 grinding stones are employed with most ferrous materials.

Fine grinding

Fine grinding produces a surface with such a small amount of deformation that it can be removed during polishing. Five different grades of SiC paper (220, 320, 500, 800 and 1200 mesh) or a thin hard composite disc with $9\ \mu\text{m}$ DP-suspension can be used for fine grinding. For non-sintered components and powders, it is usually possible to begin fine grinding with SiC paper 500 or 800.

3.4.2 Polishing

After grinding, the pores on a sample surface will be almost completely smeared. The aim of polishing is to open all the pores, and to show the true area-fraction of porosity, and to remove scratches. A 3 μm DP-suspension is recommended for the first polishing step. The abrasive first step opens the pores closest to the specimen surface. Samples should be examined under the microscope after the first step. Polishing times of up to 15 minutes may be required to open all the pores on a large and soft ferritic specimen. A 1 μm DP-suspension on a somewhat softer cloth is recommended as a final polishing step.

3.4.3 General rules to improve sample preparation

Before proceeding with each step in grinding and polishing, make sure that all forms of damage from the previous step, such as scratches, pull-outs or embedded grains, are removed completely. If this is not done, artifacts from an early step may show on the finished surface, and it may be impossible to be sure about their origin. Keep preparation times as short as possible. Extended preparation times may damage the sample and the true pore and edge roundness will not be achieved.

3.5 Etching

The most commonly used etchants for powder metallurgical materials are included in this section.

3.5.1 Nital Fe 1

100 ml -95% Ethyl alcohol, 1 ml concentrated HNO_3 .

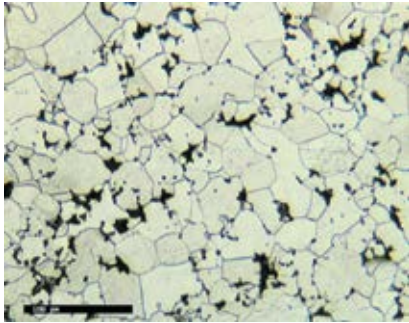
Etching time: 10-60 seconds

Common etchant for steel with ferritic, pearlitic and bainitic structures.

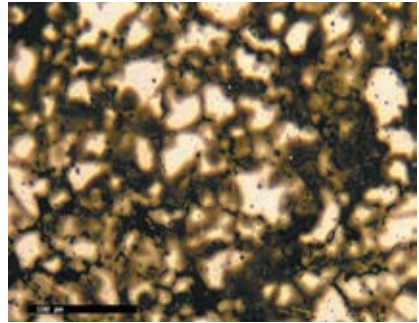
Base materials: NC100.24, SC100.26, ASC100.29, AHC100.29, PASC and PNC-grades, Astaloy™ A, Astaloy Mo and Astaloy 85 Mo.

Uses:

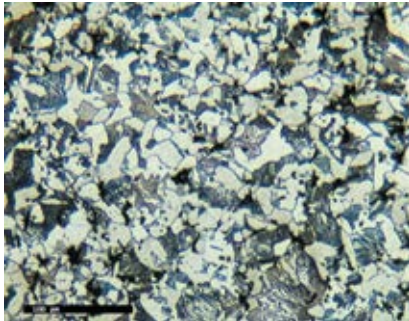
- Grain boundaries in ferrite.
- Amount of pearlite and ferrite to estimate carbon content.
- Amount of martensite to define the case depth.
- 4% Nital can be used to detect the diffusion of phosphorous in PASC and PNC materials.



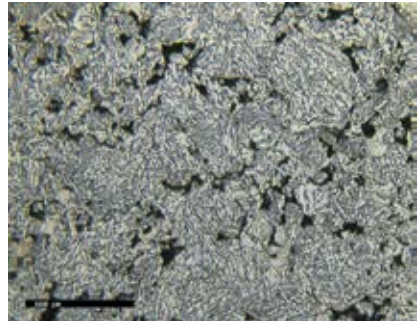
ASC100.29



ASC100.29 + 4% Cu



ASC100.29 + 0.6% C



Astaloy Mo + 0.5% C

Figure 3.6. Four steel samples with ferritic, pearlitic and bainitic structures etched with Nital Fe 1.

3.5.2 Picral

100 ml-95% Ethyl alcohol, 4 g Picric acid.

Etching time: 10-60 seconds depending on carbon content.

Etchant for materials where Ni is diffusion bonded or added in the mix.

Uses: For diffusion bonded Ni or mixed in Ni.

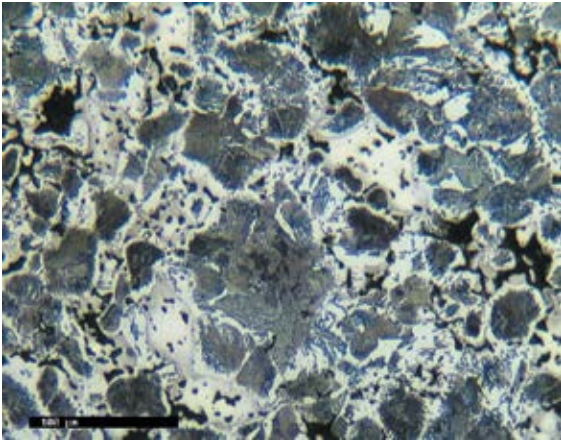


Figure 3.7. ASC100.29 + 3% Ni + 0.5% C, etched with Picral.

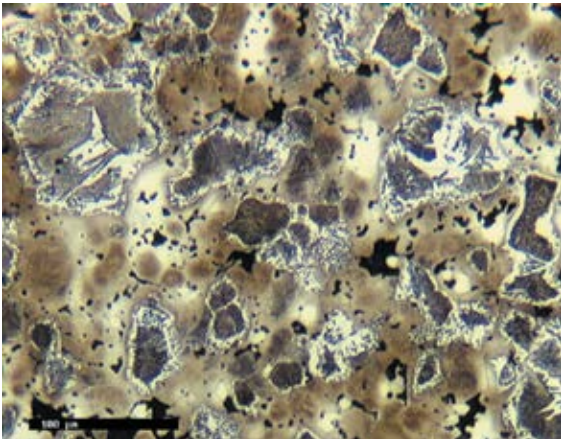


Figure 3.8. Distaloy® AE + 0.5% C, etched with Picral.

3.5.3 Nital + Picral

100 ml 95% Ethyl alcohol, 4g Picric acid +1-2 ml HNO_3 .

Etching time: 20-100 seconds depending on carbon and alloying content. Martensitic structures need longer times and sometimes it is necessary to add 2 ml HNO_3 to the etchant. It is an etchant for pre-alloyed materials with low Cr-content. **Uses:** To develop good contrast between pearlite, bainite, martensite and lower bainite.

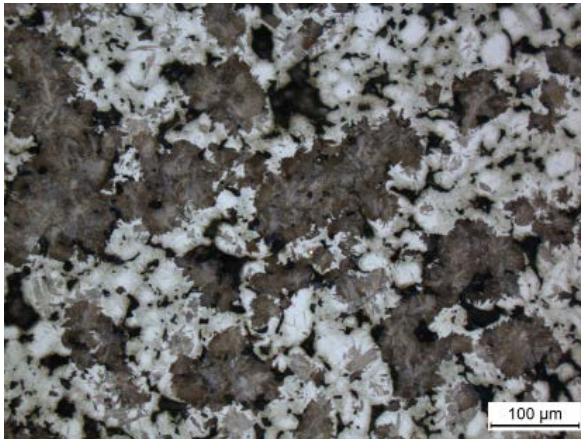


Figure 3.9. Astaloy™ CrA + 2% Cu + 0.6% C

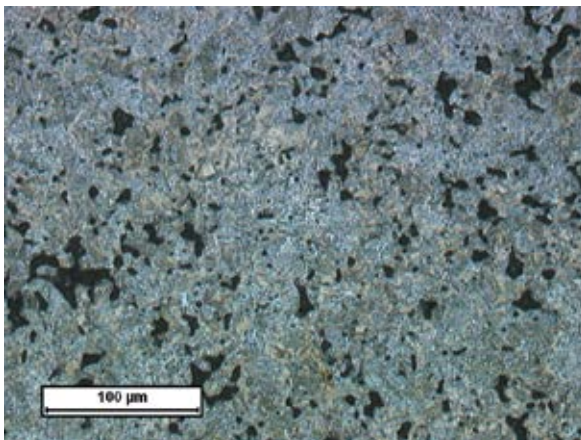



Figure 3.10. Astaloy CrM® + 0.5% C

Defective Microstructures

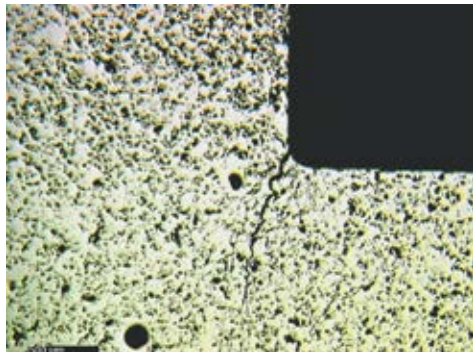
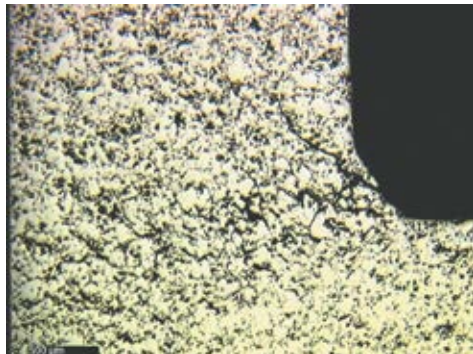
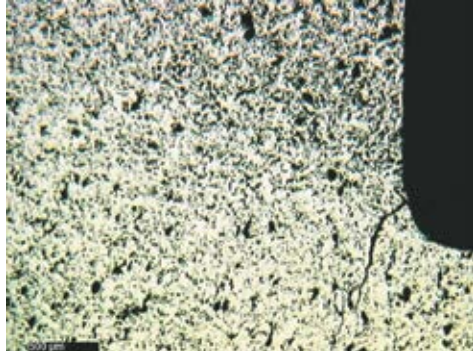


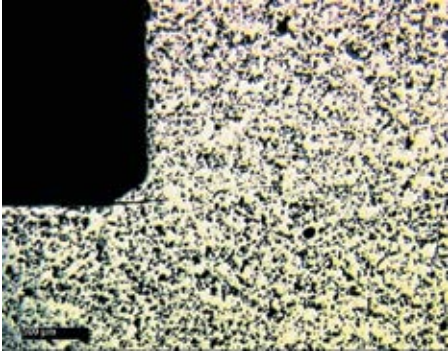
4.1	Defects in Pressing.	286
4.2	Defects in Mixing and Powder Feeding	289
4.3	Defects in Sintering	291
4.4	Defects after Secondary Operation.	298
4.5	Defects after Sample Preparation.	299
4.6	Defects in Heat Treatment	300



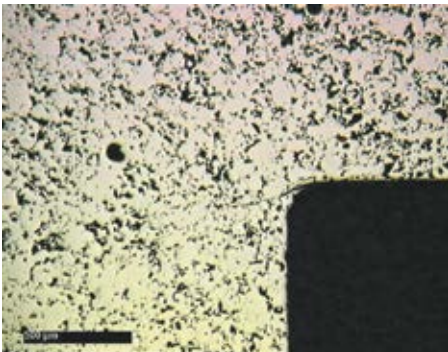
4.1 Defects in Pressing

Three images of cracks formed in pressing or ejection.

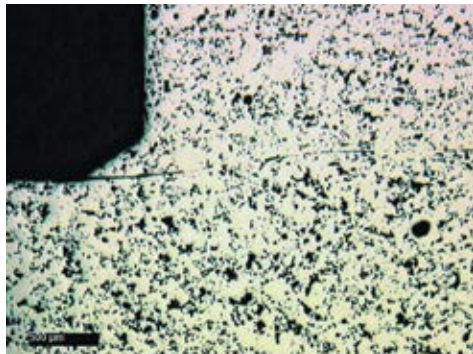
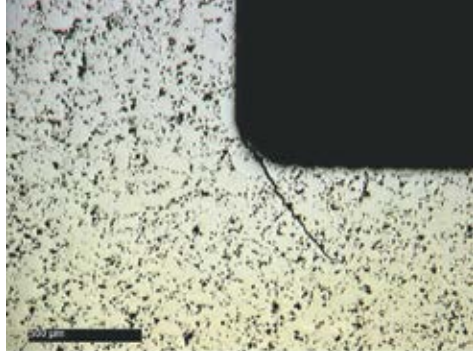




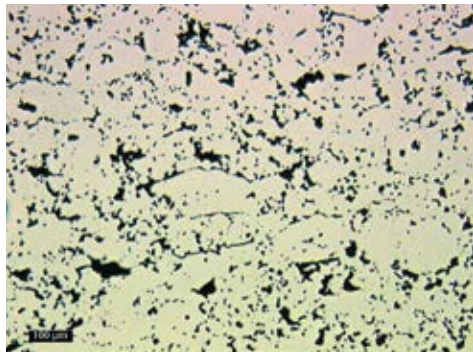
Three images of cracks formed in pressing or ejection.



Two images of cracks formed in pressing or ejection.

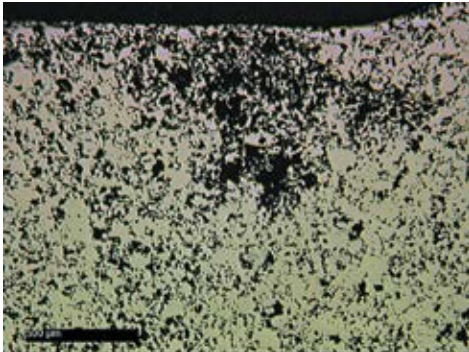


.....
Lamination cracks.

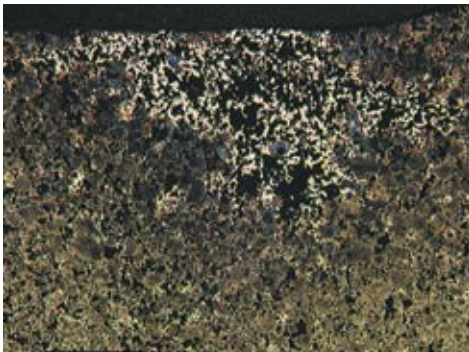


.....

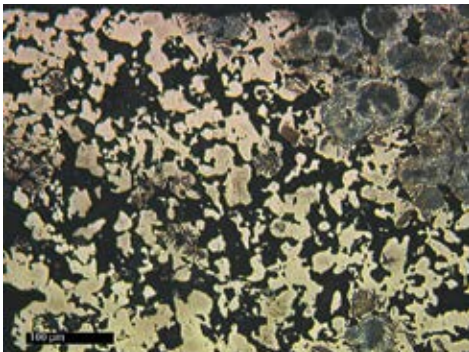
4.2 Defects in Mixing and Powder Feeding



Agglomerate of fines close to the surface.



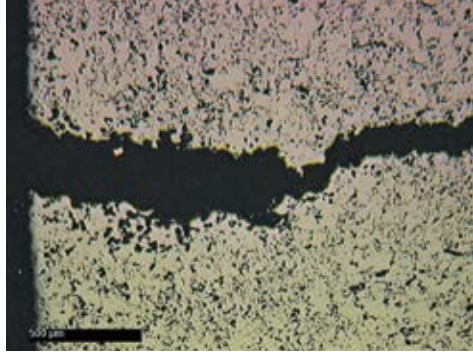
As above but etched.



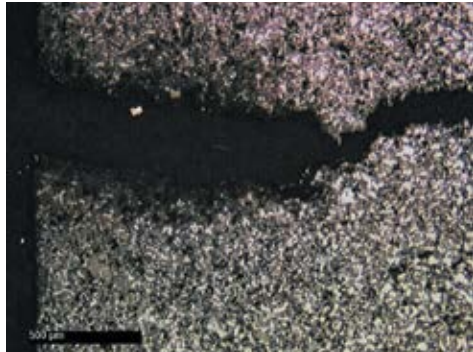
As above, in higher magnification.



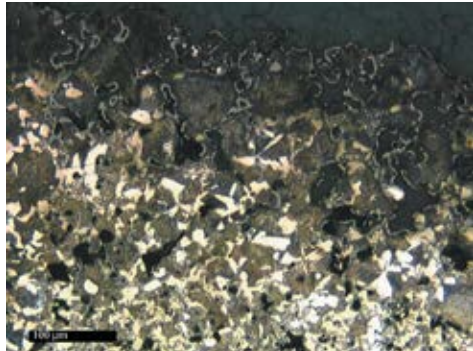
Crack due to agglomeration of graphite or lubricant and graphite.



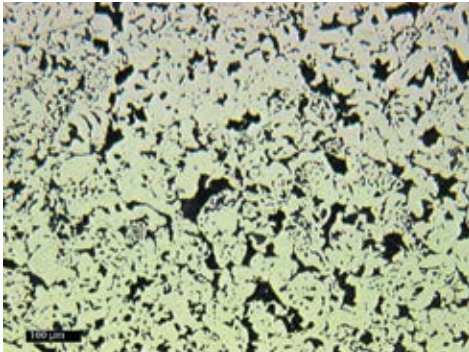
As above but etched.



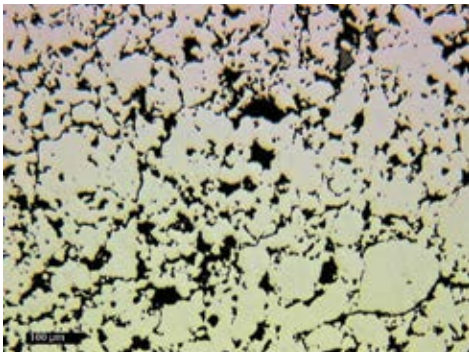
As above, in higher magnification.



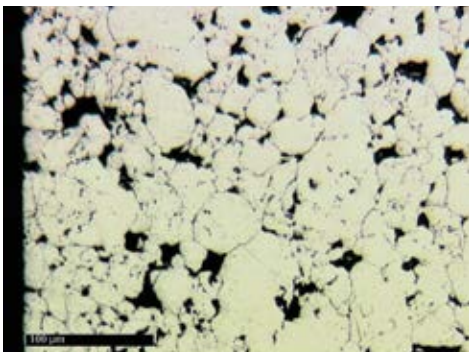
4.3 Defects in Sintering



Sponge iron material with poor sintering necks.



Diffusion alloyed material with poor sintering necks.

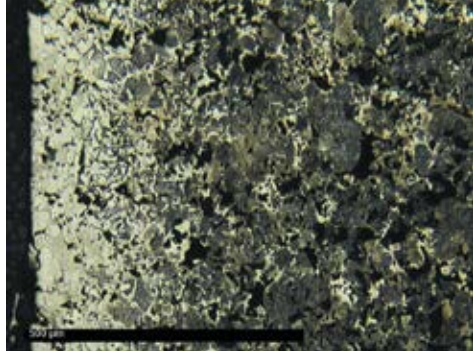


Oxidation at the surface (Astaloy CrM[®] + 0.3% C).

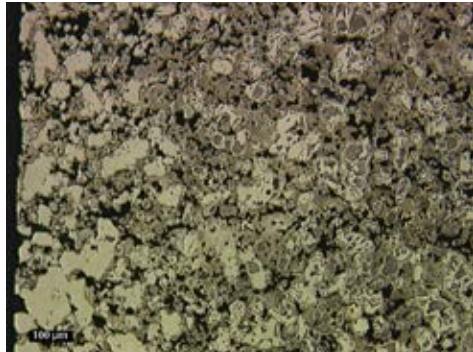


4.3.1 Decarburisation

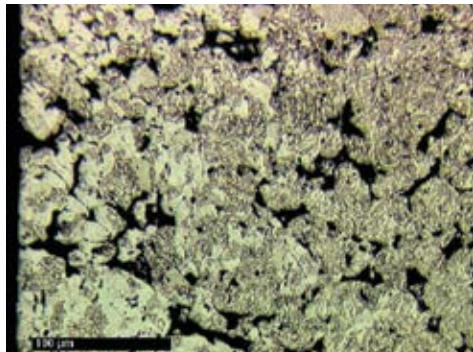
Decarburisation at the surface (NC100.24 + 0.5% Cu + 0.6% Ni + 1% C).



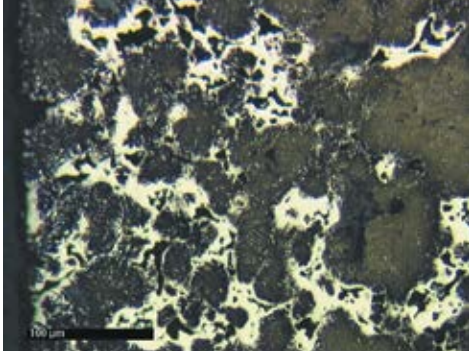
Decarburisation at the surface (Distaloy® AB + 0.6% C).



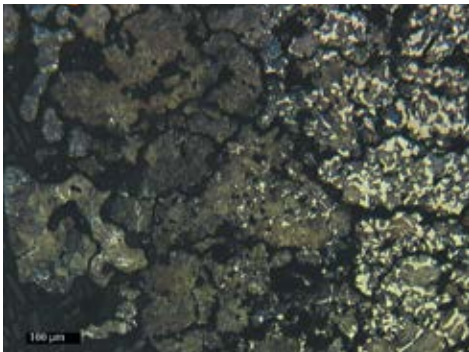
Decarburisation at the surface (Astaloy CrM® + 0.3 % C).



4.3.2 Carburisation



Carburisation at the surface (Distaloy® HP + 0.5% C).

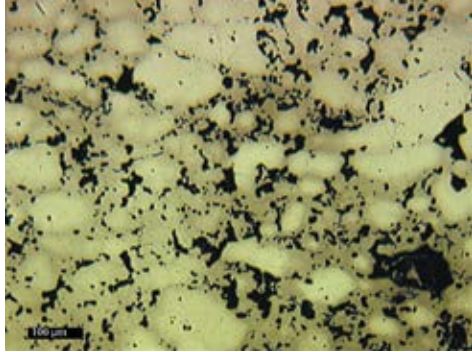


Carburisation at the surface (ASC100.29 + 0.3% P + 0% C).



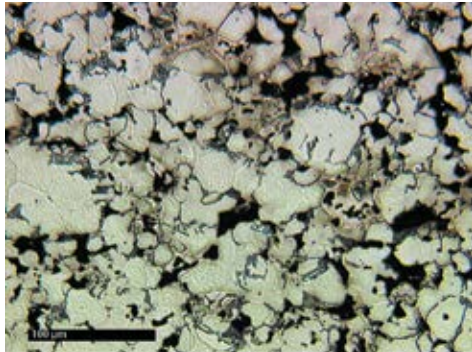
4.3.3 Too short sintering time

Insufficient diffusion of Cu.



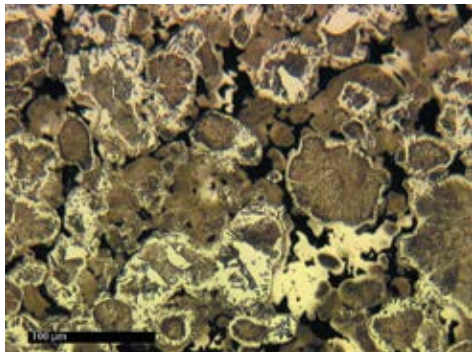
.....

Insufficient diffusion of Ni, Cu and C.

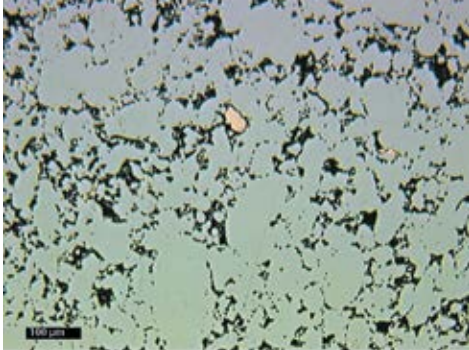


.....

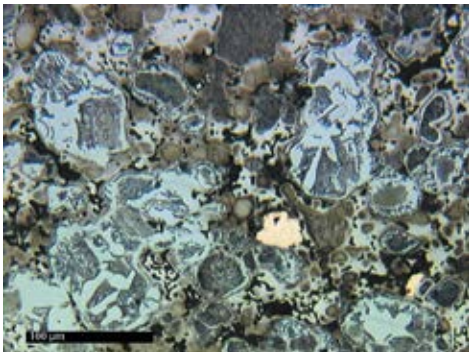
Insufficient diffusion of Ni and Cu in a diffusion alloyed material.



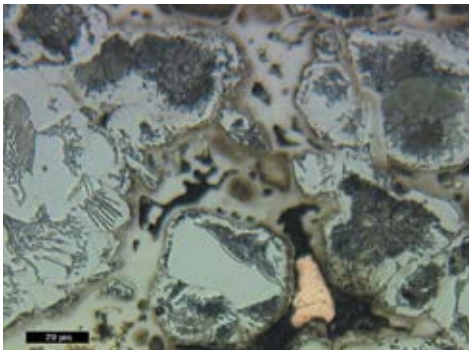
4.3.4 Too low sintering temperature



Free Cu in a diffusion alloyed material.



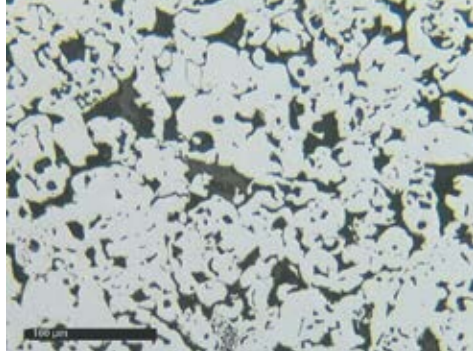
As above but etched.



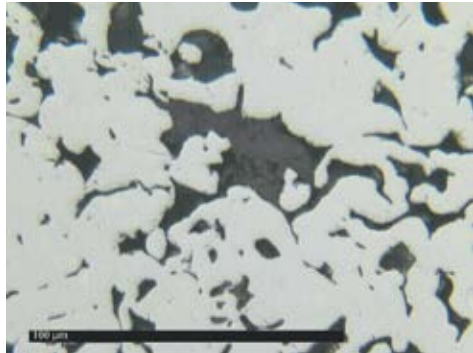
As above, in higher magnification.



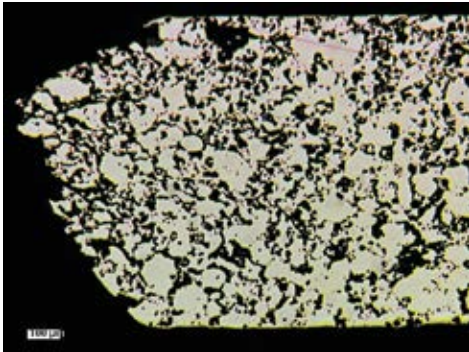
Free graphite and poor sintering necks in a sponge iron material.



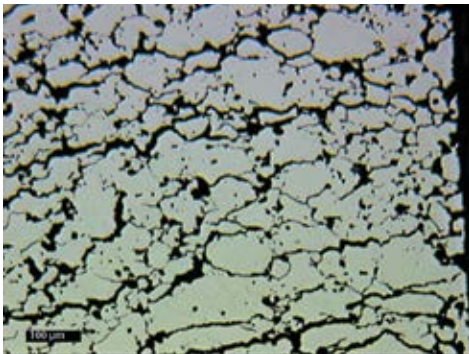
As above, in higher magnification.



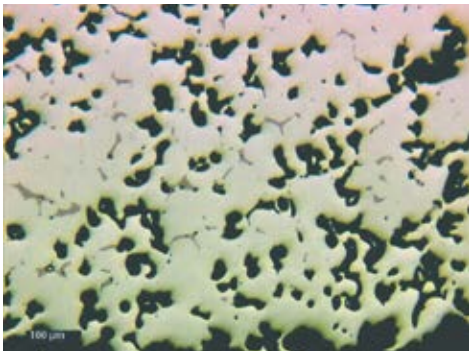
4.3.5 Other Sintering defects



Blistering on the surface.



Blistering on the surface.

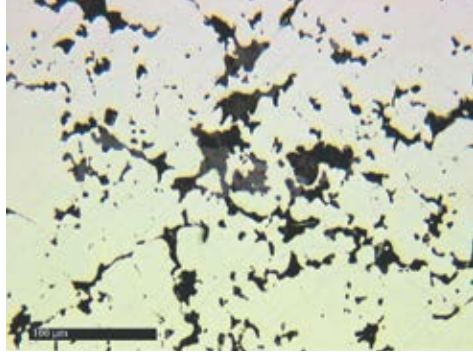


Sulphides due to a S-rich sintering atmosphere.

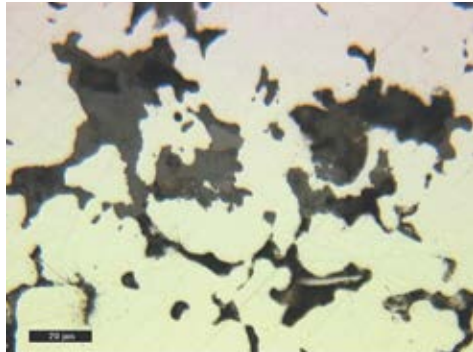


4.4 Defects after Secondary Operation

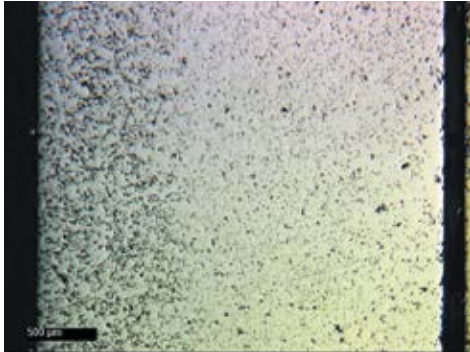
Rust in the pores after machining.



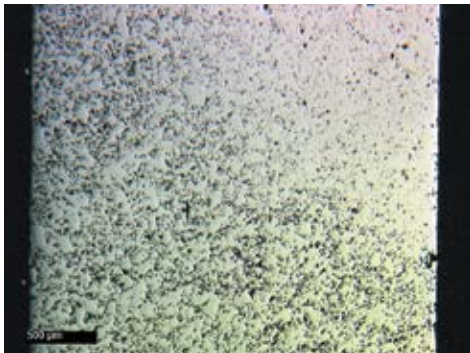
As above, in higher magnification.



4.5 Defects after Sample Preparation



Insufficient pore opening due to short polishing time.



Insufficient pore opening due to short polishing time.



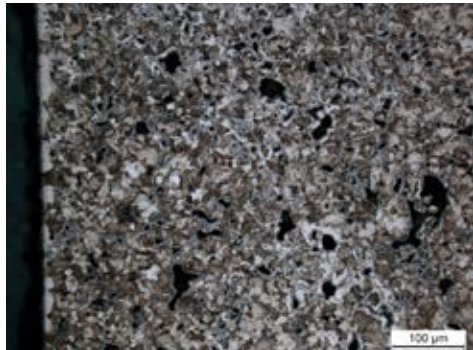
4.6 Defects in Heat Treatment

4.6.1 Nitrocarburisation

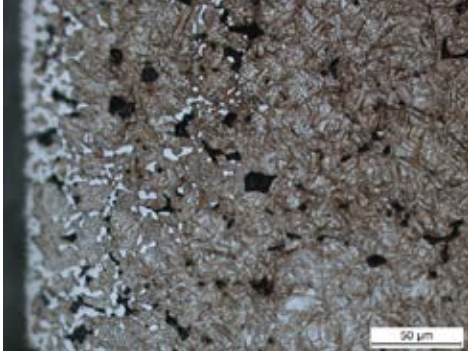
Steam treated and
over nitrocarburised.
Overview



Steam treated and
over nitrocarburised.
Surface



4.6.2 Case hardening



Overcarbured during case hardening.



Metallography

Metallography is the study of the microstructure of all types of metallic alloys. It can be divided in two areas:

- The formation and transformation of microstructure
- The relationship between microstructure and mechanical properties

Metallography is used in almost all stages of a component's lifetime – from the initial material development, through production and quality control and even failure analyses if needed.

In Powder Metallurgy (PM) the initial structure is formed in the atomising or sponge process of the iron based powders. These base powders are then often mixed with graphite and other alloying elements, i.e. copper, nickel, molybdenum and phosphorous. During the sintering these elements diffuse and new structures are formed upon cooling. Subsequent heat treatments where carbon and/or nitrogen content is increased at the surface can also be applied, followed by quenching. This results in a harder microstructure with higher strength and lower ductility. By selecting the proper combination of material and processing conditions you can tailor the microstructure and mechanical properties for each application.

The most frequently used tools for metallographic investigations are light optical microscopy (LOM) and scanning electron microscopy (SEM).